Kırıkkale University International Journal of Engineering Research and Development

International Peer Reviewed Journal
e-ISSN: 1308-5514

Volume: 9
Issue: 3
DECEMBER 2017
Special Issue

Kırıkkale Üniversitesi Uluslararası Mühendislik Araştırma ve Geliştirme Dergisi

Uluslararası Hakemli Dergi
Cilt: 9 Sayı:3 Aralık 2017 Özel Sayı

KIRIKKALE ÜNİVERSİTESİ / KIRIKKALE UNIVERSITY

Uluslararası Mühendislik Araştırma ve Geliştirme Dergisi
International Journal of Engineering Research and Development

Yazışma Adresi /Address
Kırıkkale Üniversitesi Mühendislik Fakültesi 71450-
Kampüs- Kırıkkale- TÜRKİYE
http://ijerad.kku.edu.tr
ijerad@kku.edu.tr
Tel : +90-318-357-42 42 (1001)
Fax: +90-318-357-24 59

ISSN - Online: 1308-5514

Aralık / December 2017
Özel Sayı / Special Issue

Kapak Tasarım / Graphics Design : Hüseyin AYDİLEK

MÜHENDİSLİK FAKÜLTESİ

KIRIKKALE ÜNİVERSİTESİ / KIRIKKALE UNIVERSITY

Uluslararası Mühendislik Araştırma ve Geliştirme Dergisi
International Journal of Engineering Research and Development

Amaç

Uluslararası Mühendislik Araştırma ve Geliştirme Dergisi mühendisliğin tüm disiplinlerinde çalışılmış olan orijinal ve yüksek kalitedeki araştırma sonuçlarını basan ve teşvik eden bir araştırma dergisidir. Akademisyenler, bilim adamları, üniversitelerdeki araştırmacılar ve ilgi duyan herkesin çalışmaları basım için düşünülebilir.

Aim

International Journal of Engineering Research and Development is a peer-reviewed international research journal aiming at promoting and publishing original high-quality research in all disciplines of engineering sciences and technology. Manuscripts are invited from academicians, scientists, researchers of universities and industry and for all interested people for publication consideration.

Araştırma Alanı

Mühendislik Teorisi ve Uygulamaları

Research Highlights

Engineering Theory and Applications

Kapsam

Derginin ilgi alanlarında, sınırlama olmaksızın, Elektrik-Elektronik Mühendisliği, Makina Mühendisliği, İnşaat Mühendisliği, Bilgisayar Mühendisliği ve Endüstri Mühendisliği bulunmaktadır.

Scope

Areas includes (but not limited to) all issues in Electrical&Electronics Engineering, Mechanical Engineering, Civil Engineering, Computer Engineering and Industrial Engineering.

Yazarlara Bilgi

Ayrıntılı bilgi için lütfen http://ijerad.kku.edu.tr/ adresini ziyaret ediniz.

Authors Information

For detailed information please visit http://ijerad.kku.edu.tr

İÇİNDEKİLER / CONTENTS

2. Uluslararası Savunma Sanayi Sempozyumu
2nd International Defence Industry Symposium
6-8 Nisan 2017 / 6-8 April 2017

1. Uluslararası Bilimsel ve Mesleki Çalışmalar Kongresi
1st International Scientific and Vocational Studies Congress
5-8 Ekim 2017 / 5-8 October 2017

MÜHENDİSLİK FAKÜLTESİ

Uluslararası Mühendislik Araştırma ve Geliştirme Dergisi

International Journal of Engineering Research and Development

Cilt/Volume:9 Sayı/Issue:3 Aralık/December 2017 https://doi.org/10.29137/umagd.371056

Araştırma Makalesi / Research Article

Friction Reducing Composite Plating in Rocket Launchers

Ebru SARALOĞLU GÜLER*[1], İshak KARAKAYA[2]

[1]Baskent Uiversity, Baglica Kampusu, 06790 Ankara, TURKEY
[2] Middle East Technical University, Ankara Kampusu, Ankara 06800, TURKEY

Başvuru/Received: 06/05/2017 **Kabul/Accepted**: 06/09/2017 **Son Versiyon/Final Version**: 26/12/2017

Abstract

Composite plating is commonly used for reducing friction and wear. It is a method that can be used in the environments exposed to friction such as rocket launchers. Steel specimens were coated by nickel including MoS2 particles in this study. The effects of MoS2 particle concentration and particle size on the coefficient of friction and the amount of wear were determined by pin on disc tribometer. It is revealed that the particles with small size and high concentration are more effective in decreasing the friction coefficient.

Key Words

"MoS_2, nickel, electroplating, friction, wear"

*** esguler@baskent.edu.tr***

1. INTRODUCTION

Friction and wear of surfaces that are in contact with each other especially under high vacuum is an important issue that has to be considered according to Hilton and Fleischauer (1992). Hilton and Fleischauer (1992) claimed that films such as molybdenum disulphide or soft metals like gold, lead, or silver are efficiently used to overcome this problem. Siopis and Cowan (2014) stated that rocket sleds, launchers, and large caliber gun applications are the areas where mechanical wear at high sliding velocities has to be considered The friction at the contact regions between the launch package (slider) and rail/bore (guider) may lead to severe wear of both components that will end up with short life time and decreased performance of these devices according to Siopis and Cowan (2014). Therefore, friction decreasing applications are attracted. For instance, Charles et. al. (1963) put forward that a wheeling system is proposed for the launching of rockets from aircraft especially in the backward direction. Composite deposition including particles with self-lubricating property can be another solution for friction and wear. Electrodeposition is a well-known technique to embed particles into the matrix to improve the frictional properties of the surface. The particles that are commonly used to decrease friction and wear rate are MoS2-W MoS2, W-diamond in the studies of Cardinal et. al. (2009), Huang and Xiong (2008) and Hou et. al. (2014), respectively.

Pin-on-disc tribometer is the most widely used equipment to determine the wear rate and friction coefficient of materials. The tester consists of a stationary pin under an applied load in contact with a rotating disc. Either the pin or the disc can be tested depending on the geometry of the sample that is going to be examined. A load cell attached to the pin-on-disc tester is used to measure the evolution of the friction coefficient with sliding distance (ASTM-G99-95a, 2000)

The aim of this study is to observe the effects of MoS2 particle concentration (three concentrations) and particle size (two different sizes) on friction and wear behavior.

2. EXPERIMENTAL STUDIES

2.1 Electrocodeposition (Composite electroplating)

The constituents of the Watts bath are 300 g/l NiSO4.6H2O (63035981; Umicore, Belgium), 50 g/l NiCl2.6H2O (7791-20-0; Selnic, France), and 40 g/l boric acid (minimum %99.9 H3BO3, Etibank, Turkey) and additives from SurTec 855 which are 4 ml/l carrier, 10 ml/l leveler, 1 ml/l brightener and 1 ml/l wetting agent. Two different sizes 1.440 µm (Merck-product no: 1122570250) and 5.156 µm (Sigma Aldrich-product no: 69860) of MoS2 particles were used to agitate for 5 hours in 50 ml Watts solution to make slurry and then the slurry was added to the desired volume. The substrates were 4x4 cm AISI 304 stainless steels. The previously optimized parameters to produce coatings with low internal stress (thickness: 50 µm, pH: 2, temperature: 50 ºC and current density: 4.8 A/dm2) in the study of Saraloglu Guler et. al.(2013:5496) were used during the experiments. Optical micrograph and X-ray diffraction analysis were completed after the deposition process.

2.2 Tribological Investigation

Nickel coated and composite (nickel + MoS_2) coated AISI 304 stainless steel specimens were tested using a standard pin-on-disc tribometer (CSM Instruments) at ambient conditions. 6 mm diameter 100Cr6 steel pin (ISO 683-17:1999) was rotated within the pin holder. A constant load of 1N was applied during the experiments. The linear sliding speed and the wear track radius were 5 cm/s and 2 mm, respectively. The tests were run for 4000 cycles. The wear volumes of the specimens were calculated by measuring the width of the wear track by optical microscope. The calculations were conducting according to ASTM standard G99 assuming that the pin wear is negligible (ASTM-G99-95a, 2000). The wear rate was calculated by dividing the volume loss by both the total sliding distance and applied load.

$$\text{Disk Volume Loss}, mm^3 = \frac{\pi \times R \times (d^3)}{6 \times r} \quad (1)$$

Where **R:** wear track radius (2mm), **d:** wear track width, **r:** pin end radius (3mm)

3. RESULTS

MoS_2 particles that have the concentration of 30 g/l in the Watts bath and having the size of 1.44 µm were distributed homogeneously in the nickel matrix (Figure 1). The presence of MoS_2 was confirmed by X-ray diffraction analysis of the specimen coated from the electrolyte containing 10 g/l MoS_2 particles with the size of 1.44 µm is given in Figure 2. Quantitative analysis of the coating by Rigaku is also given in Table 1. The specimens were subjected to tribological investigation following the deposition processes to observe the effects of size and concentration of MoS_2 particles. Figure 3 shows the results of pin on disc experiments regarding the change in the COF as a function of number of cycles for three MoS_2 concentrations: 5, 10 and 30 g/l and the average COF values are 0.51, 0.46 and 0.41 respectively. The corresponding wear rates are listed in Table 2.

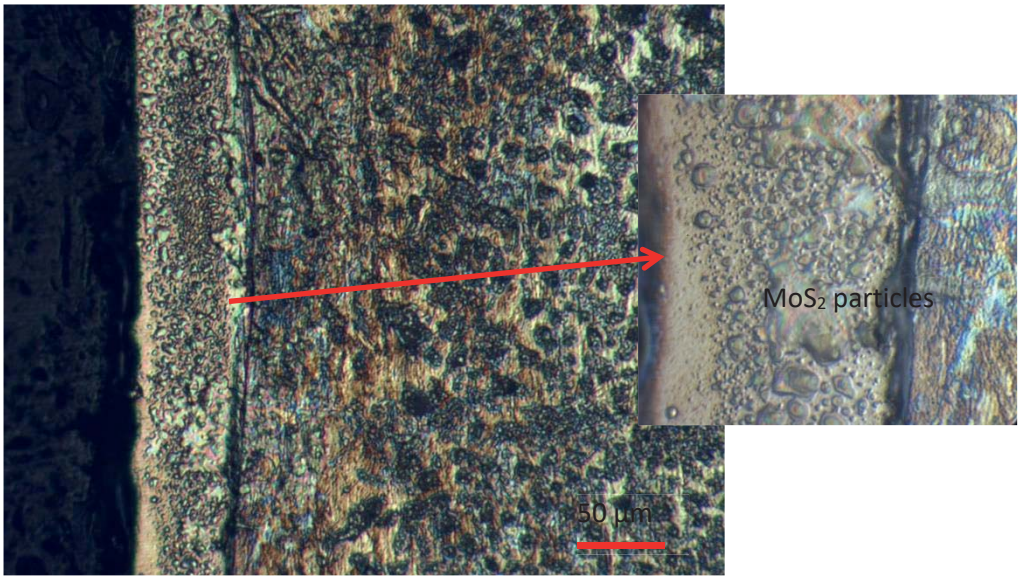

Fig. 1. Optical micrograph of Ni-MoS_2 composite coating on AISI 304 stainless steel substrate from the electrolyte containing 30 g/l MoS_2 with 1.44 µm particle

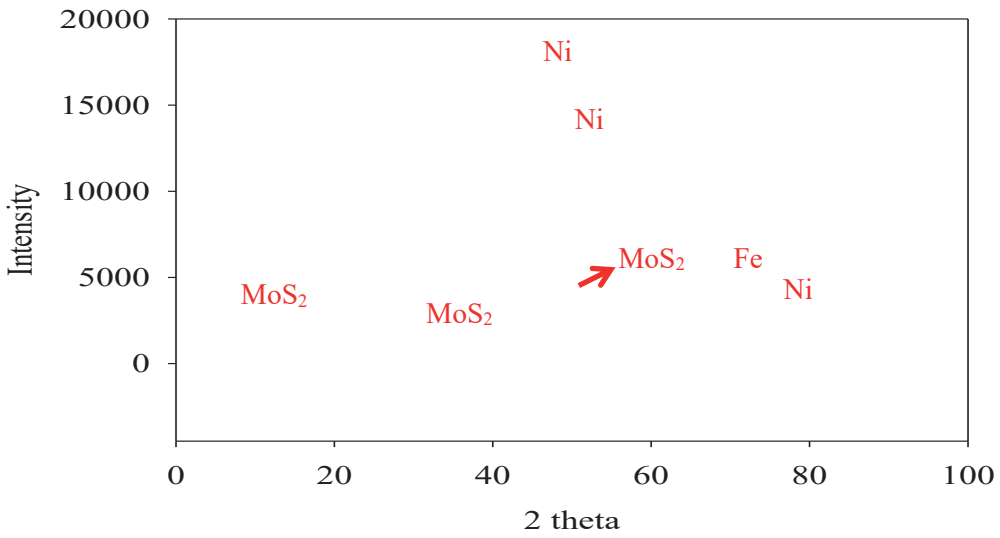

Fig. 2. X-ray diffractogram of Ni-MoS_2 composite coating on AISI 304 stainless steel substrate from the electrolyte containing 10 g/l MoS_2 with 1.44 µm particle

Table 2: Quantitative analysis by Rigaku software of the sample in Figure 2

Element/compound	% percent
Ni	82.5
Fe	11.2
MoS_2	6.3

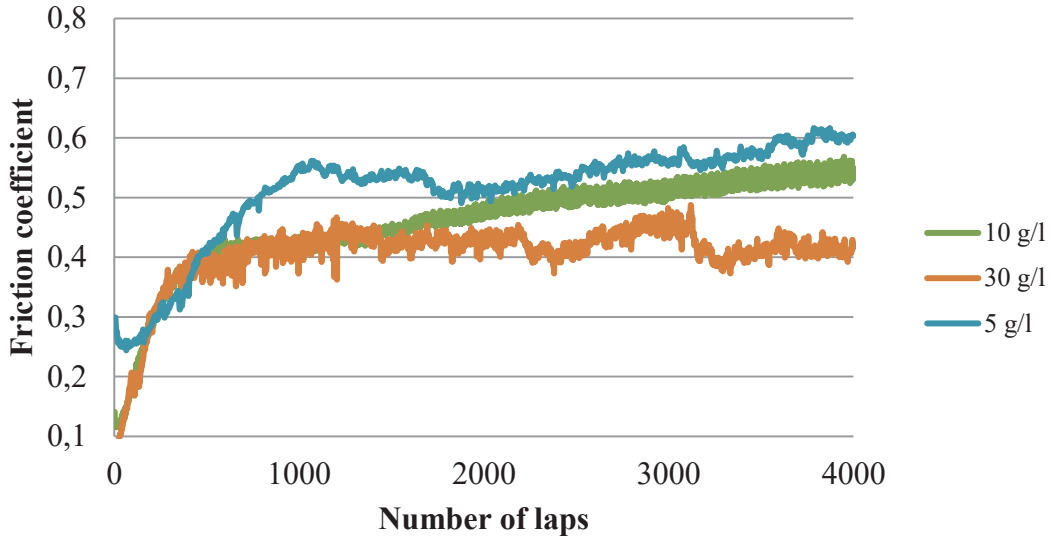

Fig. 3. Change in COF as a function of number of cycles for the Ni-MoS_2 composite coating samples showing the effect of MoS_2 concentration

Table 2. The deposition conditions and the average COF of the Ni-MoS_2 coated AISI 304 stainless steel samples (pH=2, current density=4.8A/dm^2, particle size=1.440 µm, T=50 °C, coating thickness = 50µm)

MoS_2 Concentration (g/l)	COF	Wear Volume (mm^3)	Wear Rate (mm^3/Nmx10E-3)
5	0.51	0.0048	0.094
10	0.46	0.0387	0.759
30	0.41	0.0679	1.329

The COFs of the composite coatings significantly decreased from 1.12 that is the COF value of pure nickel coated specimen to as low as ~0.40. According to the study of Huang and Xiong (2008), the COF of Ni-plated steel specimen was 0.45 and then decreased to 0.2 upon addition of 30 g/l MoS_2 into the Watts bath. The COF values are system dependent so the difference may stem from the change in the test conditions like ceramic pin (Al_2O_3) was used and the sliding velocity was 35.5 cm/s that are both higher than the parameters used in this study of Huang and Xiong (2008). Figure 4 shows the change in COF as a function of number of cycles for the Ni-MoS_2 composite coating samples showing the effect of both MoS_2 size and concentration. Table 3 summarized the conditions for four samples given in Figure 4. The deposition conditions and their wear volumes and rates were listed together with the corresponding COF values in Table 4.

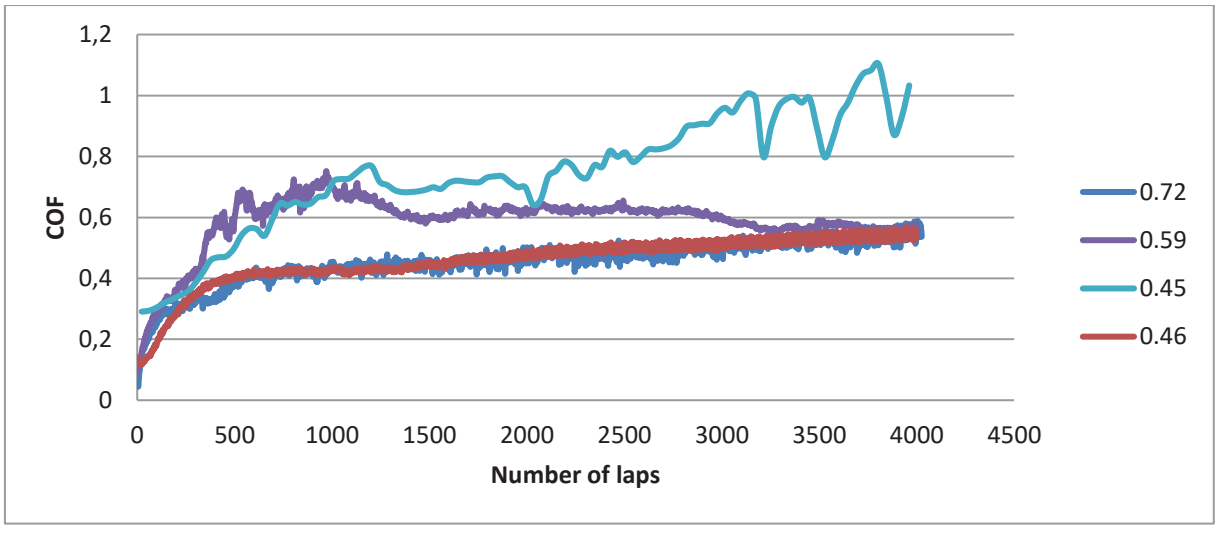

Fig. 4. Variation of the COF of composite coating samples as a function of number of cycles showing the effect of MoS_2 size and concentration given in Table 3.

Table 3. The deposition conditions and the average COF of the Ni-MoS_2 coated AISI 304 stainless steel samples (pH=2, current density=4.8A/dm^2, T=50 °C, coating thickness =50µm)

MoS_2 Concentration (g/l)	MoS_2 Size (µm)	COF
10	1.440	0.59
30	1.440	0.46
30	5.156	0.45
10	5.156	0.72

After pin on disc tribometer experiments, the specimens with the wear track were subjected to surface profilometer that shows the depth of track. A profilometer for the specimen with an average COF of 0.51 is given in Figure 5.

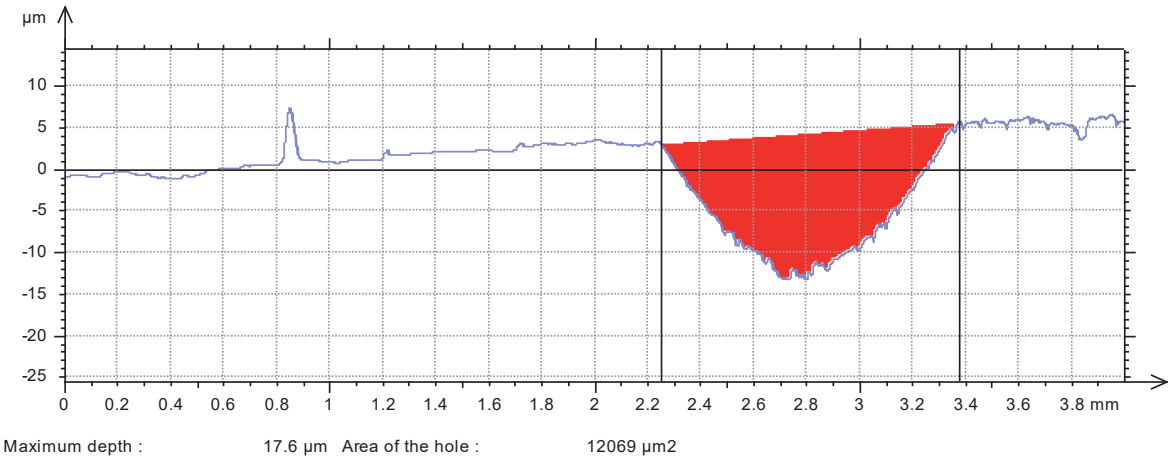

Fig. 5. Surface profilometer for specimen with an average COF value of 0.51.

References

ASTM-G99-95a (2000), Standard Test Method for Wear Testing with a Pin-on-Disk Apparatus, ASTM International.

Cardinal, M.F., Castro, P.A., Baxi J., Liang, H., Williams, F.J. (2009). Characterization and frictional behavior of nanostructured Ni-W-MoS2 composite coatings. Surface and Coatings Technology, 204(1-2), 85-90.

Charles, J., Barker, L. and Kern, W. K. (1963). Aircraft rocket launcher US 3077144 A

Hilton, M.R. and Fleischauer,P.D. (1992). Applications of Solid Lubricant Films in Spacecraft. Surface and Coating Technology, 54-55, 435-441.

Hou, K.-H., Wang, H.-T., Sheu, H.-H. and Ger, M.-D. (2014). Preparation and wear resistance of electrodeposited Ni–W/diamond composite coatings. Applied Surface Science, 308, 372–379.

Huang, Z.-j. and Xiong D.-s. (2008). MoS2 coated with Al2O3 for Ni-MoS2/Al2O3 composite coatings by pulse electrodeposition. Surface and Coatings Technology, 202(14), 3208-3214.

Saraloglu Guler, E., İ. Karakaya, and E. Konca (2013). Effect of Electrodeposition Parameters on the Current Density of Hydrogen Evolution Reaction in Ni and Ni-MoS2 Composite Coatings. Int. J. Electrochem. Sci., 8, 5496 - 5505.

Siopis, M.J. and Cowan, R.S. (2014). Electromagnetic Launch Technology (EML). International Symposium on Electromagnetic Launch Technology, 7-11 July, San Diego, 865.

MÜHENDİSLİK FAKÜLTESİ

Uluslararası Mühendislik Araştırma ve Geliştirme Dergisi

International Journal of Engineering Research and Development

Cilt/Volume:9 Sayı/Issue:3 Aralık/December 2017 https://doi.org/ 10.29137/umagd.371057

Araştırma Makalesi / Research Article

Bir Yüksek Karbonlu Toz Metal Çeliğin Östemperlenmesi Üzerine Bir Çalışma

A Study on Austempering a High Carbon Powder Metal Steel

Onur ALTUNTAŞ[1], Ahmet GÜRAL[2]

[1]Gazi Üniversitesi, Teknik Bilimler MYO, Makin ve Metal Teknolojileri. Bölümü, Ankara, TÜRKIYE
[2]Gazi Üniversitesi Teknoloji Fakültesi Metalurji ve Malzeme Mühendisliği, Ankara, TÜRKIYE

Başvuru/Received: 06/05/2017 **Kabul/Accepted**: 06/09/2017 **Son Versiyon/Final Version**: 26/12/2017

Öz

Bu çalışmada NC100.24 saf demir tozlarına ağırlıkça %1,5 oranında doğal grafit tozları ilave edilerek sade yüksek karbonlu çelik toz metalurjisi numuneler elde edilmiştir. Hazırlanan karışım oda sıcaklığı, 100°C ve 200°C sıcaklıkta ve 700 Mpa presleme basıncında tek eksenli preslendikten sonra 1150°C de atmosfer kontrollü fırında sinterlenmiştir. Ardından östemperleme ısıl işlemi için numuneler 950°C de östenitlenip 300 °C sıcaklıktaki tuz banyosunda 30 dakika süre ile östemperleme işlemine tabi tutulmuştur. Isıl işlem sonrası gerçekleşen yapı dönüşümleri optik mikroskop yardımıyla incelenmiştir. Farklı sıcaklıklarda presleme işlemleriyle yoğunlaşma oranın sertlik ve beynitik dönüşünlere etkileri çalışılmıştır. Yüksek carbonlu toz metal malzemelerin yoğunluklarının artırılmasıyla, beynitik yapı dönüşümleri geliştirilmiş ve sertlik değerleri etkili bir şekilde artırılımıştır.

Anahtar Kelimeler

"toz metal çelik, östemperleme, sinterleme, mikroyapı"

Abstract

In this study, 1.5% by weight of natural graphite powders were added to NC 100.24 pure iron powders to obtain plain high carbon steel powder metallurgy specimens. After respectively uniaxial pressing at room temperature, 100 °C and 200 °C and under 700 MPa pressing pressure, the specimens were sintered in an atmospheric controlled furnace at 1150 ° C. The spec,mens were then austenitized at 950 ° C for half an hour in a salt bath at 300 ° C for austempering heat treatment. The structure transformations after the heat treatment were examined using optic microscope. Through pressing processes at different temperatures, the effects of densification rate on the hardness and bainitic transformation were investigated. It was seen that by increasing the densitity of high carbon powder metal materials, the bainitic structure transformation was improved and thus hardness value was effectively increased.

Key Words

"powder metal steel, austempering, sintering, microstructure"

** onuraltuntas@gazi.edu.tr*

1.GİRİŞ

Ötektoid dönüşüm sıcaklıklarından östenitin perlite ve martensite dönüşümü sıcaklıkları arasında eşsiz bir mikroyapı oluşmaktadır. Bu ara sıcaklıklarda oluşan yapı perlit ve martensitten çok farklı mekanik özellikler göstermekte olup, "beynit" olarak adlandırmıştır (Krauss, 2005) Beynit tanım olarak, ferrit ve lamelli olmayan sementitin (Fe_3C) karışımından oluşan oldukça tok ve sünek bir yapıdır (Smith,2000). Beynit, izotermal dönüşüm diyagramlarına göre perlit burnunun altında izotermal sıcaklıkta östenitin dönüşümü sonucu oluşan bir yapıdır. Östenitin bozunması sırasında soğuma difüzyon kontrollüdür ve bu esnada perlitin oluşmasına imkân yoktur. Ayrıca soğuma yeterli miktarda yavaş olduğu için martensit oluşumunu da engellemektedir (Caballero vd. 2002:279) Şekil 1.'de verilen Zaman-Sıcaklık-Dönüşüm (ZSD) diyagramında perlit ve martensit oluşum sıcaklıkları arasında beynit oluşumu için gerekli olan soğutma ve izotermal bekleme koşulları görülmektedir (Krauss, 2005). Östemperleme, özellikle belirli seviyelerde sertliğe rağmen süneklik ve darbe dayanımını artırmak ve su verme esnasında oluşan çatlakların azaltılması için geleneksel su verme temperleme ısıl işlemlerine alternatif bir ısıl işlemdir. Östemperleme özellikle kalın kesitli sade karbonlu çeliklerin yaklaşık 50 HRC sertlikte mükemmel tokluk ve süneklik sağlayan bir ısıl işlemdir. Sade karbonlu çeliklerde alt beynit yaklaşık 350 °C' nin altıdaki sıcaklıklarda oluşur. Düşük sıcaklıklarda 250-350 ° C'ler arasında difüzyon hızının düşük olmasından dolayı alt beynit içerisindeki sementit ferrit plakalarının içerisinde çökelir. Alt beynitin oluşmasındaki mekanizma, martensitin oluşması ve temperlenmesiyle oluşan mekanizmaya benzerlik göstermektedir. Bu mekanizma, kayma işlemi ile östenitten aşırı doymuş ferritin oluşması ve ardından ferrit içerisinde sementitin çökelmesidir (Smith,2000)

Meng Yin Tu ve arkadaşlarının yapmış olduğu çalışmada (Meng Yin Tu vd 2007) aynı sertliğe sahip temperlenmis martensitik yapının ve alt beynitik yapının mekanik özellikleri karşılaştırılmış olup, alt beynitik yapının sünekliği ve tokluğu temperlenmis martensite göre çok daha yüksek olduğu ortaya konmuştur. Aynı çalışmada gözlenen başka bir durum ise, alt beynitik yapıda hasarı oluşturan çatlak taneler arası ilerlerken, temperlenmis martensitik yapıda ise tane içinden ilerlediğidir. Nedeni ise temperleme sırasında karbürlerin tane sınırlarında çökelmesi olarak gösterilmiştir.

Chakraborty ve arkadaşlarının yapmış oldukları çalışmada ise (Chakraborty vd 1999) SAE 52100 rulman çeliğinin uygun östemperleme sıcaklığında tutulup daha sonra su verilmesiyle beynitik ve martensitik olmak üzere karışık içyapıya sahip çeliklerin sadece temperlenmis martensitik yapıyla karşılaştırıldığında mekanik özellikleri olan çekme ve darbe dayanımında iyileşme görülmüştür.

Kumari ve arkadaşlarına göre östemperleme ısıl işleminin sıcaklığının artışıyla aşınma oranının arttığı bulunmuştur. C oranın artışı ve buna bağlı olarak karbür oranın artması aşınma hızını ve oranını azaltıcı yönde etki yapmaktadır (Kumari ve Rao, 2009:1082)
Çeliklerde beynitik yapılar, geniş çapta dayanım ve süneklik sunmaktadırlar. Yüksek karbonlu alt beynitik mikroyapıya sahip bir çelik; 1400 MPa çekme dayanımına ve 55 HRC sertliğe ulaşabilmektedir. Bu dayanımlar, ince ferrit plakalarına, yüksek dislokasyon yoğunluğuna ve ince sementit dağılımları ile elde edilir. Dönüşüm sıcaklığı düştükçe, beynitik ferrit daha ince karbür dağılımına sahip olur. Bu durumda beynitik ferrit daha yüksek sertlik ve dayanım sağlamaktadır. Su verilmiş ve temperlenmiş çelikler ile kıyaslandığında, östemperlenmiş çelikler benzer sertlik ancak daha yüksek tokluk sergilemektedir. Su verme sonrası oluşan martensit oldukça sert ve kırılgandır. Bu nedenle su verilmiş ve temperlenmiş çeliklerin tokluğu östemperlenmiş çeliklere göre oldukça düşüktür.

Beynitik çeliğin mikroyapısı, çeliğin mekanik özelliklerini etkilemektedir. Araştırmacılar (Krauss, 2005 , Smith,2000, Callister vd,2007, Bhadeshia vd 2006),üst beynitik mikroyapıya sahip bir çeliğin alt beynitik çelik ile kıyaslandığında daha düşük tokluk ve sünekliğe sahip olduğunu bildirmektedir (Krauss, 2005).
Bu çalışmada, genellikle içerdikleri gözenek ve yetersiz sinterlemeden dolayı düşük mekanik özelliklere sahip yüksek karbonlu toz metal çeliklere farklı sıcaklıklarda presleme sonrası östemperleme ısıl işlemlerinin uygulanmasıyla özellikle yoğunluk/sertlik özelliklerinin geliştirilebileceği amaçlanmıştır.

2.MATERYAL METOT

Çalışmada kullanılan yüksek C'lu TM malzemesinin üretiminde NC 100.24 (Höganäs AB) saf demir tozları içerisine ağırlıkça % 1.5 oranında doğal grafit tozu ilave edilmiştir. Hazırlanan bu karışım tozları 700 MPa basınç altında oda sıcaklığında, 100 ve 200°C tek eksenli pres ile şekillendirilmiş, 1150 ° C de atmosfer kontrollü fırında sinterlenerek toz metal numuneler üretilmiştir. Sinterleme öncesi ve sonrası numunelerin yoğunlukları hassas terazi ve elektronik kumpas kullanılarak matematik hesaplamalarla ölçülmüş ve grafik olarak sunulmuştur. Sinterlenen numuneler 950°C de 3dk östenitlendikten sonra %50 KNO_3 ve %50 $NaNO_3$ tuz banyosunda 300 °C de 30 dk süre ile östemperleme ısıl işlemi uygulanmıştır. Östemperleme ısıl işlem çevriminin şematik özeti Şekil 1'de gösterilmiştir.

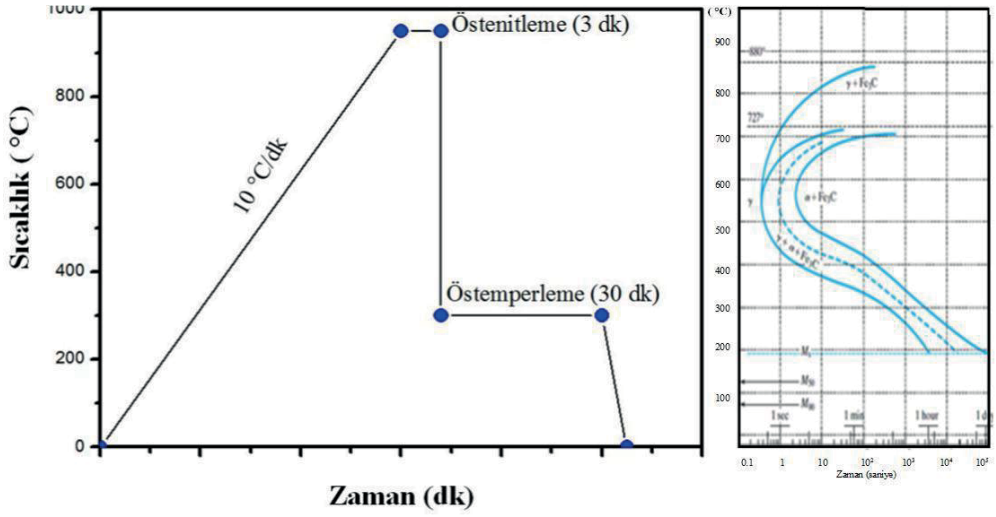

Şekil 1: Östemperleme ısıl işlemi şematik gösterimi ve ötektoid üstü bir ZSD diyagramı (Shackelford, 2016)

Üretilen bu numunelerde mikroyapı incelemeleri için zımpara ve parlatma işleminin ardından %2 Nital ile dağlanmıştır. Numunelerin ısıl işlem öncesi ve sonrası makro sertlikleri Vickers sertlik ölçümleri Shimadzu Sertlik cihazında 2 kg yük kullanılarak, her bir numune için en az 5 farklı noktadan sertlik değeri alınarak ortalama HV2 değerleri tespit edilmiştir. Yukarıda anlatılan deney numunesine ait akış şeması Şekil 2 de şematik olarak gösterilmiştir.

3.SONUÇLAR VE TARTIŞMA

Şekil 3'de sırasıyla oda sıcaklığı,100 ve 200° C sıcaklıkta tek eksenli presleme ile şekillendirilen 1150 °C de Ar ortamında sinterlenmiş numunelerin mikroyapıları sırasıyla verilmiştir. Mikroyapılardan görüldüğü gibi sinterleme sonrası tüm numunelerde beklenen birincil sementit (ok ile gösterilmiş) ve perlit lamelleri görülmektedir. Ancak toz metal parçalarda tam yoğunluğa ulaşmak için uygulanan sıcaklık ile birlikte presleme sonrası mikroyapıdaki gözeneklerin önemli oranda azaldığı görülmektedir. Pek çok mühendislik malzemesinde artan sıcaklıkla beraber düşen akma dayanımı ve sertlikten dolayı plastik deformasyon kolaylaşır. Bu da preslenmeye olan direnci azaltacağından geleneksel toz metalürji malzemelerinde yüksek yoğunluğa ulaşabilmek için tercih sebebidir (Süleyman Sarıtaş vd.2009).

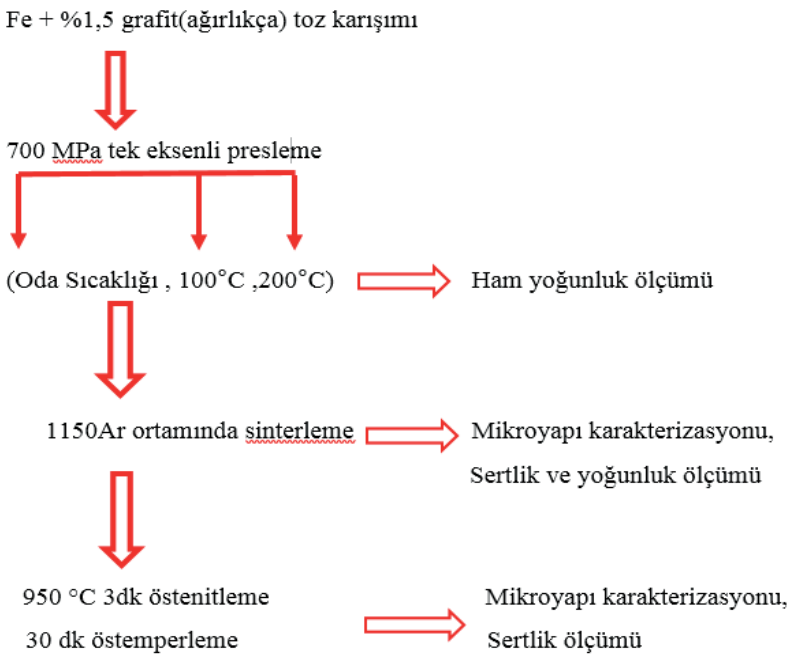

Şekil 2: Çalışmada gerçekleştirilen işlem akış şeması

Sıkıştırma kalıbının ısıtılması ile preslenen numunelerin artan presleme sıcaklığı ile hem ham yoğunluklarında hem de sinterleme sonrası yoğunluklarında artış görülmüştür. Sıcak presleme, gerilme destekli yoğunlaşmanın bir ifadesi olup sıcak presleme

sırasında ilk yoğunlaşma, parçacıkların yeniden düzenlenmesi ve parçacık temas noktalarındaki plastik akış ile olur. Etkili gerilme kendiliğinden akma gerilmesinin altına düştüğünde daha fazla yoğunlaşma meydana gelmektedir (Süleyman Sarıtaş vd.2009). En yüksek yoğunluk değeri 200°C sıcaklıkta preslenip sinterlenen numunede elde edilmiş olup ham yoğunluk ve tam yoğunluk değerleri sırasıyla 6,74 gr/cm^3 ve 7,1 gr/cm^3 olarak belirlenmiştir. Şekil 4'de numunerlerin yoğunluk değerleri grafik olarak gösterilmiştir. Şekil 5'te numunelerin nispi yoğunluk değerleri gösterilmiştir. Bu değerlere göre 200°C sıcaklıkta preslenip sinterlenen numunenin yaklaşık % 91 teorik yoğunluğa ulaştığı görülmektedir. Şekil 3'deki sinterleme sonrası mikroyapılar incelendiğinde yoğunluk artışının mikroyapıdaki mevcut gözenek/boşlukları küçülttüğü söylenebilir.

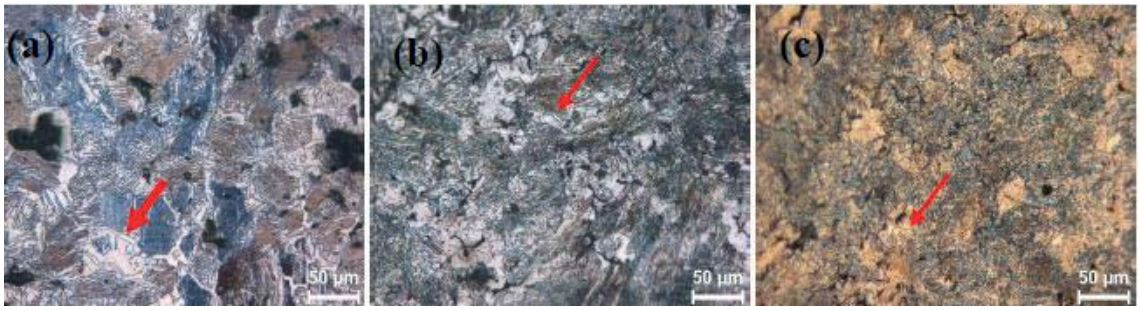

Şekil 3: Farklı sıcaklıklarda (a) Oda sıcaklığı, (b) 100°C, (c) 200°C) preslenmiş ve 1150 °C'de sinterlenmiş numunelere ait optik mikroyapılar

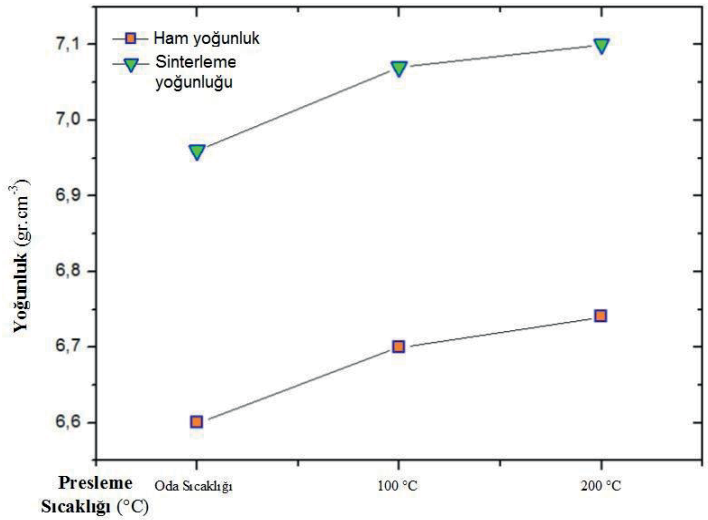

Şekil 4: Presleme ve sinterleme sonrası numunelerin yoğunluk grafiği

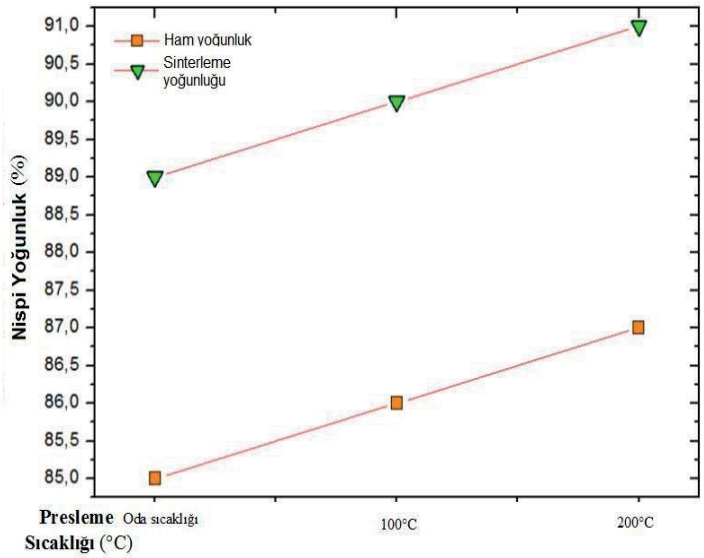

Şekil 5: Presleme ve sinterleme sonrası numunelerin nispi yoğunluk grafiği

Şekil 6'te ise 300°C tuz banyosunda 30 dk süre ile östemperlenmiş numunelerin mikroyapıları görülmektedir. Östemperleme ısıl işlemi sonucu izotermal dönüşüm oluşurken mikroyapıda kısmen beynitik yapıların oluştuğu görülmektedir. Bununla beraber, kısmen ferritik alanlar da görülmektedir. Numunelerin tamamında ferritik alanların görülmesinin muhtemel nedeninin sinterlemeden kaynaklı dekarbürizasyon olduğu düşünülmektedir. Bu alaşımın 30 dk süre östemperleme işlemi ile izotermal dönüşüm ile beynitik yapıları iğnemsi morfolojisinde olduğu görülmektedir. Muhtemelen bu sürede kısmen martensitik yapılarda oluşmuş olabilir. İğnemsi yapılar, kısa süreli östemperleme ısıl işlemi ile oluşmuştur.

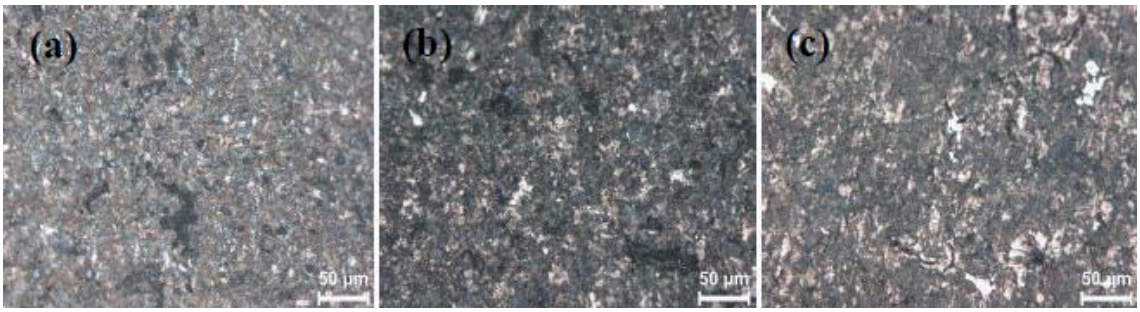

Şekil 6: (a) Oda sıcaklığında, (b) 100°C, (c) 200°C sıcaklıkta preslenip sinterlenmiş numunelerin östemperleme sonrası mikroyapıları

Şekil 7'deki grafikte numunelerin HV2 makro sertlik değerleri görülmektedir. Tozların sıcaklık ile birlikte preslenmesi ile elde edilen yoğunluk değerleri farklılık göstermiş ve bu yoğunluk farklılıklarının da sertliğe etki eden faktörlerden olduğu düşünülmektedir. Şekil 7'den görüldüğü gibi farklı sıcaklıklarda preslenmiş toz metal çeliklerin sinterleme sonrası (Brincil sementit+perlitik mikroyapılı) numunelerde sertlik önemli oranda değişmezken 300 °C tuz banyosunda 30dk süre izotermal tavlama ile numunelerde meydana gelen mikroyapısal değişimlerden dolayı ısıl işlem sonrası sertlik değerleri önemli ölçüde artış göstermiştir. Bu sonuç üretilen toz metal çeliklerinin yoğunluklarının östemperleme ısıl işlemlerinde olduğu gibi izotermal dönüşüm sırasında östenitten üretilen ferrit ana yapıda yeni mikro fazların çökelmesi kinetiğini hızlandırdığı anlaşılabilir. Diğer bir ifade ile izotermal dönüşümle beynit dönüşüm oranı yüksek yoğunluklu toz metal çeliklerde daha fazla olmaktadır. Östemperleme ısıl işlemi uygulanan malzemede matris yapıdaki beynitin oranı arttıkça numunelerin sertliğinde bir artış görülmekte olduğu bildirilmiştir(Ovalı, vd.2011) Bu çalışmada en yüksek sertlik değeri 200 °C sıcaklıkta 700 MPa basınç altında preslenip 1150°C sıcaklıkta sinterlenen, 7,1 g.cm^{-3} yoğunluğa ve % 91 nispi yoğunluğa sahip numunelerde 300°C sıcaklıkta 30 dk süre ile izotermal sonrasında yaklaşık 650 HV2 olarak elde edilmiştir. Bu yüksek sertlik değerleri de toz metal çeliklerde yüksek aşınma ve tokluk direnci sağlanabileceğini gösterdiğinden özellikle yatak malzemeleri gibi ürünlerin geliştirilmesinde östemperleme ısıl işlemlerinin uygulanabiliceğini göstermektedir.

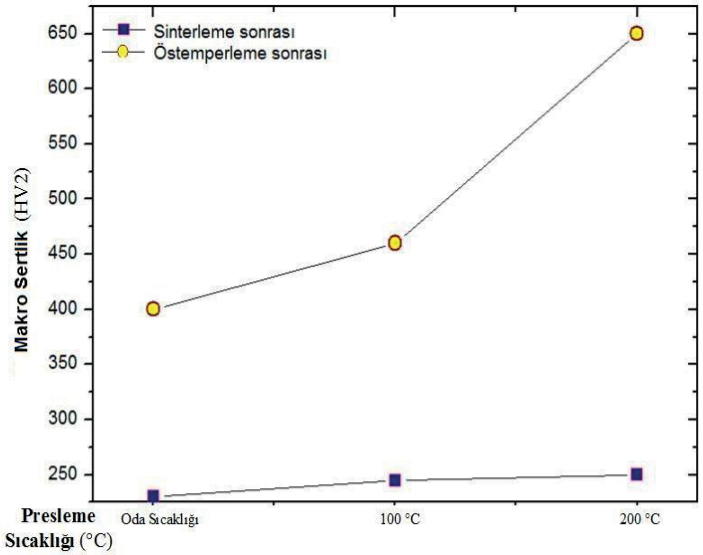

Şekil 7: Sinterleme ve östemperleme sonrası numunelerin sertlik grafiği

4.SONUÇLAR

Bu çalışmada elde edilen deneysel sonuçlara göre 200°C sıcaklıkta ılık preslemenin en yüksek yoğunluk değerini (7,1 gr/cm^3) verdiği belirlenmiştir. 300 °C tuz banyosunda 30dk süre izotermal tavlama ile iğnemsi beynitik yapının oluştuğu ve bu mikroyapıdaki numunenin 650 HV2 makro sertlik değeri belirlenmiştir. İzotermal tavlama süresinin ve yoğunluklarının daha da arttırılması ile beynitik dönüşümlerin artacağı ve böyle yüksek karbonlu toz metal çeliklerin mekanik özelliklerinin önemli oranda geliştirileceği düşünülmektedir.

REFERANSLAR

Bhadeshia, H.K.D.H., Honeycombe, R. (2006). Steels: Microstructure and Properties, 3rd edition, Butterworth-Heinemann, USA,

Caballero, F.G., Bhadeshia, H.K.D.H., Mawella, K.J.A., Jones, D.G., Brown, P. (2002).Very Strong Low Temperature Bainite, Materials Science and Technology, 18(3): 279-284.

Callister, W.D., Rethwisch, D.G. (2007). Materials Science and Engineering: An Introduction, Wiley, New York, USA,

Chakraborty, J., Bhattacharjee, D. and Manna, I.(1999), Scientific Services and Research and Development, Tata Steel, Jamshedpur 831 001, Jharkhand, India.
Krauss, G. (2005) Steels: Processing, Structure, and Performance, ASM International.

Kumari, U. R., Rao P. P(2009) "Study of wear behaviour of austempered ductile iron", J Mater Sci, 44:1082–1093,

Meng Yin Tu, Cheng-An Hsu, Wen-Hsiung Wang, Yung Fu Hsu**,** (2007.)Comparison of microstructure and mechanical behaviour of lower bainite and tempered martensite in JIS SK5 steel. Elsevier

Ovalı, İ. Mavi, A. (2011)., "Ösferrit Hacim Oranın Çift Fazlı Küresel Grafitli Dökme Demirlerin Yüzey Pürüzlülüğü Üzerindeki Etkisi" 6th International Advanced Technologies Symposium (IATS'11), Elazığ,

Randall M. G. (2007) Çeviri Editörleri,. Sarıtaş S. vd Toz Metalurjisi ve Parçacıklı Malzeme İşlemleri, (Kitap), Ankara,

Shackelford, James F. (2016). *Introduction to Materials Science for Engineers (8th Ed.)*, England, Pearson Education Limited

Smith W.F. (2000) (Çev.: Erdoğan, M.) Mühendislik Alaşımlarının Yapı ve Özellikleri, Nobel Yayın, Ankara.

Vardiya çizelgeleme problemleri bazı kısıtlar altında, çalışan personellerin görev dağıtımından oluşmaktadır. Bu kısıtları birbiriyle uyumlu bir biçimde yürütmek zor bir iştir. Temel kısıtlar ayrı ayrı değerlendirilip birbirleriyle çakışmaması sağlanmalıdır. Çizelgeleme hazırlanırken personellerin çalışma tercihleri, izin günleri, hafta sonları çalışma günleri ve yıllık tatil dönemleri gibi hususlara dikkat edilmesi gerekmektedir.

Bu çalışmada vardiya çizelgeleme problemi ele alınmıştır. Çalışmada güvenlik görevlilerinin aylık çalışma çizelgesi yapılmış ve işgücü minimize edilmeye çalışılmıştır. Çizelgelemeyi yaparken çalışanların sayıları, cinsiyetleri ve çalıştıkları bölümleri aynı anda değerlendirerek çizelgeleme oluşturulmuştur. Kırıkkale Üniversitesi güvenlik görevlilerinin vardiya çizelgelemesi, ilgili bölüm amiri tarafından yapılmaktadır. Uygulanmakta olan planda sözleşmeli erkek güvenlik görevlisi sayısı 81, kadrolu erkek güvenlik görevlisi sayısı 60 ve sözleşmeli kadın güvenlik görevlisi sayısı 9 olup toplamda 150 güvenlik görevlisi çalışmaktadır. Bu çalışmada problem hedef programlama yöntemi ile çözülmüştür ve Kırıkkale Üniversitesi Güvenlik Müdürlüğünde uygulanmıştır.

Yapılan çalışmanın planı şu şekildedir: Çalışmanın ikinci bölümünde vardiya çizelgeleme konusu, üçüncü bölümünde hedef programlama, dördüncü bölümünde literatür araştırması, beşinci bölümde yapılan uygulama anlatılmış ve altıncı bölümde de yapılan çalışmanın sonuçları değerlendirilmiştir.

2. VARDİYA ÇİZELGELEME

Vardiyalı çizelgeleme, başlangıç ve bitiş saatlerinin işletmenin yapısına ve faaliyet gösterdiği işkoluna göre değişiklik gösteren işgücünü, maliyetleri minimize ederek, maksimum fayda elde etmeyi amaçlayan bir sistemdir. İş günü genellikle sabah, akşam ve gece vardiyası olarak bölümlendirilir (Yüksel, 2004).

Vardiya çizelgeleme problemleri bir kurum veya kuruluşta çalışan personellerin belirlenmiş olan vardiyalara kurumun çalışma koşullarını yansıtarak düzenli ve sistemli bir çalışma planı oluşturmaktır. Bu çizelgelemelerde bazen çalışan personellerin özel izin ve istekleri yerine getirilerek, bazen de personelleri uzman oldukları iş kollarına atayarak çalışma planlarına ek olarak değerlendirilebilmektedir. Vardiyalı çalışma sistemi, kamu ve özel sektörde olmak üzere birçok yerde kullanılmakta olan bir sistemdir (Varlı ve Eren, 2016). İş gücünün planlı bir şekilde teknolojik yeniliklere uyum sağlayarak kullanılmasıyla verimli sonuçların elde edilmesini sağlamaktadır. Etkili bir vardiya planından insanların fiziksel ve zihinsel sağlığı üzerindeki kötü faktörleri minimize etmesi ve performans açısından da maksimum değerde fayda sağlanması beklenir.

Vardiya Çizelgeleme konusunda ilk olarak George Bernard Dantzig (1954) yılında çalışmıştır. Amacı her grup için maliyeti minimize ederek, gerekli personel ihtiyacını sağlamaktır. Vardiya çalışması güvenlik, ulaşım, iletişim ve sağlık endüstrisi gibi hizmet ya da üretimin ekonomik ve kamusal açıdan sürekliliği olan alanlarda tercih edilen bir sistemdir. Vardiya planlaması problemlerinin çözümünde kullanılan çok fazla yöntem vardır. Bunlardan bazıları, tam sayılı programlama, hedef programlama, dinamik programlama ya da sezgisel programlama yöntemleridir. Bu çalışma da hedef programlama yönteminden yararlanılmıştır.

3. HEDEF PROGRAMLAMA

Hedef programlama çalışmalarının ilki Charnes vd. (1655) yılında gerçekleşmiştir. Charnes ve Cooper (1961) yılında ise hedef programlamayı geliştirmeye çalışmışlardır.

Hedef programlama çok kriterli karar verme tekniklerinden bir tanesidir. Bu yöntem de amaç fonksiyonun maksimizasyonu ya da minimizasyonu yerine var olan kısıtlarla belirlenen hedeflerden sapma değişkenleri minimize yapılmaya çalışılmaktadır. Yani hedef programlamada sorunun amacı, sapmayı ifade eden değişkenlerin toplamının minimize edilmesidir

Sapma değişkenleri hedef programlamada genellikle di+ ve di- simgesiyle gösterilir. Sapma değişkenleri negatif değerli olmazlar ve bir hedefin hem üstünde hem altında bir anda olunamayacağından, bunlardan birinin değeri de daima 0 olur. Hedef kısıtlayıcılarına bağlı olarak sapma değişkenleri istenen veya istenmeyen değişken olarak da adlandırılabilir. Hedef programlama her amacın verilen hedeflere mümkün olduğunca ulaşmasını amaçlar ve hedefteki sapmaları minimize etmektir (Ignizio, 1985).

Matematiksel gösterimi şu şekildedir;

$$Min\ Z = \sum_{i=1}^{t} (d_i^+ + d_i^-)$$

$$\sum_{j=1}^{n} w_{ij} x_j + d_i^+ + d_i^- = k_i$$

$$d_i^+ * d_i^- = 0$$

$$x_j, d_i^+, d_i^- \geq 0 \text{ i=1...t} \quad \text{j=1...n}$$

Değişkenler

x_j: j. Karar değişkeni

w_{ij}:i. hedefin j. karar değişkeni katsayısı

k_i : i. hedef için ulaşılmak istenen değer

d_i^+: i. hedefin pozitif sapma değişkeni

d_i^-: i. hedefin negatif sapma değişkeni

4. LİTERATÜR ARAŞTIRMASI

Vardiya çizelgeleme ile ilgili birçok farklı sektörde çalışma bulmak mümkündür. Çalışmaların büyük bir bölümü sağlık sektöründe hemşire çizelgeleme konusunda yapılmış olsa da özel şirketlerde, fabrikalarda ve devlette çalışan personeller için de farklı iş disiplinleri kullanılarak çalışmalar yapılmıştır. Vardiya çizelgeleme ile ilgili yapılmış birtakım çalışmalara aşağıda değinilmiştir.

Segal (1974), vardiya uzunluğuna dayanan çizelgeleme problemlerini, geliştirdiği şebeke diyagramı formülasyonu ile çözümlemiştir. Keith (1979) vardiya çizelgeleme konusunda tam sayılı programlama modeli geliştirmiştir. Bu modelde işgücündeki eksiklik ve fazlalığa izin verilmiş buna göre çizelgelemede maliyeti minimize etmeye çalışmıştır. Özkarahan ve Bailey (1988) çalışmasında hem hastane için hem de hemşire isteklerini yerine getirmek için bir model oluşturmuştur. Günler ile saatler arasında bir esneklik oluşturulmuş ve hastanelerde uygulamaya koyulmuştur. Sowalter ve Mabert (1988) hemşire çizelgelemesinde farklı bir yöntem geliştirmiştir. Çalışmasında vardiyanın başlama ve bitiş sürelerine esneklik sağlamışlardır. Ancak vardiya sürelerinin farklı olması hemşirelerin dinlenme zamanlarında problemler yaşamalarına sebep olmuştur. Burada amaç hemşire maliyetinin minimize edilmesidir. Aykin (1996) optimal vardiya planlaması için geliştirmiş olduğu tam sayılı matematiksel modeli bulanıklaştırarak farklı bir problem üzerinde uygulamıştır. Thompson (1996) çalışanların çalışma sürelerinin sınırlı olduğu durumlar için vardiya planlaması oluşturmuş ve çalışmasında vardiya uzunluğu, molalar, vardiya başlama ve bitiş zamanları konusunda fazlaca esnekliğe izin veren optimal vardiya çizelgesini oluşturmayı amaçlayan tam sayılı programlama modelini geliştirmiştir. Bard vd. (2003) ABD posta servisinde personel planlaması üzerine işgücünün en küçüklenmesini amaçlayarak bir çalışma gerçekleştirmişlerdir. Tam ve yarı zamanlı çalışanlarla tam sayılı modelleme yöntemini kullanarak problemi çözümlemişlerdir. Topaloğlu ve Özkarahan (2004) çalışmalarında tur çizelgeleme problemini araştırmışlardır. Amaçları çalışanların istek ve ihtiyaçlarına yönelik bir çizelgeleme oluşturmaktır. Çözüm için Hedef programlama modelini önermişlerdir. Ernst vd. (2004) yaptıkları çalışmada personel çizelgeleme problemi üzerine yapılan çalışmaları uygulandıkları alanlara göre sınıflamıştır. Uygulama alanlarına göre çalışmaları, üretim finansal hizmetler, organizasyon yönetimi, çağrı merkezleri turizm hizmetleri, sağlık hizmetleri, lojistik sistemler, sivil hizmetler ve güvenlik ve acil hizmetler vb. gruplara ayırarak sınıflandırmıştır. Çözüm yöntemlerine göre ise; yapay zekâ, matematiksel modeller, sezgisel modeller (heuristik modeller), kısıt programlama, talep modelleme olarak sınıflandırmıştır. Ernst vd. (2004) Geçmişte yapılan çalışmalara göre 700'den fazla problemin modellerini ve çözümlerini incelemişlerdir. Moz ve Pato (2004) çalışmalarında Portekiz devlet hastanesinde hemşirelerin nöbet planlamasının çözümü için bir model oluşturulmuştur. Problem tam sayılı programlama yöntemi ile çözümlenmiştir. Azaiez ve Sharif, (2005) bu çalışmada anket metodunu kullanmışlardır ve bunun sonucuna göre hemşire ve hastanenin istekleri karşılanmaya çalışılmıştır. Riyadh Al-Kharj Hastanesinde 0-1 tam sayılı hedef programlama yaklaşımını kullanarak bir hemşire çizelgeleme problemini incelemişlerdir. Çalışmada fazla mesai gibi durumları minimize etmeyi amaçlarken hemşirelerin istekleri de göz önünde bulundurulmuştur. Hemşirelerin tercihlerini öğrenmek için anket çalışması yapılmıştır. Hedef programlama modeli ile problemin çözümü sağlanmıştır. Seçkiner ve Kurt (2005) çalışmalarında belirli bir işçi, belirli zamanda, minimum maliyete göre çizelgelenmiş ve farklı faktörleri de göz önünde bulundurmuşlardır. Horn vd. (2007) yaptıkları çalışmada Avustralya Kraliyet Donanması için karakol botları ve mürettebatını çizelgeleme problemini incelemişlerdir. Sungur (2008) çalışmasında güzellik salonu çalışanlarının çizelgelemesini yapabilmek için, her bir işçinin haftanın hangi günlerinde ve günün hangi saatlerinde çalışacağını belirlemiştir. Amaç, her bir çalışma günü ve saati için ihtiyaç duyulan işgücü sayısını minimum maliyetle karşılamak şartıyla, her bir tura atanacak işgücü sayısının belirlenmesidir. Bozbura vd. (2008) yaptıkları çalışmalarında kritik görevlerdeki işçilerin nöbet planlaması problemini incelemişlerdir. Üretim maliyetlerinin minimize edilmesi amaçlanmıştır. Brunner vd. (2009) bir hastanede psikiyatr bölümünde çalışan doktorların vardiya çizelgeleme problemini araştırmışlardır. Amaç hastanenin maaş maliyetlerini minimize etmesidir. Günther ve Nissen (2010) çalışmalarında meta-sezgisel optimizasyon olan parçacık sürüm optimizasyonunu kullanmışlardır. Bu yöntemle vardiya çizelgeleme çalışmalarını geliştirebileceklerini düşünmüşlerdir. Oluşturdukları model ile bir lojistik şirketi çalışanlarına çizelgeleme yaparak uygulamaya koymuşlardır. Karaatlı (2010) çalışmasında hemşirelerin iş yoğunluklarına göre, bulanık çok amaçlı doğrusal bir model önerisinde bulunmuştur. Burke vd. (2010) çok fazla kısıttan oluşan hemşire çizelgeleme problemini değişken komşu arama algoritmasını tam sayılı programlama ile birleştirerek çok amaçlı melez bir model oluşturmuştur. Glass ve Knight (2010) çalışmalarında hemşireler için nöbet çizelgeleme problemini incelenmişlerdir.

Problemin çözümünde karışık tam sayılı programlama yöntemini kullanmışlardır. Ronnberg ve Larsson (2010) çalışmalarında bir hastane çalışanlarının vardiya planlaması konusunda bir matematiksel model geliştirilmiştir. Wright ve Bretthauer (2010) çalışmalarında hastanede çalışan hemşirelerin en verimli şekilde vardiya planlamasını oluşturmak için bir çözüm uygulamışlardır. Brunner ve Edenharter (2011) çalışmalarında bir hastanede çalışan personellerin çalışma çizelgesini hazırlamışlardır. Karışık tam sayılı programlama modeli kurarak sezgisel algoritma ile çözmüşlerdir ve hastanede uygulamaya konmuştur. Bağ vd. (2012) yaptıkları çalışmada hemşire çizelgeleme problemini incelemişlerdir. Hedef programlamada ağırlıkları ANP ile belirlenmiştir. Kurulan model, Kırıkkale'de hizmet veren bir devlet hastanesinde uygulanmıştır. Çalışmanın sonunda mevcut durum ve sonuç kıyaslanmıştır, sonuçlar değerlendirilmiştir. Fırat ve Hurkens (2011) çalışmalarında tam sayılı programlama kullanmışlardır. Kıdeme göre farklı yetenek isteyen işleri o kişilere atayarak iş düzeni çizelgelemesi yapmışlardır. Li vd. (2012) çalışmalarında hedef programlama ile sezgisel yöntemleri bir arada kullanmıştır, hibrit bir yaklaşımla personel çizelgelemesi yapmışlardır. Labadi vd. (2014) çalışmalarında çok amaçlı hedef programlama kullanmışlar ve Banka Bilgi Teknolojileri personeli için çizelgeleme çalışması yapmışlardır. Öztürkoğlu ve Çalışkan (2014) çalışmalarında hemşire çizelgeleme problemini incelemişlerdir. Kurdukları modelin amacı, çizelgeleme boyunca hemşirelerin kendilerine tanınan esnek işe başlama saatlerinden yararlanarak istedikleri saatte işe başlamaları halinde elde edecekleri tatmini maksimize etmektir. Todovic vd. (2015) çalışmasında hedef programlama modeli kullanmıştır. Bosna Hersek'teki bir polis karakolu ele alınmış ve buradaki polis memurlarının vardiya çizelgelemesi üzerine çalışılmıştır. Ünal ve Eren (2016) yaptığı çalışmada nöbet çizelgeleme problemi üzerine çalışmıştır. Çalışanlardan ilk önce çalışamayacakları günleri belirlemeleri istenmiştir. Daha sonra kıdem seviyeleri göz önünde bulundurularak nöbet çizelgeleme yapılmıştır. Yağcıoğlu vd. (2016) çalışmasında bir kredi yurtlar kurumunda güvenlik görevlisi sayısının minimize edilmesi için vardiya çizelgeleme problemini ele almıştır. Varlı ve Eren (2017b) çalışmalarında bir fabrikada çalışan şeflerin iş gücü çizelgelemeleri için bir matematiksel model geliştirmişlerdir. Varlı vd. (2016a) raylı sistemlerde çalışan vatmanları birer ekip halinde ele alarak aylık çalışma planlarının düzenlenmesi için bir çalışma sunmuşlardır. Varlı vd. (2016b) Ankara M1 (Batıkent-Kızılay) hattında çalışan vatmanların tecrübelerine göre ihtiyaç duyulan iş gücünün karşılanması adına bir matematiksel model önermişlerdir. Varlı ve Eren (2017a) çalışmalarında Kırıkkale'de hizmet veren bir hastanede çalışan hemşirelerin vardiya planlarının adil bir şekilde yapılmasını sağlamışlardır. Şahiner vd. (2017) çalışmalarında hemşire çizelgeleme problemini ele almışlardır. Hemşirelere verilen kişisel izinler ve doğum izinleri gibi özel sebeplerle birlikte bir hedef programlama modeli sunmuşlardır. Özcan vd. (2017) çalışmalarında hidroelektrik santrallerinde çalışan personellerin aylık vardiya çizelgelerini işletmenin kuralları doğrultusunda planlamışlardır. Her bir vardiyaya belirlenen kıdem seviyelerine göre atamalar gerçekleştirmişler ve geliştirdikleri matematiksel model ile personellerin daha dikkatli ve konsantre bir şekilde çalışmalarını sağlamışlardır.

5. UYGULAMA

Bu çalışmada Kırıkkale Üniversitesi'nde çalışan güvenlik görevlilerin aylık çalıştıkları bölümlere adaletli ve dengeli bir şekilde atanması istenmiştir. Bu görevliler sözleşmeli erkekler ve kadınlar, kadrolu erkekler olmak üzere çalışma koşulları değerlendirilmiştir. Ek olarak bu sınıflandırmalara göre kişisel kısıtlarda kullanılmıştır. Güvenlik görevlilerinin çalıştıkları 19 bölüm ve 3 vardiya vardır. Çalıştıkları bölümler şu şekildedir: A giriş kapısı (AK), B giriş kapısı (BK), C giriş kapısı (CK), Tıp (TF), Diş Hekimliği (DHF), Mühendislik (MF), Güzel Sanatlar (GSF), Eğitim (EF), Fen Edebiyat (FEF), Veterinerlik (VF), Hukuk (HF), İktisadi ve İdari Birimler (İİBF), İslami İlimler (İİF) Fakülteleri, Beden Eğitimi Ve Spor Yüksekokulu (BESYO), Meslek Yüksek Okulu (MYO), Kütüphane (KTP), Öğrenci İşleri (Öİ), Rektörlük A (RA), Rektörlük B (RB) ve Kamera (KMR) yerleridir. Vardiyalar ise Sabah-S, Akşam-A, Gece-G olarak gösterilmiştir. Her bir vardiyanın saat dilimleri ise Sabah (08:00-16:00), Akşam (16:00-24:00), Gece (24:00-08:00).

Çalışmada oluşturulan matematiksel modellerde aşağıda verilen güvenlik görevlilerinin çalışma prensipleri kullanılmıştır.

Güvenlik Görevlilerinin Çalışma Koşulları:

- Her bölümde ihtiyaç duyulan görevli sayısı karşılanmalıdır.
- Kadrolu güvenlik görevlileri ardı ardına en fazla 5 gün çalışmalıdır haftada 2 gün izin verilmelidir.
- Sözleşmeli erkek güvenlik görevlileri ardı ardına en fazla 6 gün çalışmalıdır ve haftada 1 gün izin verilmelidir.
- Sözleşmeli bayan güvenlik görevlileri sadece sabah vardiyasında çalışmalıdır.
- Üç vardiya çalışan her bir güvenlik görevlisi için gece vardiyasında çalıştığı takdirde ertesi gün ki sabah ve akşam vardiyalarında çalışmamalıdır.

MÜHENDİSLİK FAKÜLTESİ

Uluslararası Mühendislik Araştırma ve Geliştirme Dergisi

International Journal of Engineering Research and Development

Cilt/Volume:9 Sayı/Issue:3 Aralık/December 2017 https://doi.org/10.29137/umagd.371100

Araştırma Makalesi / Research Article

Ballistic Impact Simulation of Ceramic/Metal Armor Structures

Kemal ARSLAN[*1], Recep GUNES[2]

[1]*Erciyes University, Graduate School of Natural and Applied Sciences, Kayseri 38039, TURKEY*
[2]*Erciyes University, Department of Mechanical Engineering, Kayseri 38039, TURKEY*

Başvuru/Received: 06/05/2017 **Kabul/Accepted**: 06/09/2017 **Son Versiyon/Final Version**: 26/12/2017

Abstract

The study presents a comparative numerical investigation on ballistic performance of ceramic/metal armor structures. 2D axisymmetric numerical model was developed for ballistic impact simulations using LS-DYNA® finite element software. The armor structures included combinations of boron carbide (B_4C), Al6061-T6 and 4340 steel constituents. The interfaces in the armor structure were modelled with an epoxy resin adhesive. In order to define proper material behavior, Johnson-Holmquist-Ceramics material model for B_4C and Plastic-Kinematic material model for Al6061-T6, 4340 steel and epoxy resin was used. The armor structures were subjected to 7.62 mm ogive-nosed steel projectile impact. In the first section, the influence of back plate material on the ballistic performance of the armor structure for bi-layers ceramic/metal configuration (ceramic front face and metal back plate) was investigated for Al6061-T6 and 4340 steel materials under same thickness and areal density. In the second section, the effect of removing half thickness of the metal constituent from the back plate and placing on the front face was investigated for both Al6061-T6 and 4340 steel materials. Finally, the influence of adhesive thickness on the ballistic performance of the armor structure was investigated. Perforation response of the armor structures were examined in terms of residual velocity of the projectile and damage mechanisms of the armor structure.

Key Words

"Ballistic impact; Finite element analysis; Ceramic/Metal armor; Perforation"

** karslan@erciyes.edu.tr*

1. INTRODUCTION

Ceramics have been one of the most important component for armor structures with their high specific strength, hardness and thermal resistance properties. However, they are not preferred as a monolithic armor by reason of their brittle structure. Therefore, they are widely used as front face plate with ductile materials in order to deform projectile geometry, decrease the effect of shock waves on substrates and spread the impact load over a large region. In order to provide structural integrity and absorb the remaining kinetic energy of the projectile, more ductile and tougher materials are used as back plate in ceramic-faced armor structures. There are generally two different options for back plate material: metals and fiber-reinforced polymer (FRP) composites. FRP composites can be used as back plate for better performance, but metals can be preferable by reason of being more economical than FRP composites and providing protective function [López-Puente et al. (2005)]. The use of ceramic/metal bi-layer armor structures provides lighter designs compared to monolithic metal armors showing the same or better ballistic protection. Several researchers have investigated the ballistic impact response of different ceramic/metal armor structures using experimental, numerical and analytical methods or combinations of these methods [Zaera and Sánchez-Gálvez (1998), Zaera et al. (2000), Lee and Yoo (2001), Arias et al. (2003), Gonçalves et al. (2004), Mahdu et al. (2005), Chi et al. (2013), Serjouei et al. (2015), Tang and Wen (2017)].

In this study, a numerical study was carried out on ballistic performance of ceramic/metal armor structures subjected to 7.62 mm ogive-nosed steel projectile impact using 2D axisymmetric finite element model. The effect of different back plate material under same thickness and areal density, transforming the armor structure from bi-layers to tri-layers configuration under same areal density and the influence of adhesive thickness were investigated.

2. NUMERICAL MODEL

Ballistic impact simulation of ceramic/metal armor structures was performed using explicit finite element code, LS-DYNA®. The armor structures were subjected to 60° conical-nosed cylindrical steel projectile with 7.62 mm diameter.

In the armor structures, boron carbide (B_4C) ceramic constituent, Al6061-T6 and 4340 steel metal constituents were used. The interfaces in the armor structure were modelled with an epoxy resin adhesive. The dimensions of the steel projectile were 7.62 mm in diameter and 28.1 mm in length [Fawaz et al. (2004)]. 2D axisymmetric numerical model shown in Fig. 1 was developed for ballistic impact simulations. In the first section, bi-layers ceramic/metal configuration, ceramic front face and metal back plate, was considered and the influence of the back plate material on the ballistic performance of the armor structure was investigated for two different metal, Al6061-T6 and 4340 steel, under same thickness and areal density. In the second section, tri-layers metal/ceramic/metal configuration was considered in order to prevent ceramic fragmentation from the front face and compared with the bi-layers configuration. In tri-layers configuration, half thickness of the metal constituent was removed from the back plate and placed on the front face. Namely, the total weight of the armor structure remained constant except the second adhesive layer. Finally, the effect of adhesive thickness for the armor structure with 4340 steel back plate was investigated for two different thickness. The total armor thickness was considered as 15 mm with 5 mm thickness of ceramic front face and 10 mm thickness of metal back plate. For the first and second section investigation, the thickness of the adhesive layer was modelled as 0.5 mm and in order to investigate the effect of adhesive thickness, the thicknesses of 0.5 mm and 1.0 mm were considered.

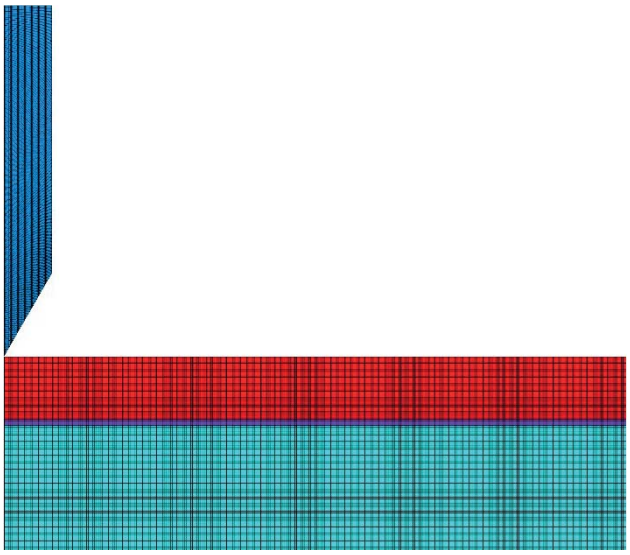

Fig. 1. Finite element models of the ceramic/metal armor structure and steel projectile.

The projectile and armor structure were represented with 2D and 4-node solid element with its axisymmetric option and the element size of the finite element model was determined as 0.125 mm performing successive analyses. The constituents of the armor were represented with two different material models in LS-DYNA®. The steel projectile, Al6061-T6, 4340 steel and epoxy resin were modelled using an elastic-plastic material model, MAT_PLASTIC_KINEMATIC (MAT_003) [Kreig and Key (1976)] and the ceramic constituent B_4C was modelled with a plasticity damage model, MAT_JOHNSON_HOLMQUIST_CERAMICS (MAT_110) material model which is useful for modelling ceramics, glass and other brittle materials [Johnson and Holmquist (1993)]. The material model parameters of the steel projectile [Fawaz et al. (2004), Tasdemirci et al. (2012)], Al6061-T6 [Nechitailo and Batra (1998)], 4340 steel [Nechitailo and Batra (1998)], epoxy resin [Huang and Chen (2016)] and B_4C [Johnson and Holmquist (1999)] were listed in Table 1 and Table 2, respectively.

Table 1. Material properties of the steel projectile, Al6061-T6, 4340 steel and epoxy resin.

Material parameters	**Steel projectile**	**Al6061-T6**	**4340 steel**	**Epoxy resin**
Density (kg/m^3)	7890	2700	7850	1150
Young's modulus (GPa)	202	73.3	200	1.14
Poisson's ratio	0.3	0.33	0.29	0.49
Yield stress (MPa)	1069	298	970	43
Tangent modulus (GPa)	2	0.38	0.47	0.036
Effective plastic strain at failure	0.80	0.85	0.77	0.60

Table 2. Johnson-Holmquist-Ceramics material model input parameters for B_4C.

Density (kg/m^3)	G (GPa)	A	B	C	M	N
2510	197	0.927	0.7	0.005	0.85	0.67
EPSI	T (GPa)	SFMAX	HEL (GPa)	PHEL (GPa)	BETA	
1.0	0.26	0.2	19	8.71	1.0	
D1	D2	K1 (GPa)	K2 (GPa)	K3 (GPa)		
0.001	0.5	233	-593	2800		

G – Shear modulus; A – Intact normalized strength parameter; B – Fractured normalized strength parameter; C – Strength parameter (for strain rate dependence); M – Fractured strength parameter (pressure exponent); N – Intact strength parameter (pressure exponent); EPSI – Reference strain rate; T – Maximum tensile pressure strength; SFMAX – Maximum normalized fractured strength; HEL – Hugoniot elastic limit; PHEL – Pressure component at the Hugoniot elastic limit; BETA – Fraction of elastic energy loss converted to hydrostatic energy; D1 – Parameter for plastic strain to fracture; D2: Parameter for plastic strain to fracture (exponent); K1 – First pressure coefficient (equivalent to the bulk modulus); K2: Second pressure coefficient; K3 - Third pressure coefficient

In order to simulate failure mechanisms of the metal constituents and epoxy resin, effective plastic strain at failure value (erosion criterion) of the materials which is available for Plastic-Kinematic material model was defined. For Johnson-Holmquist-Ceramics material model, the erosion criterion is based on failure strain (FS) value where the element is deleted when the plastic strain exceeds the identified failure strain. The FS value is a material erosion criterion and is not involved in the damage calculations. It allows to remove highly distorted redundant elements from the calculations and does not affect the simulation predictions [Cronin et al. (2003)]. The FS value was defined as 1.25 in this study. In addition, in order to avoid high level distortions in elements, Flanagan-Belytschko viscous form hourglass option [Flanagan and Belytschko (1981)] was defined.

In order to consider mechanical contact between projectile and armor structure and possible self-contacting surfaces, CONTACT_2D_AUTOMATIC_SINGLE_SURFACE algorithm was defined. The contact between the ceramic and metal constituents was provided by modelling an epoxy resin adhesive layer in finite element model. The adhesive layer was modelled as tied with the ceramic front face and metal back plate. Furthermore, an approximate effective plastic strain at failure value of 0.60 was defined for epoxy resin in order to model possible separations at the interface.

The armor structure was clamped with a distance of 10 mm from the edge and the velocity of the projectile was considered as 1000 m/s which perforates the armor structures by reason of comparison of the configurations in terms of residual velocity of the projectile. Besides, different configurations of the armor structure were also examined in terms of damage mechanisms.

3. RESULTS AND DISCUSSION

Ballistic impact performance of ceramic/metal armor structures was investigated under 7.62 mm ogive-nosed steel projectile impact and simulation results were examined in terms of residual velocity of the projectile and damage mechanisms of the armor structure.

In the first section, the effect of the back plate material on the ballistic performance of the armor structure was investigated for two different metal, Al6061-T6 and 4340 steel. The metal back plates were examined under same thickness and areal density. The time history of the projectile velocity for same thickness of the back plates was given in Fig. 2. The residual velocity of the projectile for Al6061-T6 and 4340 steel back plates was 635.7 m/s and 170.5 m/s, respectively. The residual velocity of the projectile for 4340 steel was about 73.2% less than for Al6061-T6. On the other hand, the weight of the armor with 4340 steel was 2.3 times more than with Al6061-T6 under same thickness configuration. The damage shapes of the armor structures for same thickness of the back plates were given in Fig. 3. The armor structures with different metal back plates showed different damage mechanisms. In general, the ceramic front plate exhibited extremely radial cracks and rarely axial cracks while ductile perforation occurred in the metal back plates. In details, the strength and stiffness of the back plate influenced the damage level of the ceramic front plate. For the armor structure with 4340 steel back plate, damage level (crack size, crack propagation and ceramic conoid) occurred in ceramic front plate was higher than with Al6061-T6 back plate by reason of stiffer structure of 4340 steel. Al6061-T6 provided more ductile behavior to the armor structure. Moreover, shear cracks resulted in the adhesive layer and separation occurred at the interface for 4340 steel back plate whereas any failure did not observe in the adhesive layer for Al6061-T6 back plate.

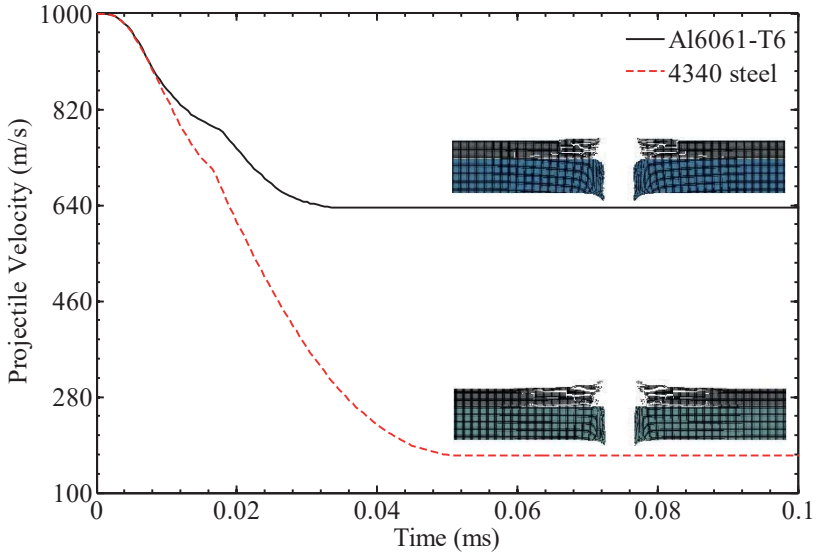

Fig. 2. The time history of the projectile velocity for Al6061-T6 and 4340 steel back plates under same thickness.

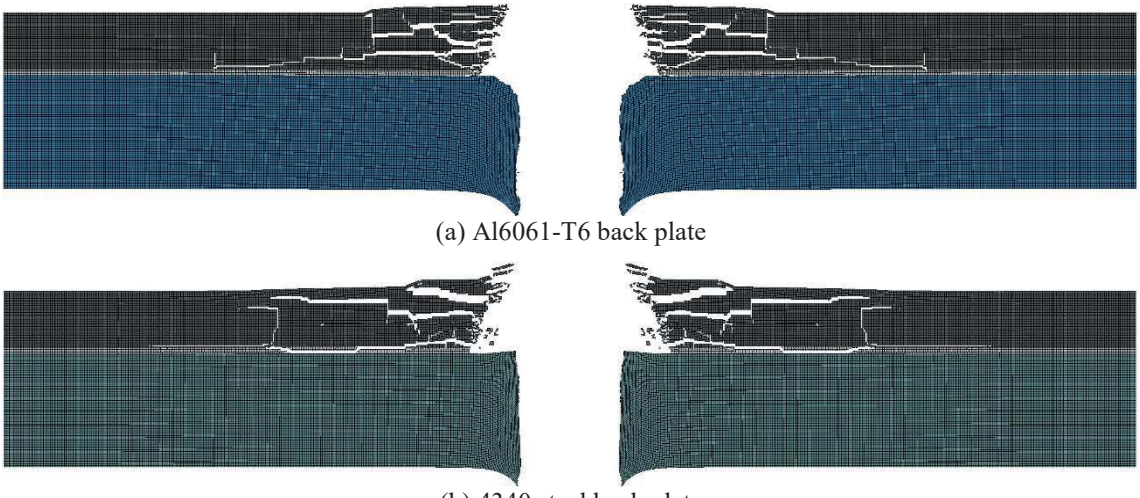

(a) Al6061-T6 back plate

(b) 4340 steel back plate

Fig. 3. The damage shapes of the armor structure for Al6061-T6 and 4340 steel back plates under same thickness.

For the same areal density configuration, the thickness of 4340 steel back plate for same areal density with 10 mm thickness of Al6061-T6 was determined as about 3.44 mm. The time history of the projectile velocity for same areal density of the back plates was given in Fig. 4. The residual velocity of the projectile for Al6061-T6 and 4340 steel back plates was 635.7 m/s and 592.9 m/s, respectively. The residual velocity of the projectile for 4340 steel was about 6.7% less than for Al6061-T6. Although the thickness of 4340 steel back plate was 2.9 times less than Al6061-T6, the armor structure with 4340 steel back plate exhibited better ballistic performance in terms of residual velocity of the projectile. The damage shapes of the armor structures for same areal density of the back plates were given in Fig. 5. The damage level such as crack propagation for 4340 steel back plate decreased for same areal density configuration compared with same thickness configuration by reason of decrement in the stiffness related with reduction in the plate thickness. The shear cracks occurred in same thickness configuration did not resulted in same areal density configuration for adhesive layer.

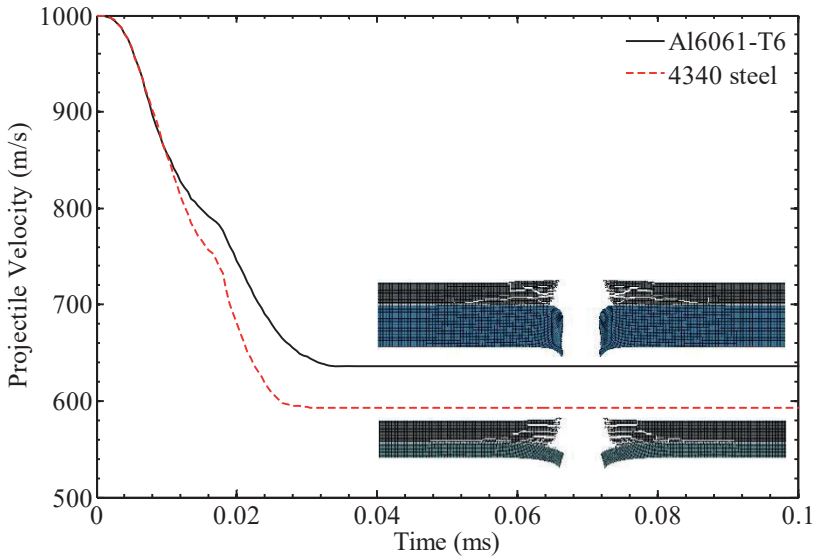

Fig. 4. The time history of the projectile velocity for Al6061-T6 and 4340 steel back plates under same areal density.

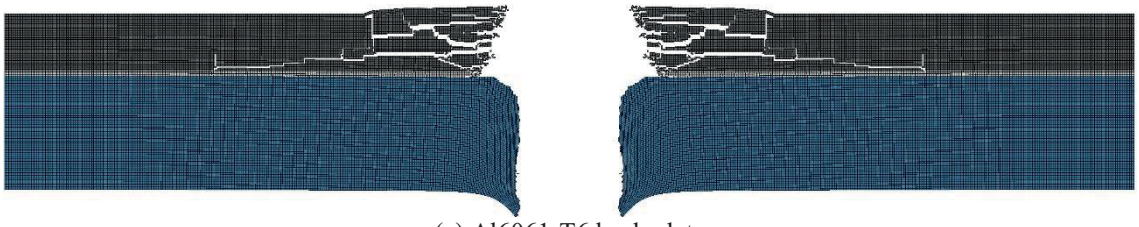

(a) Al6061-T6 back plate

(b) 4340 steel back plate

Fig. 5. The damage shapes of the armor structure for Al6061-T6 and 4340 steel back plates under same areal density.

In the second section, the effect of removing half thickness of the metal constituent from the back plate and placing on the front face on the residual velocity of the projectile and damage mechanisms of the armor structure was investigated. In other words, bi-layers ceramic/metal and tri-layers metal/ceramic/metal configurations were compared. The aim of placing half thickness of the metal constituent on the front face was to investigate prevention level of the top metal layer from ceramic fragmentation. These configurations were investigated for both Al6061-T6 and 4340 steel back plates. The time history of the projectile velocity for bi-layers and tri-layers configurations of Al6061-T6 was given in Fig. 6. The residual velocity of the projectile for bi-layers and tri-layers configurations was 635.7 m/s and 720.7 m/s, respectively. The residual velocity of the projectile for bi-layers configuration was about 11.8% less than for tri-layers configuration. Transforming the armor structure from bi-layers to tri-layers configuration reduced to ballistic performance of the armor structure in terms of residual velocity of the projectile. The damage shapes of the armor structures for bi-layers and tri-layers configurations of Al6061-T6 were given in Fig. 7. In general, a considerable

enhancement was not observed in tri-layers configuration in terms of damage level. However, tri-layers configuration partially prevented the fragmentation at the top side of the ceramic plate.

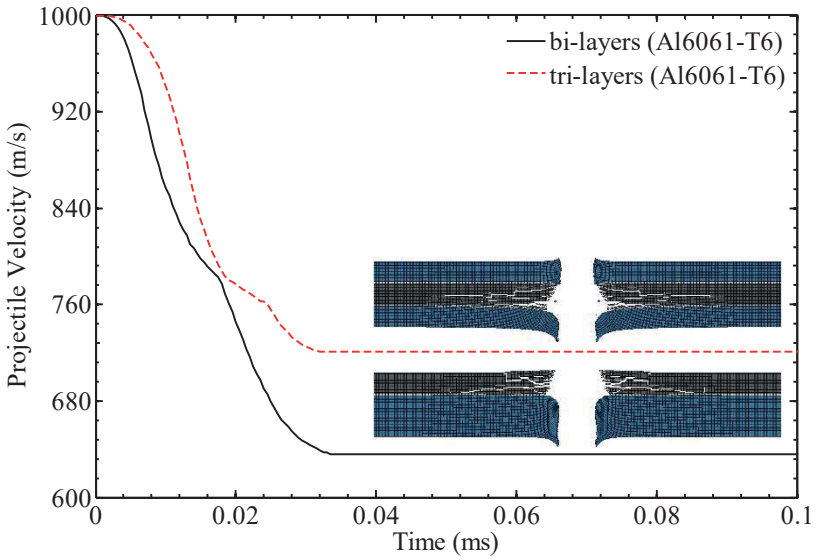

Fig. 6. The time history of the projectile velocity for bi-layers and tri-layers configurations of Al6061-T6.

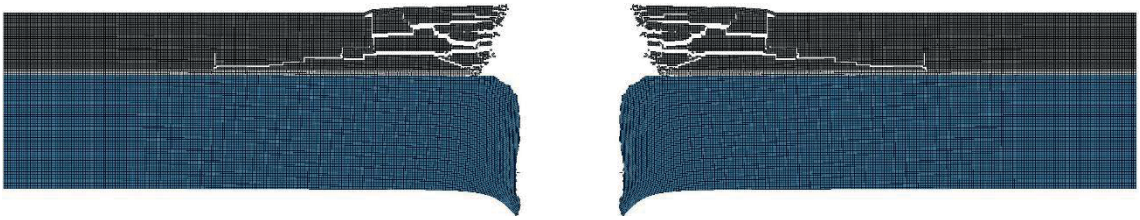

(a) Bi-layers configuration (Al6061-T6)

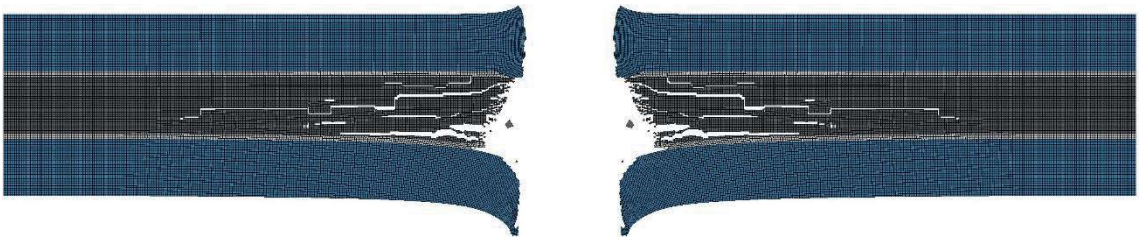

(b) Tri-layers configuration (Al6061-T6)

Fig. 7. The damage shapes of the armor structure for bi-layers and tri-layers configurations of Al6061-T6.

The time history of the projectile velocity for bi-layers and tri-layers configurations of 4340 steel was given in Fig. 8. The residual velocity of the projectile for bi-layers and tri-layers configurations was 170.5 m/s and 297.3 m/s, respectively. The residual velocity of the projectile for bi-layers configuration was about 42.7% less than for tri-layers configuration. Similar to the armor structure with Al6061-T6 back plate, transforming the armor structure from bi-layers to tri-layers configuration reduced to ballistic performance of the armor structure in terms of residual velocity of the projectile. The damage shapes of the armor structures for bi-layers and tri-layers configurations of 4340 steel were given in Fig. 9. In contrary to the armor structure with Al6061-T6 back plate, tri-layers configuration of 4340 steel decreased the damage occurred in ceramic plate. In tri-layers configuration, crack formation was concentrated at the bottom side of the ceramic plate and top side of the ceramic plate was prevented from fragmentations occurred in bi-layers configuration. Although ballistic performance of the armor structure with 4340 steel constituent decreased in terms of residual velocity of the projectile, damage and fragmentation level occurred in ceramic plate enhanced.

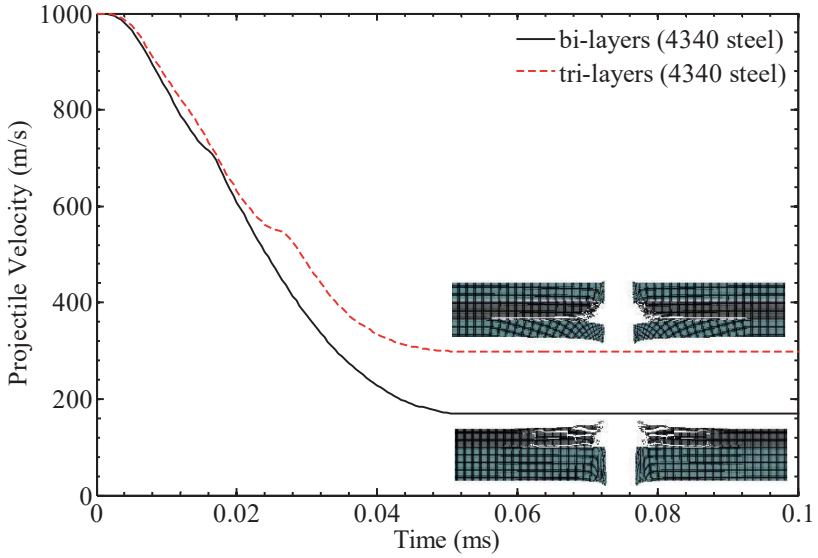

Fig. 8. The time history of the projectile velocity for bi-layers and tri-layers configurations of 4340 steel.

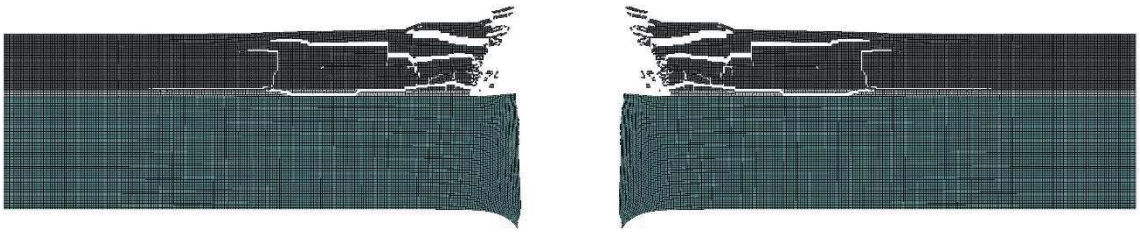

(a) Bi-layers configuration (4340 steel)

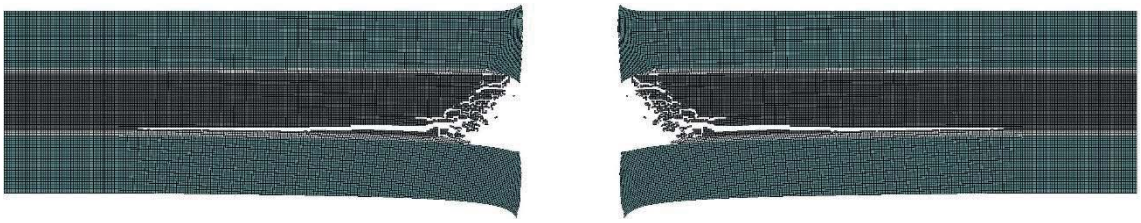

(b) Tri-layers configuration (4340 steel)

Fig. 9. The damage shapes of the armor structure for bi-layers and tri-layers configurations of 4340 steel.

The influence of adhesive thickness (t) was investigated for the armor structure with 4340 steel back plate for two different thicknesses, 0.5 mm and 1.0 mm. The time history of the projectile velocity for different adhesive thicknesses was given in Fig. 10. The residual velocity of the projectile for the adhesive thickness of 0.5 mm and 1.0 mm was 170.5 m/s and 214.8 m/s, respectively. The residual velocity of the projectile for the adhesive thickness of 1.0 mm was about 26.0% more than for the adhesive thickness of 0.5 mm. Increasing the adhesive thickness from 0.5 mm to 1.0 mm caused to decrement in the ballistic performance of the armor structure in terms of the residual velocity of the projectile similar to the study of López-Puente et al. (2005). The damage shapes of the armor structures for different adhesive thicknesses were given in Fig. 11. The crack formation occurred in the ceramic front plate decreased, however the size of ceramic fragments increased with increasing adhesive thickness. For the adhesive thickness of 0.5 mm, more crack paths, longer crack propagation and smaller ceramic fragments occurred in the ceramic front plate. Additionally, no shear cracks was observed in the adhesive layer for the thickness of 1.0 mm whereas shear cracks occurred in the adhesive layer for the thickness of 0.5 mm.

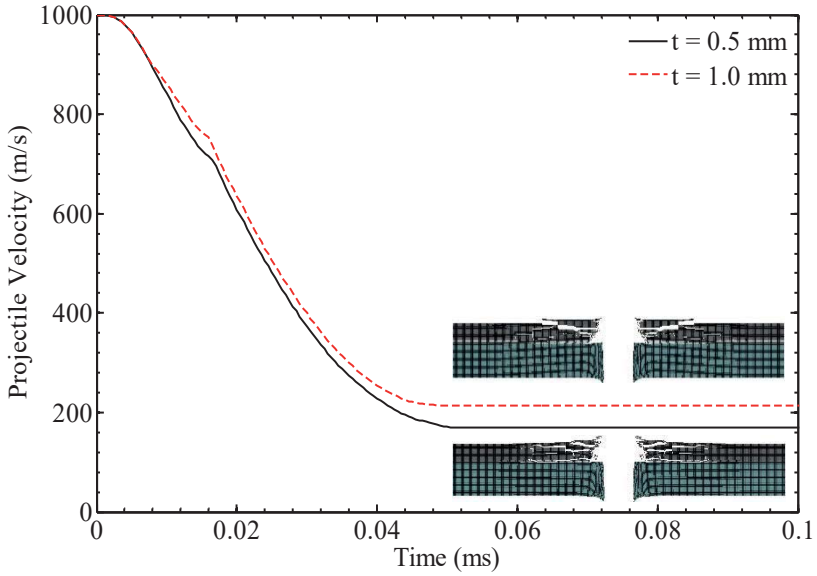

Fig. 10. The time history of the projectile velocity for different adhesive thicknesses (4340 steel back plate).

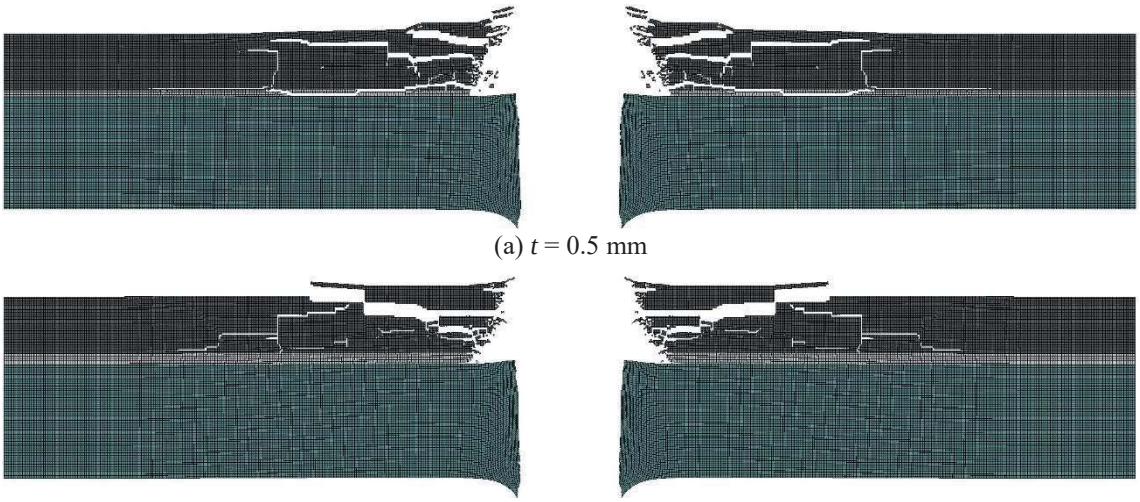

(a) t = 0.5 mm

(b) t = 1.0 mm

Fig. 11. The damage shapes of the armor structure for different adhesive thicknesses (4340 steel back plate).

4. CONCLUSION

A comparative numerical study was performed on ballistic impact response of ceramic/metal armor structures subjected to 7.62 mm ogive-nosed steel projectile. The simulation results were examined in terms of residual velocity of the projectile and damage mechanisms of the armor structures.

- The bi-layers armor structure with 4340 steel back plate exhibited better ballistic performance than with Al6061-T6 back plate under both same thickness and areal density in terms of residual velocity of the projectile.
- The damage level (crack size, crack propagation and ceramic conoid) occurred in ceramic front plate for 4340 steel back plate was higher than for Al6061-T6 back plate by reason of stiffer structure of 4340 steel under both same thickness and areal density configuration.
- Shear cracks resulted in the adhesive layer for only the armor structure with 4340 steel back plate for same thickness configuration.
- Transforming the armor structures from bi-layers to tri-layers configuration reduced to the ballistic performance of the armor in terms of residual velocity of the projectile for both back plates.

- Tri-layers configuration of 4340 steel decreased the damage occurred in ceramic plate and top side of the ceramic plate was fully prevented from fragmentations whereas an enhancement was not observed in tri-layer configuration of Al6061-T6 in general and ceramic fragmentation at the top side of the ceramic plate partially prevented.
- Increasing the adhesive thickness from 0.5 mm to 1.0 mm reduced to ballistic performance of the armor structure in terms of the residual velocity of the projectile.
- Increasing the adhesive thickness from 0.5 mm to 1.0 mm prevented the shear cracks in the adhesive layer, crack formation and propagation in the ceramic front plate and however caused to increment in the size of ceramic fragments.

Finally, this is a comparative numerical investigation on the ballistic performance of a ceramic/metal armor and authors do not claim that the armor structure can be practicable in this investigated form. It should be verified by experimental tests and optimized in terms of geometrical and mechanical properties of the constituents.

REFERENCES

Arias, A., Zaera, R., López-Puente, J., & Navarro, C. (2003). Numerical modeling of the impact behavior of new particulate-loaded composite materials. Composite Structures, 61, 151-159.

Cronin, D.S., Bui, K., Kaufmann, C., Mclntosh, G., & Berstad, T. (2003). Implementation and validation of the Johnson-Holmquist ceramic material model in LS-DYNA. 4th European LS-DYNA Users Conference, 22-23 May, Ulm/Germany, 47-59.

Chi, R., Serjouei, A., Sridhar, I., & Tan, G.E.B. (2013). Ballistic impact on bi-layer alumina/aluminium armor: A semi-analytical approach. International Journal of Impact Engineering, 52, 37-46.

Flanagan, D.P., & Belytschko, T. (1981). A uniform strain hexahedron and quadrilateral and orthogonal hourglass control. International Journal for Numerical Methods in Engineering, 17, 679-706.

Fawaz, Z., Zheng, W., & Behdinan, K. (2004). Numerical simulation of normal and oblique ballistic impact on ceramic composite armours. Composite Structures, 63, 387-395.

Gonçalves, D.P., de Melo, F.C.L., Klein, A.N., & Al-Qureshi, H.A. (2004). Analysis and investigation of ballistic impact on ceramic/metal composite armour. International Journal of Machine Tools & Manufacture, 44, 307-316.

Huang, C., & Chen, Y. (2016). Design and impact resistant analysis of functionally graded Al_2O_3–ZrO_2 ceramic composite. Materials and Design, 91, 294-305.

Johnson, G.R., & Holmquist, T.J. (1993). An improved computational model for brittle materials. High-Pressure Science and Technology, 981-984.

Johnson, G.R., & Holmquist, T.J. (1999). Response of boron carbide subjected to large strains, high strain rates and high pressures. Journal of Applied Physics, 85, 8060-8073.

Kreig, R.D., & Key, S.W. (1976). Implementation of a time dependent plasticity theory into structural computer programs. Constitutive Equations in Viscoplasticity: Computational and Engineering Aspects, eds., J.A. Stricklin and K.J. Saczalski, ASME, New York, 125-137.

López-Puente, J., Arias, A., Zaera, R., & Navarro, C. (2005). The effect of the thickness of the adhesive layer on the ballistic limit of ceramic/metal armours. An experimental and numerical study. International Journal of Impact Engineering, 32, 321-336.

Lee, M., & Yoo, Y.H. (2001). Analysis of ceramic/metal armour systems. International Journal of Impact Engineering, 25, 819-829.

Mahdu, V., Ramanjaneyulu, K., Bhat, T.B., & Gupta, N.K. (2005). An experimental study of penetration resistance of ceramic armour subjected to projectile impact. International Journal of Impact Engineering, 32, 337-350.

Nechitailo, N.V., & Batra, R.C. (1998). Penetration/Perforation of aluminum, steel and tungsten plates by ceramic rods. Computers & Structures, 66, 571-583.

Serjouei, A., Chi, R., Zhang, Z., & Sridhar, I. (2015). Experimental validation of BLV model on bi-layer ceramic-metal armor. International Journal of Impact Engineering, 77, 30-41.

Tang, R.T., & Wen, H.M. (2017). Predicting the perforation of ceramic-faced light armors subjected to projectile impact. International Journal of Impact Engineering, 102, 55-61.

Tasdemirci, A., Tunusoglu, G., & Guden, M. (2012). The effect of the interlayer on the ballistic performance of ceramic/composite armors: Experimental and numerical study. International Journal of Impact Engineering, 44, 1-9.

Zaera, R., & Sánchez-Gálvez, V. (1998). Analytical modelling of normal and oblique ballistic impact on ceramic/metal lightweight armours. International Journal of Impact Engineering, 21, 133-148.

Zaera, R., Sánchez-Sáez, S., Pérez-Castellanos, J.L., & Navarro, C. (2000). Modelling of the adhesive layer in mixed ceramic/metal armours subjected to impact. Composites Part A: Applied Science and Manufacturing, 31, 823-833.

MÜHENDİSLİK FAKÜLTESİ

Uluslararası Mühendislik Araştırma ve Geliştirme Dergisi

International Journal of Engineering Research and Development

Cilt/Volume:9 Sayı/Issue:3 Aralık/December 2017 https://doi.org/10.29137/umagd.371105

Araştırma Makalesi / Research Article

Position Estimation with Fuzzy Logic Based Dead Reckoning for GPS-Denied Environment

Murat LÜY[1], Faruk ULAMIŞ[2] , Ertuğrul ÇAM[1]

[1]Kırıkkale Üniversitesi, Mühendislik Fakültesi Elektrik Elektronik Mühendisliği, KIRIKKALE, TURKEY
[2]Kırıkkale Üniversitesi, Hacılar Hüseyin Aytemiz Meslek Yüksek Okulu, KIRIKKALE, TURKEY

Başvuru/Received: 06/05/2017 **Kabul/Accepted**: 06/09/2017 **Son Versiyon/Final Version**: 26/12/2017

Abstract

The importance of security precautions has been increased as a consequence of raised terrorist incidents. Terrorist acts that move into the city from country sides have made tracking of security and military personnel more important. GPS signals, densely utilized for this tracking, pose a problem in signal blockage situation and GPS-denied environments. The main goal of this research is that to develop a practical positioning system for walking military personnel in GPS denied environments. The system is very useful for GPS signal blockage environments, such as tunnels, thick-walled structures and dense high rise buildings, etc.
Proposed system contains a 6-degree of freedom (DOF) inertial measurement unit (IMU) and digital compass attached to the military personnel's shoe. Tri-axis accelerometer and gyroscope measurements are obtained by IMU. These measurements are applied to fuzzy logic algorithms and total displacement for each step is calculated. Digital compass is utilized to determine direction of personnel. Thus, current location has been estimated with the known starting point.

Key Words

"Inertial Measurement Unit, Fuzzy Logic, GPS-denied environment, Dead reckoning."

** farukulamis@kku.edu.tr*

1. INTRODUCTION

Nowadays, navigation is a crucial part of our daily life. However, position estimation for outdoor can be obtained by GPS easily, positioning indoor environment is still a challenging research field which has various application like emergency first responder, military events and security personals (Riebeck et al., 2007; Foxlin, 2005; Samama et al., 2008)
Although there are many studies on positioning indoor environment, it is still open area to research. Indoor positioning system can be separated two branch broadly. First one is infrastructure based system which are Wi-Fi (Retscher et al., 2006), Ultra-Wide Band (UWB) (Ingran et al., 2004), Radio Frequency identification (RFID)(Huang et al., 2015). Infrastructure based indoor positioning requires sensors or beacons that must be placed indoor environment beforehand.
Wi-Fi, RFID and UWB methods are based on radio signals. So the most significant problem in these methods is signal blockage problem. In particular, although UWB offers high precision solutions for indoor positioning, there is a need for infrastructure setup in these three methods and IR methods. So the infrastructure means cost. But besides the problem of cost; In case of an emergency such as an earthquake, fire, or in the event of a power failure, these infrastructures may become damaged or become unusable. As a result, systems that require infrastructure are problematic, especially in military and emergency situations.
The visual based approach is an indoor positioning method that does not require infrastructure setup. In recent years, the fact that visual sensors are cheap and available on all smartphones has brought this method to the forefront. So visual-based approach has become popular for indoor positioning especially robotic navigation and unmanned aerial vehicles (JongBae & HeeSung, 2008). However, there are some disadvantages using visual based approach in practice. The first one is a huge database must be available before navigation. The second disadvantage is the need for high processing power when comparing images with thousands of images in the database. On the other hand in situations such as blurred images and low ambient light, the system cannot perform image matching.
Recent developments in micro-electromechanical systems (MEMS) and fiber optic gyroscope technologies have reduced the size of inertial sensors and made them cheaper. On the other hand, as a result of these sensors produce their own data, there is not problems like signal blockage or signal jamming.
There are several methods for inertial sensor based indoor positioning (Widyawan et al., 2008), (Ojeda&Borenstein, 2008). One of the most powerful and easy of these methods is pedestrian dead reckoning (Jimenez et al., 2009). The main idea of pedestrian dead reckoning method is to utilize accelerometer signals to detect steps, estimate step length and propagate position using a measured heading (such mechanization requires that possible means of transportation other than walking are excluded). Heading can be computed using gyro measurements, digital compass or using both.

The main goal of the research presented here is to develop an algorithm for Pedestrian Dead Reckoning (PDR) based indoor position system. For this purpose, a foot mounted system which contains 6-degree of freedom (DOF) inertial measurement unit (IMU), a magnetic compass and a microprocessor is utilized for indoor PDR system. The main part of PDR system is to determine step length and it is quite depended on walking status. For determining walking status, a fuzzy logic walking status (FLWS) algorithm is proposed in this study.

2.SYSTEM ARCHITECTURE

The algorithm for achieving an accurate positioning solution is represented as shown in Fig. 1. Hardware of the system includes three components called MPU 6050 Inertial Measurement Unit (IMU), HMC 5883 Digital Compass and Arduino Nano as a microprocessor. MPU6050 IMU has 6-Degree of freedom (DoF) and generates 3-axis accelerometer and gyroscope measurements. HMC 5883 digital compass has 12-bit ADC to enable 1° to 2° compass heading accuracy for determining heading. IMU and digital compass have I2C serial bus for allowing easy interface with Arduino platform.

Each sensor is utilized for PDR algorithm. PDR has three main step to estimate position. The first one is step detection, second one is heading estimation. The last and the most important one is step length estimation. IMU is utilized to detect each step. After step detection, walking status of pedestrian (slow, fast and running) is recognized by Fuzzy Logic Walking Status (FLWS) algorithm. Then step length is estimated by PDR using number of step and walking status of each step. Digital compass is used to determine heading of pedestrian.

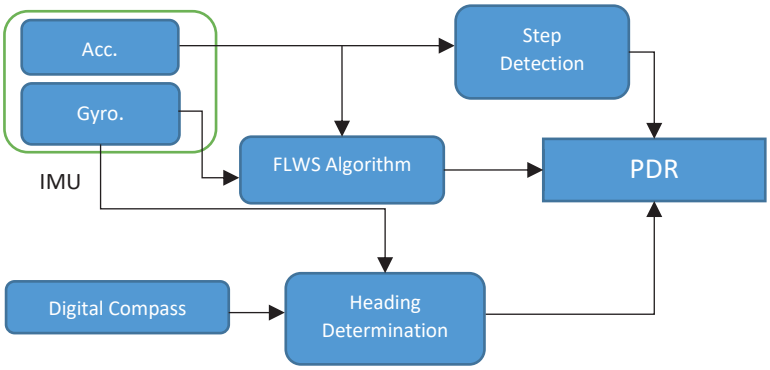

Fig. 1. FLWS Based PDR Algorithm

3. PDR SYSTEM

The basic pattern of pedestrian motion during a walk is a repeatable and cyclical event. Each step consist of two phase as shown figure 2. The first one called "stand phase" is a duration while foot is on the ground and second one called "swing phase" which is start with foot's lifting off the ground and carried forward to begin the stance phase again.

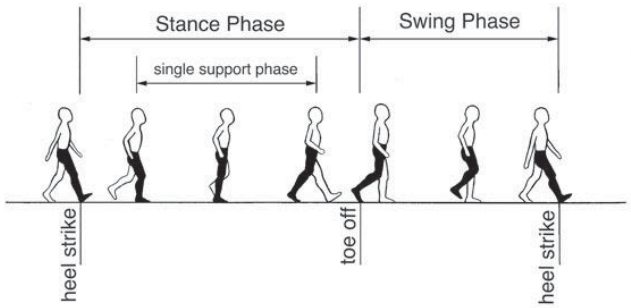

Fig. 2. Swing and stance phases while walking

PDR, which is a method adding distance travelled to the known start point, is proper solution to estimate position of pedestrian for indoor environment. To accomplish an accurate estimation, PDR has three main parts: step detection, heading estimation and step length estimation. After these three module, PDR algorithm calculates the total displacement.

3.1. Step Detection

The first step of the proposed algorithm is step detection. In order to get reliable estimation, step detection must be done accurately. When the location of sensor position is considered, many type of studies have already been done, e.g. the waist, trunk, leg, foot or even the head (Huang et al., 2015). In this study, foot-mounted IMU location have been implemented because of its two advantages. The first advantage of foot-mounted system is to easy detection of Zero Velocity Update (ZUPT) and the second one is make step detection easy compared to other IMU locations. Tri-axis accelerometer and tri-axis gyroscope measurements can be obtained as shown figure 3.

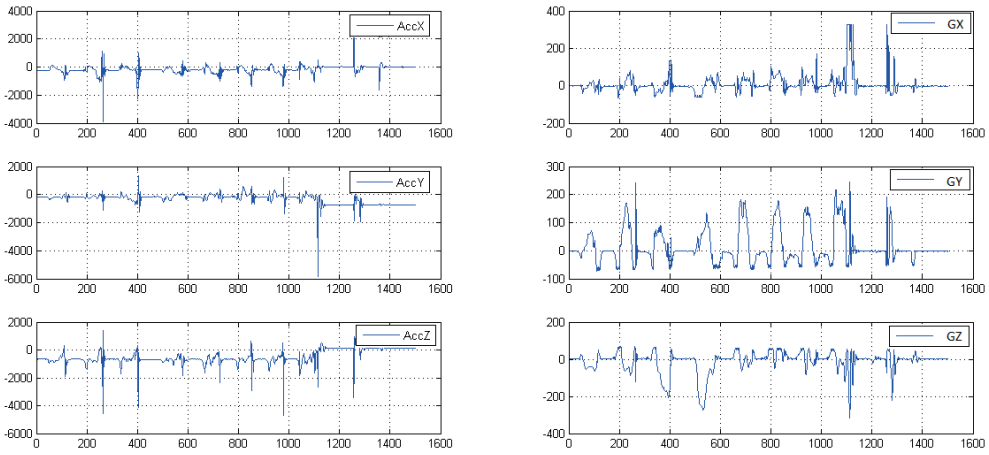

Fig. 3. Tri-axis gyroscope and accelerometer measurement from foot-mounted IMU

There are many techniques for step detection in the literature (acceleration peaks, magnitudes and thresholding). Most of this techniques use the data obtained by accelerometer and gyroscope. In this study, acceleration signal is analyzed to detect step. There are two methods which is used acceleration signals; peak detection and zero-crossing detection.
Zero crossing method counts zero velocity level to determine each step. For minimizing or eliminating false step detection, a time interval thresholding has been utilized. The disadvantage of this method is that the time interval between footfalls varied for subjects. As a consequence, it is very hard to detect step accurately without calibration process using this method.
Second method is to detect accelerometer measurements peak values. The peaks of acceleration values correspond to the step occurrences. Because the peaks of acceleration is generated by vertical impact when the foot hits the ground. Peaks of acceleration for step detection is used in this study.

3.2 Heading Estimation

Broadly, heading of pedestrian can be done with three methods; gyroscope signal, digital compass and both sensors. IMU gives tri-axis angular velocity and heading is obtained by integration of this signal. While integration, not only true values but also noise and errors like drift are processed. As a result, errors are accumulated over time. So, gyroscope measurement cannot used alone generally. On the other hand; digital compass uses earth's magnetic fields and this magnetic field is relatively weak and electrical fields can distort the output of this kind of sensors. The characteristics of two sensors are summarized in Table 3, where advantage of one sensor is disadvantage of the other (Kim et al., 2004).

Table 1. Comparision magnetic compass and gyroscope based system

	Advantage	**Disadvantage**
Magnetic compass	Absolute azimuth Long term stable accuracy	Unpredictable external disturbances
Gyroscope	No external disturbances Short term accuracy	Relative azimuth drift

To overcome two kind of disadvantages; both sensors are used generally. Gyroscope is used for correcting the magnetic disturbance, at the same time magnetic compass is used for determining and compensating the errors occurred by inertial sensor.

3.3 Step Length Estimation

Total displacement is calculated by estimating step length in every valid detected step. Generally, estimation of step length can be separated into two methods: static method and dynamic method. In static method, every step length are assumed to same, which can be determined through equation (1).

$$step\_size = height \times k \quad (1)$$

with k equal to 0.415 for men and 0.413 for women.

Contrary to static method, every step length are not equal. Especially, walking status of pedestrian is the most effective factor for step length. In this study, walking status of pedestrian is recognized by a fuzzy logic algorithm. After recognizing walking status of pedestrian, step length can be estimated more accurately.
The main idea of PDR is walking distance and heading of the walking period to current position of pedestrian from a known previous position which can be seen Figure 4. (Judd & Levi, 1996)

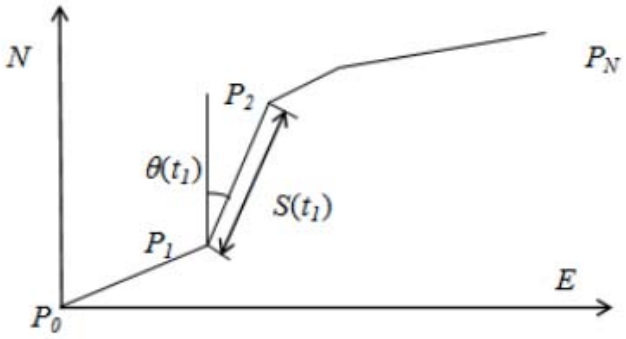

Fig. 4. Calculation of step length for each stride.

Total displacement can be calculated 1 and 2.

$$E(t_n)=E(t_0) + \sum_0^{n-1} S(ti)xsin(\Theta(ti)) \quad (2)$$

$$N(t_n)=N(t_0) + \sum_0^{n-1} S(ti)xcos(\Theta(ti)) \quad (3)$$

Where E(t1),N(t1) is previous position, E(tn),N(tn)) is current position and Θ is heading during the walking period.
For the length of each step can be calculated as follow;

$$S(t)=C_{walking\ status}\ x\ NS \quad (4)$$

Where C is coefficient of walking status and NS is number of steps taken in the same direction

3.4. Fuzzy Logic Walking Status Algorithm

The Fuzzy logic concept is first introduced by L. A. Zadeh in 1965 [13]. Since it was introduced, it has been used for solving many kind of complex problem related to human experience. Basically, Fuzzy logic seems closer to the way our brains work and it solves problems by considering all available information and making the best possible decision given the input, in the same way that humans do.
Step length estimation for each stride is crucial and the most effective parts of the PDR system considerably. Since the total displacement is estimated by sum of all steps, total error grows exponentially. In this study, for minimizing the errors for each step a fuzzy logic walking status (FLWS) algorithm is proposed shown figure 5.

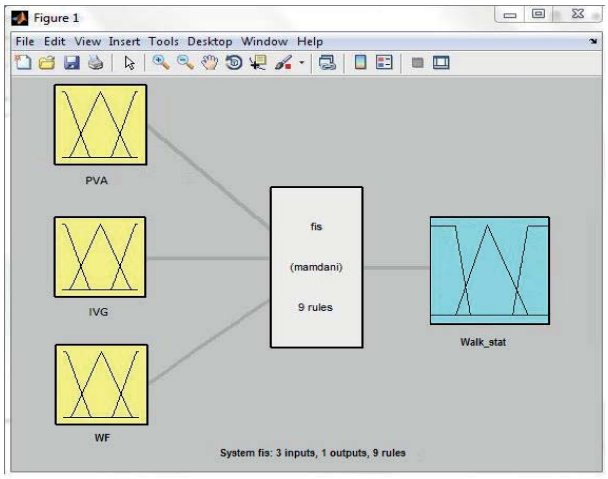

Fig. 5. Proposed fuzzy logic algorithm

There are three main factors affecting step length is that; stride related on walking frequency (WF), peak value of accelerometer (PVA) and integration value of gyroscope (IVG). These measurements are input for the proposed fuzzy logic algorithm. The output of the algorithm is walking status of pedestrian.
Status of walking which are "stop, normal walking and running" is determined by FLWS algorithm. The output of FLWS algorithm is shown figure 6.

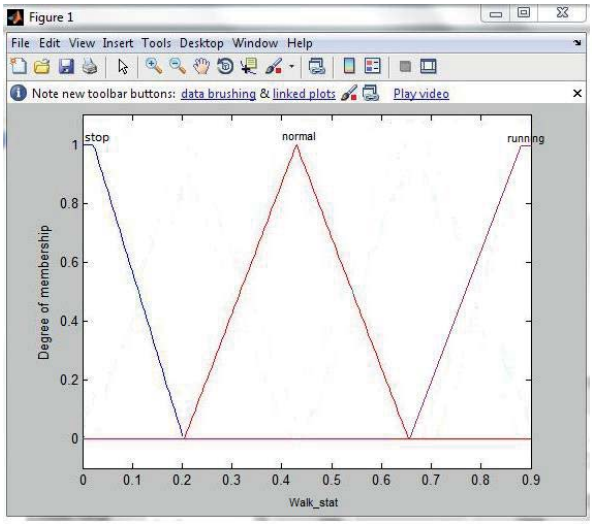

Fig. 6. Output of fuzzy algorithm.

4. EXPERIMENTAL RESULTS

In order to verify proposed PDR algorithm, various experiments were conducted. Thick black shown figure 7 is the route of a pedestrian. The pedestrian was started at the green point and followed the route and finished at the red point. Before perform PDR algorithm, 45 experiments were done to determine walking status and the result can be seen table 2.

Table 2. Result of FLWS algorithm

	Number of experiment	True	False	percentage
Stop	5	5	0	100 %
Normal walking	20	19	1	95 %
Running	20	19	1	95 %

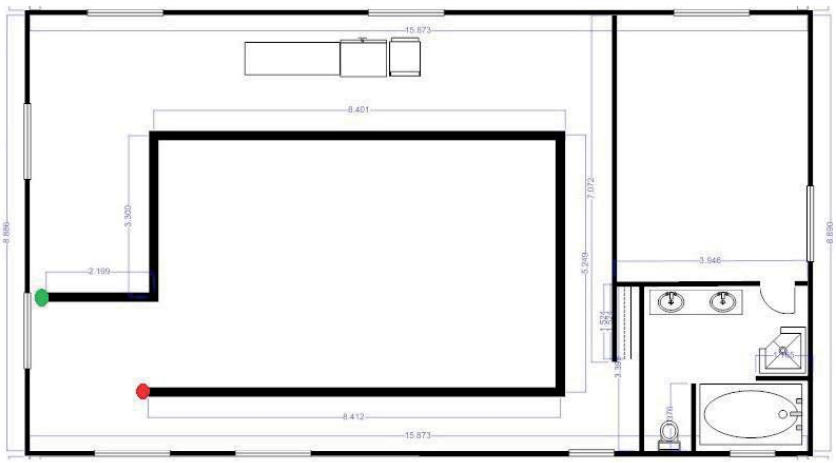

Fig. 7. Route of Pedestrian

The first experiment was performed at normal walking speed. Figure 8 shows the total displacement of pedestrian. Total displacement error is 3 % and second experiment was performed at running which result can be seen figure 9 and total displacement error is 7%.

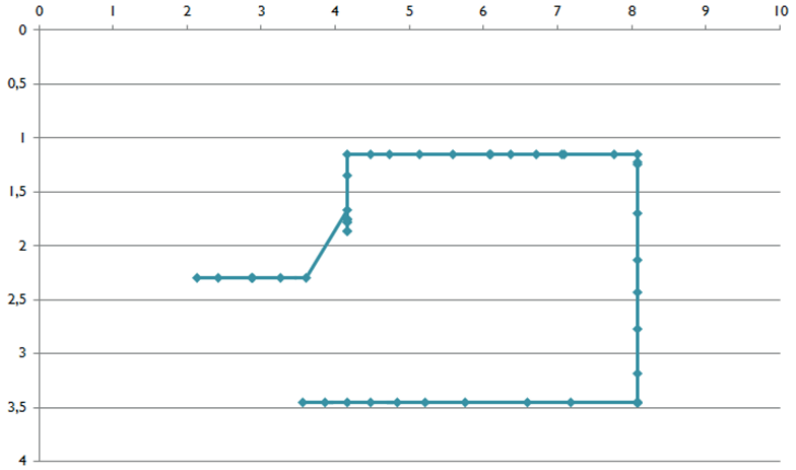

Fig. 8. Total displacement while normal walking

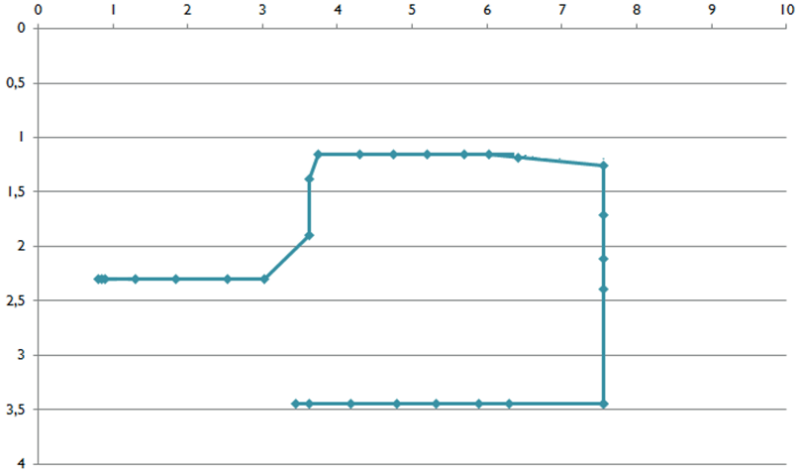

Fig. 9. Total displacement while running

5. CONCLUSION

In this paper, we proposed the PDR system for indoor position tracking which is based on fuzzy logic walking status to enhance the accuracy of step length estimation. Proposed system have three main part which are step detection, heading and step length to accomplish sufficient position estimation. Step detection of system has done peak detection of accelerometer values. Heading is estimated by both magnetometer and IMU sensors. Walking status is estimated by FLWS algorithm and positon of pedestrian is estimated. Experimental results show that proposed system provide a good estimation performance.

This study was supported by Kırıkkale University Scientific Research Projects Coordination Unit as BAP project (Project No:2016/127).

REFERANSLAR

A.R. Jimenez et al., “A Comparison of Pedestrian Dead-Reckoning Algorithms suing a Low-Cost MEMS IMU”, IEEE International Symposium on Intelligent Signal Processing, 26-28 August, 2009 Budapest, Hungary

C.-H. Huang, L.-H. Lee, C. C. Ho, L.-L. Wu, and Z.-H. Lai, “Realtime RFID indoor positioning system based on kalman-filter drift removal and heron-bilateration location estimation,” Instrumentation and Measurement, IEEE Transactions on, vol. 64, no. 3, pp. 728–739, 2015.

E. Foxlin. Pedestrian tracking with shoe-mounted inertial sensors. IEEE Comput. Graph. Appl., 25(6):38–46, 2005.

G. Retscher, E. Moser, D. Vredeveld, D. Herberling, "Performance and accuracy test of the WLAN indoor positioning system 'ipo'", Proc. 3rd Workshop on Positioning, Navigation and Communcation, pp. 7-15, 2006

Judd T, Levi R W. Dead reckoning navigational system using accelerometer to measure foot impacts: U.S. Patent 5,583,776[P]. 1996-12-10.

Kim, Jeong Won, et al. "A step, stride and heading determination for the pedestrian navigation system." Positioning 1.08 (2004):0.

K. JongBae and J. HeeSung, "Vision-based location positioning using augmented reality for indoor navigation," IEEE Trans. Consum. Electron., vol. 54, no. 3, pp. 954–962, Aug. 2008

Lauro Ojeda and Johann Borenstein. Non-gps navigation with the personal dead-reckoning system. In SPIE Defense and Security Conference, Unmanned Systems Technology IX, April 9-13 2007.

N. Samama. Global Positioning: Technologies and Performance, volume 1. Wiley-Blackwell, 2008.

Riebeck M. Stark, A. and J. Kawalek. How to design an advanced pedestrian navigation system: Field trial results. In 4th IEEE Workshop on Intelligent Data Acquisition and Advanced Computing Systems: Technology and Applications, IDAACS, April, 15 2007.

S.J. Ingran, D. Harmer, M. Quinlan,"UltraWideBand indoor positioning systems and their use in emergencies", Proc. Position, Location and Navigation Symposium, pp. 706-715,2004.

Widyawan, M. Klepal, and S. Beauregard. A backtracking particle filter for fusing building plans with pdr displacement estimates. In Proc. 5th Workshop on Positioning, Navigation and Communication WPNC 2008, pages 207–212, 27–27 March 2008.

Zadeh, Lotfi A. "Fuzzy sets." Information and control 8.3 (1965): 338-353.

MÜHENDİSLİK FAKÜLTESİ

Uluslararası Mühendislik Araştırma ve Geliştirme Dergisi

International Journal of Engineering Research and Development

Cilt/Volume:9 Sayı/Issue:3 Aralık/December 2017 https://doi.org/10.29137/umagd.371119

Araştırma Makalesi / Research Article

Influence of Nano-$CaCO_3$ Particles on Shear Strength of Epoxy Resin Adhesives

Halil Burak KAYBAL[1], Hasan ULUS*[2], Ahmet AVCI[1]

[1]Selcuk University, Faculty of Engineering, Department of Mechanical Engineering, TURKEY.
[2]Selcuk University, Huglu Vocational High School, TURKEY.

Başvuru/Received: 06/02/2017 **Kabul/Accepted**: 11/04/2017 **Son Versiyon/Final Version**: 15/06/2017

Abstract

Epoxy resins are a very common type of adhesive materials in several fields like the automotive industry, marine, probably the most important is in the aerospace industry. Adhesive joints of carbon fiber reinforced epoxy composite laminates are worked using an epoxy resin as the adhesive. In this paper, Adhesive joints were modified nano-CaCO3 in order to enhance the shear strength of epoxy adhesives. The enhancements of shear strength of epoxy adhesive joints reinforced with different nano-CaCO3 particles loading have been studied. The adhesive properties were measured by tensile lap shear test as a function of nano-CaCO3 amount and damaged adhesive surface roughness. Also, the fracture surfaces were examined with Scanning Electron Microscopy (SEM).

Key Words

"Adhesive; epoxy; carbon fiber; shear strength; nano-CaCO3"

*** hasanulus@selcuk.edu.tr***

1. INTRODUCTION

Epoxy adhesives are commonly used in applications in aerospace, automotive, marine and construction industries due to their adhesive strength, durability and toughness, chemical resistance, ease of application (Lu, 2000; Jeong, 2005; Jiang, 2005; Tan, 2006; Tee, 2007; Zhrang, 2016). Recently, the mechanical properties enhancement of the epoxy adhesives has been performed by the use of nanoparticle reinforcement such as nano-rubber particles, carbon nanotubes, graphene and silver nanowires, nano-clay, alumina and silica nanoparticles (Khoee, 2010; Sydlik, 2013; Fu, 2014; Wu, 2006; Xian, 2006; Kim, 2013; Ulus, 2016). Enhancement of tensile properties of epoxy adhesives is important due to the adhesively bonded joints in a structure generally subjected to a combination of tensile and shears loads (Murakami, 2015). While there are many research on the nanoparticle filled epoxy adhesives, there are few research about nano CaCO3 epoxy adhesives. Furthermore, since no publications were found in literature related to the carbon fiber (CF) reinforced epoxy laminated composites adhesive joining, this study was performed.

The present work aimed to improve adhesive joining of Epoxy/CF laminated for use in the above mentioned fields. For this purpose, firstly Ep/CF laminated composites were produced via (Vacuum Assisted Resin Infusion Method) VARIM and for prepare the shear lap test specimens. Also, modification of epoxy resin investigates with tensile tests as dog bone specimens.

2. EXPERIMENTS

The epoxy resin as the commercially available diglycidylether of bisphenol-A (DGEBA) supplied by Momentive Hexion Inc. Nano-CaCO3 was purchased from Mk Nano Co. The average particle size of nano-CaCO3 was 40 nm (as can be seen in Fig. 1). Carbon fiber fabric and the all other vacuum infusion equipments were provided by Dost Kimya Inc., Turkey. The area density of carbon fiber was 300 g/m2 and each bundle consisted of 12000 filament.

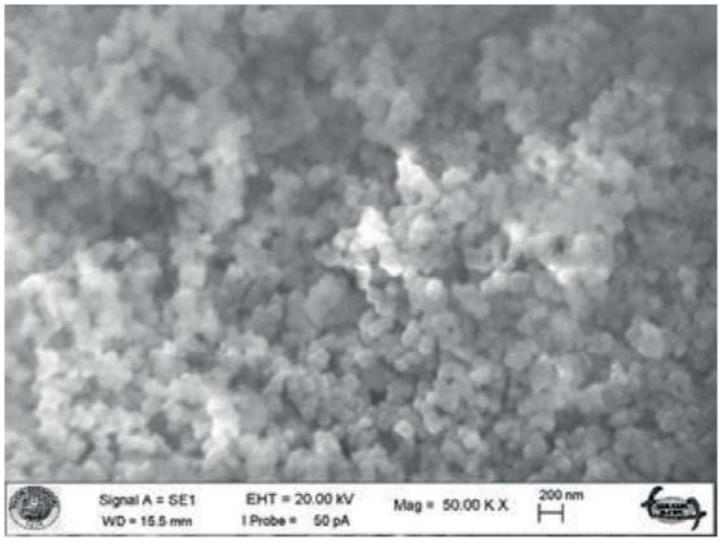

Fig. 1. SEM images of nano-CaCO3

2.1. Preparation of nano-$CaCO_3$-Epoxy composites

The nano-CaCO3 weight content was range from 1 to 5 wt%. The epoxy and nano-CaCO3 were stirred for 30 min with an ultra sonicator. Curing agent was added after dispersing process in epoxy and degassed at 25 °C/0.6 bar for 20 min. The steel mold covered with release agent and mixture was poured into preheated mold. Curing was performed at 80 °C for 1 h, at 120 °C for 2 h and then it was slowly cooled to room temperature in the oven. All samples were removed from mold and conventionally polished with SiC sandpapers with grit numbers of 800 to minimize effect stress concentration caused by sharp edges.

2.2. Preparation of nano-$CaCO_3$-Epoxy/CF composites

Carbon fiber reinforced epoxy laminated nanocomposites were prepared by means of VARIM (Ulus and Avci, 2015). Then, the cured panel was taken out and specimens were cut according to Standard Test Method for Lap Shear Adhesion for Fiber Reinforced Plastic Bonding (ASTM D5868-01) standards. All samples polished with SiC sandpapers identically.

2.3. Preparation of nano-$CaCO_3$-Epoxy/Adhesives

Firstly prepared specimens according to the recommended dimension (100 mm × 25.4 mm x 0.76 mm) were abraded with silicon carbide paper to roughen the adhesive surfaces then degreased with acetone to remove any dust and dry at 35 °C for 10 min. The

nano-adhesives were prepared by addition of epoxy resin to achieve 1, 2, 3, 4 and 5 wt% nano-CaCO3 content, which were then mixed via ultra sonicator for 30 min and degassed in a vacuum oven 25 °C/0.6 bar for 20 min. Then the hardening agent was added into the mixture according to supplier instructions. The adhesive area was signed as 25.4 mm × 25.4 mm. The schematic view of the samples was given in Fig. 2. The nano-adhesive mixture was applied on the adhesive area on both piece and pressed down via clamp. The adhesive was cured at 80 °C for 1 h, at 120 °C for 2 h.

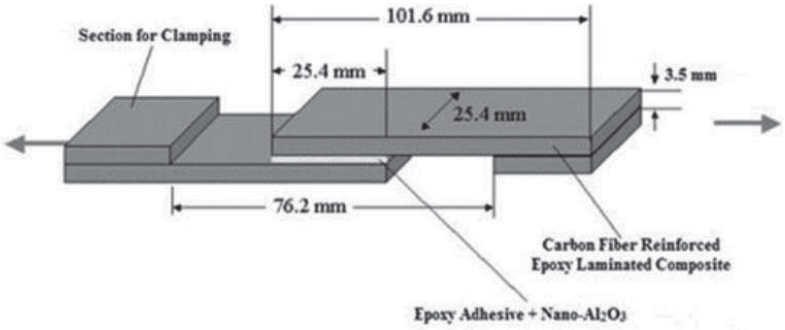

Fig. 2. ASTM-D5868-01 Standard of the shear test

3. RESULTS AND DISCUSSIONS

3.1. Tensile Tests of Epoxy Adhesives

Tensile tests were performed to understand the effect of modification of epoxy adhesive. These tests were performed according to ASTM D3039 / D3039M. Tensile stress-strain curves of modified epoxy with as a function of different weight percentages of nano-CaCO3 in the adhesive showed in Fig. 3. It is clearly seen in Fig.3, elongation of epoxy and tensile strength behavior show noticeable change. The 2 wt% nano CaCO3-Epoxy adhesive shows most efficient nanoparticle loading when it compared with the 0 wt% nano CaCO3-Epoxy adhesive.

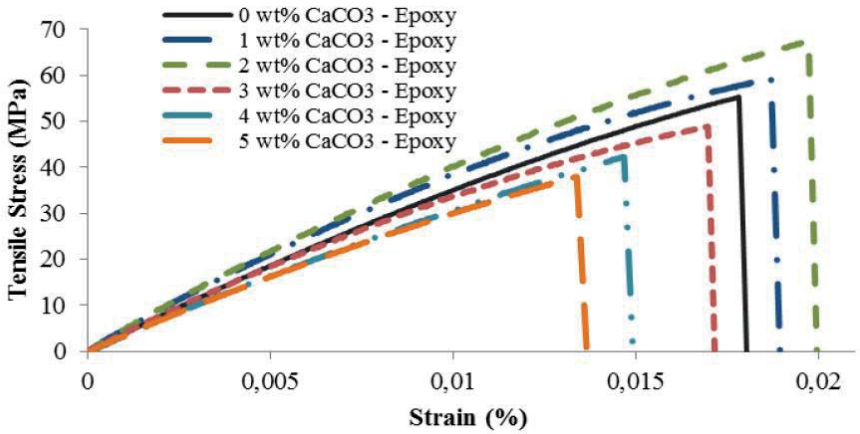

Fig. 3. Load displacement curves of Calcium Carbonate -Epoxy adhesives with different nano-CaCO3 contents (Ulus, 2016)

Table 1 summarizes the tensile properties values of modified and unmodified epoxy adhesives. The tensile strain and strengths were determined from the maximum stress or strain point.

Table 1. The strength and strain value at the peak loads (Ulus, 2016)

Material	Strength (MPa)	Strain (mm/mm)	Increase (MPa %)
0 wt% CaCO3 - Epoxy	53,47	55.3 ± 1.8	-
1 wt% CaCO3 - Epoxy	64,23	59.2 ± 2.6	20
2 wt% CaCO3 - Epoxy	71,65	67.6 ± 2.3	34
3 wt% CaCO3 - Epoxy	60,40	48.7 ± 2.5	13
4 wt% CaCO3 - Epoxy	43,22	42.3 ± 3.2	-19
5 wt% CaCO3 - Epoxy	35,70	37.8 ± 4.1	-33

3.2. Tensile lap shear tests of Epoxy Adhesives

Tensile lap shear tests were carried out according to ASTM-D5868-01 standard. It can be seen in Fig.4. that shear load and shear displacement of the 2 wt% nano CaCO3-Epoxy/CF adhesive was determined optimum concentration.

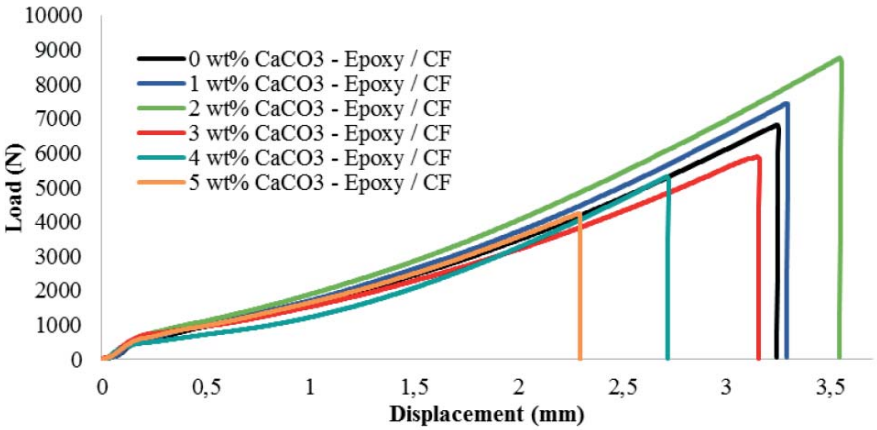

Fig.4. Load-displacement curves of Calcium Carbonate-Epoxy/CF adhesives with different nano- CaCO3 contents

Table 2 shows the results of the tensile lap shear tests. The shear displacement and shear load were determined from the maximum load or displacement point.

Table 2. The load and displacement value at the peak loads.

Material	Load (N)	Displacement (mm)	Increase (N %)
0 wt% CaCO3 - Epoxy	6819	3,25	-
1 wt% CaCO3 - Epoxy	7439	3,30	9
2 wt% CaCO3 - Epoxy	8760	3,6	28
3 wt% CaCO3 - Epoxy	5890	3,16	-13
4 wt% CaCO3 - Epoxy	5318	2,72	-22
5 wt% CaCO3 - Epoxy	4249	2,30	-37

3.3. Optical Microscope Examination

Adhesive bonding surfaces of different samples are shown in the Fig.5. It is clearly observed that optic micrograph of neat adhesive surface exhibits. The adhesive surface for the 0 wt% nano CaCO3-Epoxy is described in Fig. 5(a) which reveals a brittle behavior characterized by distinctive epoxy cracking. Nevertheless, 2 wt% CaCO3-Epoxy adhesive surface displays deformation evidence based on more roughly adhesive surface in Fig. 5(b). Besides, fiber bundle breakage sighted seriously on the bonding surface. It can be clearly understand that having added in Epoxy/CF composite, 2 wt% CaCO3 nanoparticles are boosted toughening mechanism on adhesive surface.

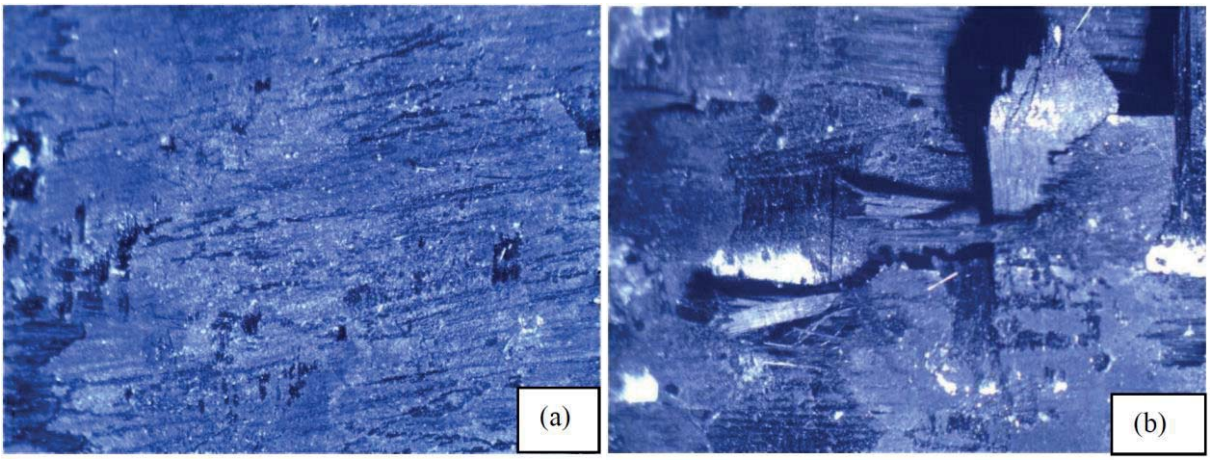

Fig.5. Optic micrographs of adhesive surface a) Epoxy/CF b) 2 wt% CaCO3 - Epoxy/CF

3.4. Analysis of SEM Images

The toughening influences of nano-CaCO3 were survey to understand in fracture surfaces of nanocomposite specimens. The SEM micrographs of 2 wt% nano-CaCO3 in the epoxy matrix are shown in Fig.6. The fracture morphology of the 2 wt% CaCO3-Epoxy specimen shows very homogenous nanoparticle dispersion.

There are a number of toughening mechanisms in literature which can be associated to the amount of energy absorbed and fracture toughness increases as the main toughening mechanisms are crack deflection, crack pinning, debonding and pull-out (Opelt, 2016; Wetzel, 2006; Zhou and Ruan, 2007; Wagner, 2013; Johnsen, 2007). The fracture surfaces of the composites after the shear test were analyzed by SEM and the results are shown in Fig.7. Micrographs show a clear difference fiber pull-out in 0 wt% CaCO3-Epoxy/CF farther than 2 wt% CaCO3-Epoxy/CF in Fig.7 (a)-(b). This deduction indicates that interaction of fiber-matrix in neat

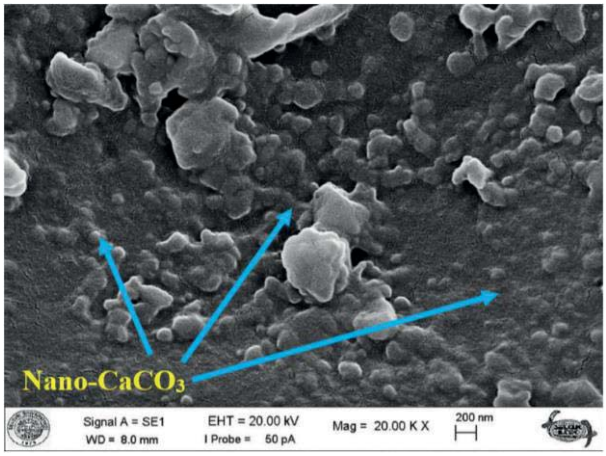

Fig.6. Dispersion of nano-CaCO3

Epoxy/CF is weak. Besides, plastic deformation in the nano modified 2 wt% CaCO3-Epoxy/CF more than 0 wt% CaCO3-Epoxy/CF in the fiber gap surfaces. Therefore, the toughness of 2 wt% CaCO3-Epoxy/CF higher than 0 wt% CaCO3-Epoxy/CF.

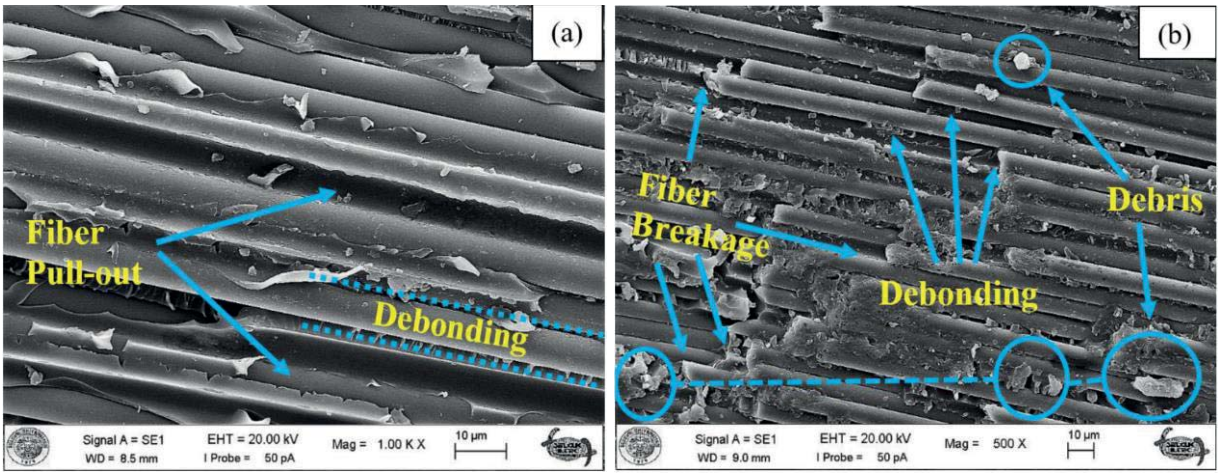

Fig.7. Micrographs of fracture surface: (a) 0 wt% CaCO3-Epoxy/CF (b) 2 wt% CaCO3/Epoxy/CF

4. CONCLUSION

In this paper, nano-CaCO3-Epoxy mixture were prepared with different nanoparticle loading and the effects of nano particle adding on epoxy adhesive were investigated. Experimental results show that the 2 wt% nano CaCO3 modification significantly improved epoxy adhesive strength by 28%. The optic microscopy investigate revealed that the adhesive surfaces had different morphologies. This differences and nanoparticle effect which are observed via SEM are associated with adhesives strength increasement. The results of the conducted experiments show that the nano CaCO3 modification in epoxy resin enhance adhesive properties of nanocomposites. The adhesions of the fiber – matrix and interlaminar in the 0 wt% CaCO3 - Epoxy matrix are determined as weaker than that of the modified 2 wt% CaCO3/Epoxy matrix. Fracture surface micrographs revealed that the relationship between strength increasement and toughening behaviours.

REFERENCES

Fu YX, He ZX, Mo DC and Lu SS, (2014). "Thermal conductivity enhancement of epoxy adhesive using graphene sheets as additives", International Journal of Thermal Sciences, 86, 276-283.

Kaybal, H.B., Ulus H., Avci A., (2016). "Tensile Properties Improvement of Nano CaCO3 Reinforced Epoxy Nanocomposites" 16 th. International Materials Symposium (IMPS'16), 12-14 October 2019, Denizli, Turkey.

Jeong WJ, Nishikawa H, Itou D and Takemoto T, (2005). "Electrical characteristics of a new class of conductive adhesive". Materials transactions, 46(10), 2276-2281

Jiang H, Moon KS, Lu J and Wong CP, (2005) "Conductivity enhancement of nano silver-filled conductive adhesives by particle surface functionalization", Journal of electronic materials, 34(11), 1432-1439.

Johnsen BB, Kinloch AJ, Mohammed RD, Taylor AC, Sprenger S, (2007). "Toughening mechanisms of nanoparticle-modified epoxy polymers", Polymer, 48; 530-541.

Khoee S and Hassani N, Adhesion, (2010). Strength improvement of epoxy resin reinforced with nanoelastomeric copolymer, Materials Science and Engineering: A, 527(24), 6562-6567.

Kim DH and Kim HS, (2013). "Waterproof characteristics of nanoclay/epoxy nanocomposite in adhesively bonded joints". Composites Part B: Engineering, 55, 86-95.

Lu D and Wong CP, (2000),"Development of conductive adhesives for solder replacement", Components and Packaging Technologies, IEEE Transactions on, 23(4), 620-626.

Murakami S, Sekiguchi Y, Sato C, Yokoi E and Furusawa T, (2015). "Strength of cylindrical butt joints bonded with epoxy adhesives under combined static or high-rate loading", International Journal of Adhesion and Adhesives.

Opelt CV and Coelho LA, (2016). "Reinforcement and toughening mechanisms in polymer nanocomposites–Reinforcement effectiveness and nanoclay nanocomposites". Materials Chemistry and Physics, 169, 179-185.

Sydlik SA, Lee JH, Walish JJ, Thomas EL and Swager TM, (2013). "Epoxy functionalized multi-walled carbon nanotubes for improved adhesives". Carbon, 59, 109-120.

Tan F, Qiao X, Chen J and Wang H, (2006). "Effects of coupling agents on the properties of epoxy-based electrically conductive adhesives", International journal of adhesion and adhesives, 26(6), 406-413.

Tee DI, Mariatti M, Azizan A, See CH and Chong KF, (2007). "Effect of silane-based coupling agent on the properties of silver nanoparticles filled epoxy composites". Composites Science and Technology, 67(11), 2584-2591.

Tüzün FN and Tunalıoğlu MŞ, (2015). "The effect of finely-divided fillers on the adhesion strengths of epoxy-based adhesives", Composite Structures, 121, 296-303.

Ulus H, Üstün T, Şahin, ÖS, Karabulut SE., Eskizeybek V, and Avcı A, (2015). "Low-velocity impact behavior of carbon fiber/epoxy multiscale hybrid nanocomposites reinforced with multiwalled carbon nanotubes and boron nitride nanoplates". Journal of Composite Materials, DOI: 0021998315580835.

Wagner HD, Ajayan PM and Schulte K, (2013). "Nanocomposite toughness from a pullout mechanism". Composite Science Technology, 83: 27-31.

Wetzel B, Rosso P, Haupert F and Friedrich K, (2006). "Epoxy nanocomposite fracture and toughening mechanisms", Engineering Fracture Mechanics, 73: 2375-2398.

Wu HP, Liu JF, Wu XJ, Ge MY, Wang Y W, Zhang G.Q. and Jiang JZ, (2006). "High conductivity of isotropic conductive adhesives filled with silver nanowires", International journal of adhesion and adhesives, 26(8), 617-621.

Xian G, Walter R, and Haupert F, (2006). "Friction and wear of epoxy/TiO 2 nanocomposites: Influence of additional short carbon fibers Aramid and PTFE particles", Composites Science and Technology, 66(16), 3199-3209.

Zhang R, Moon KS, Lin W and Wong CP, (2010). "Preparation of highly conductive polymer nanocomposites by low temperature sintering of silver nanoparticles". Journal of Materials Chemistry, 20(10), 2018-2023.

Zhou TH, WH Ruan, Rong MZ, Zhang MQ and Mai YL, (2007). Keys to toughening of non-layered Nanoparticles/Polymer composites, Adv. Mater (19); 2667-2671.

MÜHENDİSLİK FAKÜLTESİ

Uluslararası Mühendislik Araştırma ve Geliştirme Dergisi

International Journal of Engineering Research and Development

Cilt/Volume:9 Sayı/Issue:3 Aralık/December 2017 https://doi.org/10.29137/umagd.372934

Araştırma Makalesi / Research Article

Plazma Püskürtme Yöntemiyle Çelik Levha Üzerine Farklı Alaşımların Kaplanması

Coating of Different Alloys on Carbon Steel by Plasma Spray Method

Ömer Alparslan KAYA[1], Kevser ÇAKIR[1], Yahya BOZKURT[1]

[1]Marmara Üniversitesi,Teknoloji Fakültesi, Metalurji ve Malzeme Mühendisliği Bölümü, İstanbul, TÜRKIYE

Başvuru/Received: 06/05/2017 **Kabul/Accepted**: 06/09/2017 **Son Versiyon/Final Version**: 26/12/2017

Öz

Günümüzde metal ve alaşımların yüksek sıcaklık, korozyon, aşınma gibi ağırlaşan çalışma şartlarında istenilen özelliklerini sağlayamadığı durumlarda plastikler, kompozitler, süper alaşımlar ve ileri teknoloji seramikleri gibi malzemeler devreye girmektedir. Bu nedenle ileri teknoloji seramikleri metal malzeme yüzeyine farklı kaplama teknikleri ile (CVD, PVD ve Isıl püskürtme tekniklerinden olan plazma püskürtme ile) uygulanmaktadır. Bu yöntemlerle kaplanan metal ile alaşımlar demir-çelik, uzay ve havacılık, savunma sanayi, otomotiv, makine ve imalat gibi birçok sektörde kullanılmaktadır. Bu çalışmada, plazma püskürtme yöntemi ile altlık malzemesi olarak karbon çeliği üzerine kaplama işlemi yapılmıştır. Plazma püskürtme yöntemiyle iki farklı kaplama malzemesi olan Cr2O3 ve Al2O3- TiO2(87-13) çelik malzemeler üzerine ayrı ayrı uygulanmıştır. Numuneler, mikroyapısal ve mekanik olarak incelenerek, her iki kaplama malzemesi kıyaslanmıştır.

Anahtar Kelimeler

"Plazma püskürtme tekniği, kaplama, karbon çeliği altlık malzeme, Krom oksit seramik kaplama, Alüminyum ve Titanyum oksit seramik kaplama."

Abstract

Recently, metal and composition can not manage difficult conditions like the high temparature, corrosion, abrasion. Plastics, super composition, composites and massive technological ceramic were preferred in stead of metal and composition. Because of that advanced technological ceramics applicated onto the metal surface with different techniques (CVD, PVD, plasma spray method which one of termal spray methods, etc.) When the metals and compositions were coating with those methods they can available for iron-steel industry, defense industry, space and aeronautics, automoive, machine and manufacturing. In this study, Cr2O3 and Al2O3-TiO2 (87-13)ceramic coatings have been applied onto carbon steel substrates by plasma spray technique. Coated samples have been analyzed and investigated with microstructurel and mechanical tests respectively. Finally both coated samples have been compared.

Key Words

"Plasma spraying technique, coating, carbon steel substrate, Chromium oxide ceramic coating, Aluminium oxide and Titanium oxide ceramic coating"

** ybozkurt @marmara.edu.tr*

1. GİRİŞ

Dünya üzerindeki her malzeme zamanla korozyon sebebiyle veya kullanım ortamına bağlı olarak aşınmaya uğrar. Bu aşınmayı engellemek için ya bulunması ve işlenmesi zor olan özel üretilmiş pahalı malzemeler kullanılmış, ya da aşınma sonucunda malzeme değişimine gidilmiştir. Buda büyük oranda üretimin durması, sonuçta da maliyetlerin artması anlamına gelmektedir. Bunu engellemek adına malzemeleri kaplama fikri ortaya çıkmıştır (M. R. Dorfman, 2012).

Yüzey kaplama tekniklerinin geniş bir sınıflandırması vardır. Bu sınıflandırma içerisinde yüzey kaplama tekniklerinden olan termal püskürtme kaplamaların kullanımı teknolojideki gelişmelerle paralel gelişmelerle artmaktadır (Rickbery vd, 1991).

Termal sprey kaplama, toz veya tel halindeki kaplama malzemesinin elektrik arkı, alev veya plazma ile ergitilerek, bir püskürtme gazı yardımıyla ergimiş partikülleri altlık malzemeye yapışmasını sağlayan yöntemlerin genel adıdır. Termal sprey kaplamalar korozyonu, abrazyon, erozyon, kazıma gibi aşınma olaylarını engellemek, oksidasyonu ve sıcak korozyonu önlemek, ısı yalıtımı, elektrik iletimi veya yalıtımı amacıyla kullanılabilir. Ayrıca yenileme ve onarma, son hale yakın üretim, yenilenebilir kaplama ve dekoratif amaçlarla da kullanılabilir (M. R. Dorfman, 2012).

Termal spreyin en büyük avantajı istediğin tip metal formundaki malzemeye kaplama yapılmasının mümkün olmasıdır. Bu sayede maliyeti düşük olan malzemenize kaplama yapılarak sertliği ve aşınma dayanımı sağlanabilmektedir.

Tablo1: Yüzey Kaplama Tekniklerinin Karşılaştırılması (Rickbery vd, 1991.s4-13)

	GAZ (BUHAR) FAZI			**SIVI FAZ**		**ERGİMİŞ-YARI SIVI FAZI**		
	PVD	**CVD**	**İyon Aşılama**	**Sol-Jel**	**Elektroliz le Kaplama**	**Lazer**	**Isıl Püskürtm e**	**Kaynak**
Kaplama Kalınlığı (mm)	0,3'e kadar	0,5'e kadar	0,005'e kadar	0,002'ye kadar	0,02-0,5 arası	0,05-2 arası	0,05-2 arası	1-20 arası veya daha fazla
Çökelti Hızı (kg/s)	0,5'e kadar	1'e kadar	Yok	0,1-0,5	0,1-0,5	0,1-1	0,1-10	3 ile 50 arasında
Kaplanacak Parça Boyutu	Kaplamanın yapılacağı hücre boyutuyla sınırlandırılmıştır.			Çözelti banyoyla sınırlandırılmıştır.		Bu işlemlerden bazıları uygulandığı hücre boyutu ile sınırlandırılmasına rağmen çoğunluğunda sınırlandırılma yoktur.		
Kaplanacak Ana Malzeme Cinsi	Oldukça geniş seçim yapabilir.	Çökelme sıcaklığı tarafından sınırlandırılmı ştır.	Oldukça geniş seçim yapabilir	Oldukça geniş seçim yapabilir.	Oldukça geniş seçim yapabilir.	Oldukça geniş seçim yapabilir	Oldukça geniş seçim yapabilir	Çoğunlukl a çeliklere
Ön İşlem	Kimyasal işlemler +İyon bombardıma nı	Çeşitli işlemler	Kimyasal işlemler + İyon bombardımanı	Kum püskürtme veya kimyasal temizleme	Kimyasal temizleme ve dağlama	Mekanik ve kimyasal temizleme		
Son İşlem	Yapılmaz.	Ana malzeme gerilmelerin giderilmesi	Yapılmaz.	Yüksek sıcaklıkta kalsinasyon	Yapılmaz veya sadece ana malzemenin gerilmelerinin giderilmesi işlemi yapılır.			
Çökelti Kalınlığının Kontrolü	İyi	Vasat/İyi	İyi	Vasat/İyi	Vasat/İyi	Elle yapılanlar değişik sonuçlar verebilir otomatik yapılanlar iyi		
Bağlanma Mekanizması	Atomik	Atomik	Yok	Yüzey kuvvetler		Mekanik/Kimyasal		Metalurjik
Ana Malzeme Distorsiyonu	Düşük	Yüksek	Düşük	Düşük		Düşük/Orta		Yüksek olabilir.

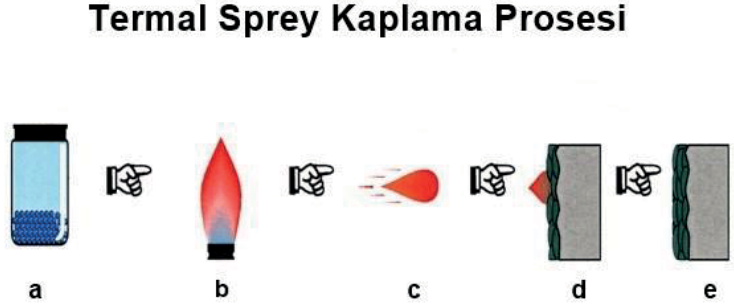

Şekil 1: Termal Sprey Tekniğinin Şematik Görünüşü a)Tel veya Toz Kaplama Malzemesi b) Elektrik veya Gaz Isı Kaynağı c) Hızlandırılan Ergimiş Tanecik d)Esas Metal Yüzeyine Çarpan ve Düzleşen Tanecikler e) Tamamlanmış Kaplama (AWS, International Thermal Spray Association, 2017)

Tablo 2: St-37 Yapı Çeliği Kimyasal Bileşimi(%ağırlık)

Alaşım Elementi	C	Si	Mn	P	S	Mg	Cr	Ni	Mo	Cu	Al	V	W	Fe
St-37	0.217	0.001	0.426	0.026	0.022	0.0001	0.064	0.001	0.001	0.001	0.017	0.001	0.003	99.219

Tablo 2'de kimyasal analizi verilen altlığın üzerine ara bağlayıcısı olmadan Plazma Alev Püskürtme ile Al2O3+TiO2(87-13) ve Cr2O3 kaplama yapılmıştır. Kullanılan tozların özellikleri aşağıdaki gibidir:

İstatistiklere göre makine elemanlarının ortalama %70'inin hurdaya ayrılma sebebi aşınmadır. Bunun sonucu olarak meydana gelen malzeme kayıpları, aşınan parçaların yenileriyle değiştirilmesi zorunluluğu, makinelerin bakım-onarım faaliyetleri için harcanan zaman ve emek ve bu faaliyetler için istihdam edilen teknik personel göz önüne alındığında her yıl milli sermayeye oldukça büyük yükler getirmektedir. Bu çalışmada St-37 genel yapı çeliği üzerine plazma sprey yöntemiyle farklı alaşımlar kaplanmıştır. Plazma Alev Püskürtme ile Al2O3+TiO2 (87-13) ve Cr2O3 Altlık Malzemesi St-37 Çeliği: Mn, Si gibi alaşım elementlerinin bir veya ikisinin çeliğin içindeki değerleri, en az Mn % 1,65 Si %0,60 geçmiyor ve kimyasal bileşiminde başka herhangi bir alaşım elementinin belirli bir miktarda en az bulunması istenmiyorsa bu çelikler, karbonlu çelikler sınıfına girer. (Çağrı Barut, 2010)

2. DENEYSEL ÇALIŞMALAR

2.1. Deneyde Kullanılan Malzemeler

Genel çelik kullanımında en yaygın kullanıma sahip St-37 yapı çeliği seçilmiştir. Kimyasal bileşimi Tablo 2'deki gibidir.

Tablo3: Kullanılan Tozların Özellikleri (METCO Technical Bulletin, 1983)

Kullanılan Tozlar	Seramik Toz 1	Seramik Toz 2
Kimyasal Kompozisyon	%87Al_2O_3 %13TiO_2	%92 Cr_2O_3 %5SiO_2 %3TiO_2
Toz Boyut Dağılımı	-325+5 µm	-53+15µm
Ergime Sıcaklığı(ºC)	2010	2435
Yoğunluk (gr/cm^3)	3.4	4.8
Toz Morfolojisi	Köşeli	Düzensiz

2.2. Deneyde Kullanılan Kaplama Yöntemi

Bir gaz, genellikle argon, ancak zaman zaman azot, hidrojen veya helyum dahil, bir tungsten katot ve suyla soğutulmuş bir bakır anot arasında akmasına izin verilir. İki elektrod arasında yüksek frekanslı bir deşarj kullanılarak bir elektrik arkı başlatılır ve sonra da güç kullanarak sürdürülür. Ark, gazı iyonlaştırarak yüksek basınçlı bir gaz plazması oluşturur. Gaz sıcaklığındaki 30.000 ºC'yi aşan artış, gaz hacmini ve dolayısıyla nozülden çıktığında basıncını ve hızını arttırır. (Süpersonik olabilen gaz hızı, parçacık hızı ile karıştırılmamalıdır.) Plazma püskürtme meşalelerinde güç seviyeleri genellikle 30 ila 80 kW aralığında olmakla birlikte 120 kW gibi yüksek de olabilir. Argon genellikle ana gaz olarak seçilir, çünkü kimyasal olarak inerttir. Gazın entalpisi diatomik

gazların, hidrojen veya azotun eklenmesiyle arttırılabilir. (R.C. Tucker, 1994) Plazma püskürtme yönteminde, yüksek sıcaklıkt aki kimyasal kararlılık, mükemmel aşınma direnci ve korozyona karşı dayanıklılığından dolayı seramik (özellikle oksit esaslı) esaslı tozlar, metalik tozlara nazaran daha çok kullanılır (Wang, Y, 2000). Alüminyum oksit (Al2O3) kaplamalar başarılı seramik kaplama türevlerindendir. Üstün nitelikli metal işleme performanslı, katı seramik kesiciler arasında en çok bilinen ve kullanılan tür olarak açıklanabilirler. Semente karbür kaplamalara göre daha kırılgan yapıları nedeniyle düşük gerilimli kesme işlemlerinde kullanılırlar ancak buna karşın yüksek hızlardaki işlemlerde kimyasal yapılarını muhafaza ederler (A.Özkan vd,2008).

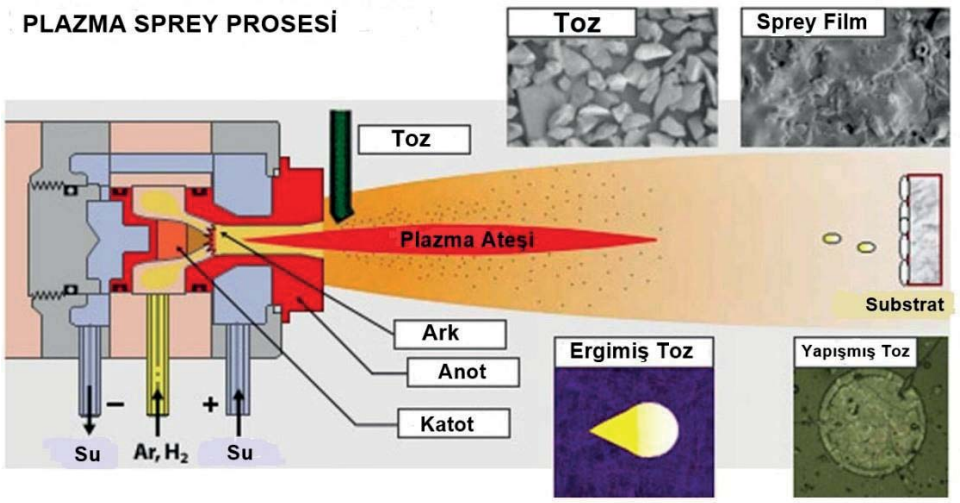

Şekil 2: Plazma Sprey Kaplama Yönteminin Şematize Edilmiş Hali (Sakarya Üniversitesi, Teslab, Plazma Sprey, 2017)

Kaplama kalitesi plazma sprey sistemindeki pek çok değişkene bağlıdır. Bunların arasında en önemlileri şöyle sıralanabilir:

- Kaplanacak yüzeydeki soğuma,
- Plazma tabancası ile kaplama yüzeyi arasındaki mesafe,
- Kaplama yüzey üzerindeki iç gerilmeler,
- Püskürtülen tozların ergime durumları ve yüzeye çarpan parçacıkların hızı,
- Karşılıklı ıslatma ve akışkanlık davranışları şeklindedir. (Nuri Aydınlı, 2008)

Plazma Sprey Kaplama Yönteminin Avantajları: Plazma püskürtmenin en büyük avantajı, metallerden, ısıya dirençli seramiklere kadar pek çok maddeyi aşağıdaki avantajlarla birlikte küçük veya büyük parçalar üzerine püskürtebilmesidir.

- Korozyon koruması
- Aşınma direnci
- Boşluk kontrolü – aşındırıcılar ve aşınacak malzemeler
- Isı ve oksidasyon direnci
- Sıcaklık yönetimi
- Elektrik direnci ve iletkenlik

Tablo 4: Plazma Sprey Tekniği Parametreleri

Parametreler	**Standart Ayarları**
Kaplanacak(altlık) malzeme	St-37
Enjektör nozul çapı (mm)	1.8
Enjektör mesafesi (mm)	6
Enjektör açısı	90°
Plazma püskürtme mesafesi (mm)	120
Akım(A)	600
Voltaj(V)	67
Gaz	Ar
Taşıyıcı gaz akışı (lt/dak.)	3-4
Argon gaz akışı (lt/dak.)	35
Plazma tabancası tipi	Metco 3MB
Metco 3MB Plazma tipi	$Ar+H_2$
Nozul tipi	W katod ; Cu anod

Bu çalışmada St-37 yapı çeliği altlığımız kaplama yapılmadan önce ön hazırlık aşamalarına tabii tutuldu.

2.3. Kaplama Öncesi Hazırlık

Plazma püskürtme yöntemi ile kaplama yapmadan önce kaplama tozunun malzemeyle iyi bir birleşme yapabilmesi için kumlama işlemi uygulandı. Kumlama işlemi esnasında Sampi marka kumlama cihazı kullanıldı. Yüzeyler pürüzlendirildi.

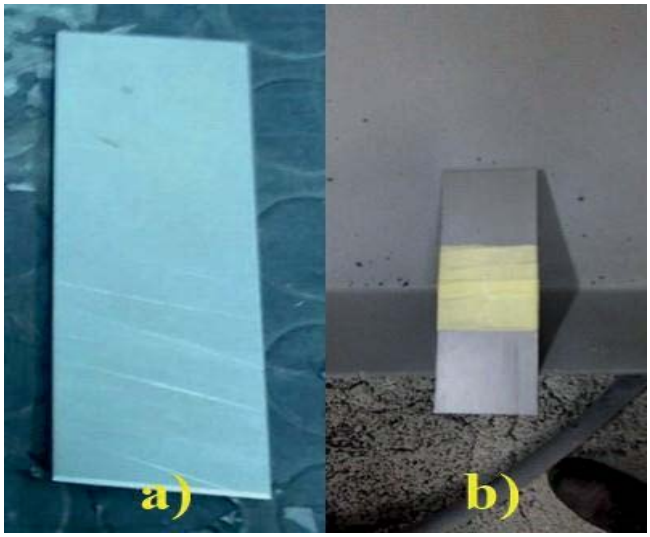

Şekil 3: a-b) Sampi marka kumlama cihazıyla kumlanmış yüzeyler

2.4. SEM ile İnceleme

SEM cihazıyla incelemeden önce hazırlık aşamasında önce numuneleri 7*7 mm boyutunda pres makinasıyla kesme işlemi uyguladık. Ardından kestiğimiz numuneleri SEM kalıplarına yapıştırdık. Numuneleri iletken hale getirmek için vakumlu ortamda 75 saniye boyunca 10 amstrong kalınlığında altın-paladyum kaplama yapıldı.

Malzemeler kaplandıktan sonra SEM mikroskobunda incelenmek üzere numune tutucuya yerleştirildi. Ardından yerleştirme koluyla numuneler tabancanın görüş alanına yaklaştırıldı.

Tabancanın görüş alanında olan numunelere elektron bombardımanı gönderildi. Altın-paladyum kaplama yapıldığından dolayı elektronlar malzemeye güzelce temas ederek 50, 150, 300, 1000 ve 2000 kat büyütülerek görüntü alındı.

1. ***Numune:*** Plazma Püskürtme – Al_2O_3+TiO_2 (87-13)

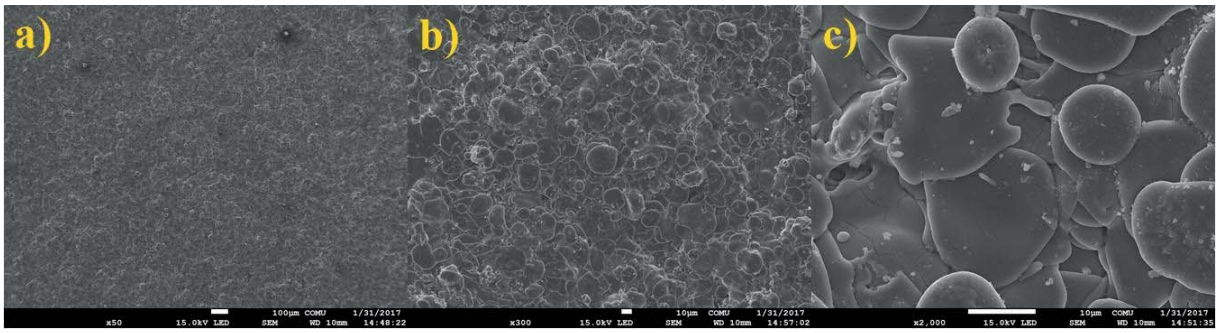

Şekil 4: SEM Görüntüleri a) x50 büyütme 100 µm b) x300 büyütme 10 µm c) x2000 büyütme 10 µm

2. Numune: Plazma Püskürtme- Cr_2O_3

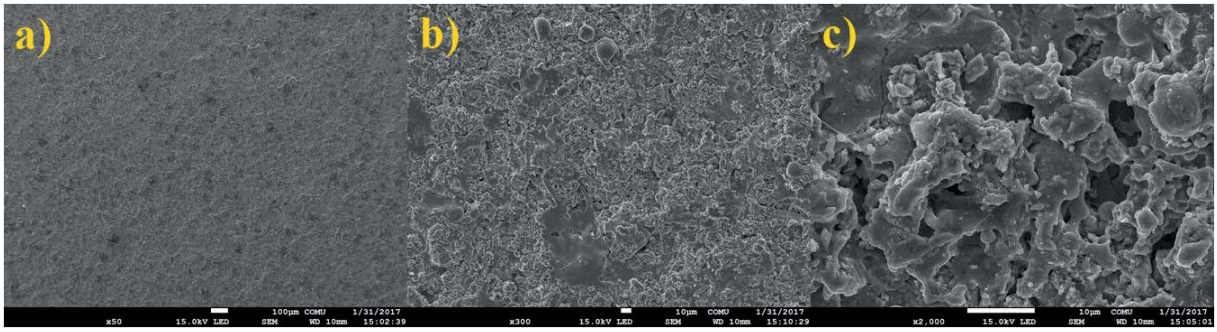

Şekil 5: SEM Görüntüleri a) x50 büyütme 100 µm b) x300 büyütme 10 µm c) x2000 büyütme 10 µm

2.5. Kaplamaların Mikrosertlik Ölçümü

Kaplanan numunelerin sertlik değerleri, ASTM E384 normuna göre Şekil 10'da gösterilen, Shimadzu HV2 marka mikrosertlik cihaz ile 200 gr yük 10 s. uygulanarak yapılmıştır.

Şekil 6: Shimadzu HV2 Mikrosertlik Ölçüm Cihazı

Tablo 5: Mikrosertlik Değerleri

Kaplama	Sertlik Değeri
1.Numune (Al_2O_3+TiO_2 (87-13))	343.57
2.Numune (Cr_2O_3)	442.37
Altlık Malzeme	115.56

Mikrosertlik değerleri her numuneden 10 adet sertlik değeri alınıp ortalaması ile belirlenmiştir.

3. SONUÇ

St-37 altlık malzeme üzerine plazma sprey kaplama tekniği kullanılarak Al_2O_3+TiO_2 (87-13) ve Cr_2O_3 ara bağlayıcı olmaksızın 2 adet numune kaplanmıştır. SEM mikroskobunda görüldüğü üzere aynı yöntemle fakat farklı alaşımlarla kaplanan malzemelerin bağlarının farklı olduğu kanıtlanmıştır. Aynı altlık malzemesi üzerinde çalışılan kaplamalarda alaşım malzemesi Cr_2O_3 olan kaplama bağının, alaşım malzemesi Al_2O_3+TiO_2 olan kaplama bağına nazaran daha güzel yüzeye yapıştığı gözlemlenmiştir. 2000x büyütmede karşımıza çıkan görünüm bunu destekler niteliktedir. Al_2O_3/TiO_2 oranının ayarlanmasıyla, kaplamanın yoğunluğunu ve dolayısıyla mekanik özellikleri tahmin etmek ve kontrol etmek mümkündür (E. Klyatskina ve arkadaşları, A study of the influence of TiO_2 addition in Al_2O_3 coatings sprayed by suspension plasma spray, 2015, 25-29). E. Klyatskina ve arkadaşlarınınyaptığı çalışma bunu destekler niteliktedir.

Bunların yanı sıra yapılan mikrosertlik deneylerinde ise; Al_2O_3+TiO_2 (87-13) kaplamasının altlık malzemesinin sertliğini 3 kat, Cr_2O_3 kaplamasının da altlık malzemesinin sertliğini 4 kat arttırdığı kanıtlanmıştır.

Özetle yapılan bu çalışmada St-37 altlık malzemenin mekanik özellikleri literatürde de incelendiği üzere gelişmiştir. Ve kaplama yöntemlerinin özelliklerinin kullanılan kaplama hammaddeye bağlı olarak değişimi sebebiyle kıyaslanamamıştır. Ancak kullanıla n kaplama hammaddesi mekanik özelliklerine bakılarak kaplama yöntemi seçimi yapılması gerektiği öngörülmektedir. Bu çalışmada Al2O3+TiO2 (87-13) ve Cr2O3 hammaddelerinin plazma püskürtme yöntemiyle kaplanmasında istenilen kalitede kaplama ürünü elde edilememiştir. Bu konuda ki çalışmalarımız literatür ışığında devam etmektedir.

TEŞEKKÜR

Kaplama konusunda bize atölyesini açan Yüzey Mühendisliğe, SEM cihazıyla ölçüm yapmamız için bizlere yardımcı olan Çanakkale Onsekiz Mart Üniversitesi Merkez Laboratuvarı çalışanlarına, sertlik testi için Marmara Üniversitesi Teknoloji Fakültesi çalışanlarına, bu çalışmada bizlere yol gösteren hocalarımıza, her zaman yanımızda olan ve bizlerden desteklerini esirgemeyen ailelerimize sonsuzteşekkürlerimizi sunarız.

REFERANSLAR

A.Bhatia, Thermal Spraying Technology and Applications Washington: U.S. Army Corps. Of Engineers., 1999 Ahmet Akgül, S.Serdar Pazarlıoğlu, Doğan Tutak, Zafer Özomay, Hüseyin Beytut, Cem Özakhun, & Serdar

Salman Matbaa Sektöründe Aşınmış Çelik Esaslı Bir Malzeme İçin Seramik Kaplama Uygulaması International Iron & Steel Symposium, 02-04 April 2012, Karabük, Türkiye 587

Ahmet Güleç, Fatih Üstel, Özgür Cevher, Ahmet Türk, Akın Akıncı, Fevzi Yılmaz (2010) Elektrik Ark Sprey Kaplama Teknolojisi Uygulamaları, , Sakarya Üniversitesi, Mühendislik Fakültesi, Metalurji ve Malzeme Mühendisliği Bölümü, Esentepe Kampüsü, 54187 Adapazarı

Arif Özkan, Fatih Baba, Suat Ayan (2006) Seramiklerin Makine Elemanları ve Mekanizmaları Üzerine Uygulanabilirliği ve İmalat Yöntemlerinin İrdelenmesi

Bartın Üniversitesi, Termal Bariyer Kaplama Ders Notu, s 43-46#

Çağrı Barut (2010) St 37 Karbonlu Çelik Malzeme Ara Bağlantı Aparatı Delme ve Bükmenin Teorik ve Deneysel İncelenmesi-Karabük Üniversitesi Teknik Eğitim Fakültesi Makine Tasarım Öğretmenliği

M. R. Dorfman, "19 - Thermal Spray Coatings," in Handbook of Environmental Degradation of Materials (Second Edition), Oxford: William Andrew Publishing, pp. 569–596, 2012.

Nuri Aydınlı, Plazma Sprey Kaplamada Olivin Değerlendirilmesi ve Kaplama Özelliklerinin İncelenmesi, Sakarya Üniversitesi, Fen Bilimleri Enstitüsü

Patrick R., Development of Conventional and Nanocrystalline Bond Coats by Cold Gas Dynamic Spraying for Aerospace Thermal Barrier Coatings, PhD Theses, University of Ottowas, Ottowa Ontario Canada, 1-227, July 19, 2010.

Rickbery , D.S.,Matthews A. Advantages Surface Coatings: a Handbook of Surface Engineering ,New York, U.S.A., 1991.s4-13

Robert C. Tucker, Jr., ASM Handbook, Volume 5: Surface Engineering C.M. Cotell, J.A. Sprague, and F.A. Smidt, Jr., editors,(p 497-509), Termal Spray Coatings, , Praxair Surface Technologies, Inc.

Wang, Y., Jiang, S., Wang, M., Wang, S., Xiao, T.D., Strutt, P.R., Abrasive wear characteristic of plasma sprayed nanostructured alumina/titania coatings, Wear 237, 2000, 176–185.

MÜHENDİSLİK FAKÜLTESİ

Uluslararası Mühendislik Araştırma ve Geliştirme Dergisi

International Journal of Engineering Research and Development

Cilt/Volume:9 Sayı/Issue:3 Aralık/December 2017 https://doi.org/ 10.29137/umagd.360670

Araştırma Makalesi / Research Article

Implementation of ZigBEE (IEEE 802.15.4) Based Wireless ECG Measurement System

Atakan AKBULUT [*1], Şükrü EKİN[1], Ömer TUNÇ, Ali ÖZEN[1]

[1]Nuh Naci Yazgan University-HARGEM, Faculty of Engineering, Electrical and Electronics Engineering, 38010 Kayseri

Başvuru/Received: 08/10/2017 **Kabul/Accepted**: 01/12/2017 **Son Versiyon/Final Version**: 26/12/2017

Abstract

This study presents a realization of a ZigBEE based wireless ECG system for remotely monitoring the patient's electrocardiogram (ECG) via wireless heart sensor (AD8232). The presented wireless ECG system is composed of hardware such as Arduino micro-controller connected to the electrodes on the patient, personal laptop, tablet PC, smart phone etc. for ECG signal monitoring, AD8232 sensor for measuring heart rate, ZigBEE transceiver (XBee S2C) for wireless transmission of ECG signal, and software such as Serial Plot or Arduino Serial Plotter. The results from the tests show that the system designed over a single node can work seamlessly in an open area of approximately 20 to 100 meters and take ECG measurements wirelessly. Additionally, the obtained results from the tests show that the ECG measurements can be taken wirelessly within a range of 20 to 80 meters when the obstacles are also placed between ZigBEE transmitter and receiver.

Key Words

"Wireless ECG, ZigBEE, Arduino, remote patient monitoring, heart sensor"

akbulutatakann@gmail.com

1. INTRODUCTION

Important developments have been made in wireless communication systems over the past 50 years. Improvements in high-frequency semiconductor circuits and the reduction of antenna dimensions have contributed significantly to radio communications. Another important factor is the development of battery technology and the efficient use of amplifiers that operate on radio frequency multiples (Somay, 2009).

Establishment of sensor networks with digital radio and the creation of a large-scale network structure is the only way to shape the technology that has been developing and matured for the last few years. This format comes with the emergence of standards such as IEEE 802.15.4 (ZigBEE) (IEEE Standard, 2007).

The integration of biomedical sensors with wireless network technology may have great potentials in medical applications. Technological innovations in the field of disease prevention and patient health protection have led to the development of areas such as monitoring systems. One of the most important developments is the development of real-time monitors that use intelligent and wireless communication technology. The IEEE 802.15.4 standard targets low power, low data rate wireless network applications such as wireless body area network (WBAN), home automation and environmental monitoring network. One of the promising applications of the future is medical care. In advanced hospitals, light and pille-operated sensor nodes equipped with a range of biomedical sensors can be connected to a large number of patients with physiologic data and vital signs. Data such as body temperature, blood pressure, electrocardiogram (ECG), electroencephalography (EEG) and heart rate of patients can be perceived and transmitted to the medical center where these data can be used for monitoring the health status of patients and for further analysis. Biomedical sensor networks can also help ensure freedom of movement while ensuring that patients are constantly monitored and cared (Romer & Friedemann, 2004).

ECG is a method of examination that allows us to visualize the electrical activity that occurs during the contraction and relaxation phases of the atrium and ventricles of the heart on time and mV on the millimeter paper. ECG devices are used by the wired method to diagnose cardiac disorders such as fibrillation (shock), heart attack, and cardiac arrhythmia in patients.

Intensive care patients are usually connected to wired ECG devices to provide immediate intervention in any cardiac problems and monitoring with medical devices to reduce deaths. However, the inadequate equipment of ECG devices is a big problem. Researches are being conducted all over the world for the development of these devices. In this system intended to be performed in this study, it is aimed to transmit more than one heart signal wirelessly. In this way, it is aimed to increase the speed of sudden intervention and decrease in cost.

Many procedures are required to obtain the ECG signal from human beings. The working principle of the human body comes in the form of electricity signals and nerve conduction in mV degree. The bio potential signal is the electrical signal of the mV degree produced by the body with the purpose to work regularly of the human body. Bio potential signals are the survival factors of living things such as blood pressure, heart rate, heart rhythm and brain functions. The ECG signal is obtained by taking the electrical signals generated by the heart with specific surface electrodes and generating an ECG signal to provide an idea about patient and diagnose.

In cable ECG devices, 6 chest probes and 3 peg type electrodes are generally used. The cost and deterioration of these electrodes is a major problem. It is misunderstood that ECG devices appear to be portable. The ECG device must be constantly on the patient's side. Another problem is that the electrodes must be removed in order to meet the basic needs of the patient. This leads to problems caused by the patient and the person interested in it. In patients with variable status and undergoing fibrillation, the electrodes of the ECG device should remain connected during the day.

When ECG device design is considered as a wireless, it will be improved in terms of cost, number of personnel and speed of intervention. One of the most important features is also that the ECG of more than one patient is transmitted to a single computer environment. Thus, the time and interest allocated to the patient will increase. In case of any problem will be taken information about patient and will be monitored continuously without affecting the daily activities of the patient.

ECG signals show the electrical activity of the heart. Patients can be monitored continuously while performing daily activities in household conditions. The sensors placed in the body of the patient are used to record the measurement data. The measured data is filtered and then displayed graphically using Matlab, Java, etc. software. This data is transmitted using wireless transmission to the doctor who examines the ECG signals and guides the patient if there is any emergency medical aid required and also monitors and keeps a track of all the patient’s data periodically. Wireless transmission is made using the ZigBEE technique, which is an effective way to transfer data. The data from each sensor is detected using the USB link terminal on the computer. Then the data from a patient at home or hospital is transmitted to the doctor using ZigBEE.

This study aimed at establishing a portable and battery-operated meter read by a wireless connection with developing digital radio systems.

In this study, analogue signals were measured with the help of the multi-channel ADC unit in Arduino processors, and this information was transferred to a USB extension device using the IEEE 802.15.4 (ZigBEE) radio network and from there it was transferred to PC for observation and storage. As a result, experimental data on the determination of the limits of the measurements made from the far distance have been obtained.

In this study, we present a realization of a ZigBEE based wireless ECG system for remotely monitoring the patient's electrocardiogram via wireless heart sensor (AD8232). The AD8232 offers a new alternative for measuring the heart rate remotely in real time during patient care. The presented wireless ECG system is composed of hardware such as Arduino micro-controller connected to the electrodes on the patient, personal laptop, tablet PC, smart phone etc. for ECG signal monitoring, AD8232 sensor for measuring heart rate, ZigBEE transceiver (XBee S2C) for wireless transmission of ECG signal, and software such as Serial Plot or Arduino Serial Plotter. The results from the tests show that the system designed over a single node can work seamlessly in an open area of approximately 20 to 100 meters and take ECG measurements wirelessly. Additionally, the obtained results from the tests show that the ECG measurements can be taken wirelessly within a range of 20 to 80 meters when the obstacles are also placed between ZigBEE transmitter and receiver. This range can be extended thanks to the ability of the ZigBEE to operate with nodes. This will provide the possibility for a patient to freely navigate in the room or in the hospital while the ECG measurements are being followed. Tests have shown that data can be obtained with high accuracy from the sensor units in motion.

The rest of the paper is organized as follows: Section 2 introduces the implementation of wireless ECG measurement system using ZigBEE (IEEE 802.15.4) standard. Section 2.1 explains the designed wireless ECG measurement system and measurement conditions. Section 3 presents the experimental studies to verify the feasibility and robustness of the designed wireless ECG measurement system and finally, the paper is concluded in Section 4.

2. IMPLEMENTATION OF WIRELESS ECG MEASUREMENT SYSTEM USING ZigBEE (IEEE 802.15.4) STANDARD

ZigBee transmitter / receiver (transceiver) units using the ISM 2400-2483 MHz band from radio frequency bands are manufactured as a single semiconductor chip. Therefore, this study should be evaluated primarily as the establishment of existing transmitter / receiver units and the investigation of implementation achievements. It is expected from this study that it is extended the use of wireless area networks by identifying the application features, problems and limits of the service belong to the developed technology.

The subject of the study is a communication system using IEEE 802.15.4 (ZigBEE) structure for use in a general purpose wireless measurement system. Experiments with the Arduino mini, capable of 200k sampling in the second, have shown that the measurement system can respond to the bandwidth requirement of approximately 20 kHz. Therefore, this shows that ZigBEE's communication limit of data rate of 250 kbits / s is reached. Real-time audio signals can be carried with such a measurement system. However, such systems that have low data rates and are not suitable for synchronous communication are not well suited for real-time audio and video transport applications. Since the IEEE 802.15.4 standard is a standard operating at very low power, the field units used can be fed with battery blocks. Thus, measurements made independent of the power grid can be much more sensitive.

Considering the characteristics of this general-purpose measuring system, biomedical signals can be carried by such a system. The combination of biomedical sensors and wireless sensor networks may have a very high potential in medical applications. Performance analyses of IEEE 802.15.4-based biomedical measurement systems have been found to be useful in evaluating transmission delay, end-to-end delay, and packet delivery rate in studies done (Liang & Balasingham, 2007).

In this field, studies such as wearable ECG measurement system designs and smart home applications that can perform real-time health checks and seek help in risk situations have been done (Park et al., 2006), (Dağtaş et al., 2007).

This study aimed that realizing a general purpose sensor network with a wireless unit requiring high data rate or accurate measurement.

2.1. Designed Wireless ECG Measurement System

The block diagram of the designed wireless ECG measurement system is shown in Figure 1.

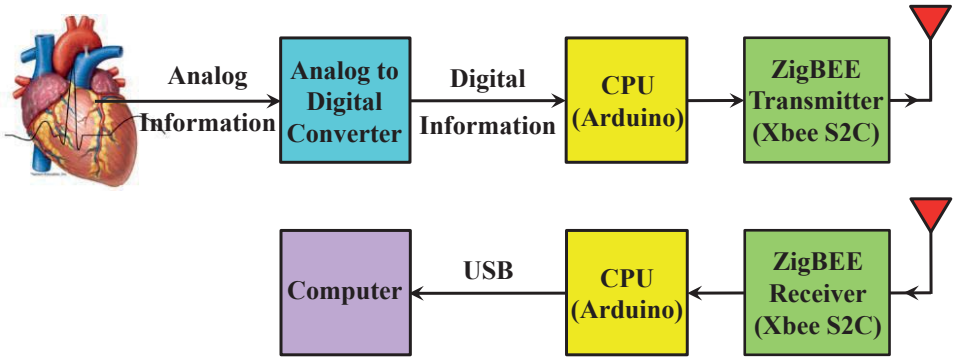

Figure 1: Block diagram of designed wireless ECG measurement system (Akbulut et al., 2017).

The analog signal from the heart sensor (AD8232) is digitally converted by a 10-bit analog to digital converter (ADC), the resulting digital information is processed by the Arduino mini-series processor, and with the Xbee S2C transmitter chip the radio frequency (RF) is also sent from the assigned channel. The signal on the RF channel is detected by the Xbee S2C series receiver chip on another sensor network unit in the receiver, demodulated and decoded, and is transmitted to the Arduino series processor. The Arduino processor transfers the information sequence it receives to the computer that it is connected via USB (universal serial bus). The program running on the computer draws the information sequence received via USB on the screen with the help of the Serial Plot or Arduino Serial Plotter program and displays the signal (Akbulut et al., 2017), (Margolis, 2011).

3. EXPERIMENTAL STUDIES

The experimental studies have composed of two stages. In the first stage studies are performed in open area with line of sight (LOS). In the second stage studies are implemented in none-LOS (N-LOS) environment when the obstacles are also placed between ZigBEE transmitter and receiver. The attenuation analysis of the obtained measurements in dB was made with the XCTU interface program (Akbulut et al., 2017).

3.1. Experimental Results in LOS Environment

In the first phase of the study, in order to test the operation of the wireless ECG measurement system measurements were taken when between the ZigBEE transmitter and the ZigBEE receiver units were in case of LOS in an open area.

Wireless ECG measurements were taken when the distance between the transmitter and receiver was 5 meters in Figure 2, 10 meters in Figure 4, 20 meters in Figure 6 and 30 meters in Figure 8. Additionally, in Figure 3, 5, 7 and 9, it is performed the attenuation analysis in dB for the same measurements.

Figure 2 shows the ECG chart when the distance between the transmitter and the receiver is 5 meters, and Figure 3 shows the dB attenuation analysis for this graph.

Figure 2: Wireless ECG measurement for distance of 5 meters.

When Figure 2 is examined, it is seen that the ECG signal is obtained with high accuracy.

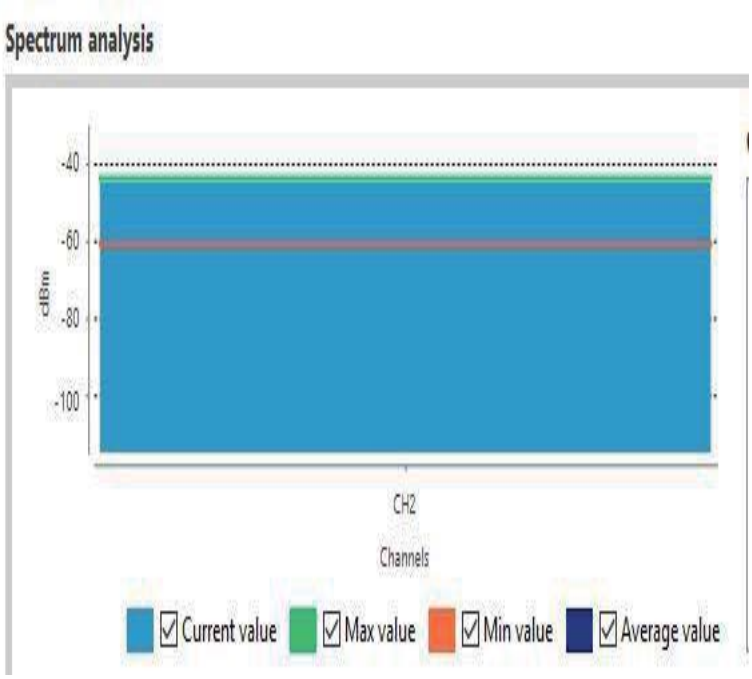

Figure 3: Attenuation analysis of wireless ECG measurement for distance of 5 meters.

When Figure 3 is investigated, it is determined that there is a loss of about 5 dB in the measured ECG signal. It is observed that Figures 2 and 3 confirm with each other.

Figure 4 shows the ECG graph measured at a distance of 10 meters between the transmitter and the receiver and the dB attenuation analysis of this graph is shown in Figure 5.

Figure 4: Wireless ECG measurement for distance of 10 meters.

When Figure 4 is examined, it is seen that the ECG signal is similarly obtained with high accuracy.

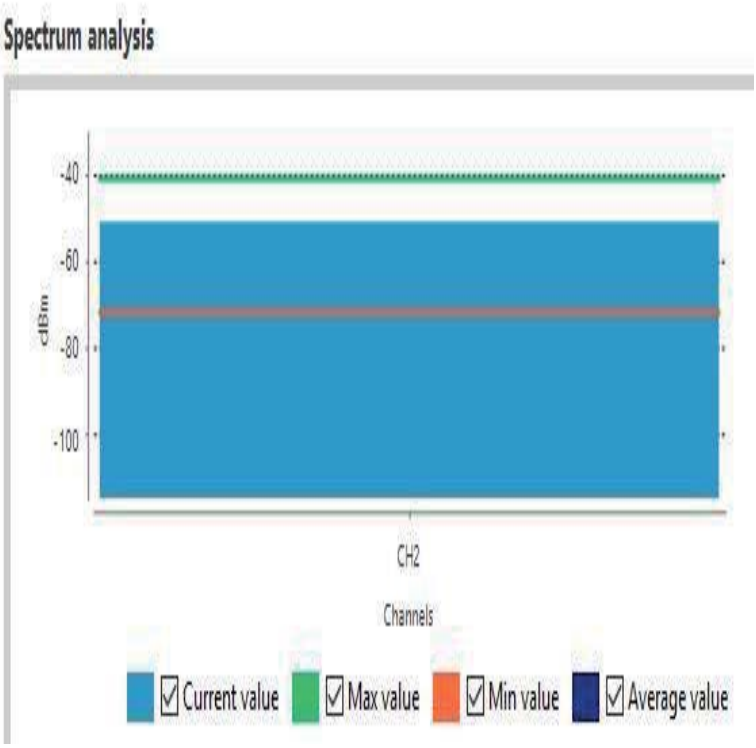

Figure 5: Attenuation analysis of wireless ECG measurement for distance of 10 meters.

When Figure 5 is investigated, it is determined that there is a loss of about 10 dB in the measured ECG signal. It is observed that Figures 4 and 5 verify with each other.

Figure 6 shows the ECG graph measured at a distance of 20 meters between the transmitter and the receiver, and the dB attenuation analysis of this graph is shown in Figure 7.

Figure 6: Wireless ECG measurement for distance of 20 meters.

When Figure 6 is investigated, it is seen that impairments in the ECG signal are increased.

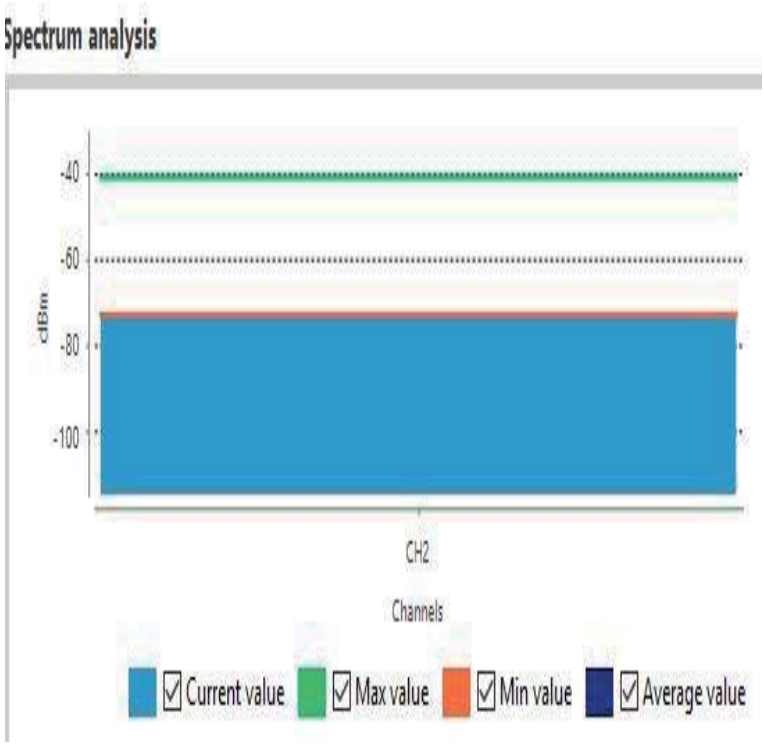

Figure 7: Attenuation analysis of wireless ECG measurement for distance of 20 meters.

When Figure 7 is examined, it is determined that there is a loss of about 35 dB in the measured ECG signal.

Figure 8 shows the measured ECG graph when the distance between the transmitter and the receiver is 30 meters and Figure 9 shows the dB attenuation analysis of this graph.

Figure 8: Wireless ECG measurement for distance of 30 meters.

When Figure 8 is investigated, it is seen that the deteriorations in the ECG signal increases more. Figure 9 shows that there is a loss of approximately 55 dB in the measured ECG signal.

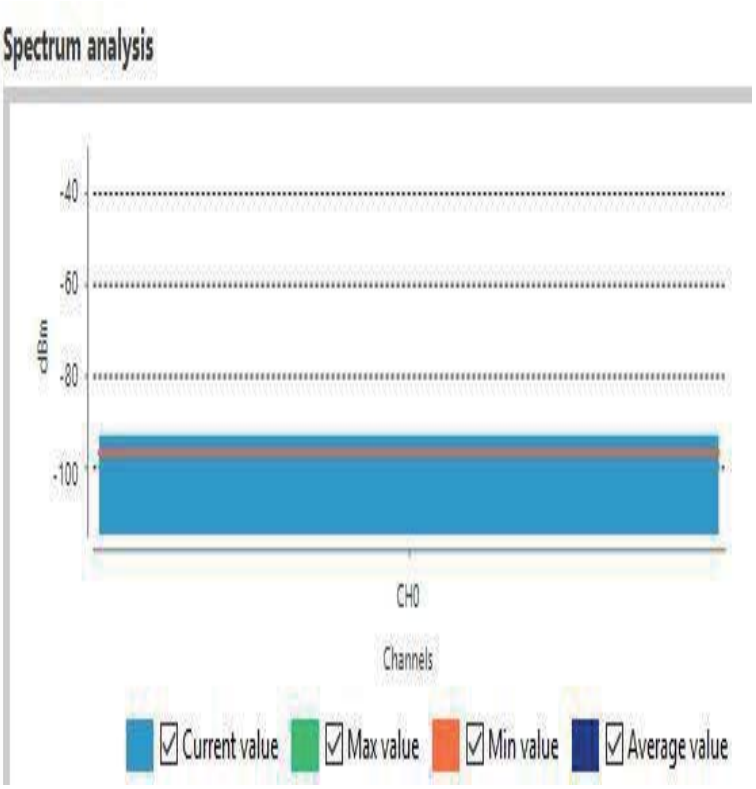

Figure 9: Attenuation analysis of wireless ECG measurement for distance of 30 meters.

3.2. Experimental Results in N-LOS Environment

In the second phase of the study, in order to test the operation of the wireless ECG measurement system measurements were taken where the ZigBEE transmitter and the ZigBEE receiver units did not see each other (in case of N-LOS).

In Figure 10, wireless ECG measurements are taken in case of the distance between the transmitter and the receiver is 10 meters and the door obstruction. Also, in Figure 11, the attenuation analysis is performed in terms of dB of this measurement.

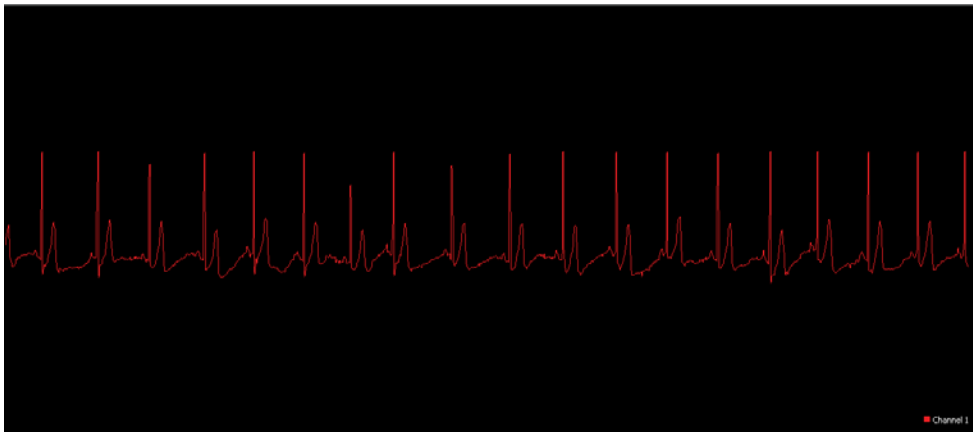

Figure 10: Wireless ECG measurement when there is door obstacle for distance of 10 meters.

When Figure 10 is investigated, it is seen that the ECG signal is distorted due to the door obstruction. When Figure 11 is examined, it is determined that there is a loss of about 20 dB in the measured ECG signal.

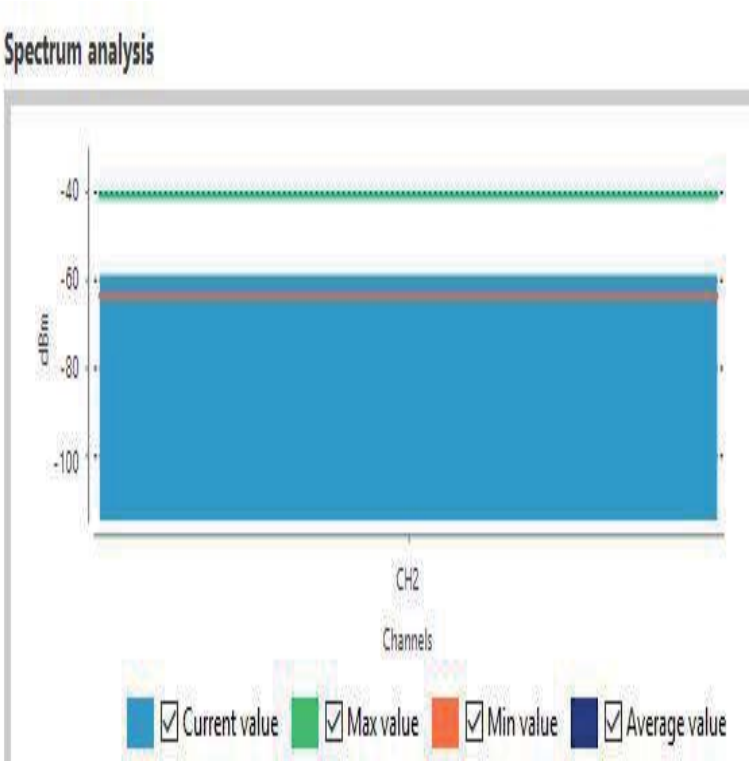

Figure 11: Attenuation analysis of wireless ECG measurement when there is door obstacle for distance of 10 meters.

In Figure 12, wireless ECG measurements were taken in case of the transmitter is on the ground floor and the receiver is on the upper floor (first floor).

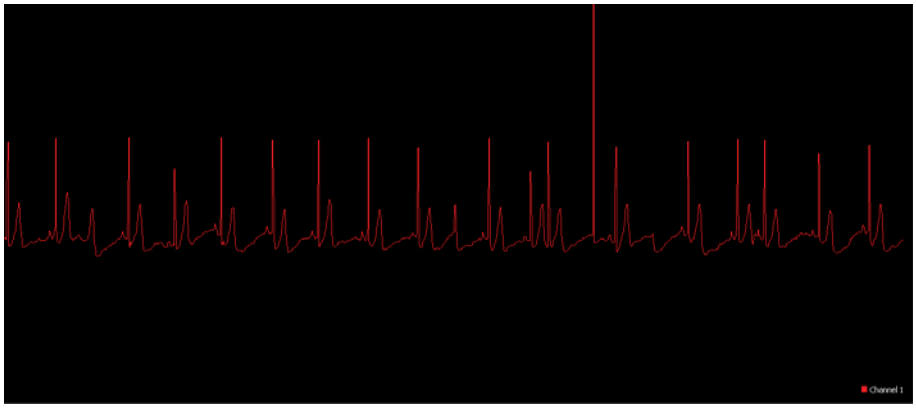

Figure 12: Wireless ECG measurement when the transmitter is on the ground floor and the receiver is on the first floor.

When Figure 12 is investigated, it is seen that there are corruptions in the ECG signal due to the layer between the transmitter and the receiver.

In Figure 13, wireless ECG measurements were taken when the transmitter is on the ground floor and the receiver is on the two upper floor (second floor).

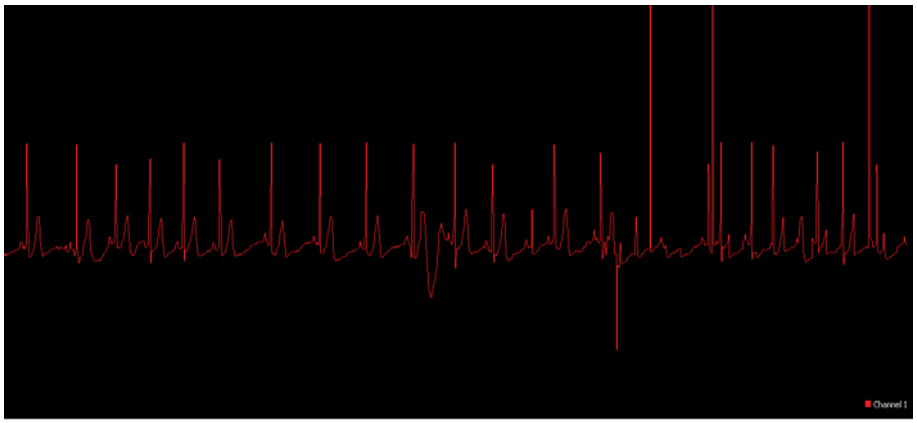

Figure 13: Wireless ECG measurement when the transmitter is on the ground floor and the receiver is on the second floor.

When Figure 13 is examined, it is seen that the deterioration increases in the ECG signal due to the fact that there are two layers between the transmitter and the receiver.

In Figure 14, wireless ECG measurements were taken when the transmitter is on the ground floor and the receiver is on the upper three layers (third floor).

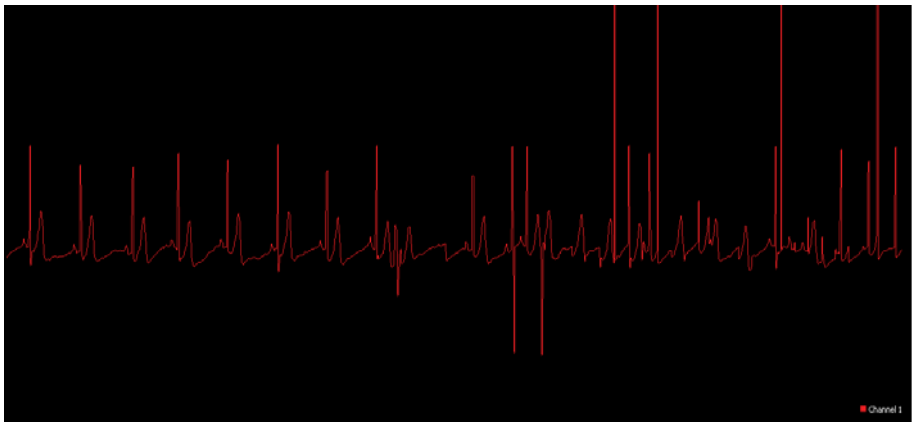

Figure 14: Wireless ECG measurement when the transmitter is on the ground floor and the receiver is on the third floor.

When Figure 14 is investigated, it is observed that the deterioration of the ECG signal has increased to an extreme extent due to the three floors between the transmitter and the receiver.

In Figure 15, measurements of the designed wireless ECG device have been compared simultaneously with measurements of real ECG device in the hospital environment. In a real ECG device, 6 electrodes are attached to the chest and 4 electrodes are attached to the hands and ankles. This comparison of these ECG signals shows what extent the ECG signal is taken correctly from the body and transmitted wirelessly.

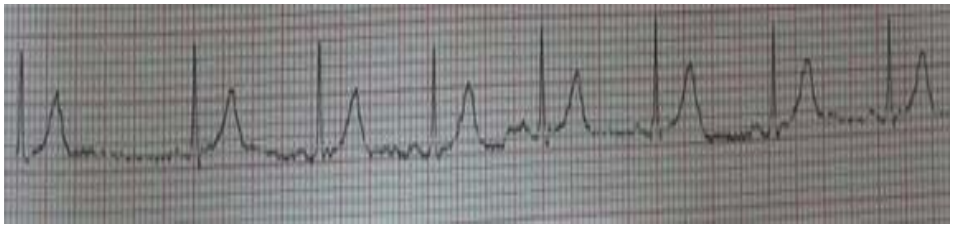

a) Real ECG measurement

b) Designed wireless ECG measurement

Figure 15: Comparison of the designed wireless ECG measurements with real wired ECG.

When Figure 15 is examined, it is seen that the measurements taken with the designed wireless ECG system are approximately the same as the real ECG measurement. As a result, the ECG signal taken from any person is transmitted wirelessly to the intended system without any problems.

4. CONCLUSIONS

Wearable and mobile systems continue to evolve rapidly in order to save the patient from disturbing cable extensions and be able to follow the required measurements on the move. In this context, the structure of the wireless sensor networks and the installation methods were investigated and the implementation of a wireless ECG measurement system using IEEE 802.15.4 (ZigBEE) was performed in this study.

The results from the tests show that the system designed over a single node can work seamlessly in an open area of approximately 20 to 100 meters and take ECG measurements wirelessly. In addition, the results from the tests show that the ECG measurements can be taken wirelessly within the range of 20 to 80 meters when there are obstacles between the ZigBee transmitter and the receiver.

REFERENCES

Akbulut A., Ekin Ş., Tunç Ö. (2017), Implementation of ZigBEE (IEEE 802.15.4) Based Wireless ECG System, Bachelor Thesis, Nuh Naci Yazgan University, Department of Electrical and Electronics Engineering, Kayseri, Turkey.

Dağtaş S., Pekhteryev G. and Şahinoğlu Z. (2007), "Multi-stage Real Time Health Monitoring via ZigBEE in Smart Homes".

IEEE Standard (2007), IEEE Standard for Part 15.4: Wireless Medium Access Control (MAC) and Physical Layer (PHY) specifications for Low Rate Wireless Personal Area Networks (LR-WPANs).

Liang X. and Balasingham I. (2007), "Performance Analysis of The IEEE 802.15.4 Based ECG Monitoring Network".

Margolis M. (2011), "Arduino Cookbook ", First Edition, Chapter 14.

Park C., Chou P., Bai Y., Matthews R. and Hibbs A. (2006), "An Ultra Wearable, Wireless, Low Power ECG Monitoring System".

Romer K. and Friedemann M. (2004), "The Design Space of Wireless Sensor Networks", 54–61.

Somay A. (2009), "Implementation of A Wireless Measurement Probe using IEEE 802.15.4 (ZigBEE) Standard", Ms.C. Thesis, Graduate School of Natural and Applied Science, Black Sea Technical University, Trabzon.

MÜHENDİSLİK FAKÜLTESİ

Uluslararası Mühendislik Araştırma ve Geliştirme Dergisi

International Journal of Engineering Research and Development

Cilt/Volume:9 Sayı/Issue:3 Aralık/December 2017 https://doi.org/10.29137/umagd.348744

Araştırma Makalesi / Research Article

The Role of FGATool in Fractional Order System Analysis Education

Bilal Şenol[1]

[1]*İnönü University, Faculty of Engineering, Computer Engineering Department, Malatya,TURKEY*

Başvuru/Received: 08/10/2017 **Kabul/Accepted**: 01/12/2017 **Son Versiyon/Final Version**: 26/12/2017

Abstract

The scenario for engineering education is changing by the effect of theoretical developments in recent years. Appropriate usage of computer technology gives great opportunity to follow these changes and provides student achievement. This paper presents FGATool, a Matlab based interface developed to take role in fractional order system analysis education. Fractional order calculus can be an unfamiliar concept for students, thus it is an indisputable fact that some analysis tools will be useful in the education process. The tool is experienced in classes of master students and the outcomes are recorded. Two main modules of FGATool are presented with their mathematical background all over the paper. Analysis of fractional order systems with fixed and uncertain parameters separately can be realized without complicated technical background. FGATool is also thought to be useful with its user-friendly interface.

Key Words

"Fractional order systems, FGATool, Stability analysis, System uncertainties."

** bilal.senol@inonu.edu.tr*

1. INTRODUCTION

A fractional order system can be modeled by a differential equation with orders of arbitrary real numbers. First idea of the concept lays back to late 17th century on a correspondence between Leibniz and L'Hopital. Fractional order calculus is an unfamiliar subject for researchers and especially for students who are new to non-integer world. Thus, some tools will be useful for the education process of fractional order analysis.

Nowadays, fractional order calculus can be used in many areas as an alternative technique for analysis of control systems. It also finds numerous applications in control engineering (Caponetto et al., 2010; Balenau, et al., 2016; Azar et al., 2017; Monje et al., 2010)

Recent years brought intensive usage of computer technology in all areas of education processes. It is a certain fact that computers make human lives easier in so many ways. As the main subject of this paper, control analysis education techniques has also been improved with the help of computer technology (Senol et al., 2012; Senol, 2017)

There can be found some interfaces related to fractional order system analysis in the literature. For example, the CRONE toolbox is famous to be one of the first studies in this direction (Oustaloup, 1991). *ninteger* and PIDLAB are also effective analysis tools (Valerio, 2005). PIDLAB and FOMCON can be shown as a similar tool for fractional order system analysis (Martin&Milos, 2006; Tepljakov, 2017). First version of FGATool named as UFT-FOCS can be shown as a preliminary level analysis tool (Senol, 2012; Senol&Yeroglu, 2015a)

This paper presents FGATool which is developed for easy analysis of fractional order systems. Main difference and proposal of FGATool is its ease of use for researchers who are new to the subject. The tool consists of two main modules for fractional order systems with fixed parameters and for fractional order systems with uncertain parameters. Each module includes six analysis tools. The tool can be freely downloaded from www.fgatool.com.

Organization of this paper is as follows. Section 2 includes a brief introduction to fractional order systems. Section 3 presents the features of FGATool and section 4 shows the usage and effect of FGATool for the control education process. Section 5 has the conclusion.

2. FRACTIONAL ORDER SYSTEMS

A model represented with a differential equation which has orders of non-integer numbers can be classified as a fractional order system. Let us consider the following differential equation which has arbitrary real orders.

$$\begin{aligned} &a_n D^{\alpha_n} y(t) + a_{n-1} D^{\alpha_{n-1}} y(t) + \ldots + a_0 D^{\alpha_0} y(t) = \\ &b_m D^{\beta_m} u(t) + b_{m-1} D^{\beta_{m-1}} u(t) + \ldots + b_0 D^{\beta_0} u(t) \end{aligned} \tag{1}$$

where, a_i and b_j are the coefficients of the differential equation. α_i and β_j are the real orders. The differential equation in Eq. 1 can be rewritten as a transfer function using the Laplace transform considering zero initial conditions as (Senol et al., 2017)

$$G(s) = \frac{Y(s)}{U(s)} = \frac{b_m s^{\beta_m} + \ldots + b_1 s^{\beta_1} + b_0 s^{\beta_0}}{a_n s^{\alpha_n} + \ldots + a_1 s^{\alpha_1} + a_0 s^{\alpha_0}} . \tag{2}$$

Characteristic equation of the transfer function which will be used in some analysis techniques in this paper can be obtained in the following form.

$$\Delta(s) = Y(s) + U(s) \tag{3}$$

We can convert the transfer function in Eq. 2 from s domain to the frequency domain by replacing s to $j\omega$ as follows.

$$G(j\omega) = \frac{Y(j\omega)}{U(j\omega)} = \frac{b_m (j\omega)^{\beta_m} + \ldots + b_1 (j\omega)^{\beta_1} + b_0 (j\omega)^{\beta_0}}{a_n (j\omega)^{\alpha_n} + \ldots + a_1 (j\omega)^{\alpha_1} + a_0 (j\omega)^{\alpha_0}} \tag{4}$$

Similarly, characteristic equation in Eq. 3 can be written in the frequency domain as,

$$\Delta(j\omega) = Y(j\omega) + U(j\omega) \tag{5}$$

Fractional order of $j\omega$ can be expressed as follows (Yeroglu&Senol, 2013)

$$(j\omega)^{\mu} = \omega^{\mu} (\cos\frac{\pi}{2}\mu + j \sin\frac{\pi}{2}\mu) \tag{6}$$

FGATool is also an effective analysis tool for fractional order systems with uncertain parameters. Coefficients of the numerator and denominator polynomials can vary in an interval in this case. Consider the fractional order plant in Eq. 2 where the coefficients change in an interval.

$$G(s,\mathbf{q}) = \frac{Y(s,\mathbf{q})}{U(s,\mathbf{q})} = \frac{b_m(\mathbf{q})s^{\beta_m} + \ldots + b_1(\mathbf{q})s^{\beta_1} + b_0(\mathbf{q})s^{\beta_0}}{a_n(\mathbf{q})s^{\alpha_n} + \ldots + a_1(\mathbf{q})s^{\alpha_1} + a_0(\mathbf{q})s^{\alpha_0}} \tag{7}$$

where, the coefficients $b_j(\mathbf{q})$ and $a_i(\mathbf{q})$ linearly depend on $\mathbf{q} = [q_0, q_1, \cdots, q_q]^T$ which is in the uncertainty box (Senol et al., 2014a),

$$Q = \{\mathbf{q} : q_i \in [\underline{q_i}\ \ \overline{q_i}],\quad i = 1,2,\cdots,q\}. \tag{8}$$

$\underline{q_i}$ and $\overline{q_i}$ respectively represent the lower and upper limits of the uncertain parameters q_i. Frequency domain representation of the uncertain plant in Eq. 7 is given in the following way.

$$G(j\omega,\mathbf{q}) = \frac{\sum_{k=0}^{m}\left(b_k(\mathbf{q})(r_{bk}\omega^{\beta_k})\right) + \sum_{k=0}^{m} j\left(b_k(\mathbf{q})(i_{bk}\omega^{\beta_k})\right)}{\sum_{l=0}^{n}\left(a_l(\mathbf{q})(r_{al}\omega^{\alpha_k})\right) + \sum_{l=0}^{n} j\left(a_l(\mathbf{q})(i_{al}\omega^{\alpha_k})\right)} \tag{9}$$

where, r_{bk}, r_{al} and i_{bk}, i_{al} are constants of real and imaginary parts respectively. Similar to Eq. 5, an uncertain characteristic equation in the frequency domain can be expressed as,

$$\Delta(j\omega,\mathbf{q}) = Y(j\omega,\mathbf{q}) + U(j\omega,\mathbf{q}) \tag{10}$$

There can be found numerous studies related to fractional order systems with fixed and uncertain parameters (Senol et al., 2017; Yeroglu&Senol, 2013; Senol et al., 2014a; Senol et al., 2014b; Matusu&Prokop, 2011; Senol&Yeroglu, 2013). Next section of this paper gives brief information about features of FGATool.

3. FGATOOL

FGATool is a MATLAB based interface that is developed for easy analysis of fractional order systems. The tool can be freely downloaded from www.fgatool.com and can be started by typing *fgatool* in Matlab console window. Main window of FGATool is illustrated in Figure 1.

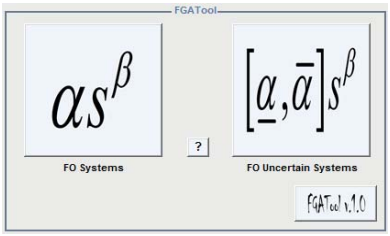

Figure 1: Main window of FGATool

Two main modules of the tool can be listed as,

- Fractional Order Systems
- Fractional Order Uncertain Systems

This section briefly introduces both modules.

3.1. FO Systems

Main appearance of Fractional Order Systems module is given in Figure 2.

Fractional Order Systems module includes the following analysis tools.

- Step Response
- Bode, Nyquist, Nichols
- Hermite-Biehler Analysis
- Roots Region Analysis
- Root Finder
- Frequency Properties

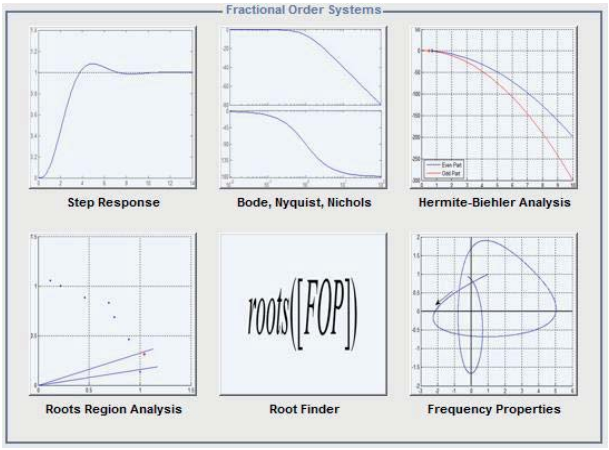

Figure 2: Fractional Order Systems module

Step Response and Bode, Nyquist, Nichols modules are developed using the mathematical background in (Xue et al., 2007). Hermite-Biehler Analysis module is an extension of the interlacing theorem for classical polynomials (Senol et al., 2014b). Roots Region Analysis module works on the roots laying on the first Riemann sheet (Senol et al., 2014a). Root Finder module proposes a method to find the roots of a fractional order polynomial (Senol et al., 2017). Frequency Properties module tests the stability on frequency plot of fractional order polynomials (Şenol&Yeroğlu, 2015b).

3.2. FO Uncertain Systems

Main appearance of Fractional Order Uncertain Systems module is given in Figure 3.

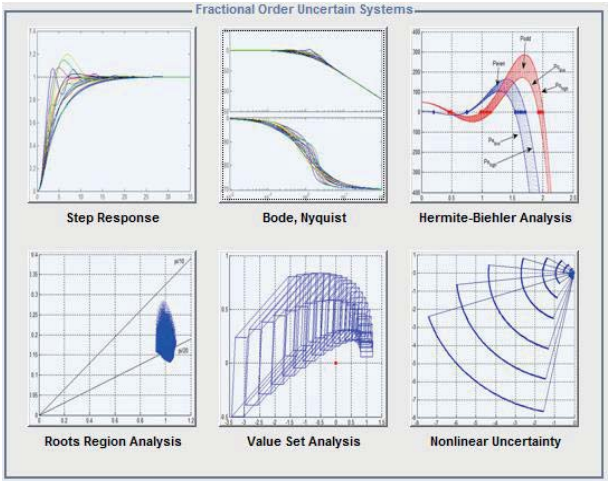

Figure 3: Fractional Order Uncertain Systems module

Fractional Order Uncertain Systems module includes the following analysis tools.

- Step Response
- Bode, Nyquist
- Hermite-Biehler Analysis
- Roots Region Analysis
- Value Set Analysis
- Nonlinear Uncertainty

Value Set Analysis and Nonlinear Uncertainty tools are based on the references (Matusu&Prokop, 2011; Senol&Yeroglu, 2013) respectively. Next section presents usage of FGATool and the easiness that FGATool brought for the control education world.

4. EXAMPLES ON FGATOOL

As known, Matlab has become a world standard with its analysis tools development environment (Senol et al., 2012). In numerous universities and research laboratories, Matlab is used for symbolic and numerical computations. Although Matlab has strong tools for control systems' analysis, fractional order systems cannot be analyzed with base features of Matlab. Thus, some tools will be needed in this case. This section presents the easiness that FGATool brings for the researchers who are interested in fractional order systems.

Let us consider the following plant with orders of fractional numbers.

$$G(s) = \frac{1}{s^{3.1} + 2s^{2.2} + 2s^{1.1} + 1} \tag{11}$$

It is not possible to build this transfer function with Matlab command *tf()*. However, it is easy to define this plant with FGATool and obtain its step response, Bode, Nyquist and Nichols plots. Figure 4 shows the *Step Response* module of FGATool with the parameter entry for the plant in Eq. 11.

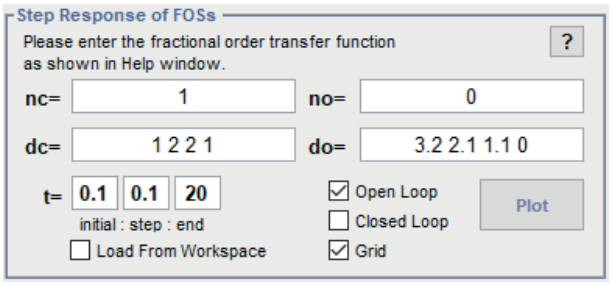

Figure 4: Parameter entry for the plant in Eq. 11.

One can easily obtain the step response of the plant in Eq. 11 by clicking Plot. Figure 5 illustrates the unit step response of Eq. 11 obtained using FGATool.

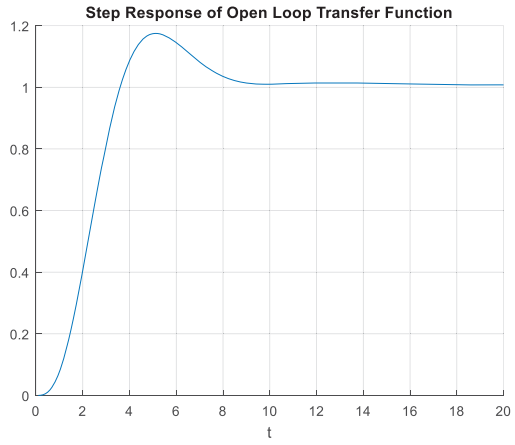

Figure 5: Step response of the plant in Eq. 11.

Characteristic equation of a transfer function should be used in some analysis techniques. Consider the following characteristic equation of the plant in Eq. 11.

$$\Delta(s) = s^{3.1} + 2s^{2.2} + 2s^{1.1} + 2 \tag{12}$$

The Hermite-Biehler Theorem, also known as the interlacing property of Hurwitz polynomials is an effective analysis method developed for classical systems. Its extension for fractional order case can be found in (Senol et al., 2014b). In order to test the interacing property of any system, even and odd parts of its characteristic equation has to be found. The stability condition is to have the roots of even and odd parts placed in the positive complex plane and interlace one by one.

Considering the characteristic equation form in Eq. 5, even and odd parts can be calculated using following equations.

$$\begin{aligned} \Delta^e(j\omega) &= \sum_{i=0}^{n}\left[a_i \cos\left(\frac{\pi}{2}\alpha_i\right)\right]\omega^{\alpha_i} \\ \Delta^o(j\omega) &= \frac{\sum_{i=0}^{n} j\left[a_i \sin\left(\frac{\pi}{2}\alpha_i\right)\right]\omega^{\alpha_i}}{j\omega} \end{aligned} \tag{13}$$

With the help of FGATool, plots of the even and odd parts of Eq. 12 can be drawn easily. Figure 6 illustrates the interlacing roots of even and odd parts of the characteristic equation in Eq. 12.

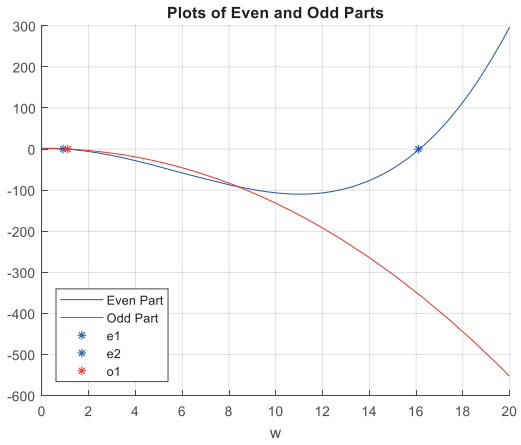

Figure 6: Plots of even and odd parts of Eq. 12.

As the plots of even and odd parts cross the reference line in turn, the fractional order plant in Eq. 11 is stable.

Another analysis method implemented in FGATool investigated the stability by checking the roots placed on the first Riemann sheet (Senol et al., 2014a). The method works on extending the fractional orders of the characteristic equation to integer numbers with a least common multiplier K. For the characteristic equation in Eq. 12, fractional orders can be extended to integer numbers with K=10. Extended integer order form of Eq. 12 is obtained as,

$$\Delta(s^{10}) = s^{31} + 2s^{21} + 2s^{11} + 2 \qquad (14)$$

Now, 31 roots of Eq. 14 can be calculated easily with Matlab *roots()* command. Then, angle values of each root have to be calculated in radians. Stability condition is to have some of the roots in the region $\pi / K < \arg(r_i) < \pi / 2K$ and to have no roots in the region $\pi / 2K < \arg(r_i) < 0$. r_i are the roots calculated from the integer order characteristic equation. This can be checked easily using FGATool. Figure 7 shows the entry of Eq. 14 on FGATool *Roots Region Analysis* module.

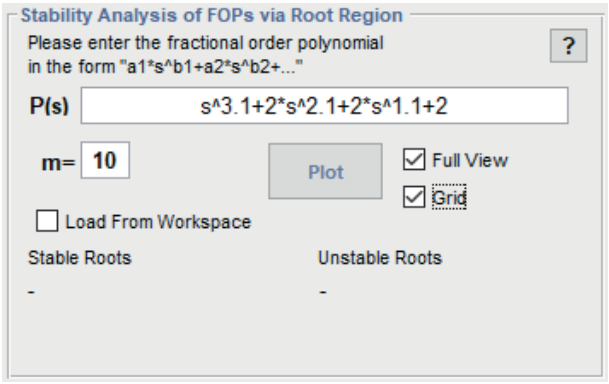

Figure 7: Parameter entry for the characteristic equation in Eq. 12.

Figure 8 illustrates the roots of Eq. 14 placed in the first Riemann sheet. Figure 8shows that there are two roots in the stability region (marked with *) and there is no root in the instability region. Thus, the fractional order plant in Eq. 11 is stable.

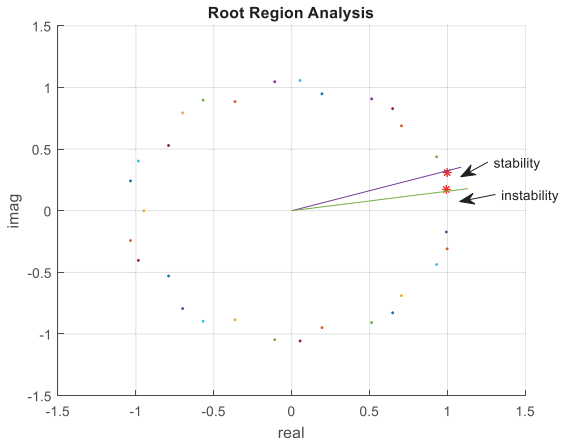

Figure 8: Roots region analysis of the fractional order plant in Eq. 11.

FGATool also includes a module to compute the roots of a fractional order polynomial. Consider the fractional order characteristic equation in Eq. 12. Figure 9 illustrates the parameter entry for *Root Finder* module.

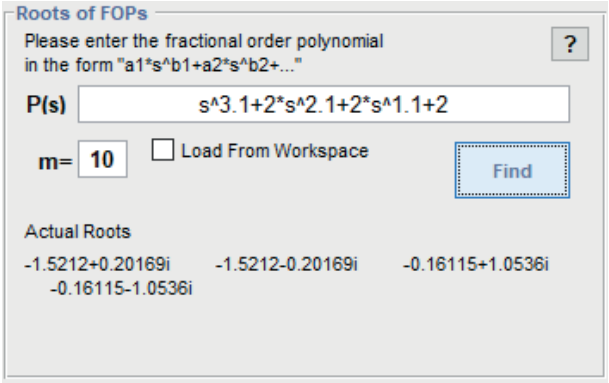

Figure 9: Roots of the characteristic equation in Eq. 12.

As can be seen in Figure 9, roots of Eq. 12 are negative signed. Another feature of FGATool checks the stability of a fractional order polynomial by its *Frequency Properties* module. This module gives the frequency plot of the polynomial. Stability condition is to have the plot start in the positive real axis, move strictly counterclockwise direction and pass $\alpha+1$ regions. α is the order of the polynomial. Frequency plot of the characteristic equation in Eq. 12 is given in Figure 10. It is clear in Figure 10 that the plot provides the stability condition.

Thus, stability of the fractional order plant in Eq. 11 has been analyzed via different methods using FGATool. Researchers and students can freely use FGATool without much knowledge of fractional order calculus and this shows the easiness that FGATool brought to the control world.

Now, let us consider the following fractional order plant with uncertain parameters.

$$G(s) = \frac{1}{s^{3.1} + [1,3]s^{2.2} + [2,3]s^{1.1} + 1} \qquad (15)$$

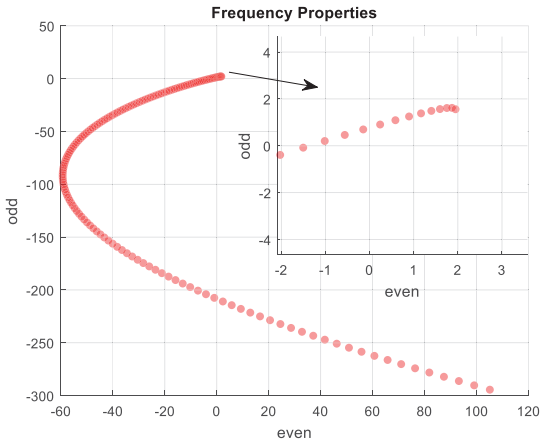

Figure 10: Frequency plot of Eq. 12.

There are two parameters in Eq. 15 that are uncertain. All conditions that the uncertain parameters form have to be investigated. Figure 11 shows the parameter entry for the uncertain plant in Eq. 15.

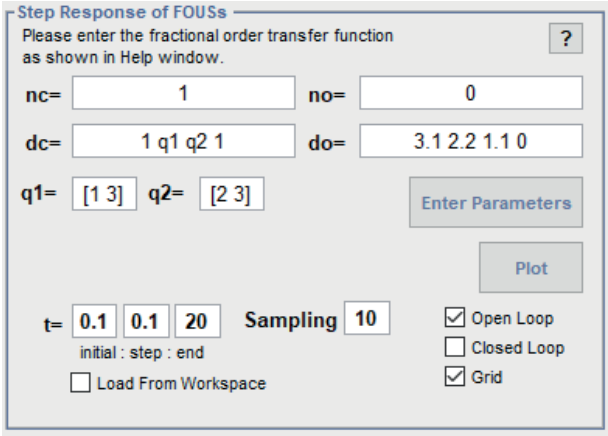

Figure 11: Parameter entry for the uncertain plant in Eq. 15.

Step responses obtained by considering 10 samples on each interval of the uncertain plant in Eq. 15 is illustrated in Figure 12. Roots region analysis considering the roots on the first Riemann sheet can be seen in Figure 13.

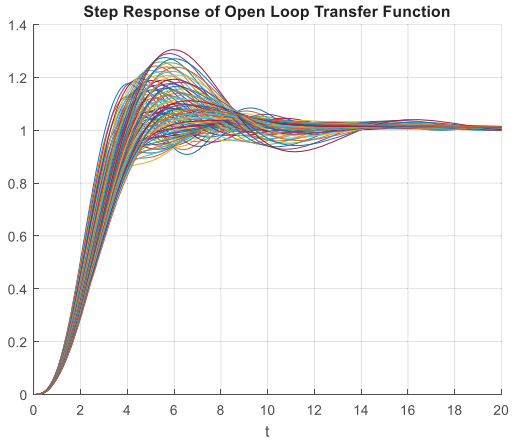

Figure 12: Step responses of the uncertain plant in Eq. 15.

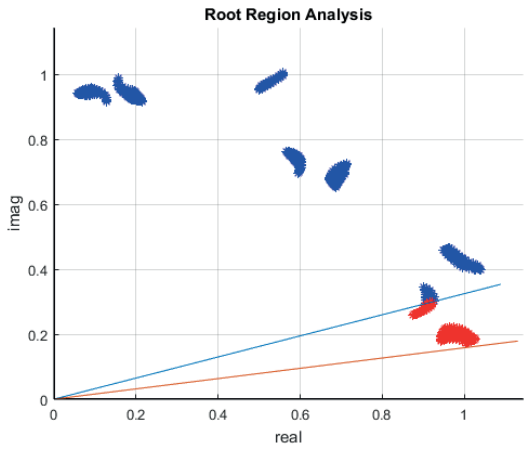

Figure 13: Roots region analysis of the uncertain plant in Eq. 15.

It is clear from Figure 12 and Figure 13 that the fractional order plant in Eq. 15 satisfies the stability criterion with its changing parameters.

5. CONCLUSION

This paper aims on a study to develop a computer interface to help student achievement in fractional order control education. However fractional order calculus describes real world processes better then classical case, its mathematical background may not be easy for student understanding. Education process for fractional order calculus will be improved with the help of easy to use computer interfaces. FGATool, a graphical analysis tool for fractional order systems with fixed and uncertain parameters is brought to the literature in this paper. This tool is thought to be useful for researchers and student who are interested in fractional order world.

REFERENCES

Azar, A. T., Sundarapandian, V. and Adel O. (2017). Fractional order control and synchronization of chaotic systems, vol. 688, Springer.

Baleanu, D. et al., (2016). Fractional calculus: models and numerical methods, vol. 5. World Scientific.

Caponetto, R., Dongola, G., Fortuna L. and Petras I. (2010). Fractional Order Systems, Modeling and Control Applications, World Scientific, Singapore.

Martin, C. And Miloš, S. (2006). PID controller design on Internet: www.PIDlab.com, Department of Cybernetics, University of West Bohemia in Pilsen.

Matusu, R. and Prokop, R. (2011). Graphical analysis of robust stability for systems with parametric uncertainty: an overview, Transactions of the Institute of Measurement and Control, vol. 33 (2), pp. 274–290.

Monje, C. A., Chen, Y. Q., Vinagre, B. M., Dingyü, X. and Feliu, V. (2010). Fractional-order systems and controls, Springer, New York.

Oustaloup, A. (1991). La Commande CRONE: Commande Robuste d'Ordre Non Entier, Hermes.

Senol, B. (2017). FGATool for Time and Frequency Analysis of Systems with Uncertainties, International Conference on Artificial Intelligence and Data Processing (IDAP17).

Senol, B. and Yeroglu, C. (2013). Frequency boundary of fractional order systems with nonlinear uncertainties, Journal of the Franklin Institute, vol. 350 (7), pp. 1908-1925.

Senol, B. and Yeroglu, C. (2015a). Kesir Dereceli Sistemlerin Grafiksel Analiz Arayüzü, Otomatik Kontrol Türk Milli Komitesi Toplantısı 2015 (TOK15).

Senol, B., Ates, A., Alagoz, B. B. and Yeroglu, C. (2014a). A numerical investigation for robust stability of fractional-order uncertain systems, ISA Transactions, vol. 53 (2), pp. 189-198.

Senol, B., Matušů, R. and Gul, E. (2017). Fractional Order Stability of Systems, International Conference on Artificial Intelligence and Data Processing (IDAP17).

Senol, B., Yeroglu, C. and Erturkler M. (2012), Development of a User Friendly Toolbox for Advanced Control Education, 2012 International Conference on Fractional Differentiation and its Applications (ICFDA).

Senol, B., Yeroglu, C. and Tan, N. (2014b). Analysis of Fractional Order Polynomials Using Hermite-Biehler Theorem, 2014 International Conference on Fractional Differentiation and its Applications (ICFDA).

Şenol, B. and Yeroğlu, C. (2015b). Kesir Dereceli Belirsiz Sistemler İçin Dayanıklı Analiz Araçlarının ve Arayüz Programlarının Geliştirilmesi, Ph. D. Thesis, www.bilalsenol.com.

Tepljakov, A. (2017) Fractional Order Modeling and Control (FOMCON), www.fomcon.net.

Valerio, D. (2005) Ninteger v. 2.3 Fractional control toolbox for MatLab, http://web.ist.utl.pt/~duarte.valerio.

Xue, D., Chen, Y. Q. and Atherton, A. (2007). Linear Feedback Control: Analysis and Design with MATLAB, SIAM Press.

Yeroglu, C. and Senol, B. (2013). Investigation of robust stability of fractional order multilinear affine systems: 2q-convex parpolygon approach, Systems & Control Letters, vol. 62 (10), pp. 845-855.

MÜHENDİSLİK FAKÜLTESİ

Uluslararası Mühendislik Araştırma ve Geliştirme Dergisi

International Journal of Engineering Research and Development

Cilt/Volume:9 Sayı/Issue:3 Aralık/December 2017 https://doi.org/10.29137/umagd.348636

Araştırma Makalesi / Research Article

Design of a New Bed Base Mechanism System

Hüseyin Mutlu *[1], Burak Emre YAPANMIŞ [2]

[1]Mersin University, Faculty of Engineering, Mechanical Engineering, 33110, MERSİN
[2]Mersin University, Faculty of Engineering, Mechanical Engineering, 33110, MERSİN

Başvuru/Received: 08/10/2017 **Kabul/Accepted**: 01/12/2017 **Son Versiyon/Final Version**: 26/12/2017

Abstract

In daily life, most of the devices, machines and furniture, which we use in our homes and make our life easier, have many different opening and closing systems. Some criteria may be required for the opening/closing shape of systems. For example, in some systems, it may be desirable that opened part uses minimum volume, facilitates daily life, or the system is balanced in each opening position. Those type of opening and closing systems are widely used sofa beds, seats and bed bases in the furniture sector. Many opening/closing systems have various locking mechanisms which are used to ensure opened final position or in some cases it is held in the final position by the force of the human arm. In this study, a kinematic analysis was carried out to design a base mechanism which could be stabilized at every position instead of the final position, and a virtual prototype was made.

Key Words

Bed-base mechanism, Kinematic analysis, Virtual prototyping, Galerkin method

hmutlu@mersin.edu.tr

1. INTRODUCTION

Weights, which rotate around an axis, are used in household goods, in the automotive sector and a lot of machines, tools, devices in industry life because of various reasons. The door of the dishwasher, oven's door, freezers whose doors are opened from the upper side, bonnet and trunk lid of the car can be shown as examples. In addition, it is also possible to encounter such caps in many applications. In some of the applications, the cap is ensured final position with the force of the human arm while in some of the applications caps remain the final position thanks to some mechanism. This process is done with the aid of a rod or a kind of guy wire after opened bonnet of the car. For some of the bed base mechanism, it is still used the human arm for the end position. It can be an accident which can cause injury or death in manual position balance applications which include heavy caps. In addition, lifting heavy caps with the human arm is not a desirable situation for human nowadays.

In this study, a new mechanical design has been improved to ensure that each position in the cap is statically balanced. The designed system is basically based on the principle that the amount of potential energy saved or lost by weight of the system is stored in the spring or returns to the system by the spring. In order to keep balance in every position of the system, change of the potential energy of the system must be equal to the change of the elasticity energy of the spring. The functional relationship between the changing of potential energy of the system and the changing of elastic energy in spring is not linear. That's why a mechanism is needed to ensure this relationship. In this work, crank and connecting rod mechanism, whose part count is less, are selected to obtain a linear function. The angular rotation of the system to be balanced is transferred to the crank arm. This angular rotation is transferred from the piston which is last part of slider-crank mechanism to spring as a linear motion. This transfer is carried out according to a transfer function depending on the kinematic dimensions of the slider-crank mechanism. If the transfer function is determined according to the relation between the weight of the system and energy of the spring, the system will be balanced. This is possible by the selection of the kinematic dimensions of the slider-crank mechanism properly. The determination of the mechanism dimensions according to the functional relationship between the input and output parts is called function synthesis in Andrew, Murray and Myszka (2017), Kafash and Nahvi (2017), Chavan, and Joshi (2010), Norton (2002).

There are two approaches to solving the problem of function generation. The first, investigation of the mechanisms that generate the desired function without errors. The second is to find the unknown parameters of the mechanism that can generate the desired function in an acceptable approximation. The number of mechanisms which generate the desired function is limited, this obstacle is mentioned in Artobolevskii (1975). It is difficult to produce accurate results because of the complexity of the algorithm. It is more logical to use approximate synthesis methods instead of exact synthesis because the investigation of the mechanism which generates function without error is both expensive and difficult.

Graphical approaches have been used to find solutions for the synthesis problems due to the fact that mathematical relations between the input and output part of the mechanics are very complicated. However, graphical method solutions, which can be examined in Darina, Peter and Gabriel (2016),are a long way to go for each new data. Computers have provided the opportunity to develop many analytical methods in the problem of function generation. The common point of many analytical methods developed is to minimize the difference between the desired function and the function generated by the mechanism. The methods have different names like galerkin, least square, accuracy points according to the mathematical approaches used when the error function is minimized. Bahmyari, Khedmati and Soares (2017) is example for galerkin method; Akcali and Dittrich (1989), Ramírez, Nogueir, Khelladi, Chassaing and Colominas (2014) can be given as example for the least squares method; for accuracy point method Diab and Smaili (2008), Jaiswal and Jawale (2017) can be shown.

2. MATERIALS AND METHOD

In this study, analytical solution method is used to design the slider-crank mechanism according to the function synthesis. Then simulation of the bed base mechanism is performed.

2.1. Mathematic Model of Equilibrium Mechanism

The kinematic diagram and parameters of the mechanism that rotates around a certain axis and self-balancing at each position are shown in Figure 1. In order to the weight of the system passing through from θ_0 angular position to any θ angular position can be statically balanced by means of a linear spring, the sum of the elastic energy in the spring and the potential energy of the weight at two positions as θ_0 and θ should be equal to each other in Equation 1.

$$Wl\sin\theta_0 + \frac{1}{2}kx_0^2 = Wl\sin\theta + \frac{1}{2}kx^2 \quad (1)$$

Here, k is the spring constant, x_0 is the amount of elongation at θ_0 angular displacement, x is the amount of elongation at θ angular displacement. Equation 1 can be written as Equation 2.

$$Wl(\sin\theta_0 - \sin\theta) = \frac{1}{2}k(x^2 - x_0^2) \tag{2}$$

If x is left alone in Equation 2, in Equation 3 can be obtain.

$$x = \sqrt{x_0^2 + \frac{2Wl}{k}(\sin\theta_0 - \sin\theta)} \tag{3}$$

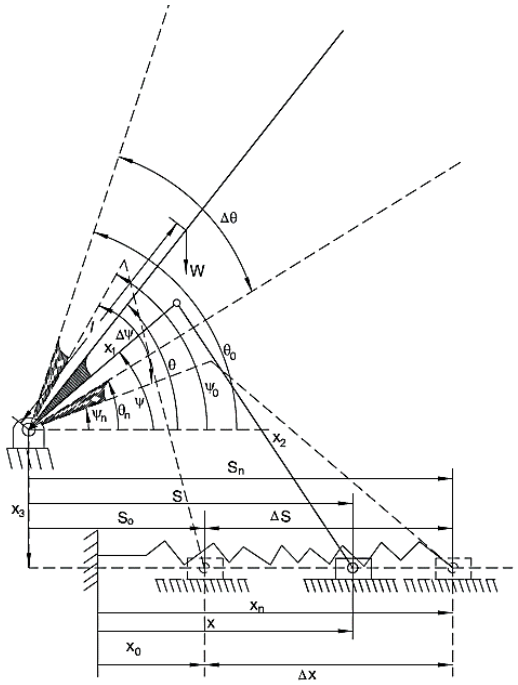

Figure 1. Kinematic parameters of equilibrium mechanism

Slider-crank mechanism design in Figure 1 have been carried out using the following inputs:

x_0: The amount of elongation in the spring when the object to be balanced is in the initial position (mm).
W: Weight of object to be balanced (Newton).
l: Distance from the axis of rotation of the object to the center of gravity (mm).
k: Linear spring coefficient (Newton/mm).
θ_0: The angle between the center of gravity and the axis passing through the axis of rotation, (degree).
$\Delta\theta$: Angular motion amount of object to be balanced (degree).

Kinematic dimensions of the slider-crank mechanism are x_1, x_2, x_3 and s_0 are shown in Figure 1. These parameters definition are as follows:

x_1: Crank length of slider-crank mechanism (mm).
x_2: Connecting rod length of slider-crank mechanism (mm).
x_3: Vertical distance between crankshaft joint point and piston (mm).
ψ_0: Initial angle of the crank rod (degree).
s_0: Horizontal distance between crankshaft joint point and piston joint point (mm).

Equation 3 is valid provided that $\theta_0 > \theta > \theta_n$. Slider-crank mechanism is settled on the purpose of elongation of linear spring, it is shown in Figure 1. The relationship between the angular rotation ψ of the input arm of the mechanism and the linear displacement s of the output arm is as follows:

$$s = f(\psi), \quad \psi_0 \geq \psi \geq \psi_n \tag{4}$$

The following equations always apply for Equation 3 and Equation 4.

$$\Delta x = \Delta s;\ \ \Delta\theta = \Delta\psi$$
$$\Delta x = x_n - x_0;\quad \Delta s = s_n - s_0 = x(\theta_n) - x(\theta_0) \tag{5}$$

If the kinematic dimensions of the slider-crank mechanism are determined in such a way that the difference of the functional changes between Equation 3 and Equation 4 is minimized, self-balance will be possible to in every position.

2.2. Designed Slider-Crank Mechanism

Function synthesis of slider-crank mechanism are performed according to functional relation between rod angle (ψ) with displacement of piston (s). Design parameters of slider-crank mechanism are represented in Figure 2. Here, x_1 is the length of the crank, x_2 is the length of the rod, x3 is the vertical distance from of piston to the crank pin center, ψ is the crank arm's motion start angle and s0 is the perpendicular distance from the piston to the $A0_1$ line. Two different functions can be mentioned in the design of the slider-crank mechanism. The firstly, it is the functional relationship between the arm's rotate angle (ψ) and linear displacement of the piston (s). The other is a relation between the arm's rotate angle (ψ) and horizontal angle of connecting rod (δ). In this study, ψ-s functional relation is concerned. As shown in Figure 2, the squares of the vectorial expression are written from the AO_1BC loop and horizontal angle of the connecting rod is eliminated as a result the following equation;

$$x_1^2 - 2sx_1 Cos\psi + 2x_1x_3 Sin\psi + x_3^2 + s^2 - x_2^2 = 0 \tag{6}$$

Relation between connecting rod angle with function variable and relation between displacement of the piston with function dependent variable can be written as;

$$\psi = \psi_0 + \psi';\qquad \psi' = R_x(x - x_0);\qquad R_x = \frac{\Delta\psi}{\Delta x}$$
$$s = s_0 + s';\qquad s' = R_y(y - y_0);\qquad R_y = \frac{\Delta s}{\Delta y} \tag{7}$$

In Equation 7, $\Delta\psi=\psi_n+\psi_0$, $\Delta s=s_n+s_0$ are crankshaft and piston operating range, respectively, $\Delta x=x_n+x_0$, $\Delta y=y_n+y_0$ are amount of changes of dependent and independent variable.

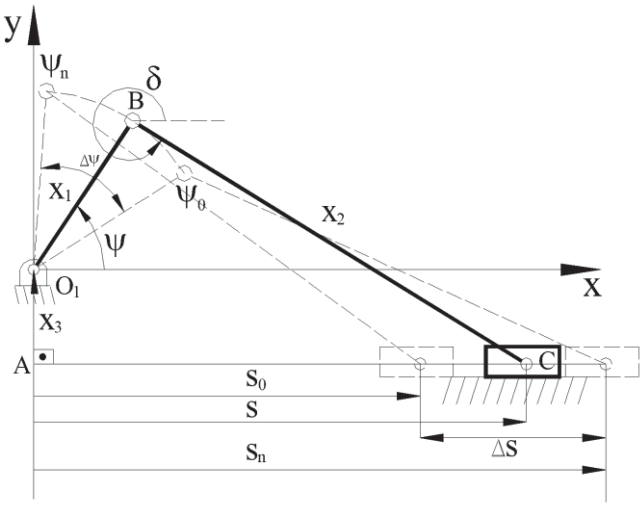

Figure 2. Slider-crank mechanism parameters

If Equation 7 is substituted in Equation 6, equation of motion is obtained such as G($s_0, \psi_0, x_1, x_2, x_3, x, y$).

$$2s's_0 + s'^2 + Z_3(Sin\psi_0 Cos\psi' + Cos\psi_0 Sin\psi') + Z_1(-s_0 Cos\psi_0 Cos\psi' + s_0 Sin\psi_0 Sin\psi'$$
$$- s'Cos\psi_0 Cos\psi' + s'Sin\psi_0 Sin\psi') + Z_2 = 0 \tag{8}$$

In Equation 8, $Z_1 = 2x_1;\quad Z_2 = x_1^2 + x_3^2 + s_0^2 - x_2^2;\quad Z_3 = 2x_1x_3$. Equation 8 can be converted five unknown nonlinear equations that can be calculated according to Subspace, Galarkin and the other methods are as follows:

$$(a_i s_0 + g_i) + Z_3(c_i Sin\psi_0 + b_i Cos\psi_0) + Z_1(-c_i s_0 Cos\psi_0 + b_i s_0 Sin\psi_0 - d_i Cos\psi_0 + e_i Sin\psi_0) + f_i Z_2 = 0 \quad i = 1,2,3,4,5 \tag{9}$$

In this work, Galarkin method is prefered. (ai, bi, ci, di, ei, fi, gi) coefficients are calculated according to Galerkin method as follows.

$$a_i = 2\int_{x_0}^{x_n} s' w_i(x)dx; \quad b_i = \int_{x_0}^{x_n} Sin\psi' w_i(x)dx; \quad c_i = \int_{x_0}^{x_n} Cos\psi' w_i(x)dx; \quad d_i = \int_{x_0}^{x_n} s' Cos\psi' w_i(x)dx$$
$$e_i = \int_{x_0}^{x_n} s' Sin\psi' w_i(x)dx; \quad f_i = \int_{x_0}^{x_n} w_i(x)dx; \quad g_i = \int_{x_0}^{x_n} s'^2 w_i(x)dx \qquad i = 1,2,3,4,5 \tag{10}$$

Equation 9 is rearranged and Z_1,Z_2,Z_3 are eliminated thus Equation 9 obtain depend on ($\tan\psi_0$) and (s_0).

$$a_{pk} s_0^2 + (b_{pk} + c_{pk}\cos 2\psi_0 + d_{pk}\sin 2\psi_0)s_0 + e_{pk} + f_{pk}\cos 2\psi_0 + g_{pk}\sin 2\psi_0) = 0 \quad k = 1,2 \tag{11}$$

Coefficients in Equation 11 can be calculated by computer-aided mathematics programs. If s_0 is eliminated and ψ_0 is applied mathematical manipulation which is performed in Akcali and Mutlu (2006), 12 th-degree polynomial can be obtained as follows:

$$w_0 + w_1 t + w_2 t^2 + w_3 t^3 + w_4 t^4 + w_5 t^5 + w_6 t^6 - w_5 t^7 + w_4 t^8 - w_3 t^9 + w_2 t^{10} - w_1 t^{11} + w_0 t^{12} = 0 \tag{12}$$

wi i=1,2.,...,6 in Equation 12 can be calculated computer aided mathematics. Here, t= $tan\frac{\psi_0}{2}$. There are twelve solutions of the ψ_0.

$$\psi_{oi} = 2\ arctan\ t_i; \quad i = 1,2....,12 \tag{13}$$

If s_0^2 is eliminated in Equation 11, s_0, x_1, x_2, x_3 can be written as follows for i=1,2,….,12;

$$s_{oi} = -\frac{a_{p1}e_{p2} - a_{p2}e_{p1} + (a_{p1}f_{p2} - a_{p2}f_{p1})\cos 2\psi_{0i} + (a_{p1}g_{p2} - a_{p2}g_{p1})\sin 2\psi_{0i}}{a_{p1}b_{p2} - a_{p2}b_{p1} + (a_{p1}c_{p2} - a_{p2}c_{p1})\cos 2\psi_{0i} + (a_{p1}d_{p2} - a_{p2}d_{p1})\sin 2\psi_{0i}}; i = 1,.,12 \tag{14}$$

$$x_{1i} = \frac{Z_{1i}}{2} \quad i = 1,2,....,12 \tag{15}$$

$$x_{3i} = \frac{Z_{3i}}{2x_{1i}} \quad i = 1,2,...,12 \tag{16}$$

$$x_{2i} = \sqrt{x_{1i}^2 + x_{3i}^2 + s_{0i}^2 - Z_{2i}} \quad i = 1,2,..,12 \tag{17}$$

Z_{1i}, Z_{2i}, Z_{3i} are any term depend on a,b,c,d,e,f,g coefficients. Those values can be calculated automatically by created software program.

2.3. Design of Balancing Mechanism

Various kinematic dimensions of the slider-crank mechanism have been obtained with the help of input parameters. Among the results obtained, the best in terms of functioning error and size ratios were researched. In addition, the dimensions of the slider-crank mechanism must be compatible with the volume constraint of bed base sizes to be installed. For this purpose, kinematic dimensions of the slider-crank mechanism can be obtained by computer program after entering the input parameter. The parameters that are easiest to change by the designer are the spring coefficient (k) and the initial elongation amount (x_0) at the spring. In computer aided numerical works, as the spring constant (k) and the initial elongation amount (x_0) were increased, the arm lengths of the slider-crank mechanism decreased. As a result, the most suitable design dimensions were determined with the help of computer program.

The design results obtained in this study were determined by taking into consideration the physical dimensions and mass of the bed base. According to this, the physical parameters of the bed base input to the computer program are determined as follows:

Cap weight = 40 kg
Cap weight (W) = 392.4 N
Place of weight center (l) = 1000 mm
Initial angle of cap (θ_0) = 70^0
Required minimum angle for balance (θ_n) = 10^0
Cap work range ($\Delta\theta$) = 60^0
Selected spring coefficient (k) = 8.240 N/mm
Selected first extension amount (x_0) = 100 mm

After using input parameter, most appropriate slider-crank mechanism dimensions in Figure 1 are obtained as follows:

x_1 = -117.7 mm; x_2 = 103.8 mm; x_3 = -112.4 mm; ψ_0= -53.70; s_0 = -172.0 mm; Δs =115.6 mm

Changing of function error of slider-crank mechanism according to the angle range of cap is shown in Figure 3. This graph shows the difference between the theoretical spring elongation in Equation 3 and the spring elongation amount performed by the mechanism. As shown in Figure 3, the functional error varies uniformly from about 0.025 mm to 0.030 mm.

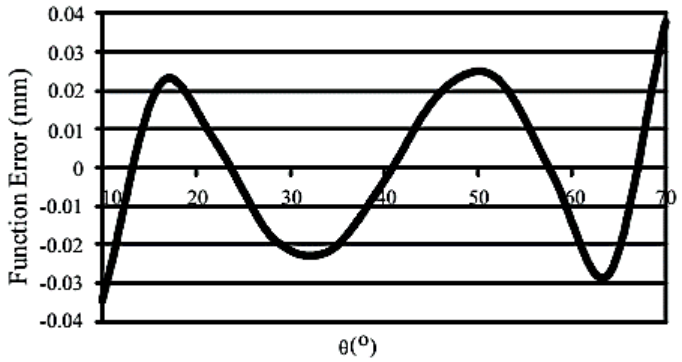

Figure 3. Functional error changing

The difference between the theoretical F force that balances the designed mechanism and the actual force (F_y) produced by the spring shows the success of the balancing. For this calculation, the external forces acting on the mechanism at any position in the working range of the slider-crank mechanism in Figure 1 can be written as:

$$W\delta h + F\delta s = 0 \tag{18}$$

To obtained the relation between the force F and the kinematic parameters of the mechanism, the following expression can be written from the loop equations of the slider-crank mechanism.

$$\frac{\delta s}{\delta \psi} = \frac{2x_1x_3\cos\psi + 2x_1 s\sin\psi}{2x_1\cos\psi - 2s} \tag{19}$$

In here, $h = l\sin\theta, \quad \delta h = l\cos\theta\,\delta\theta, \quad \delta\psi = \delta\theta$. F force can be written as following:

$$F = \frac{Wl\cos\theta(x_1\cos\psi - s)}{x_1x_3\cos\psi + x_1 s\sin\psi} \tag{20}$$

There is need an expression such as $s = f(\psi)$ in Equation 20. From the loop equation of mechanism, s can be written as follows:

$$s = \frac{-B \pm \sqrt{B^2 - 4AC}}{2A} \tag{21}$$

$$A = 1; \quad B = -2x_1\cos\psi; \quad C = x_1^2 + x_3^2 - x_2^2 + 2x_1x_3\sin\psi; \tag{22}$$

The real force F_y, as opposed to the theoretical force F which provides the equilibrium in Equation 20, as follows:

$$F_y = -k(x_0 + s - s_0) \tag{23}$$

The error E of the balancing force is given below:

$$E = F - F_y \tag{24}$$

Chancing of the error according to θ is shown in Figure 4.

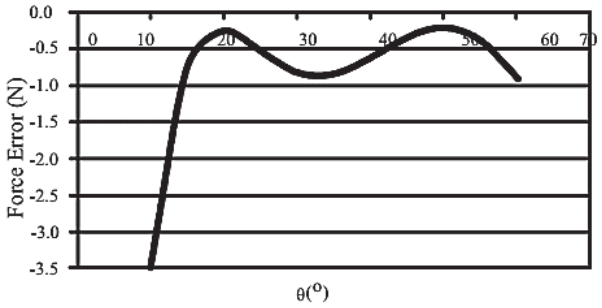

Figure 4. Balancing force error graph

As it is seen in Figure 4, the force error is maximum at the first and last position of the mechanism. Nevertheless, it does not exceed ± 0.5 N in a very wide range. It is seen on the virtual model that these differences, which are quite small, are damped by the friction forces in the bearings. The balancing mechanism obtained from the equations above has been assembled as in Figure 5. Number 1 represent to bed base, number 2 is the cap of the bed base, number 3 is designed the mechanism and number 4 is linear spring used in mechanism.

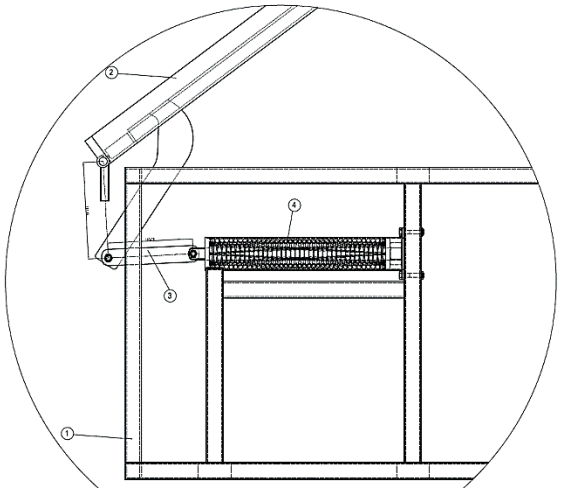

Figure 5. Inside view of the balancing mechanism

Figures 6 and 7 show the change in angular velocity and angular position of the cap when the cap is in the closed position when a person who wants to open the cap applies a force of about 36 N for 1 second to the cap. As it can be seen in Figure 6, when the cap is subjected to a force of 36 N for 1 second, the cap reaches a maximum angular velocity of 30 deg/s after 1 second. When the force is removed, the angular velocity of the cap reaches zero at about 1.1 seconds, it stabilizes itself. Meanwhile, it can be seen in Figure 7 which the cap makes an angular displacement of about 40°. The simulated images of the bed base mechanism in Figure 8 are shown.

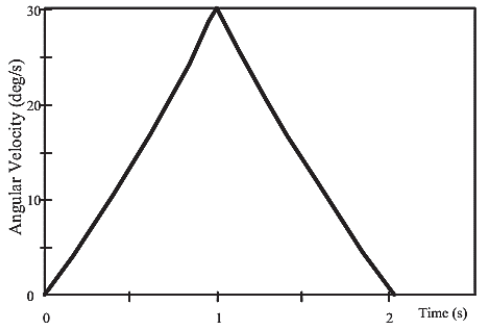

Figure 6. Change of Angular Velocity of Cap by Time

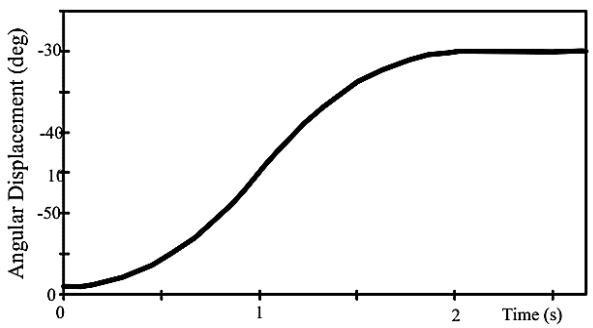

Figure 7. Change of Angular Position of Cap by Time

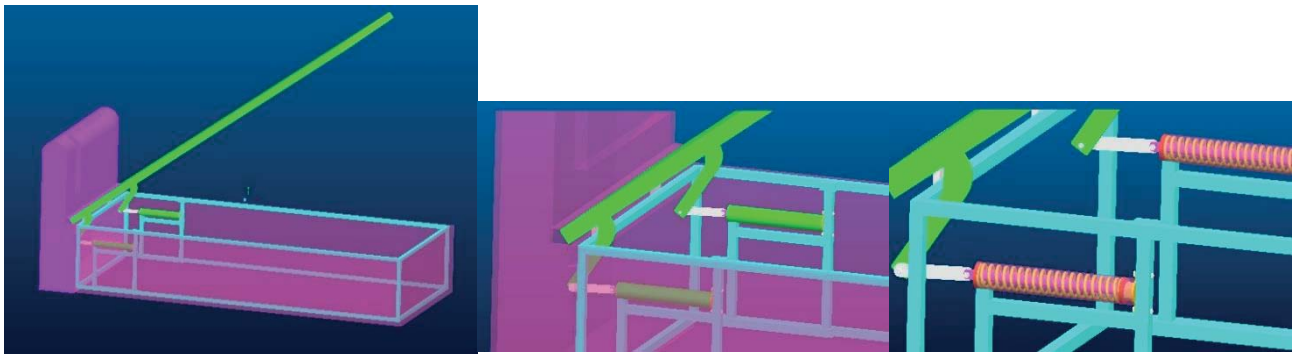

a) b) c)

Figure 8. a) bed base image b) balancing mechanism c) inside view of the balancing mechanism

3. RESULTS

The main feature of bed base that the moving the bed part and using the other part of the bed base efficiently. However, it is necessary the human arm power because of the weight of the cap of the bed base when it is opening/closing. In addition, stabilization is a very important topic for this systems.

In this work, the new bed base mechanism is designed according to balance every position. The designed system has consisted of spring and slider-crank mechanism. If the potential energy changing of the cap of the bed base is equal to elastic energy of spring, it is possible to stabilization of the cap of the bed base in every position. The balancing system for the bed bases is analytically created. Conformity of the solid model of the designed mechanism to actual operating conditions was carried out by using the SimWise 4D software. In the model, spring, the mechanism parts, the coefficient of friction between the rotary joints, the rotary and sliding joints between the members are defined in accordance with the actual working conditions. In the experiments made on the model, it was seen that the cap bed base performance has a big harmony according to the theoretical results. Moreover, if the cap is manually reach to the desired position and then release, it is observed the cap balances itself in the computer-based experiments.

In current systems, it needs to very much human power for the opening of cap and closing it when it opened. This phenomenon is getting hard to use current system in daily life. Thanks to the newly designed system, more than 40 kg weight of the bed can be opening/closing easily with less than 1 kg human force owing to weight balancing. Therefore, using bed-base system is more easy and safe via the new system.

ACKNOWLEDGEMENTS

This study was supported by The Scientific and Technological Research Council Of Turkey as 1507 - SME RDI (Research, Development & Innovation) Grant Programme project (7070056).

REFERENCES

Akcali, I., Dittrich, G. (1989). Function generation by Galerkin's method. Mech. Mach. Theory. 24(1), 39–43.

Akçali, I., Mutlu, H. (2006). A Novel Approach in the Direct Kinematics of Stewart Platform Mechanisms with Planar Platforms. ASME INTERNATİONAL, 128, 252-252.

Andrew H. A., Murray P. Myszka D. H. (2013). The Synthesis of Function Generating Mechanisms for Periodic
Artobolevskii, (1975). Mechanisms In Modern Engineering Design, Mir Publishers, MOSCOW.

Bahmyari E., Khedmati M. R., Soares C. G. (2017). Stochastic analysis of moderately thick plates using the generalized polynomial chaos and element free Galerkin method. Engineering Analysis with Boundary Elements, 79, 23–37.

Curves Using Large Numbers of Double-Crank Linkages. J. Mechanisms Robotics. 9(3), 1-8.

Darina H., Peter F., Gabriel B. (2016). Kinematical Analysis of Crank Slider Mechanism with Graphical Method and by Computer Simulation American Journal of Mechanical Engineering, 4, 329-343. doi: 10.12691/ajme-4-7-18.

Diab, N., Smaili, A. (2008). Optimum exact/approximate point synthesis of planar mechanisms. Mech. Mach. Theory 43(12), 1610–1624.

Jaiswal A., Jawale H. P. (2017). Comparative study of four-bar hyperbolic function generation mechanism with four and five accuracy points. Archive of Applied Mechanics, 12, 2037–2054.

Kafash S. H., Nahvi, A. (2017). Optimal synthesis of four-bar path generator linkages using Circular Proximity Function. Mechanism and Machine Theory, 115, 18-34.

Norton, R. L. (2002). Cam Design and Manufacturing Handbook. Industrial Press, New York.

Ramírez L., Nogueir X., Khelladi S., Chassaing J. C., Colominas I. (2014). A new higher-order finite volume method based on Moving Least Squares for the resolution of the incompressible Navier–Stokes equations on unstructured grids. Computer Methods in Applied Mechanics and Engineering, 278, 883–901.

U.S. Chavan, S.V. Joshi. (2010). Synthesis and analysis of coupler curves with combined planar cam follower mechanisms. International Journal of Engineering, Science and Technology 2, 6, 231-243.

MÜHENDİSLİK FAKÜLTESİ

Uluslararası Mühendislik Araştırma ve Geliştirme Dergisi

International Journal of Engineering Research and Development

Cilt/Volume:9 Sayı/Issue:3 Aralık/December 2017 https://doi.org/10.29137/umagd.346154

Araştırma Makalesi / Research Article

The Optimization of Solar Water Heating System Using Hybrid Algorithm (PSO/HJ) for Different Locations of Turkey

Kaan Yaman[1], Gökhan Arslan[*1]

[1]*Mersin University, Faculty of Engineering, Department of Mechanical Engineering, Çiftlikköy, 33343, Mersin, TURKEY*

Başvuru/Received: 08/10/2017 **Kabul/Accepted**: 01/12/2017 **Son Versiyon/Final Version**: 26/12/2017

Abstract

In this study, optimum dimensions of Solar Domestic Hot Water System (SDHWS) were determined according to initial capital cost and energy consumption cost in different locations of Turkey. Typical Meteorological Year (TMY) data of 12 different locations which represent climatic characteristics of Turkey were used. Analysis was performed by using Particle Swarm Optimization / Hooke-Jeeves (PSO/HJ) hybrid algorithm which is a part of EnergyPlus®-GenOpt® programs. For each location, optimum number of solar collectors and hot water storage tank volume was determined. Initial investment and energy consumption costs decreased 6.1% for Gaziantep whereas solar fraction increased 42.8% for Ankara. In average, 4.5% decrease in initial investment and energy costs and 35.4% increase in solar fraction were obtained.

Key Words

"Solar energy, domestic hot water, optimization, hybrid algorithm."

** garslan@mersin.edu.tr*

1. INTRODUCTION

Global warming, climate change, and the greenhouse effect, as well as the rise in energy prices, have become popular nowadays. According to the International Energy Agency 2014 data, the capacity of solar water heating systems (SDHWS) worldwide is 410.2 GW, whereas in Turkey, about 9.4 GW of thermal energy was produced by SDHWS in 2015 according to the General Directorate of Energy Affairs (Mauthner et al., 2014; MENR, 2017). Increasing these values with future work is key to reduce dependence on fossil fuels and related emissions.

In the literature, various SDHWS design and optimization methods have been proposed and discussed. Many researchers were conducted design and optimization of SDHWS for solar fraction (Skerlić et al., 2013; Bernardo, 2013), life cycle cost (Atia et al., 2012; Ko, 2015), life cycle savings (Araya et al., 2017), and payback period (Kim et al., 2012). Some important related works are as follows: Kalogirou (2004) proposed an approach that can be used with artificial neural networks and genetic algorithm (GA) to design and optimize various SDHWS. The optimal collector area and storage tank volume were determined for life cycle savings (Kalogirou, 2004). Hobbi and Siddiqui (2009) obtained optimal solutions by parametric approach for many decision variables such as collector area, fluid type and mass flow rate, storage tank volume, heat exchanger effectiveness, collector's aspect ratio, diameter and length of connection pipe. Recently, Araya et al. (2017) implemented an SDHWS optimization method by using GA that provides life cycle savings to 182 locations in Chile and 6 consumption profiles. Karaçavuş (2017) investigated the optimal storage tank volume, collector tilt and area for Turkey's limited number of climatic regions (Ankara, Edirne, Hakkari, İzmir, and Trabzon).

SDHWS requires careful examination of its thermal and economic performance. However, it is propounded that climate has an important effect on system performance. Thus, this paper focused to increase the number of related studies on SDHWS design and optimization. In this regard, a methodology was presented to optimize the life cycle cost of an SDHWS. In order to determine the effect of different climatic conditions, this methodology was implemented in different climatic regions of Turkey.

The remainder of the paper is organized as follows. In Sect. 2, the background of the simulation and optimization method is explained. In Sect. 3, the validation of the model is demonstrated. In Sect. 4, model results are presented and discussed. Finally, the paper concludes with inferences in Sect. 5.

2. MATHEMATICAL MODEL

SDHWS performance is affected by many parameters: solar radiation, ambient temperature, collector and tank characteristics and constructions etc. For the simulation-optimization, a mathematical model of an SDHWS was established.

2.1. Reference climatic conditions

To evaluate the impact of the climate on the performance of the SDHWS, 12 regions representing the general climate of Turkey were selected, including Ankara, Bursa, Çanakkale, Erzincan, Gaziantep, Istanbul, Izmir, Kayseri, Konya, Malatya, Mersin, and Muğla. The typical meteorological year (TMY) weather files (resolution 1 h) were used for these regions. In Table 1, coordinates of the locations are summarized.

Table 1. Coordinates of the locations.

Locations	Latitude (°N)	Longitude (°E)	Altitude (m)
Ankara	40.0	32.9	902
Bursa	40.2	29.1	100
Çanakkale	40.1	26.4	3
Erzincan	39.7	39.5	1215
Gaziantep	37.1	37.4	855
Istanbul	41.0	29.1	33
Izmir	38.4	27.2	25
Kayseri	38.8	35.4	1054
Konya	38.0	32.6	1028
Malatya	38.4	38.1	849
Mersin	36.4	33.9	15
Muğla	37.2	28.4	646

2.2. SDHWS description

Optimization problem which considered to provide domestic hot water (DHW) demand of single family is an actual SDHWS. The schematic view of the basic components of the system is shown in Fig. 1.

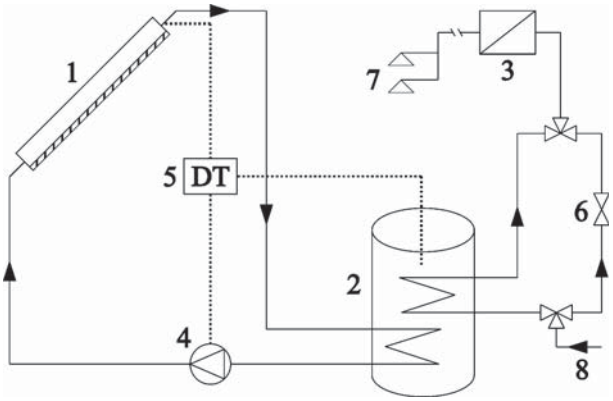

Fig. 1. Actual SDHWS: (1) flat-plate collector, (2) storage tank, (3) instantaneous water heater, (4) circulation pump, (5) differential thermostat, (6) tempering valve, (7) load, and (8) mains water.

The system is typically closed loop and consists of a flat-plate solar collector, a hot water storage tank and a circulation pump. The system meets the energy demand with natural gas in case solar energy is inadequate. In addition, the system is equipped with a differential thermostat (DT) that operates according to the solar collector output and storage tank temperature difference. Thus, if the temperature difference is higher than 5 ºC, then the circulating pump starts and stops when that difference is below 2 ºC. Energy analysis for each component of the system was performed with EnergyPlus (v8.4) software. The thermal efficiency of the collector is described using the Hottel-Whillier-Bliss equation (ASHRAE, 2001).

$$\eta = a_0 K_\theta - a_1 \frac{\left(T_{in,SC} - T_{amb}\right)}{I_{solar}} + a_2 \frac{\left(T_{in,SC} - T_{amb}\right)^2}{I_{solar}} \tag{1}$$

and

$$K_\theta = 1 - b_0\left(\frac{1}{\cos(\theta)}\right) - b_1\left(\frac{1}{\cos(\theta)}\right)^2 \tag{2}$$

where the optical efficiency, first- and second- order heat loss coefficients were determined according to the Solar Rating & Certification Corporation (SRCC, 2017). The test results of SRCC (2017) are ao=0.6, a1=-3.87, and a2=0.002. Tin is fluid temperature at the collector inlet; Tamb is the ambient air temperature; Isolar is global solar radiation on the solar collector surface. Finally, Kθ is the incidence angle modifier and θ is incidence angle and bo, b1 are -0.194 and -0.019, respectively.

The solar collector -net surface area 0.93 m2- was designed and manufactured by ACR solar (2017). The collector was oriented to the south (0°) and the tilt angle was set to be equal to 38.8°, that is the mean of the latitudes of all the regions. Moreover, the collectors were installed in the system as 4 units.

Temperature difference in the storage tank affects SDHWS thermal performance. The cylindrical storage tank was divided into 5 nodes with equal distance with each other and the height to diameter ratio was selected as 3. The volume of the storage tank was 200 L and the overall heat transfer coefficient was assumed as 0.8 W/m2 K. The energy balance at each node as defined by the following expression (Araya et al., 2017; Duffie & Beckman, 2006):

$$M_{s,n} c_p \frac{dT_{s,n}}{dt} = U_s A_{s,n}\left(T_{amb} - T_{s,n}\right) + \frac{kA_{s,n+1}\left(T_{s,n+1} - T_{s,n}\right)}{\Delta x} + \frac{kA_{s,n-1}\left(T_{s,n-1} - T_{s,n}\right)}{\Delta x} + \dot{Q}_{n+1} + \dot{Q}_{n-1} + \dot{Q}_1 + \dot{Q}_5 \tag{3}$$

where

$$\dot{Q}_{n+1} = \left(\dot{m}_L - \dot{m}_c\right) c_p \left(T_{s,n+1} - T_{s,n}\right), \ \ if \ \ \dot{m}_c < \dot{m}_L \tag{4}$$

$$\dot{Q}_{n-1} = \left(\dot{m}_c - \dot{m}_L\right) c_p \left(T_{s,n-1} - T_{s,n}\right), \ \ if \ \ \dot{m}_c > \dot{m}_L \tag{5}$$

$$\dot{Q}_1 = \dot{m}_L c_p T_{mains} - \dot{m}_c c_p T_{s,1}, \ \ if \ \ n = 1 \tag{6}$$

$$\dot{Q}_5 = \dot{m}_c c_p T_{out} - \dot{m}_L c_p T_{s,5}, \ \ if \ \ n = 5 \tag{7}$$

where the storage tank inlet of water mains is located on node 1 and the outlet of storage tank is located on node 5. Ms is mass of the storage tank; m is the flow rate and represent subscript c for collector, L for load, and s storage tank; T is the temperature, represent subscript amb for ambient, mains for mains water; U and A are the storage tank area and overall heat loss coefficient, respectively.

Auxiliary energy ($\dot{Q}_{aux}$) is determined by using Eq. (8).

$$\dot{Q}_{aux} = \eta_{aux} \dot{m}_L c_p \left(T_L - T_{s,n=5}\right) \tag{8}$$

where ηaux is the heat exchanger efficiency. Finally, the system load ($\dot{Q}_L$) is determined as:

$$\dot{Q}_L = \dot{Q}_{aux} + \dot{Q}_{SC} + \dot{Q}_{Loss} \tag{9}$$

The instantaneous peak value of hot water usage is 0.08 L/s and the daily total demand from the system is 300 L at 55 °C. The DHW profile is defined according to the ASHRAE 90.2 (2001) standard.

2.3. Optimization framework

In this study, particle swarm optimization (PSO) algorithm proposed by Kennedy and Eberhart (1995, 1997) then developed by Clerc and Kennedy (2002) with a constriction coefficient, and Hooke-Jeeves (HJ) (1961) hybrid optimization algorithm (PSO/HJ) was used. Wetter and Wright (2004) shown that using hybrid algorithms improves optimization performance. Thus, researchers have tried to make up algorithm's shortage by using another one. However, Nguyen et al. (2014) reported that hybrid algorithms were used less frequently than the other methods, based on 200 studies in the literature. In PSO algorithm is a population-based optimization method inspired by the social behavior of birds and the birds-like species. The particles -solution- in the population randomly generated by the PSO algorithm are assigned to their random initial positions (x) and velocities (v) by using the Eqs. (10) and (11), respectively.

$$v_i^{k+1} = X\left[v_1^k + c_1\varphi_1^k\left(p_{l,i}^k - x_i^k\right) + c_2\varphi_2^k\left(p_{g,i}^k - x_i^k\right)\right] \tag{10}$$

$$x_i^{k+1} = x_i^k + x_i^{k+1} \tag{11}$$

where i is the particle number; k is the iterations number; φ_1 and φ_2, are the randomly generated numbers between 0 and 1. Acceleration coefficients are selected as $c_1 = c_2 = 2.05$ (Clerc & Kennedy, 2002). The PSO performance is improved by controlling the particle velocity with the constriction factor X. The constriction factor is expressed as (Clerc, 1999):

$$X = \frac{2}{\left|2 - \omega - \sqrt{\omega^2 - 4\omega}\right|} \tag{12}$$

where $\omega = c_1 + c_2 = 4.1$. In the PSO algorithm, the number of particles and generations are limited to 15 and 20, respectively. The particles change their velocity and position relative to the best solution in the population. In this way, generations are updated to obtain the most appropriate values.

The PSO algorithm's solution is chosen as the starting point for the Hooke-Jeeves (1961) algorithm. HJ algorithm is searching for the most appropriate solution according to neighborhood relation at each iteration. The successful values obtained by HJ are

assigned as the optimal solutions. The optimization problem of the SDHWS was utilized GenOpt® (v3.1). The GenOpt was chosen because it can combine with EnergyPlus. The PSO/HJ algorithm is embodied in the GenOpt. More detailed information was given by Wetter (2016).

2.3.1. Decision Variables

Kalogirou (2004) and Abdel-Malek (1985) emphasized that the most important parameters in SDHWS performance are collector number and storage tank volume. For this reason, those parameters were taken as independent parameters in the present study. Thus, decision variables vector is as follows.

$$\vec{x} = \left[N, V\right]^T \tag{13}$$

where $\vec{x}$ is the decision variables vector, N is number of the solar collector, and V is volume of the storage tank.

2.3.2. Objective Function

The proposed methodology minimizes the overall cost of the SDHWS throughout its life cycle of investment and energy consumption costs. LCC composes of three basic elements and can be formulated as follows:

$$LCC = C_{inv} + \left(C_{O\,\&M} + C_E\right) PW \tag{14}$$

where

$$C_{inv} = C_c N + C_s V + C_{pump} \tag{15}$$

$$C_{O\,\&M} = \frac{C_{inv}}{t} 0.10 \tag{16}$$

$$C_E = \frac{Q_L C_{gas}}{\eta_{aux}} + \frac{Q_{pump} C_{elek}}{\eta_{pump}} \tag{17}$$

where C_{inv}, $C_{O\&M}$, and C_E represent the investment, maintenance & operation, energy costs, respectively. C_c, C_s, and C_{pump} are the collector, storage tank, and pump costs, respectively, and t is the life-time. In Table 2, the SDHWS cost parameters are given. The present worth factor (PW) is determined by using Eqs. (18); (19).

$$W = \frac{1-\left(1+i^*\right)^{-t}}{i^*} \tag{18}$$

$$i^* = \frac{i-e}{1+e} \tag{19}$$

where PW is a function of interest rate (i= %10) and inflation rate (e= %9). Finally, the system life-time was assumed as 25 years.

Table 2. SDHWS cost parameters.

Components	Value	Unit	Ref.
Solar collector	309	TL/m^2	MEU (2017)
Storage tank	3.1V+666.9	TL/m^3	MEU (2017)
Circulation pump	884	TL	MEU (2017)
Natural gas	0.945	TL/m^3	EMRA (2017)
Electricity	0.41	TL/kWh	EMRA (2017)

2.3.3. Constrains

One of the important effects in determining the optimal solutions of the SDHWS is the constraints that are constituted by the decision maker's wishes. Thus, a certain economic and thermal performance can be the optimal solution for the decision maker's

needs. In this paper, constraints for decision variables were determined by the authors' experience and by the expertise of previous researchers and formulated as:

$$\vec{x} = \left\{ \left(N,\, V \right) \in \square^{n} \times \square^{n} | a^{i} \le x^{i} \le u^{i}; i \in \left(1,\ldots,n \right) \right\} \tag{20}$$

where a^i and u^i show the lower and upper limit, respectively. The optimization problem tackled the discrete variables for $N \in \{1, 2, \ldots, 12\}$ and continuous variables for $V \in \{5, \ldots, 1000\}$. However, the solar fraction (SF) is constrained by using Eq. (21) to ensure system thermal performance.

$$SF = \left(Q_L - Q_{aux} \right) / Q_L \ge 0.4 \tag{21}$$

3. Model validation

The SDHWS mathematical model was compared with the experimental results that obtained by Ayompe and Duffy (2013) in Dublin, Ireland. A computer code was wrote to provide experimental conditions and to test the mathematical model. Thus, the same conditions were prepared for the system. Simulated results was evaluated with statistical criterion proposed by ASHRAE Guideline 14 (2002). Simulated results were evaluated according to normalized mean bias error N(MBE) and coefficient of variation of the root mean square error CV(RMSE). These parameters were calculated by using Eqs. (22); (23), respectively.

$$N\left(MBE \right) = \frac{\sum_{i=1}^{n} \left(y_{Exp,i} - y_{Simul,i} \right)}{n-1} \frac{100}{\overline{y}_{Exp}} \tag{22}$$

$$CV\left(RMSE \right) = \left[\frac{\sum_{i=1}^{n} \left(y_{Exp,i} - y_{Simul,i} \right)^{2}}{n-1} \right]^{1/2} \frac{100}{\overline{y}_{Exp}} \tag{23}$$

where, y_{Exp} and y_{Simul} represent according to experimental and simulated results, respectively. n is the number of simulated value. According to ASHRAE Guideline 14 (2002), acceptable tolerances for N(MBE) and CV(RMSE) are within ±5% and 15%, respectively.

Fig. 2 is illustrated the experimental and simulation results for auxiliary energy, and these results are in a good agreement. N(MBE) and CV(RMSE) are -4.8% and 6.8%, respectively. These values are within the tolerance that defined by ASHRAE Guideline 14 (2002).

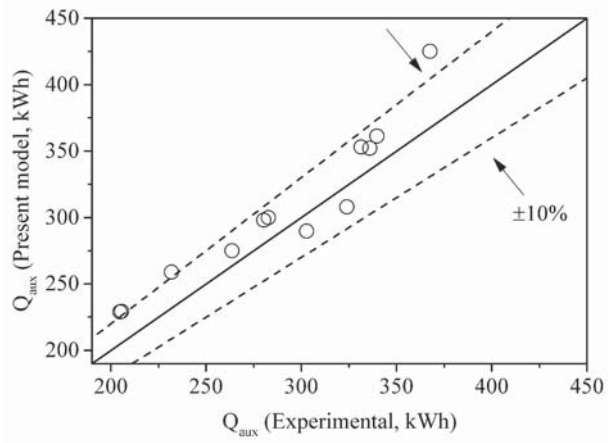

Fig. 2. Comparison of simulation and Ayompe and Duffy's (2013) experimental results.

4. RESULTS AND DISCUSSIONS

In this study, an SDHWS optimization was carried out under different climatic conditions. In Figs. 3 and 4, the optimization processes for only Erzincan and Mersin among 12 regions are shown in each iteration. The results of optimization for Erzincan and Mersin were presented in detail because they represent extreme weather conditions of Turkey. The PSO/HJ algorithm for Erzincan and Mersin reached the minimum value of LCC in 360th and 356th iterations, respectively. Whereas the optimal SDHWS for Erzincan is composed of $\vec{x} = \{7 \text{ unit}, 235.8 \text{ L}\}$, it is $\vec{x} = \{7 \text{ unit}, 315.9 \text{ L}\}$ for Mersin. However, the life cycle cost decreased by 3.3% for Erzincan and 5.9% for Mersin, while the annual solar fraction increased by 31.4% and 32.1%, respectively.

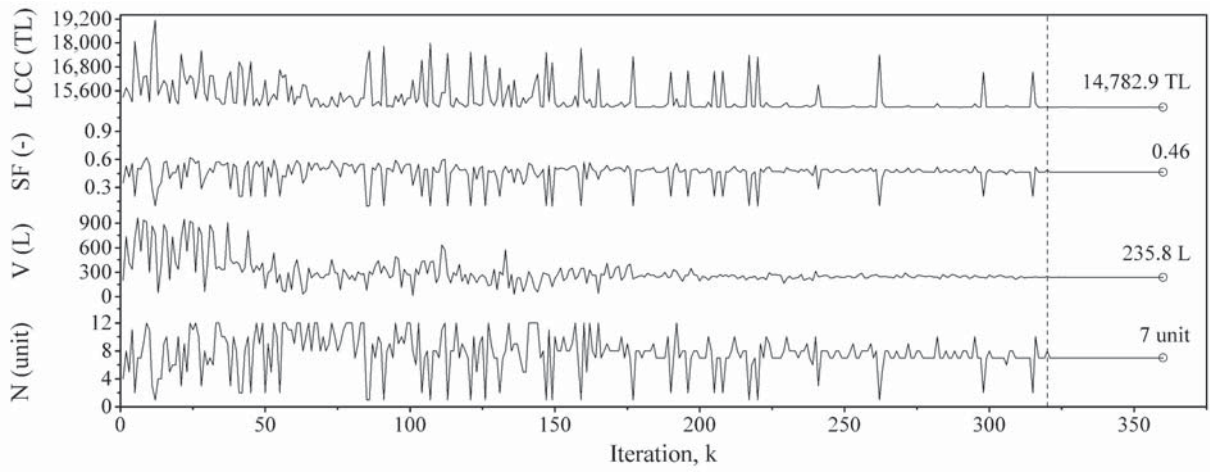

Fig. 3. Optimization of SDHWS in Erzincan; Circle-marking: Optimal solution and Dashed-line: PSO ending-HJ beginning.

The optimal results for each climate region are shown in Fig. 5 in terms of SF and LCC. In warm climates, it is expected that the LCC is lowest and the SF is highest, whereas it is opposite in cold regions. Thus, SF is high in Mersin and İzmir while LCC is high in Ankara and Erzincan. However, in mild climates, the increase of SF has a relatively positive effect on LCC in optimal solutions. Optimization results shown that the performance of an SDHWS can be improved by composing a design according to the climatic conditions.

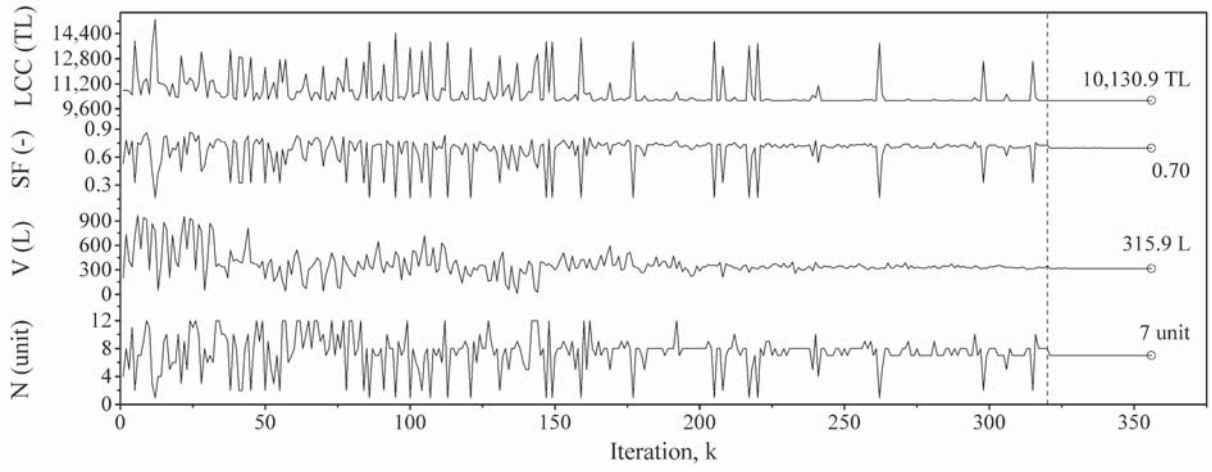

Fig. 4. Optimization of SDHWS in Mersin; Circle-marking: Optimal solution and Dashed-line: PSO ending-HJ beginning.

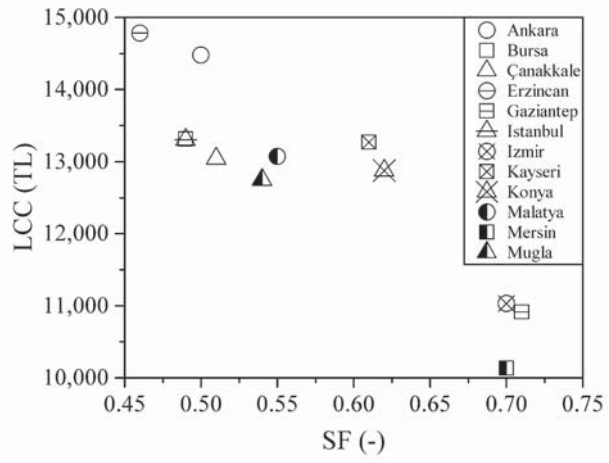

Fig. 5. Optimization results in each climate region for SF vs. LCC.

In Fig. 6, the optimization results are shown depending on the number of the collectors and storage tank volume. Variation of the number of collectors is only 1 unit, equal to 0.63 m^2 net surface area, for all climate regions. Accordingly, the storage tank volume appeared to be an important parameter in optimal system design, when considering the effect of different climatic regions. Thus, the variation of the storage tank volume was between 231.8 and 345.8 L. In warm climate regions, tank volume can be larger, whereas the opposite is recommended in cold climate regions. The large size of SDHWS technical capacities in warm climatic regions reduce the total cost. This phenomenon is the opposite in cold climates. In addition, the initial investment cost may be overlooked, when the energy cost is high.

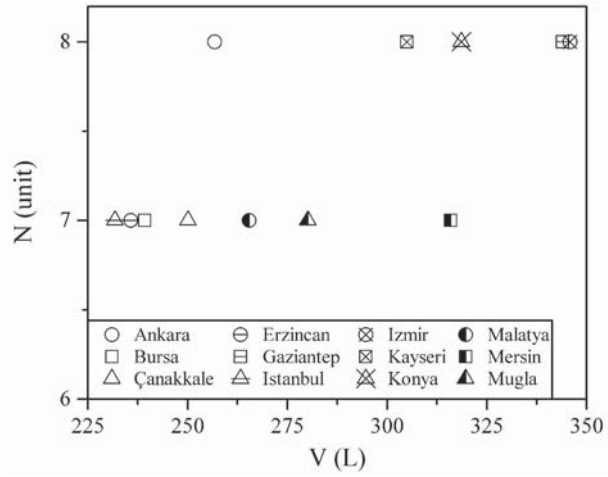

Fig. 6. Optimization results in each climate region for V vs. N.

Fig. 7 shows thermal and economic performance potential of SDHWS according to SF and LCC, respectively. The SDHWS performance potential is defined according to the percentage difference between the initial and optimal values. According to obtained optimal results, SF increased, while LCC decreased in all climate regions. Whereas the highest increase for SF was in Ankara (42.9%), the highest decrease for LCC was in Gaziantep (6.1%). According to all climatic regions, SF increased mean 35.4%, while LCC decreased mean 4.5%. This is possible according to Bornatico et al. (2012). Bornatico et al. (2012) indicated that investment and energy costs could be reduced as well as solar fraction could be increased.

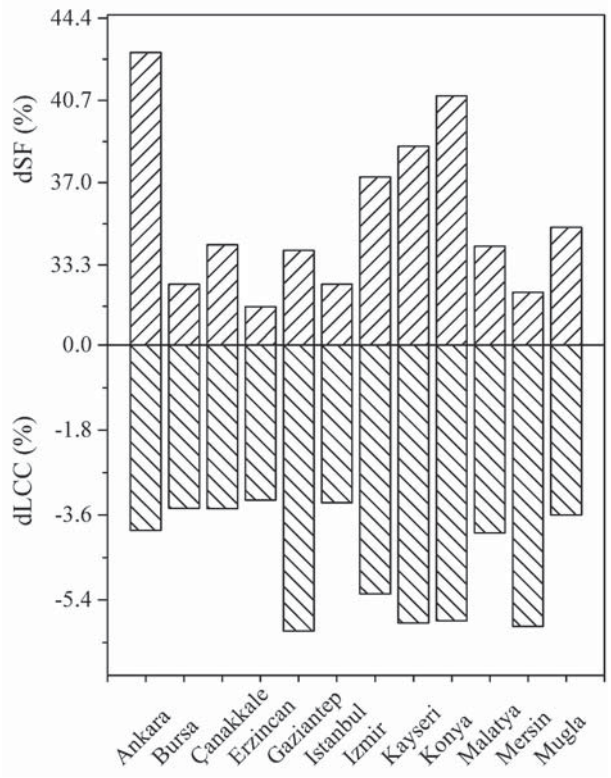

Fig. 7. Thermal and economic potentials in each climate region.

5. CONCLUSIONS

In this paper, a simulation-optimization method is presented to optimize the life cycle cost of an SDHWS. In order to determine the effect of different climatic conditions, this method was implemented in different climatic regions of Turkey. For all climate regions, the variation of the number of collectors is only 1 unit, equal to 0.63 m^2 net surface area, whereas the variation of the storage tank volume is between 231.8 and 345.8 L. The large size of SDHWS technical capacities in warm climatic regions reduce the total cost. This phenomenon is the opposite in cold climates. However, SF increased mean 35.4%, and LCC decreased mean 4.5%, according to all climatic regions. As a result, a proper design and optimization of SDHWS should be composed according to climate. In this way, SDHWS becomes more sustainable.

References

Abdel-Malek L. (1985). Optimum design of solar water heating systems. Comput Opt Res, 12(2), 219-225. doi: 10.1016/0305-0548(85)90046-2

ACR solar. (2017). Retrieved from http://www.acrsolar.com/

Araya R., Bustos F., Contreras J., & Fuentes A. (2017). Life-cycle savings for a flat-plate solar water collector plant in Chile. Renew Energy, 112, 365-377. doi: 10.1016/j.renene.2017.05.036

ASHRAE (2001). Handbook of Fundamentals. American Society of Heating, American Society of Heating, Ventilating, and Air Conditioning Engineers, Atlanta, GA.

ASHRAE 90.2. (2001). Energy efficient design of low-rise residential buildings, American Society of Heating, Ventilating, and Air Conditioning Engineers, Atlanta, GA.

ASHRAE Guideline 14. (2002). Measurement of Energy and Demand Savings, American Society of Heating, Ventilating, and Air Conditioning Engineers, Atlanta, GA.

Atia D. M., Fahmy F. H., Ahmed N. M., & Dorrah H. T. (2012). Optimal sizing of a solar water heating system based on a genetic algorithm for an aquaculture system. Math Comput Model, 55(3-4), 1436-1449. doi: 10.1016/j.mcm.2011.10.022

Ayompe L. M. & Duffy A. (2013). Analysis of the thermal performance of a solar water heating system with flat plate collectors in a temperate climate. Appl Therm Eng, 58(1-2), 447-454. doi: 10.1016/j.applthermaleng.2013.04.062

Bernardo L. R. (2013). Retrofitting conventional electric domestic hot water heaters to solar water heating systems in single-family houses-model validation and optimization. Energies, 6(2), 953-972. doi: 10.3390/en6020953

Bornatico R., Pfeiffer M., Witzig A., & Guzzella L. (2012). Optimal sizing of a solar thermal building installation using particle swarm optimization. Energy, 41(1), 31-37. doi: 10.1016/j.energy.2011.05.026

Clerc M. & Kennedy J. (2002). The particle swarm – explosion, stability, and convergence in a multidimensional complex space. IEEE Trans Evol Comput, 6, 58-73. doi: 10.1109/4235.985692

Clerc M. (1999). The swarm and the queen: towards a deterministic and adaptive particle swarm optimization. ICEC, Washington, DC, 1951-1957.

Duffie J. A. & Beckman W. A. (2006). Solar Engineering of Thermal Processes, Hoboken, New Jersey: John Wiley & Sons Inc.

EMRA. (2017). Republic of TURKEY Energy Market Regulatory Authority. Retrieved from http://www.emra...

org.tr/en/home.

Hobbi A. & Siddiqui K. (2009). Optimal design of a forced circulation solar water heating system for a residential unit in cold climate using TRNSYS. Sol Energy, 83(5), 700-714. doi: 10.1016/j.solener.2008.10.018

Hooke R. & Jeeves T.A. (1961). Direct search solution of numerical and statistical problems. J Ass Comput Mach, 8(2), 212-229. doi: 10.1145/321062.321069

Kalogirou S. A. (2004). Optimization of solar systems using artificial neural-networks and genetic algorithms. Appl Energy, 77(4), 383-405. doi: 10.1016/S0306-2619(03)00153-3

Karaçavus B. (2017). Optimization of solar domestic hot water system for certain climate zones of Turkey. J Fac Eng Archit Gazi Univ, 32(3), 843-853. doi: 10.17341/gazimmfd.337633

Kennedy J. & Eberhart R. C. (1995). Particle swarm optimization. In IEEE International Conference on Neural Networks, Perth, Australia, 1942-1948.

Kennedy J. & Eberhart R. C. (1997). A discrete binary version of the particle swarm algorithm. In Proc. of Systems, Man, and Cybernetics. 4104-4108.

Kim Y., Thu K., Kaur H., Singh C., & Choon K. (2012). Thermal analysis and performance optimization of a solar hot water plant with economic evaluation. Sol Energy, 86(5), 1378-1395. doi: 10.1016/j.solener.2012.01.030

Ko M. J. (2015). Analysis and Optimization Design of a Solar Water Heating System Based on Life Cycle Cost Using a Genetic Algorithm. Energies, 8(10), 11380-11403. doi:10.3390/en81011380

Mauthner F., Weiss W., & Spörk-Dür M. (2014). Solar heat worldwide-markets and contribution to the energy supply 2014. Technical report, International Energy Agency, Solar heating and cooling.

MENR. (2017). Solar. Retrieved from http://www.enerji.gov.tr/tr-TR/Sayfalar/Gunes.

MEU. (2017). The Ministry of Environment and Urbanization, Retrieved from http://www.csb.gov.tr/gm/donerser...

maye/index.php?Sayfa=haberdetay&Id=21332.

Nguyen A.-T., Reiter S., & Rigo P. (2014). A review on simulation-based optimization methods applied to building performance analysis. Appl Energy, 113, 1043-1058. doi: 10.1016/j.apenergy.2013.08.061

Skerlić J., Radulović J., Nikolić D., & Bojić M. (2013). Maximizing performances of variable tilt flat-plate solar collectors for Belgrade (Serbia). J Renew Sustain Energy, 5(4), 041820. doi: 10.1063/1.4819254

SRCC. (2017). The Solar Rating and Certification Corporation. Retrieved from http://www.solar-rating.org/.

Wetter M. & Wright J. (2004). A comparison of deterministic and probabilistic optimization algorithms for nonsmooth simulation-based optimization. Build Environ, 39(8), 989-999. doi: 10.1016/j.buildenv.2004.01.022

Wetter M. (2016). GenOpt-generic optimization program user manual, version 3.1.1. Berkeley, CA, Lawrence Berkeley National Laboratory Report.

MÜHENDİSLİK FAKÜLTESİ

Uluslararası Mühendislik Araştırma ve Geliştirme Dergisi

International Journal of Engineering Research and Development

Cilt/Volume:9 Sayı/Issue:3 Aralık/December 2017 https://doi.org/10.29137/umagd.350596

Araştırma Makalesi / Research Article

Prediction of Gold Prices Using Artificial Neural Networks

Kemal Adem*[1], Onur Comert[2], Numan Zengin[3], Mahmut Hekim[4]

[1] *Gaziosmanpasa University, Department of Informatics, Tokat, TURKEY*
[2] *Gaziosmanpasa University, Tokat Vocational High School, Tokat, TURKEY*
[3] *Gaziosmanpasa University, Pazar Vocational High School, Tokat, TURKEY*
[4] *Gaziosmanpasa University, Electrical and Electronics Engineering, Tokat, TURKEY*

Başvuru/Received: 08/10/2017 **Kabul/Accepted**: 01/12/2017 **Son Versiyon/Final Version**: 26/12/2017

Abstract

Gold, which has fulfilled the functions that money has in the past years, is now mostly used as a means of saving. Gold has been an investment instrument for Turkish society for many years. In addition, it is perceived as the most reliable means of investment by people in times of crisis and war. It is very important to estimate gold prices for investors who want to earn high profits from their investments. In this study, as input (independent variables), the data set consisting of Brent oil price, USD price, BIST100 index, Central Bank of the Republic of Turkey weekly interest rate, silver and copper prices was applied to the price of gold in ounce by applying Multi-Layer Perceptron Neural Network (MLPNN) is intended to be estimated. As the data set, weekly price and index values were used between January 2010 and December 2016 period. As a result of the study, suggestions were made about the effectiveness of gold on the input variables created by using MLPNN.

Key Words

"Investment, Gold prices, Prediction, Artificial Neural Network"

* *kemal.adem@gop.edu.tr*

1. INTRODUCTION

Investment; depositing money on an income-generating, movable or immovable property (Sjaastad,2008). Saving owners (investors) want to make money with the help of various investment tools. One of these alternatives is precious metals. Among the precious metals, gold comes first.

Gold, which has fulfilled the functions that money has in the past years, has not lost much in its importance, although it is often used as a means of saving money today. Gold has been seen as an investment tool in Turkish society for many years. It is perceived as the most reliable investment tool by people during crisis and war periods.

It is very important to estimate gold prices for investors who want to earn high profits from their investments. Investors' interest in gold is shaped by the influence of various factors. International gold prices; foreign exchange prices, interest rates, stocks, commodity prices and so on are some of these factors. Any change in these factors affects the supply and demand of gold.

Forecasting is to produce scenarios for the future based on existing or past data. Estimation is an important factor in planning ahead and calculating numerical values (Armutlulu,2000). Throughout their lives, people make many guesses without realizing it. Even the simplest situation that requires a decision requires estimation. Decision making is the selection of one or more definitions from among other definitions by evaluating the definitions made in determining the characters of the variables (Bağırkan,1983).

The demand for gold increases in case of a decrease interest in other investment instruments. The idle funds tend to gold in periods when interest in stock exchanges declines and real interest rates provide negative income. In the opposite case, the interest in gold of the investor falls to a very low level (ITO,1983).

There are many studies about the estimation of gold prices using different methods. Some of these are given below.

Atan et al. found that gold prices have a positive interaction with stock returns (Atan et al.,2000). Albeni and Demir found the existence of a positive relationship between the Republican gold and the financial index contrary to expectations (Albeni et al.,2005). Aye et al. developed models for estimating gold prices. They selected nominal interest rate, exchange rate, commodity prices, stock prices as factors affecting gold. The results show that dynamic model selection is the best method. The exchange rate is very high predictive power has been identified (Aye et al.,2005).

Yuksel and Akkoc investigated models for estimating the gold prices with artificial neural networks. The findings show that artificial neural networks can be successfully used in estimating gold prices. When the results of the sensitivity analysis are evaluated, it is found that silver and oil prices are the leading factors affecting gold prices (Yüksel et al.,2016). Aksoy and Topcu analyzed short and long term relationships between gold and stocks, government debt securities, consumer price index and producer price index as an investment tool in their work. Regression analysis results show that there is a negative relationship between the gold and stock returns (Aksoy et al.,2013).

Kocatepe and Yıldız estimated the direction in change of gold prices using artificial neural networks. In the study, the gram price of gold in Turkey is taken as the dependent variable. The independent variables were crude oil price, dollar index, dollar exchange rate, Standard & Poor's 500 index, BIST100 index, Turkish inflation, bond and interest rates, US inflation, bond and interest rates, silver and copper prices. In the study, for estimating the future value of the dependent variable, the one month earlier values of the independent variables were used. The success predicting the direction of change in gram gold price was found to be 75.24% (Kocatepe et al.,2016).

Kristjanpoller et al. analyzed a hybrid model (ANN–GARCH) to predict the gold spot price. The results of the study show that the proposed ANN-GARCH model performs 38% better volatility estimates of gold prices than the GARCH model. This result was found in the 21-day volatility estimates. The same situation was also estimated for 14 and 28 day changes (Kristjanpolleret al.,2016).

Abd Wahab and Nursu, is predict monthly price of gold. The monthly sample data of gold price (in RM per ounce) were taken from January 2004 to November 2015. The model performance was evaluated in term of error magnitude (EM) and directional change error (DCE). The result of the study had suggested that the ANN model with LMBP algorithm had perform the best model compared to ARIMA model and another ANN model using RBP and SCGBP algorithm (Wahab,2016).

The aim of this study is to estimate the gold prices by using artificial neural networks method with some macroeconomic variables which are thought to affect gold prices.

2. MATERIAL AND METHOD

2.1. Material

In the study, the dollar rate for the January 2010 - December 2016 period, the weekly interest rates for CBRT and the weekly closing values for commodity prices were used as the data set. These data sets were obtained from http://investing.com/. The input variables used are given in Table 1.

Table 1: Input variables used in the study

Sıra No	Input variables
1	Brent Petrol Fiyatı
2	ABD Dolar Kuru
3	BIST100 Endeksi
4	TCMB Haftalık Faiz Oranı
5	Gümüş fiyatı
6	Bakır fiyatı

Referring to previous years, exchange rates (USD) gained value in real terms from time to time and thus has created a positive return investment opportunity. From this point of view, it is thought that it can be effective on gold value as an alternative investment tool.

Interest is the rent income that is obtained as a result of the capital being rented at a specified rate and for a certain period of time (Rüzgar,2001). It is the biggest rival bank depositor to invest in capital markets in developing countries. Theoretically, the increase in interest rates increases the cost of borrowing. In terms of investors, when interest rates rise, investments will channel to that side. Therefore, the change in interest rates will affect the prices of other investment instruments.

It is included in the gold and petroleum commodity category in finance literature. Both are important factors shaping the global economy. The most important reason for the correlation between gold and oil prices is the effect of crude oil prices on inflation. Increase in oil prices increases gasoline prices, gasoline prices also affect inflation. Here, the causality effect leads to an increase in precious metals as inflation increases (Hürriyet,2017).

Securities exchanges are markets where long-term investment instruments such as stocks and bonds are bought and sold (Karan,2004). Stocks are described as the barometer of the economy. If the economy worsens, investors exit the stock market and turn towards different investment instruments.

In the markets, silver is demanded in serious transaction volumes as an alternative to gold. The intense demand for gold causes prices to rise. When the gold price reaches the psychological upper limit for investors, demand will decrease and prices will go downhill. Therefore, investors are making silver and copper transactions which are alternative assets instead of gold trading. In this case, demand for silver and copper is increasing (forexaltinpiyasasi,2017).

Time series graphs of macroeconomic input variables used in the study are given in Figure 1.

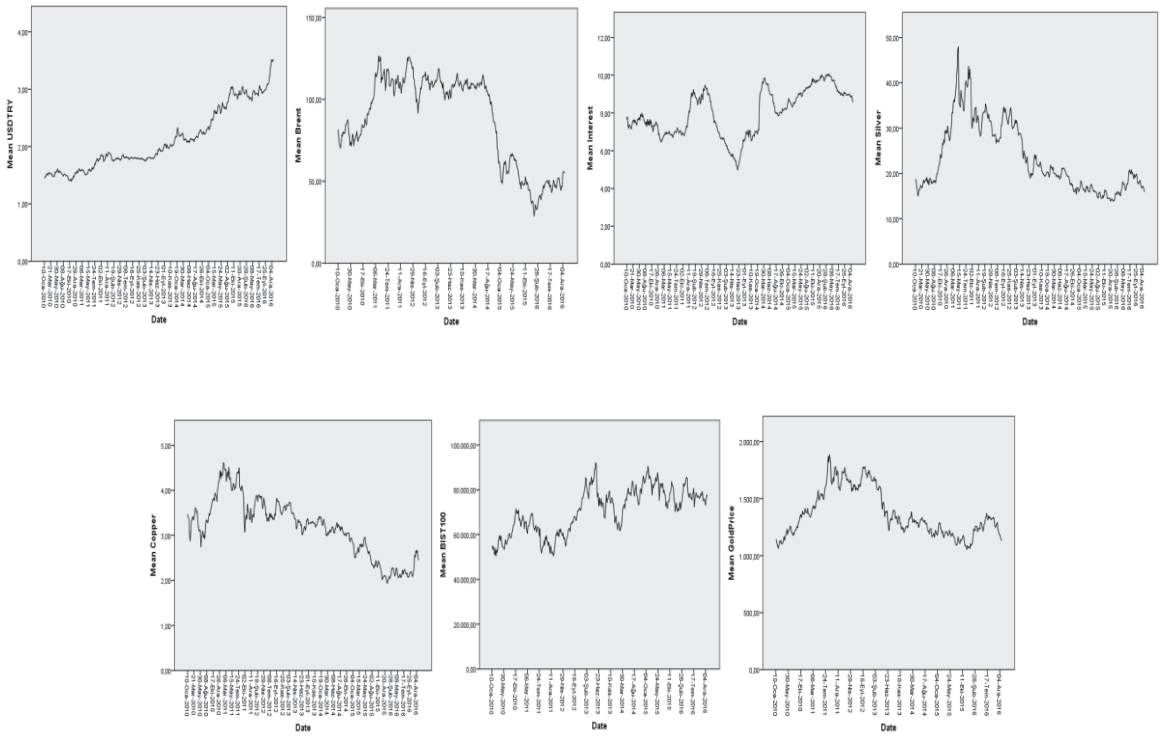

Figure 1: Time series charts for input variables

2.2. Artificial Neural Network (ANN)

Estimation is a process that produces a relationship using examples that have definite consequences and allows you to comment on the new situation through this derivation. As a prediction method, Multi-Layer Neural Network (MLNN), which is an artificial neural network model, was used in this study. In Figure 2, a sample MLNN is given.

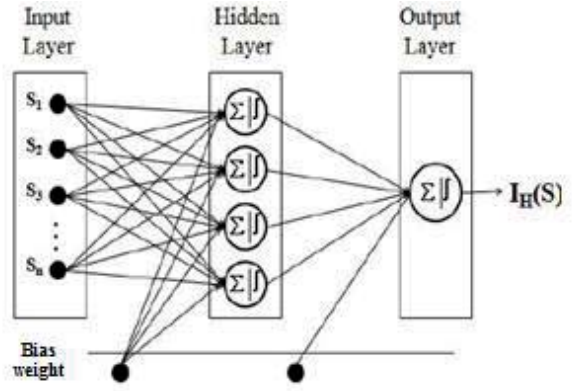

Figure 2: A sample MLNN

As shown in Figure 2, the output value (y) produced after each input ($s_1,s_2,....,s_6$) is processed in the neuron by multiplying it by a separate weight value ($w_1,w_2,...,w_6$). There are two processing units within the neuron that perform linear and non-linear processing. In the linear unit, each input is multiplied by the weight value and the result is sent to the second unit (Bellanger,2000).

The value obtained after passing through the selected activation function of the total value obtained in the second unit in which non-linear transactions are made is given to the output of the neuron. The y value at the exit of the neuron is calculated as given in Equation 1.

$$I_H(s) = f(n) \quad (1)$$

The expression *f* in Equation 1 shows the selected activation function. Commonly used activation functions are sigmoid, hyperbolic tangent and step functions. Generally, back propagation algorithm derivatives are used as training algorithm in the MLNN. With the aid of the training algorithm, the network output is optimized by adjusting the weights of the connections between the neurons.

The correctness of the value obtained at the MLNN output is based on the finding of the smallest value of the Mean Squared Error (MSE), and hence of the Root Mean Squared Error (RMSE), as expressed in Equation 2.

$$\mathrm{MSE} = \frac{1}{N} \sum_{i=1}^{N} (d_i - \bar{d}_i)^2 \quad (2)$$

$$\mathrm{RMSE} = \sqrt{\mathrm{MSE}} \quad (3)$$

$(d_i - \bar{d}_i)$ in Equation 2 indicates the distance (error) between each target variable and the correct equation to be calculated. Root Mean Square Error (RMSE) in Equation-3 is used to determine the error rate between the measured values and the estimates. The approach of the RMSE value to zero means that the estimation capability of the system is increased (Chenard et al.,2008).

In the study, the MLNN model was used to estimate the gold prices. As input to the model, data sets consisting of macroeconomic input variables (dollar rate, TCMB weekly interest rates and weekly closing values of commodity prices) were used. In this model, 10 neurons in hidden layer, sigmoid function for activation in neurons and Levenberg-Marquardt back propagation algorithm for training were used. Experiments were performed in Matlab 2016 platform.

3. DISCUSSION

In the experiments conducted using the dataset and techniques described in the previous section, it was tried to estimate the ounce value of gold prices by using the US dollar rate, BIST100 index, CBT weekly interest rate and commodity (copper and silver) prices. The correlation results obtained using the SPSS 22.0 statistical package program to analyze the relationships between input variables are shown in Table 2.

Table 2: Correlation matrix between input variables

	Gold	BIST100	USDTR	Brent	Silver	Copper	Interest
Gold	1	0,687	0,783	0,690	0,892	0,515	0,653
BIST100	0,687	1	0,770	0,676	0,742	0,699	0,846
USDTR	0,783	0,770	1	0,757	0,726	0,864	0,677
Brent	0,690	0,676	0,757	1	0,736	0,839	0,608
Silver	0,892	0,742	0,726	0,736	1	0,803	0,669
Copper	0,515	0,699	0,864	0,839	0,803	1	0,649
Interest	0,653	0,846	0,677	0,608	0,669	0,649	1

According to the correlation matrix given in Table 2, the strongest correlation with gold prices is the silver price index. This situation reveals the importance of silver, which is a direct alternative investment in gold investment. Copper is one of the most comparable commodities of gold and there is usually a positive relationship between gold and copper. However, after the 2008 crisis, there has been a decline in this correlation. Gold prices have risen rapidly after the crisis, but have fallen considerably in copper prices. The divergence between the two commodities has become increasingly apparent since the second quarter of 2010. For this reason, there is no strong correlation between gold and copper prices, as seen in the table.

In the study, a cross-validation method was applied to the data set prepared for the estimation of gold prices. In this method, the given data is randomly distributed to 3 clusters as training, validity and test. In the study, the distribution of data was 40% education, 20% validity and 40% test data. In order to make the results more objective, the data set has been relocated within the same distribution ratios and subjected to 10 different education stages. The accuracy of the training, validity, test and mean estimation of the first of these experiments is given in Fig 3.

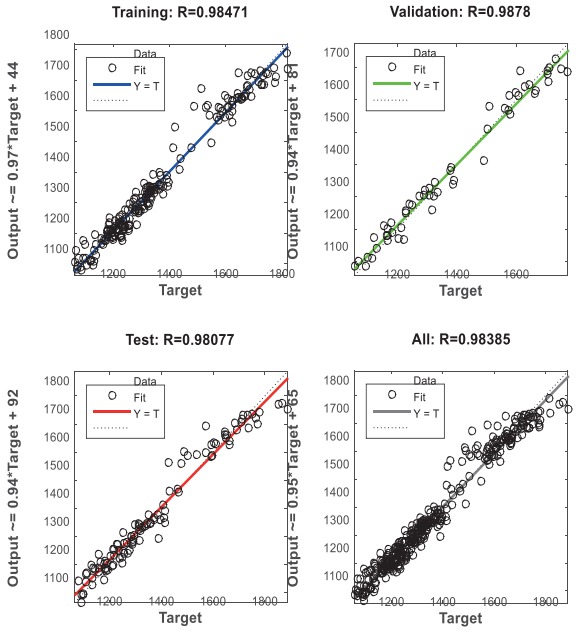

Figure 3: Success graph of ANN training (Exp. No:5)

The estimated accuracy values obtained from each experiment as given in Fig. 3 are given in Table 3. The average of these values gives the success rate of the model we have created.

Table 3: Predictive accuracy values of the MLNN experiments

Experiment	Accuracy (%)
1	98,60
2	97,73
3	98,51
4	97,56
5	98,39
6	97,95
7	99,13
8	97,87
9	97,90
10	98,01
Mean	**98,17**

The estimation accuracy of the model considered for the estimation of gold prices was 98.17% as seen in Table 3.

4. RESULTS

Estimation techniques and models are important for those who want to make estimates during decision making and investment stage. In the study, gold prices, which are important for investor decision makers, were estimated using artificial neural networks. ANN is used in the financial sector as well as in many areas because of their ease of design, rapid adaptation to probing and successful results in spite of a small number of donations. For estimating the future value of the dependent variable, the weekly values of the independent variables between 2010 and 2016 were used.

As a result of the study, it is seen that there is a strong correlation between the gold prices and the input variables used in the study. Using the artificial neural network model, gold prices were estimated with a high success rate of 98.17%. In future studies, it is considered to use the stock market indices of the developed countries. In addition to the ANN model, other data mining methods can also be applied.

REFERENCES

Aksoy, M. and Topcu, N., "Altın ile Hisse Senedi ve Enflasyon Arasındaki İlişki". Atatürk Üniversitesi İktisadi ve İdari Bilimler Dergisi, 27(1), 2013.

Albeni, M. and Demir, Y., "Makro Ekonomik Göstergelerin Mali Sektör Hisse Senedi Fiyatlarına Etkisi", Muğla SBE dergisi, Sayı 14, 2005.

Altın Bankacılığı Borsası Rafinerisi ve Türkiye, İstanbul Ticaret Odası, İstanbul, 1998, 31- s.113.Atan, M., Boztosun, D., and Kayacan, M., "Arbitraj Fiyatlama Modeli Yaklaşımının İMKB' de Test Edilmesi", 9. Ulusal Finans Sempozyumu.

Armutlulu, İ. H., *İşletmelerde Uygulamalı İstatistik*, Birinci Baskı, İstanbul: Alfa Basım Yayın Dağ, 2000, s.335.
Aye, G., Gupta, R., Hammoudeh, S. and Kim, W. J., "Foracasting the price of gold using dynamic model averaging", International Review of Financial Analysis, vol41, 2015

Bağırkan, Ş., *Karar verme*, İstanbul: Der Yayınevi, 1983, s.3.

Bellanger, M., *Digital Processing of Signal: Theory and Practice*, John Wiley and Sons, USA, 2000.

Chenard, F., Caissie, D., Stream temperature modelling using neural networks: application on Catamaran Brook, New Brunswick, Canada. Hydrol. Process, 2008. (DOI: 1002/hyp.6928).

Karan, M. B., *Yatırım Analizi ve Portföy Yönetimi*, Ankara: Gazi Kitabevi, s.33, 2004.

Kocatepe, C. İ. and Yıldız, O., "Ekonomik Endeksler Kullanılarak Türkiye'deki Altın Fiyatındaki Değişim Yönünün Yapay Sinir Ağları İle Tahmini". Düzce Üniversitesi Bilim ve Teknoloji Dergisi, 4(3), 2016.

Kristjanpoller, W. and Minutolo, M. C., "Gold price volatility: A forecasting approach using the Artificial Neural Network–GARCH model". Expert Systems with Applications, 42(20), 7245-7251, 2016.

Rüzgar, B., *Finans Matematiği*, İstanbul: Türkmen Kitabevi, 2001.
Sjaastad, L. A., *Resources Policy*, (33), 118-124, 2008.

Wahab, A., *Forecasting gold price using autoregressive integrated moving average and artificial neural network model*, (Doctoral dissertation, Universiti Tun Hussein Onn Malaysia), 2016.
.Yüksel, R. and Akkoç, S., Altın fiyatlarının yapay sinir ağları ile tahmini ve bir uygulama. Doğuş Üniversitesi Dergisi, 17(1), 39-50, 2016.

http://bigpara.hurriyet.com.tr/bigpara-uzmanlari/sevin-ekinci/altin-petrol-fiyatlari-korelasyonu_ID965958/ Accessed date: 10.10.2017.

http://www.forexaltinpiyasasi.com/altin-ve-gumus-yatirimi-iliskisi.htm Accessed date: 10.10.2017.

MÜHENDİSLİK FAKÜLTESİ

Uluslararası Mühendislik Araştırma ve Geliştirme Dergisi

International Journal of Engineering Research and Development

Cilt/Volume:9 Sayı/Issue:3 Aralık/December 2017 https://doi.org/10.29137/umagd.352935

Araştırma Makalesi / Research Article

The Effect of Primary User Traffic on the Performance of Robust and Conventional Goodness of Fit (GOF) Test based Spectrum Sensing Methods in Cognitive Radio

Timur DÜZENLİ*[1], Olcay AKAY[2]

[1]*Amasya University, Technology Faculty, Department of Electrical and Electronics Engineering, Amasya, TURKEY*
[2]*Dokuz Eylül University, Engineering Faculty, Department of Electrical and Electronics Engineering, İzmir, TURKEY*

Başvuru/Received: 08/10/2017 **Kabul/Accepted**: 01/12/2017 **Son Versiyon/Final Version**: 26/12/2017

Abstract

In cognitive radio, users of the spectrum are grouped as primary and secondary users. Primary users are license holders and a certain interval of band is assigned to them. On the other hand, secondary users determine the idle frequency intervals which are not used by primary users. To determine whether a spectrum band is idle or in use, various spectrum sensing techniques have been proposed in the literature. In the studies on goodness of fit (GOF) tests, it is assumed that primary user does not change its status during spectrum analysis. However, when the duration of analysis is long, the status of primary user may change. In this study, effect of the primary user traffic on the sensing performance of GOF test based spectrum sensing methods is investigated. According to simulation results, it has been observed that changes in the primary user status adversely affect the sensing performance.

Key Words

"Cognitive Radio, Primary User, Secondary User, Spectrum Sensing, Goodness of Fit Test, Primary User Traffic"

* *timur.duzenli@amasya.edu.tr*

1. INTRODUCTION

Goodness of fit (GOF) tests are considered as nonparametric spectrum sensing methods in the cognitive radio (CR) literature (Wang et al., 2009). They are also treated as blind spectrum sensing techniques since they do not need a priori knowledge of the primary user (PU) signal.

It is possible to improve performance of GOF tests by extending the length of the sensing period. However, use of longer sensing periods may also increase the possibility of having a dynamic PU which changes its status during the sensing period. Therefore, possible PU status changes (also called PU traffic) in the channel should also be taken into consideration by a CR. However, a great majority of the works on spectrum sensing based on GOF testing assumes that the PU does not change its status during the sensing period (Wang et al., 2009), (Rostami et al., 2012), (Lei et al., 2011). Hence, in this study, we investigate performances of GOF tests for detecting dynamic PUs under the existence of PU traffic.

The rest of the paper is organized as follows: The system model used in this study is introduced in Section 2. In Section 3, widely used GOF tests for spectrum sensing are presented. Simulation results are considered in Section 4, and finally, conclusions are given in Section 5.

2. SYSTEM MODEL

In the studies on spectrum sensing, the following system model is commonly used (Yücek and Arslan, 2009), (Düzenli and Akay, 2013)

$$H_0 : x[n] = w[n], \qquad n = 1, 2, \ldots, N$$

$$H_1 : x[n] = s[n] + w[n], \qquad n = 1, 2, \ldots, N \tag{1}$$

where $w[n]$ denotes samples of white Gaussian noise (WGN) distributed according to $\mathrm{N}\left(0, \sigma^2\right)$, $s[n]$ is the PU signal, and N is the number of total samples observed during the sensing period.

In Eq. (1), it is assumed that there is no PU status change during the sensing period. If there is a status change of the PU in the channel, then the model given in Eq. (1) can be modified as

$$H_0 : x[n] = \begin{cases} s[n] + w[n], & n = 1, \ldots, i_1 \\ w[n], & n = i_1 + 1, \ldots N \end{cases}$$

$$H_1 : x[n] = \begin{cases} w[n], & n = 1, \ldots, j_1 \\ s[n] + w[n], & n = j_1 + 1, \ldots N \end{cases} \tag{2}$$

where i_1 and j_1 are the PU status change points under H_0 and H_1, respectively.

In the same way, the system model for two status changes of the PU can be written as

$$H_0 : x[n] = \begin{cases} w[n], & n = 1, \ldots, i_1 \\ s[n] + w[n], & n = i_1 + 1, \ldots, i_2 \\ w[n], & n = i_2 + 1, \ldots, N \end{cases} \tag{3}$$

$$H_1 : x[n] = \begin{cases} s[n] + w[n], & n = 1, \ldots, j_1 \\ w[n], & n = j_1 + 1, \ldots, j_2 \\ s[n] + w[n], & n = j_2 + 1, \ldots, N \end{cases}$$

where i_1 and i_2 are the first and second status change points of the PU under hypothesis H_0, respectively. Similarly, j_1 and j_2 are the first and second status change points of the PU under hypothesis H_1.

The model in Eq. (3) can be extended for more than two PU status changes by assuming that hypothesis H_0 ends with noise-only samples and hypothesis H_1 ends with noise-corrupted signal samples (Düzenli and Akay, 2016).

It can be stated that hypothesis H_0 corresponds to the absence of the PU in the channel (null hypothesis), and oppositely, hypothesis H_1 is the case where PU is in the channel (alternative hypothesis). If H_1 is decided under hypothesis H_1, then it leads to probability of detection, P_D. That is; probability of deciding that there is PU signal in the channel. Thus, PU actually exists and is correctly detected. If H_1 is decided while H_0 is observed, then it refers to probability of false alarm, P_{FA}, which indicates deciding that the PU signal exists when there is actually no PU communication. Thus, error of false alarm leads to inefficient use of the spectrum.

P_D and P_{FA} can be expressed mathematically using the following definitions

$$P_D = P\left(T_x > \gamma_x \middle| H_1\right) \tag{4}$$

$$P_{FA} = P\left(T_x > \gamma_x \middle| H_0\right) \tag{5}$$

where T_x is the test statistic and γ_x is the decision threshold value for the test statistic. P_{FA} should be kept as small as possible in order to prevent underutilization of transmission opportunities. The decision threshold γ_x can be selected for finding an optimum balance between P_D and P_{FA}.

3. GOF Tests for Spectrum Sensing

In GOF testing, the main goal is to determine if the observed data come from a particular known distribution or not. This testing scheme can be adapted to spectrum sensing in CR. Using GOF testing, the binary hypothesis testing problem for spectrum sensing can be formulated as (Zhang, 2002)

$$H_0 : F_N\left(x\right) = F_0\left(x\right) \tag{6}$$

$$H_1 : F_N\left(x\right) \neq F_0\left(x\right).$$

In Eq. (6), $F_0\left(x\right)$ is a known cumulative distribution function (CDF) which is assumed to be present under the null hypothesis, H_0.

Assuming a Gaussian communication channel as in (Wang et al., 2009), (Rostami et al., 2012), (Lei et al., 2011), $F_0(x)$ can be taken to be equal to the CDF of zero-mean Gaussian (normal) distribution, $\mathrm{N}(0,\sigma^2)$, with variance σ^2. $F_N(x)$ corresponds to the empirical CDF which is calculated as (Rostami et al., 2012)

$$F_N(x) = \frac{\left|i : x_i \le x, 1 \le i \le N\right|}{N} \tag{7}$$

where $|.|$ denotes cardinality, x_i is the i^{th} sample of the observed data vector $\mathbf{x}$, and N represents the number of observed samples. Without loss of generality, the elements of $\mathbf{x}$ are assumed to be real-valued.

There are several GOF tests proposed in the literature. In this paper, the following widely used GOF tests are considered:

- Anderson – Darling (AD) (Wang et al., 2009), (Rostami et al., 2012), (Lei et al., 2011), (Zhang, 2002), (N.-Thanh et al., 2012), (Arshad and Moessner, 2013)
- Kolmogorov – Smirnov (KS) test (Lei et al., 2011),
- Cramer – von Misses (CM) test (Lei et al., 2011),
- Log-Likelihood Ratio (LLR) GOF tests (Zhang, 2002),
- Order statistics (OS) (Rostami et al., 2012).

3.1 Anderson-Darling (AD) Test

In the AD test, it is aimed to measure the distance between the observed data and the known noise distribution. If the result of this measurement is smaller than a certain threshold, then H_0 is decided as the valid hypothesis.

The AD decision statistic is given as (Arshad and Moessner, 2013)

$$T_{AD} = N\int_{-\infty}^{\infty}\left[F_N(x) - F_0(x)\right]^2 \psi\left(F_0(x)\right) dF_0(x) \tag{8}$$

where $\psi(.)$ is a weight function defined as $\psi(u) = \left[u(1-u)\right]^{-1}$ for the interval $0 \le u \le 1$.

It is possible to simplify the AD test statistic in Eq. (8) by performing the integral. Then, T_{AD} can be obtained as (Arshad and Moessner, 2013)

$$T_{AD} = -\frac{N^2 + \sum_{i=1}^{N}(2i-1)\left(\ln z_i + \ln(1 - z_{N+1-i})\right)}{N} \tag{9}$$

where $z_i = F_0(x_i)$.

3.2 Kolmogorov-Smirnov (KS) Test

As in the AD test, the KS test aims to obtain how far the empirical CDF of the received signal is from the known CDF of the noise. It is also possible to interpret the KS test as measuring "graphically the maximum vertical distance between the two distributions, $F_N(x)$ and $F_0(x)$" (Arshad and Moessner, 2013).

Accordingly, the KS decision statistic is defined as (Lei et al., 2011)

$$T_{KS} = \max\left|F_N(x) - F_0(x)\right| \tag{10}$$

where $F_N(x)$ is the empirical CDF as defined in Eq. (7). According to Eq. (10), the test statistic T_{KS} converges to zero under hypothesis H_0.

3.3 Cramer-von Misses (CM) Test

n the CM test, the distance between $F_N(x)$ and $F_0(x)$ is defined as (Lei et al., 2011), (Stephens, 1974)

$$T_{CM} = N\int_{-\infty}^{+\infty}\left[F_N(x) - F_0(x)\right]^2 dF_0(x) \tag{11}$$

The CM test statistic can be simplified as (Lei et al., 2011)

$$T_{CM} = \sum_{i=1}^{N}\left[z_i - \frac{(2i-1)}{2N}\right]^2 + \left(\frac{1}{12N}\right) \tag{12}$$

where $z_i = F_0(x_i)$.

3.4 Log-Likelihood Ratio (LLR) GOF tests

In GOF testing, it is possible to derive the test statistics by two basic equations which are given as (Zhang, 2002)

$$Z = \int_{-\infty}^{+\infty} Z_t dw(t) \tag{13}$$

$$Z_{\max} = \sup_{t\in(-\infty,\infty)}\left\{Z_t w(t)\right\} \tag{14}$$

where $w(t)$ is some weight function.

It is clear that performance of a test statistic generated using Equations (13) and (14) depends on Z_t and $w(t)$ which are used for calculating Z and $Z_{\max}$. For Z_t, two functions are used in the literature. They are given as Pearson statistic and the log-likelihood ratio (LLR) which are defined, respectively, as (Zhang, 2002)

$$X_t^2 = \frac{N\left\{F_N(t) - F_0(t)\right\}^2}{F_0(t)\left\{1 - F_0(t)\right\}} \tag{15}$$

and

$$G_t^2 = 2N\left[F_N(t)\log\left\{\frac{F_N(t)}{F_0(t)}\right\} + \left\{1 - F_N(t)\right\}\log\left\{\frac{1-F_N(t)}{1-F_0(t)}\right\}\right]. \tag{16}$$

It is possible to generate new powerful and distribution symmetric tests by choosing $w(t)$ and Z_t functions as presented in Table 1. The resultant test statistics Z_K, Z_A, and Z_C are given as (Zhang, 2002)

$$Z_K = \max_{1\le i\le N}\left(\left(i-\frac{1}{2}\right)\log\left\{\frac{i-\frac{1}{2}}{NF_0\left(X_{(i)}\right)}\right\}+\left(N-i+\frac{1}{2}\right)\log\left[\frac{N-i+\frac{1}{2}}{N\left\{1-F_0\left(X_{(i)}\right)\right\}}\right]\right) \tag{17}$$

$$Z_A = -\sum_{i=1}^{N}\left[\frac{\log\left\{F_0\left(X_{(i)}\right)\right\}}{N-i+\frac{1}{2}}+\frac{\log\left\{1-F_0\left(X_{(i)}\right)\right\}}{i-\frac{1}{2}}\right] \tag{18}$$

$$Z_C = \sum_{i=1}^{N}\left[\log\left(F_0^{-1}\left(X_{(i)}\right)-1\Big/\frac{\left(N-\frac{1}{2}\right)}{\left(i-\frac{3}{4}\right)}-1\right)\right]^2. \tag{19}$$

Table 1. Derivation of new GOF tests using Equations (13) through (16).

Weight Function $w(t)$	Statistic Z or $Z_{\max}$	Name of obtained GOF Test
$w(t)=1$	$Z_{\max}=\sup_{t\in(-\infty,\infty)}\left\{Z_t w(t)\right\}$ $Z_t=G_t^2=2N\left[F_N(t)\log\left\{\frac{F_N(t)}{F_0(t)}\right\}+\left\{1-F_N(t)\right\}\log\left\{\frac{1-F_N(t)}{1-F_0(t)}\right\}\right]$	Z_K
$dw(t)=F_N(t)^{-1}\left\{1-F_N(t)\right\}^{-1}dF_N(t)$	$Z=\int_{-\infty}^{+\infty}Z_t dw(t)$ $Z_t=G_t^2=2N\left[F_N(t)\log\left\{\frac{F_N(t)}{F_0(t)}\right\}+\left\{1-F_N(t)\right\}\log\left\{\frac{1-F_N(t)}{1-F_0(t)}\right\}\right]$	Z_A
$dw(t)=F_0(t)^{-1}\left\{1-F_0(t)\right\}^{-1}dF_0(t)$	$Z=\int_{-\infty}^{+\infty}Z_t dw(t)$ $Z_t=G_t^2=2N\left[F_N(t)\log\left\{\frac{F_N(t)}{F_0(t)}\right\}+\left\{1-F_N(t)\right\}\log\left\{\frac{1-F_N(t)}{1-F_0(t)}\right\}\right]$	Z_C

Since the test statistics Z_K, Z_A, and Z_C use the likelihood ratio, they are alternatively named as LLR based GOF tests.

3.4 OS based GOF Testing

OS based GOF testing uses the quantiles of the observed data to measure the degree of fit of a distribution to data. In this technique, decision is taken by using the ρ-vector of the data (Rostami et al., 2012). ρ-vector is considered in several studies on OS based GOF tests (Glen et al., 2001). Thus, calculation of ρ-vector is very crucial in OS based spectrum sensing.

Computation of the ρ-vector can be carried out using the following steps (Rostami et al., 2012):

- Step #1 - Transformation: Elements of the received signal vector, $\mathbf{x}$, are transformed via the known noise CDF, $F_0(x)$, as

$$z_i = F_0(x_i), \quad i = 1, 2, \ldots, N. \tag{20}$$

Then, a new vector $\boldsymbol{z} = [z_1, z_2, \ldots, z_N]^T$ is defined.

- Step #2 - Sorting: Elements of $\boldsymbol{z}$ are arranged in ascending order of magnitude as $z_{(1)} \le z_{(2)} \le \ldots \le z_{(N)}$. The sorted vector $\tilde{\boldsymbol{z}} = [z_{(1)}, z_{(2)}, \ldots, z_{(N)}]^T$ is formed.
- Step #3 - Beta Transformation: By transforming the elements of $\tilde{\boldsymbol{z}}$ using Beta CDF, elements of ρ-vector are obtained as $\rho_i = F_\beta(z_{(i)}; i, N-i+1)$. Thus, ρ-vector is formed as $\boldsymbol{\rho} = [\rho_1, \rho_2, \ldots, \rho_N]^T$. Here, $F_\beta(y; \alpha, \beta)$ denotes the Beta CDF with shape parameters α and β

After this step has been completed, various test statistics based on ρ-vector can be defined. For example, two candidate test statistics can be given as (Glen et al., 2001)

$$T_{OS}^1 = \sum_{i=1}^{N} |\rho_i - 0.5| \text{ and } T_{OS}^2 = \sum_{i=1}^{N} (\rho_i - 0.5)^2. \tag{21}$$

Also in (Rostami et al., 2012), the authors state that, based on simulations, they could obtain the maximum probability of detection using the following test statistic

$$T_{OS}^3 = \sum_{i=1}^{N} \left| \rho_{(i)} - \frac{i}{(N+1)^2} \right| \tag{22}$$

where $\rho_{(i)}$ is the i^{th} element of the sorted ρ-vector (in ascending order).

In the end, a decision is taken by comparing the test statistic with a pre-determined threshold, γ_{OS}, as in other GOF test statistics. This can be expressed as

$H_0 : T_{OS} \le \gamma_{OS}$, channel is idle,

$H_1 : T_{OS} > \gamma_{OS}$, channel is busy.

4. SIMULATION RESULTS

In this section, the results of the simulations carried out using the models given in Eqs. (1), (2), and (3) are presented. In the simulations, it is assumed that the PU signal is given as a flat or DC valued signal such that $\mathbf{s} = \sqrt{\eta} m$ where $m = 1$ and η corresponds to signal-to-noise ratio (SNR) (Rostami et al., 2012). The noise variance σ^2 is selected as equal to 1.

The PU status change points in the models given in Eqs. (2) and (3) are obtained according to Poisson distribution. Arrival and departure rate, λ_a and λ_d, respectively, parameters of Poisson distribution, are assigned as $\lambda_a = \lambda_d = 1$ (Beaulieu and Chen, 2010). In addition, the change point values are generated so that they are within the interval $[1, N]$ to ensure that the PU status changes occur in the sensing period.

The number of observed samples are assigned as $N = 100$ and SNR is assumed to be equal to -10 dB. The thresholds for all the considered techniques are determined experimentally using Monte Carlo simulations according to which the data under both hypotheses, H_0 and H_1, are generated for 10^5 times.

For each realization, the spectrum sensing techniques considered in this letter have been calculated under both hypotheses. Performances of probability of detection, P_D, versus probability of false alarm, P_{FA}, have been displayed in Figs. 1 and 2 using receiver operating characteristics (ROC) curves.

The abbreviations in the legends of Figs. 1 and 2 are defined as follows: "AD" for Anderson-Darling test, "KS" for Kolmogorov-Smirnov test, "CM" for Cramer-von Misses test, "ZK", "ZC", and "ZA" for the LLR based test statistics ZK, ZC, and ZA, respectively, and "OS" for the order statistics based GOF test introduced in (Rostami et al., 2012).

In Fig. 1, it can be seen that all the GOF test based spectrum sensing techniques achieve good performance in terms of probability of detection, P_D, when there is no PU status change in the channel. In addition, OS based spectrum sensing technique outperforms other methods for all P_{FA} values.

It is clear from Fig. 1 that when there is a PU status change in the channel, detection performances of all the considered techniques drastically decrease.

In Fig.2, it is assumed that strictly one status and at most two status changes occur in the channel. For the case of at most two status changes, one or two status changes of the PU occur in the channel with the same probability. That is, occurrence probabilities of the models given in Eqs. (2) and (3) are equal.

According to results in Fig. 2, it can be said that the detection performances of the GOF test based spectrum sensing methods worsen as the PU traffic density in the channel increases.

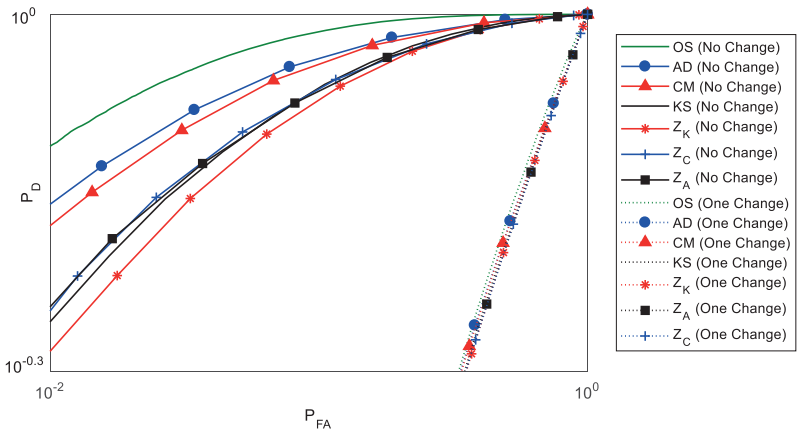

Figure 1. P_D vs. P_{FA} for no status change and one status change of the PU.

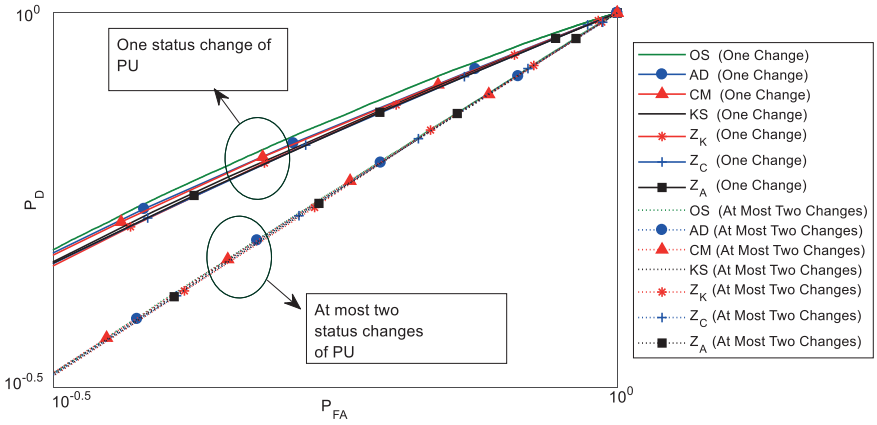

Figure 2. P_D vs. P_{FA} for one status change and at most two status changes of the PU**.**

5. CONCLUSIONS

In this study, the effect of PU traffic on the performance of GOF test based spectrum sensing methods in CR has been investigated.

Seven different GOF tests have been considered. Simulations have been carried out for the three cases of no status change, one status change, and at most two status changes of the PU in the channel. According to simulation results, it has been observed that PU traffic causes deterioration of the detection performance of the GOF test based spectrum sensing methods.

As a future study direction, we plan to search for more robust GOF test based spectrum sensing techniques in order to increase the probability of detection performance under PU traffic.

REFERENCES

Arshad, K., & Moessner, K. (2013). Robust spectrum sensing based on statistical tests. IET Comm., 7 (9), 808- 817. doi: 10.1049/iet-com.2012.0499

Beaulieu N. C., & Chen Y. (2010). Improved energy detectors for cognitive radios with randomly arriving or departing primary users. IEEE Signal Processing Letters, 17 (10), 867-870. doi: 10.1109/LSP.2010.2064768

Düzenli, T., & Akay, O. (2013). Bilişsel radyolar için birincil kullanıcı trafiği içeren kanallarda dinamik programlama ve ortalama kümülatif toplama dayalı yeni bir test istatistiğinin önerilmesi. V. İletişim Teknolojileri Ulusal Sempozyumu, İzmir, Turkey, 1-10.

Düzenli, T., & Akay, O. (2016). A new spectrum sensing strategy for dynamic primary users in cognitive radio. IEEE Communications Letters, 20 (4), 752-755. doi: 10.1109/LCOMM.2016.2527640

Glen, A. G., Leemis, L. M., & Barr, D. R. (2001). Order statistics in goodness-of-fit testing. IEEE Transactions on Reliability, 50 (2), 209-213. doi: 10.1109/24.963129

Lei, S., Wang, H., & Shen, L. (2011). Spectrum sensing based on goodness of fit tests. International Conf. on Electr., Comm. and Cont. (ICECC), Ningbo, China, 485 – 489. doi: 10.1109/ICECC.2011.6067691

N.-Thanh, N., K.-Xuan, T., & Koo, I. (2012). Comments on "Spectrum sensing in cognitive radio using goodness-of-fit testing". IEEE Trans. on Wireless Comm., 11 (10), 3409 – 341. doi: 10.1109/TWC.2012.081312.110951

Rostami, S., Arshad, K., & Moessner, K. (2012). Order-statistic based spectrum sensing for cognitive radio. IEEE Comm. Lett., 16 (5), 592 -595. doi: 10.1109/LCOMM.2012.030512.111887

Stephens, M. A. (1974). EDF statistics for goodness of fit and some comparisons. Journal of the American Statistical Association, 69 (347), 730-737.

Wang, H., Yang, E., Zhao, Z., & Zhang, W. (2009). Spectrum sensing in cognitive radio using goodness of fit testing. IEEE Trans. on Wireless Comm., 8 (11), 5427 – 5430. doi: 10.1109/TWC.2009.081586

Yücek, T., & Arslan, H. (2009). A survey of spectrum sensing algorithms for cognitive radio applications. IEEE Communications Survey & Tutorials, 11 (1), 116-130. doi: 10.1109/HMI.2016.7449196

Zhang, J. (2002). Powerful goodness-of-fit tests based on the likelihood ratio. J. R. Statist. Soc. B Part (2), 64, 281- 294. doi: 10.1111/1467-9868.00337

MÜHENDİSLİK FAKÜLTESİ

Uluslararası Mühendislik Araştırma ve Geliştirme Dergisi

International Journal of Engineering Research and Development

Cilt/Volume:9 Sayı/Issue:3 Aralık/December 2017 https://doi.org/10.29137/umagd.349955

Araştırma Makalesi / Research Article

The Development and Applications of Powder Metallurgy Manufacturing Methods in Automotive Industry

Oğuz ERDEM[1]

[1]*Ahi Evran University, Faculty of Engineering and Architecture, Mechanical Engineering*

Başvuru/Received: 08/10/2017 **Kabul/Accepted**: 01/12/2017 **Son Versiyon/Final Version**: 26/12/2017

Abstract

Over the past decade, automotive industry has developed considerably faster than other sectors in direction of consumers' demands. In order to provide worldwide emission standards, focusing on new technologies and enhancing fuel efficiency is emerged as a new trend among automobile manufacturers. Producing more efficient, lighter and eco-friendly cars without compromising performance and comfort has been the main goal of automotive industry in recent years. The high technology requirements of passenger cars with internal combustion engines as well as in hybrid and electric cars have directed the companies in sector to investigate alternative production methods. When compared with conventional manufacturing processes, powder metallurgy (PM) production methods are increasingly preferred by automobile manufacturers as they allow both profitability and part production in some special applications. In this review paper, it is aimed to give information about the development and application of PM methods in automotive sector.

Key Words

"Powder Metallurgy, Powder Injection Moulding, Metallic Foam, Automotive Industry"

* *oguz.erdem@ahievran.edu.tr*

1. INTRODUCTION

Powder Metallurgy (PM) is a technology for producing mechanical parts from metal and other powders. More recently, the vast majority of manufacturing of industrial parts is based on the PM manufacturing methods. Today, the automotive industry accounts for about 70% of the PM market (Turo et al., 2013; Gökçe et al., 2011). PM parts in the automotive sector are in high demand on an international scale due to the cost-benefit and functional flexibility they provide. PM sector, for electrical machinery industry as components; power tools, hydraulic equipment, motors and magnetic components, can supply directly or indirectly. Annual sales for PM parts in the world exceed 30 billion Euros (Turo et al., 2013; Apelian et al.,2015). The PM method's future in the automotive sector is directly related to its more complex and precise part production capability like in the aviation industry (Fan et al., 2010). Today's automotive industry is probably regarded as the sector in which the greatest amount of technology is demanded among all segments of the industry. The automotive industry is constantly in need of exploration of the latest technologies, as well as the weight reduction efforts in vehicles, the discovery of new materials to provide fuel efficiency and the reduction of emission values are becoming more and more important day by day (Sundararajan et al., 2016). Moreover, the trend of increasing performance by decreasing the engine volume known as "Engine Downsizing" is increasingly adopted by automobile manufacturers in the world. In automobiles, the weight reduction sense is often interpreted by automobile designers as the use of low density materials. The use of non-ferrous and powder-reinforced composites in automobiles is now increasingly widespread in the automotive industry through PM methods (Arslan et al., 2015; Akgun & Sahin, 2006). According to the European Aluminium Association (EAA), weight reduction of every 100 kg in cars, provides 0.6 litres of fuel savings every 100 km. 300 kg weight savings can be achieved by using aluminium in a medium sized car with a weight of 1400 kg. This gain value evolves to 20% of the total weight. In this way, the fuel savings of a car over its lifetime can be up to 3000 litres, while emissions to the environment can be reduced by 20% (Toptan et al., 2016). Brake systems are one of the points targeted in automobile weight reduction efforts. In automobiles, gray cast iron is generally used as brake disc material. In recent years, automakers have begun to produce aluminium matrix composite (Al-MC) brake discs, brake drums and other brake equipment with the PM method, which have lighter and superior properties for passenger automobiles (Toptan et al., 2016; Yu et al., 2000; Yu et al., 2005). Many studies have reported that weight gain is between 45% and 61% in the literature (Toptan et al., 2016; Kevorkijan, 2003).

Recently, the PM method is also preferred for the production of metallic foams and intensive work is being done on this area. Because of their low densities and high impact energy absorbing properties, metallic foams are used in the required areas of automobiles. The use of closed-cell aluminium foams is quite increasing nowadays in sections where weight reduction and increased reliability are required in automobiles (Yavuz et al., 2009).

In this study, it is aimed to give information about the development and application of PM methods (such as press-sinter method (PSM), powder injection moulding (PIM), metal injection moulding (MIM), metal foaming and flame spray method (FSM)) in automotive sector. From the past to nowadays examples of PM parts produced in automotive sector are given.

2. PM METHODS USED IN AUTOMOTIVE SECTOR

2.1. Press-sinter Method (PSM)

PSM is based on the principle that metal or alloy powders are mixed with various lubricants in the desired manner and then sintered in a controlled atmosphere. The pressing, also known as compression, compacting or briquetting, can be carried out either cold or hot condition depending on demand (Thümmler & Oberacker, 2009). When pressure is applied to the powder batch during pressing, the powder particles firstly slide on each other and then is condensed by high pressure transformation (German, 2007). For most applications of PSM, it is desirable that the raw strength value is to be high. If the raw density (green density) value is clarified, it is the first density of the part after pressing and before sintering (Thümmler & Oberacker, 2009). Figure 1 shows the flow diagram in PSM production of parts (German, 1984).

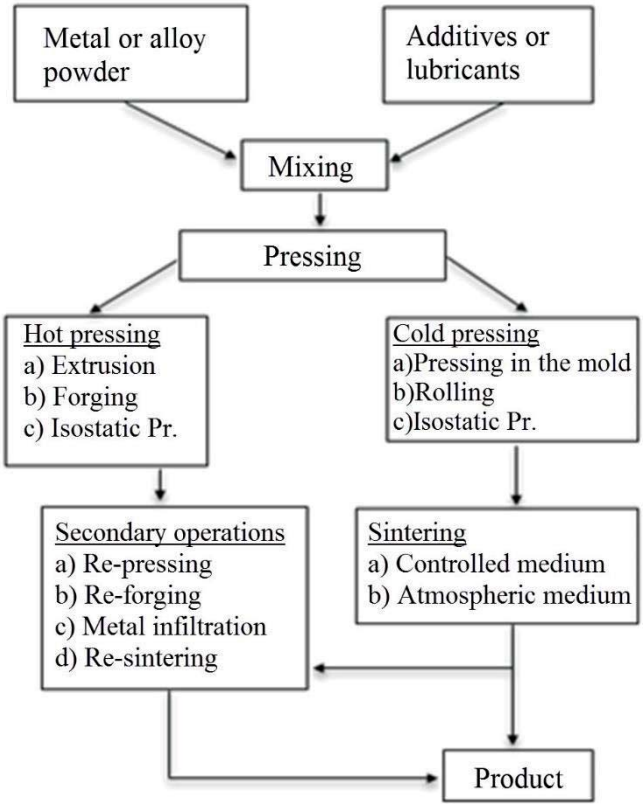

Figure 1. Flow diagram for parts production with PSM

The mixing process is carried out under controlled atmospheric conditions so that the powders are not contaminated and their properties are not changed. During mixing, lubricating agents such as stearic acid, calcium stearate, zinc stearate and lithium stearate are generally added in amounts of 0.5 to 3% to prevent friction of the powder particles which may form between each other and on the mould surfaces. In some special cases, it may also be preferred in inert gas environments to avoid oxidation during the mixing process. On the other hand, mixing is carried out by specially designed mixers (two-dimensional or three-dimensional). In automotive parts produced by PSM, pressing in the mould is generally preferred. According to the part to be produced, this process usually can be carried out in one-way or two-way moulds in cold form. Pressing pressure can vary from 0 to 800 MPa. Sintering process is generally carried out in controlled atmospheres at a temperature below 1/3 of the melting temperature of the raw material of the product to be produced (powder) and at a specified time (sintering time) (Thümmler & Oberacker, 2009).

2.2. Powder Injection Moulding (PIM) and Metal Injection Moulding (MIM)

PIM is a manufacturing method which is combining plastic injection and powder metallurgy (German, 1990). It is a moulding technology by mixing very fine-grained metal or ceramic powders with thermoplastic binders and moulding this mixture in plastic injection machines. If the powder used in the method is metal powder, it is expressed as MIM. PIM is an advanced powder processing technology developed to produce small, complex shape, precise size, precise tolerance, smooth surface, difficult to machining and excessively process able parts at reasonable cost (Karataş & Sarıtaş, 1998). PIM has four main steps; mixing, injection moulding, debinding and sintering (Upadhyaya, 2002). Mixture consisting of powder and binder is called feedstock. In order to prepare feedstock, the metal or ceramic powders are homogeneously mixed with thermoplastic binder or wax-based polymeric materials and lubricants. The initial properties of the feedstock are directly influenced by the properties of the final product after sintering. Therefore, the feedstock composition is very critical. The desired flow type is provided by the rheology study before the moulding process in the injection moulding machine. Thus, problems that may occur during moulding are avoided. Powder and binder are mixed at optimum rates and then, the feedstock is granulated. The granule feedstock is moulded into the desired shape by controlling the injection pressure, the cylinder temperature and the flow rate in the injection moulding machine. These three parameters (injection pressure, the cylinder temperature and the flow rate) are very important during moulding cycle. Injection pressure and ironing pressure are critical both in mould filling and in the preservation of the parts shape. Cylinder temperature is quite important for the feedstock not to be spoiled and also flow ability of the feedstock (German, 1990; Karataş, 1997; Erdem, 2010; Ergüney, 2005). The moulding cycle starts with closing and locking the moulds. The granules placed in the feeding hopper are melted by the heaters in the cylinder block and pushed to the mould with the help of a helical screw in the cylinder block. The feedstock transferred to the mould is kept under pressure for a while so its solidification is ensured. The injection part of the machine is withdrawn and the mould is opened to remove the part. This cycle should be completed as soon as possible at minimum cost. The task of the helical screw is to homogenize and convey the feedstock to the mould. The next stage; is to remove the binders from raw parts under controlled conditions. The debinding process is carried out in two ways: thermally (thermal decomposition) or solvent (solvent decomposition). Then the desired condensation and strength increase is achieved by the sintering process. At the end of the sintering process, a relatively low-porosity part is produced which is very close to full

density. Full dense parts produced by PIM shows close mechanical properties when compared to forged and cast parts (Karataş, 1997; Erdem, 2010). Figure 2 shows the flow diagram of PIM (German, 1990; Erdem, 2010).

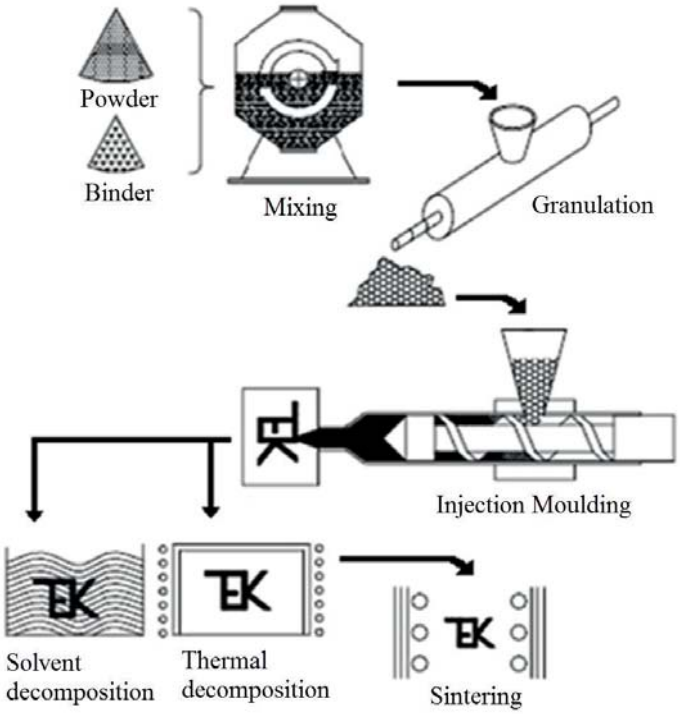

Figure 2. Flow diagram of PIM

2.3. Metal Foaming

There are two methods currently used for foaming the metal. The first is the melting method and the second is the PM method (Yavuz et al., 2009; Simone & Gibson, 1998; Banhart, 2000). Three types of foam can be produced by melting: a) injecting gas into the melt from the outside, b) adding the foaming agents to generate a gas in the molten metal, c) foaming agents previously added to the melt, which then generate foam in certain medium (Yavuz et al., 2009; Yang & Nakae, 2000).

Metallic foam production by melting process takes place mainly in three stages. In the first step, the foaming metal or alloy is melted. In the second step, gas or a foaming agent is added to generate a porous structure. In the third step, the molten metal is solidified by cooling (Yavuz et al., 2009; Baumgartaer et al., 2000). In the production of foam made by forming gas bubbles in the molten metal, the gas bubbles which tend to swell rapidly to the surface are due to the high lifting force of the liquid and where metallic foams are formed. Extremely high viscosity causes bubbles to be suppressed, while extremely low viscosity causes rapid bubbling of the bubbles (Yavuz et al., 2009; Gergely et al., 2000). Therefore, the control of the viscosity of the molten metal during foaming is very critical.

Zirconium hydride (ZrH_2) or titanium di-hydride (TiH_2) is generally used as the foaming agent in the production of metallic foams. Other chemical compounds such as calcium carbonate ($CaCO_3$), calcium hydride (CaH_2), calcium-magnesium carbonate (C_2CaMgO_6), calcium sulphate ($CaSO_4$), ferrous sulphate (FeO_4S), lead carbonate ($PbCO_3$), lead oxide (PbO) and sodium nitrite ($NaNO_2$) can be used as foaming agents under certain temperature and pressure conditions. Whether a metal will foam or not and whether it will be in the desired density depends on the decomposition rate of the gas released when the foaming agent is decomposed. The foaming agent material may be in the form of particles, granules or powder such that it can be easily dispersed in the base metal (Yavuz et al., 2009; Banhart, 2001).

The PM method is one of the most commonly used methods for the production of metal foaming and recently it is being extensively studied in this field. With the aid of the PM method, it is possible to produce sandwich foams, spherical foams and foam in profiles besides the known simple foam productions (Yavuz et al., 2009; Stöbener et al., 2003). In addition, particle reinforced foam production is also preferred in order to increase the mechanical properties of the foam material.

In the PM method for metal foaming, metal powders (generally Al powder) are mixed with the foaming agent (usually TiH_2 or ZrH_2) and pressed. As the temperature increases during the foaming process, the foaming agent in the structure dissociates and H_2 gas is released. The decomposition is visible at about 400 °C for TiH_2. This temperature is well below the melting point of aluminium (Yavuz et al., 2009; Matijasevic, 2006). During the decomposition process, expansion occurs at high temperature, in other words, foaming (Figure 3) occurs (Yavuz et al., 2009; Esmaeelzadeh & Simci, 2007; Türker, 2009). It has been proven by studies that the surface tension of the foam and the viscosity of the liquid metal change in the case of adding ceramic particles into

the melt. It is therefore known that the stability of the foam in the melt can be improved depending on these properties (surface tension and viscosity). For this reason, SiC, Al_2O_3 and various boron containing particles are added to Al-based materials predominantly. Recently, it has been discovered that powder-reinforced metallic foams (PMF) provide excellent energy damping (Yavuz et al.,). Thus, PMF is rather preferred in automobile pillar's and chassis's because of the damping property's.

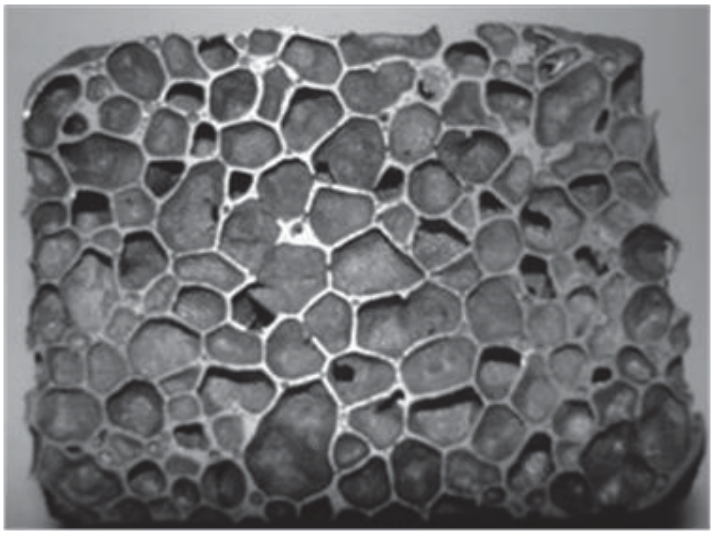

Figure 3. Aluminium based foam material

2.4. Flame spray method (FSM)

In FSM, the coating materials in powder or wire form are sprayed onto the surface of the workpiece in the presence of combustible, combustible and carrier gases from a spray gun. In the method, the powdered metal alloys in the mixture are sprayed onto the surface to be coated with the oxy-acetylene flame center by vacuuming with oxygen. It is called cold system because the surface temperature of the part during the coating process is set not to exceed 200 °C. The flame temperature is around 330 °C. Adhesion is mechanical and the thickness of the coating varies between 0.05 and 2.5 mm depending on the shape of the workpiece. Adhesion resistance is around 600-1000 PSI and the average surface roughness varies between 10-20 μm depending on the coating parameters (Figure 4) (Halamoğlu, 2003; Öner & Can, 2007).

Figure 4. FSM application

3. AUTOMOBILE COMPONENTS MANUFACTURED BY USING PM METHODS

Today, parts manufactured by PM methods are used in transmission, engine, chassis and other components of family cars, buses, trucks, light commercial vehicles and many other transport vehicles. Potential locations for PM applications in an automobile are shown in Figure 5.

The rotor and gears of the oil pump, produced with PSM and widely used in most vehicles, as well as various bearings are shown in Figure 6a and various transmission parts produced by PSM: clutch engaging hub, gear shift yokes and gears are shown in Figure 6b. Automobile gearboxes can be manual (manual shifting), semi-automatic (double clutch dsg gearbox or CVT gearbox etc.) and automatic (torque converter). The main purpose of the gears in each gearbox is to provide torque transmission reliably and silently. Extremely high geometric precision is expected in gears in gearbox applications. Therefore, the number of components produced by the PM in the synchronization module of the manual gearboxes is already quite large (Figure 7). All major components of both semi-automatic and automatic transmissions: hubs, clutch plates, clutch plate bearings, synchromesh parts and many other components have recently been manufactured by PM methods (Chang & Zhao, 2013).

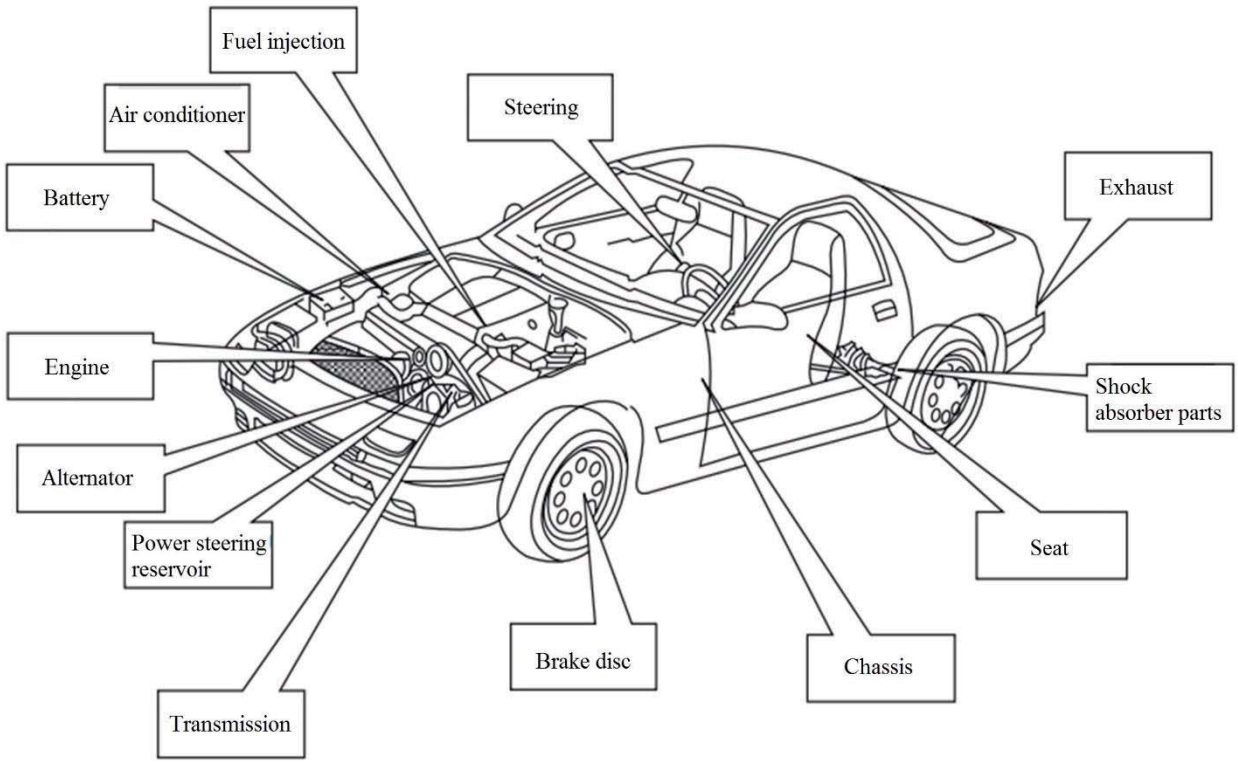

Figure 5. Potential areas for PM applications in an automobile

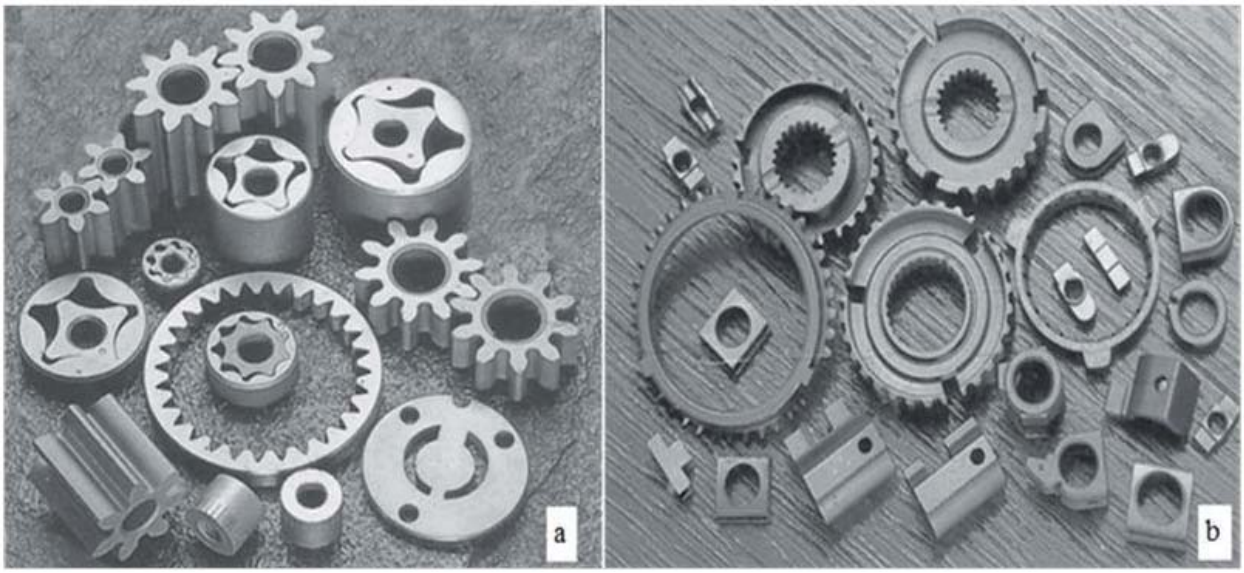

Figure 6. Automobile parts manufactured by PSM: a) oil pump parts, b) transmission parts

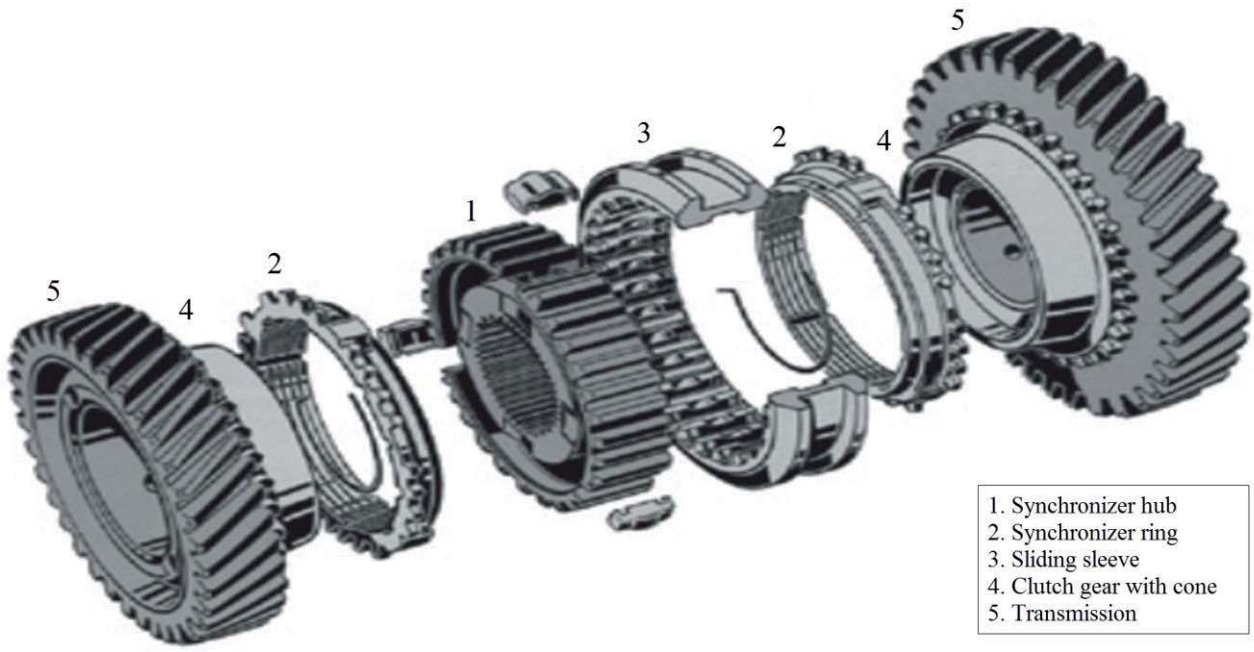

Figure 7. Synchronization module parts manufactured by PSM in gear boxes

With lower fuel consumption, more performance, more environmentally friendly automobile demands, has been led to significant changes in automobile engines. The engines are divided into categories according to the type of fuel used: petrol, diesel, hybrid or fuel cell. The schematic representation of the piston motor is shown in the Figure 8. PM methods have played an important role in the development of new engines by replacing existing engine components with better ones and increasing design possibilities (Chang & Zhao, 2013).

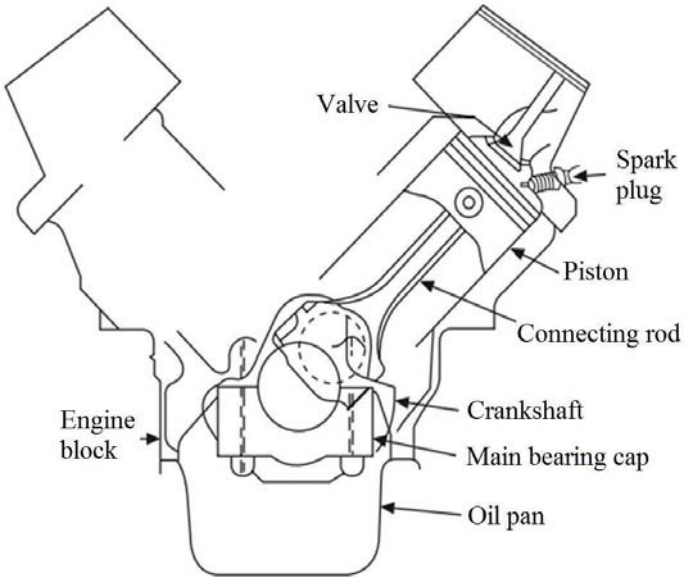

Figure 8. Schematic representation of the piston motor

The camshaft can be produced more economically thanks to the PM methods when traditionally produced from solid bars in difficult conditions by the forging method. While the camshafts are traditionally produced from solid bars under difficult conditions by forging method, owing to PM methods, they can be produced more economically. Now, it is possible to manufacture composite cams and camshafts. If clarification is required, before pressing, composite materials are obtained with reinforcements added in powder mixtures and then compression is carried out. In other words, PM allows the production of composite cams and intermediate rings as shown in Figure 9. So, it contributes to production of lighter engines and therefore provides fuel economy. The composite cams and camshafts manufactured by PSM have a high dimensional accuracy, high abrasion resistance and lighter weight (Chang & Zhao, 2013).

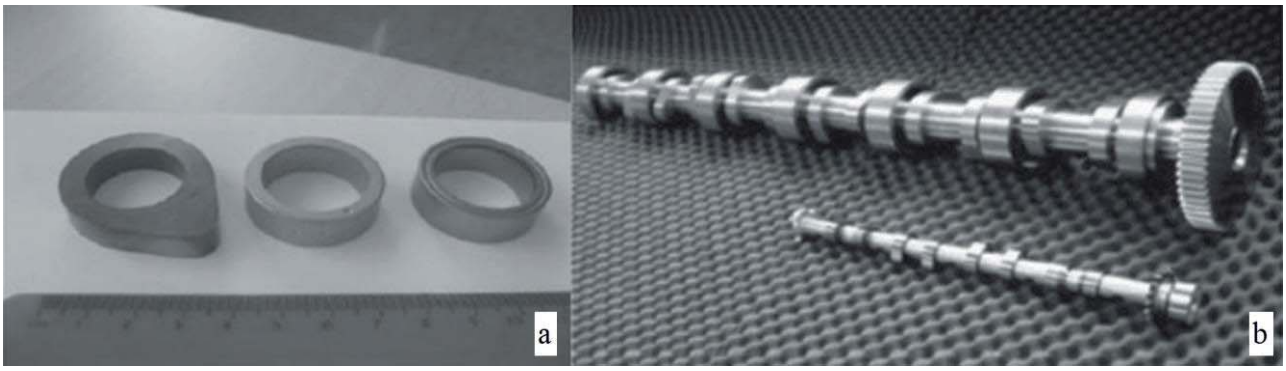

Figure 9. Composite motor components produced by PSM: a) cam and intermediate rings, b) camshaft

In the study of Arslan et al. (2015), composite cam production and characterization has been carried out using SiC added 7075 Al-alloy PM technique (production with PSM). In the work supported by ESTAŞ Eksantrik San. Inc., Pb and Mg powders are used to facilitate the sintering process. Zinc stearate is preferred as lubricant in the study. The homogenously mixed powders were poured into the metal cam mould, and then the cold pre-forming is carried out by applying a pressure of 300 MPa. Sintering was carried out to pre-formed cams in a tube furnace at 600 °C in a dry N_2 gas medium. Metallographic examination (scanning electron microscopy analysis and EDS analysis) was performed on the produced cams at the end of the study. Hardness, wear and bending tests have been performed. As a result, it was determined that hardness, bending strength and wear resistance increased as the reinforcement volume ratio increased (Figure 10) (Arslan et al., 2015).

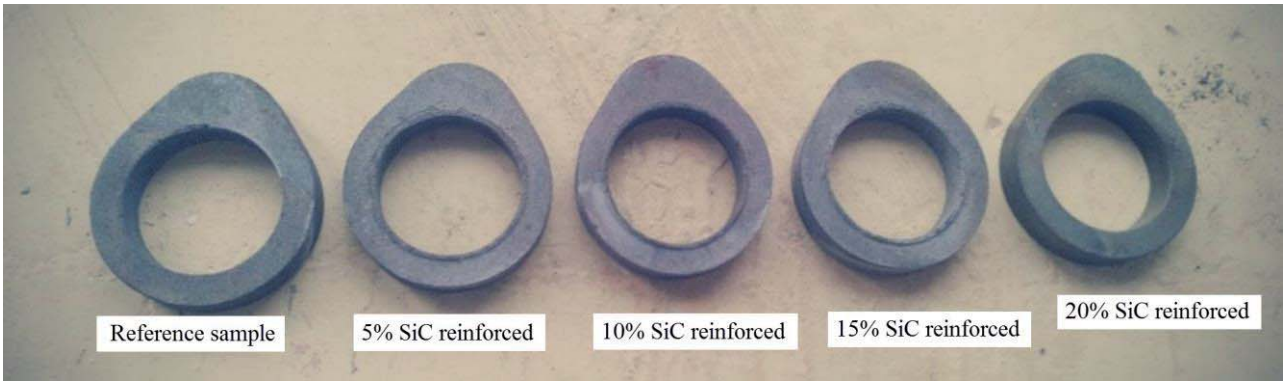

Figure 10. SiC reinforced Al-7075 matrix composite cams manufactured by PSM

The other components of the engine are: the connecting rod (Figure 11) (Fujiki, 2001) the camshaft and crankshaft gears, the timing gears, the G rotor and gear type oil pumps, the water pump impellers, the distribution pulleys (Figure 12a), the fuel pump parts (Figure 12b), the flange distributor gears, swing arm supports and attachments, engine ears, valve weights, valve housing inserts, valve lift guides, stainless steel gas flap attachments, turbochargers and fuel injector parts can also be produced by PM methods (Chang & Zhao, 2013). Over the past two decades, aluminium matrix composites (Al-MC) have been extensively explored in the automotive industry due to their lightness, high strength, high modulus of elasticity and superior abrasion resistance. One of the potential applications of Al-MC's is; Al-SiC composite brake discs (Figure 13) (Toptan et al., 2016).

Figure 11. PSM-produced rod: a) production of GKN company, b) production of Toyota engine

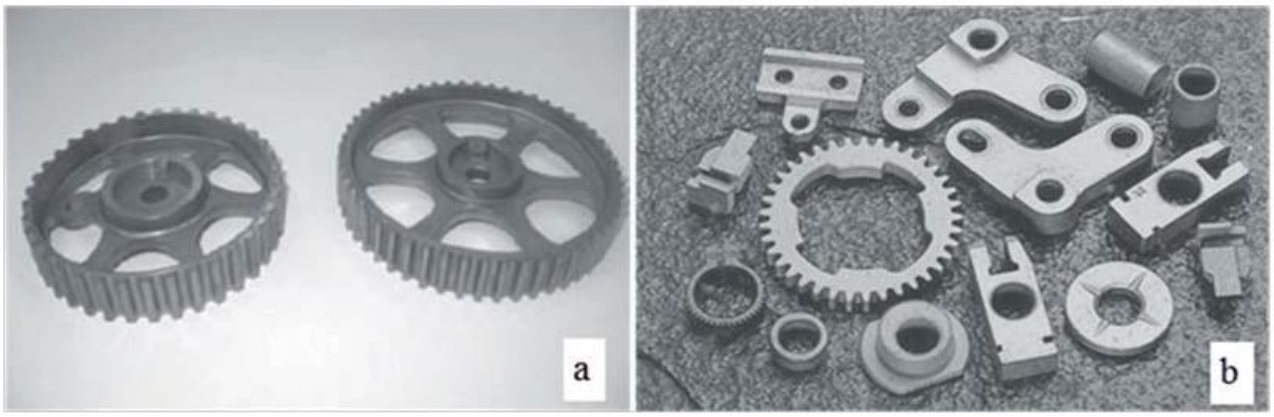

Figure 12. Parts manufactured by PSM: a) distribution pulleys, b) fuel pump parts

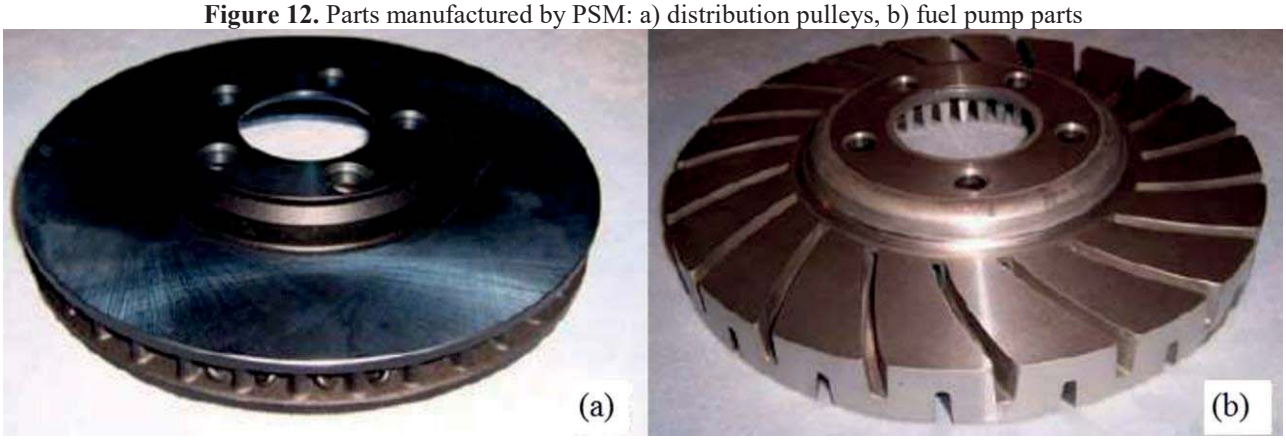

Figure 13. Brake disk: a) Brake disk (weight: 8.44 kg), manufactured from gray cast iron used in the sedan automobile, b) brake disc made of Al-SiC composite material (weight: 3.32 kg) specially designed for the same automobile

Brake pads can also be produced by PM. In the study of Ertan et al. (2010), the materials forming the brake pads (BM1: copper powder, aramid, rock wool, BM2: graphite powder, coke, ZnS, BM3: $ZrSiO_4$, Fe_2O_3, cashew powder) were mixed in a laboratory type rotary electric mixer for 5 minutes until they became homogeneous. After mixing, the mixture materials (BM1, BM2, BM3) were poured under equal weight to the 8 mould cavity found in the presses. Then brake pads are moulded at a pressure of 7.5 MPa and at a temperature of 150 °C for 5 minutes. The upper and lower surfaces of the pad-shaped powder mixture are cleaned in the grinding machine and brought to the desired size and then given to the sintering furnace (Figure 14). Later produced brake pads were subjected to friction tests. In addition to experimental studies, PSM-produced brake pad from metallic powders is also widely used in practice (Figure 15).

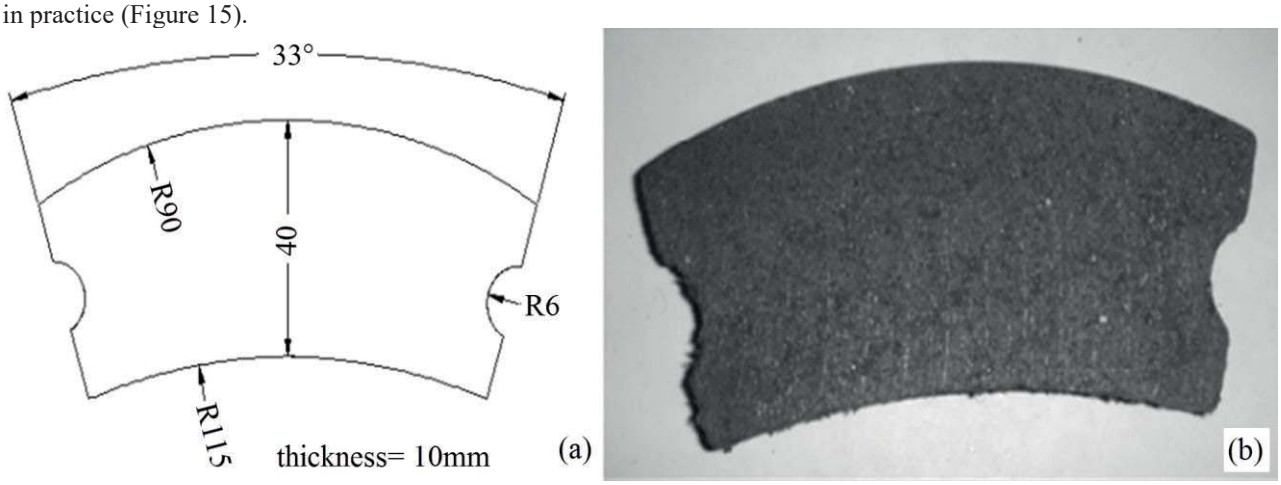

Figure 14. The brake pad manufactured by PSM: a) technical drawing, b) photo image

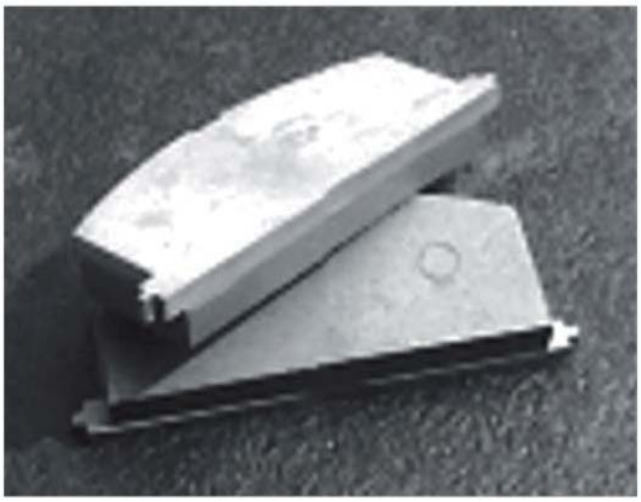

Figure 15. Metallic brake pad (PMAI)

PIM and MIM applications in the automotive industry are increasing day by day due to increasing demand in the sector. For parts production with MIM; engine (Figure 16), transmission, chassis and body parts are increasingly needed. As shown in Figure 17, the engine valve seat, various shock absorber parts and parts of the power steering system were manufactured by MIM.

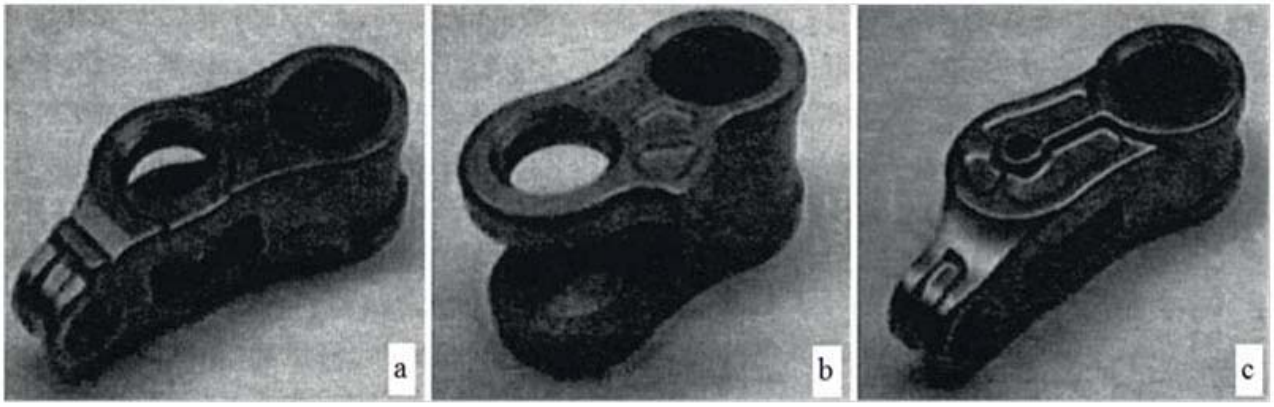

Figure 16. The swing arms manufactured by MIM for VTEC motor (HONDA): a) primary, b) middle c) secondary

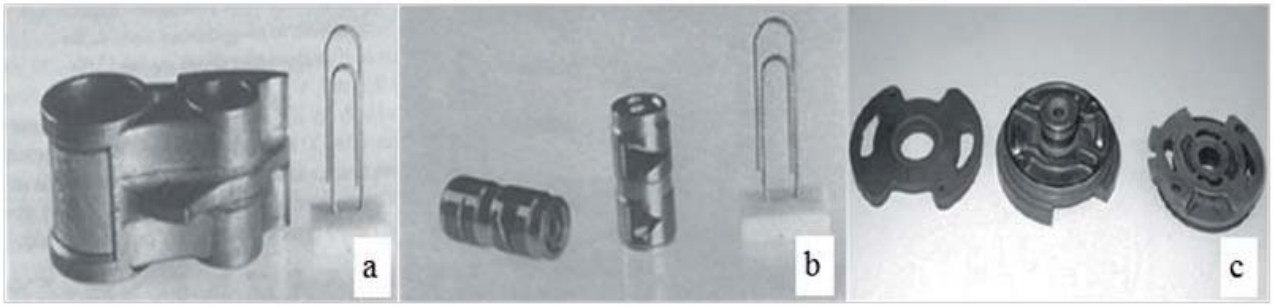

Figure 17. Parts manufactured by MIM: a) engine valve seat, b) shock absorber parts, c) parts of the power steering system

Interest in aluminium foams is increasing day by day because of the fact that their low densities and high deformation energy absorption, as well as being preferred in the areas where it is desired to increase the stability in automobiles. Given the energy absorption properties of metallic foams, in crash tests on automobiles, it has been observed that the maximum impact energy in areas with a high probability of collision is dissipated by metallic foam and also deformation is reduced (Yavuz et al., 2009; Çinici, 2004). The use of metallic foams as a filler in doors, bumpers and similar parts in automobiles is widespread. Figure 18 shows aluminium foam zones used for impact damping on the vehicle. When the acoustic effect of metallic foams is considered, it can be said that they are in a position to compete with various organic insulating materials with low cost at an impressive amount. As shown in the body of the Audi A8 (Figure 18), there are many structural foam parts on the bodywork. Because of these properties, metallic foam materials can be considered absorptive elements of impact energy (Yavuz et al., 2009). A test carried out by Steyr Daimler Puch, an Austrian automotive company, instead of the original absorber element used in the A-column, the Al foam shown in Figure 19 was used as the absorber element and subjected to the top impact test. It had been reported that successful results were obtain for the Al foam absorber element after tests (Yavuz et al., 2009).

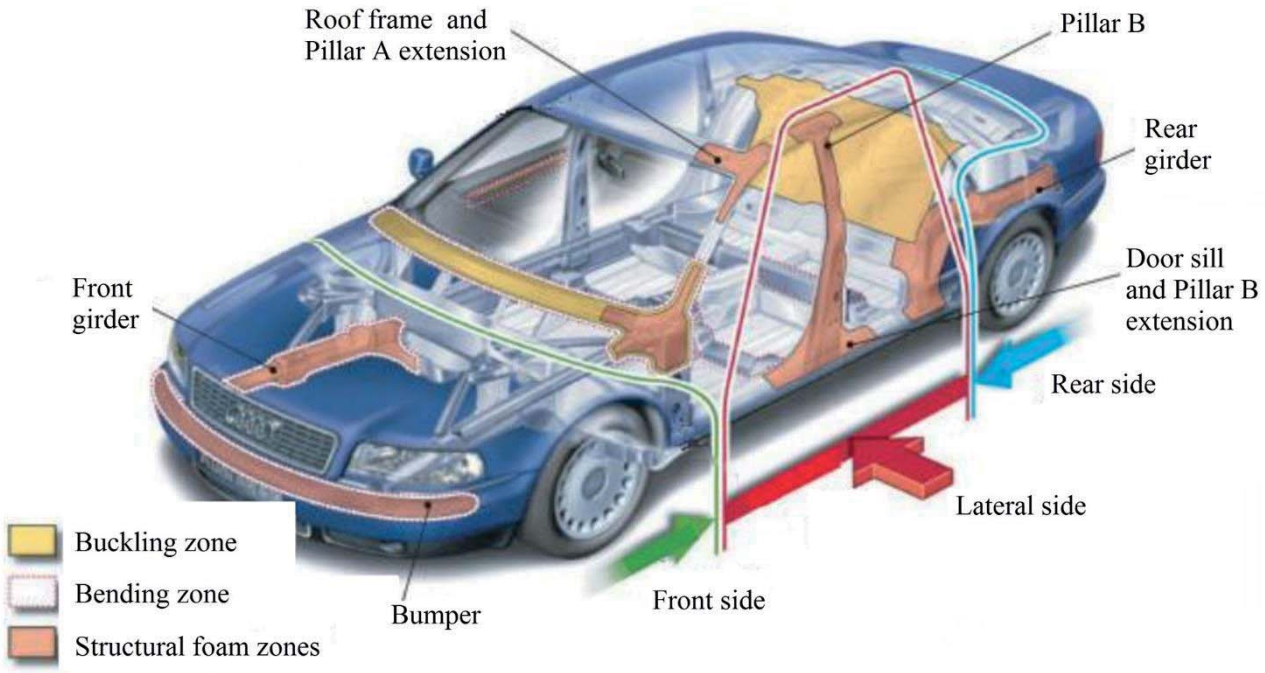

Figure 18. Structural foam materials used on Audi A8

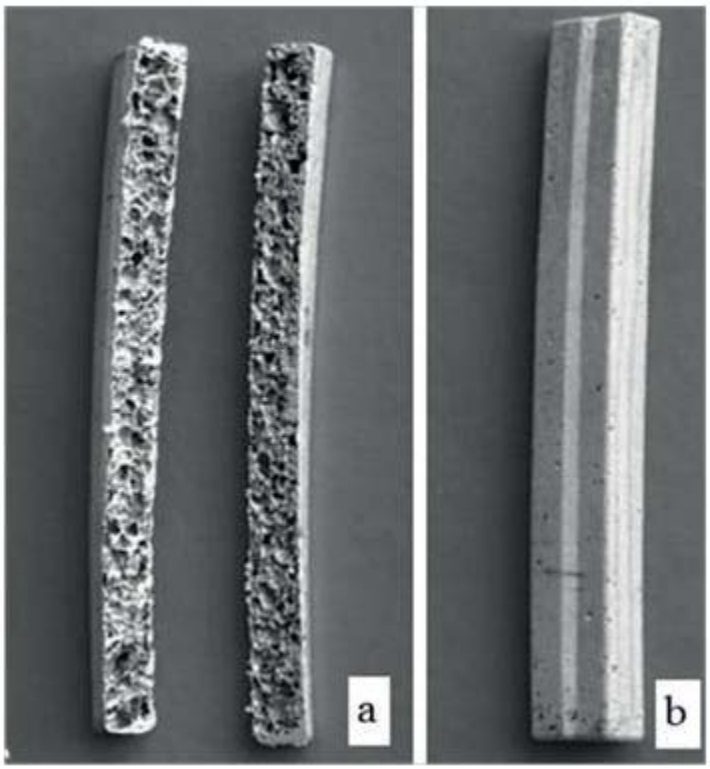

Figure 19. A-column in automobiles: a) made from Al foam, b) made from steel sheet

Also, aluminium foams have been recently used in automotive industry collision absorbers in vehicles. This new reconnaissance has contributed to the development of collision boxes. Collision boxes are usually located between the impact buffers (bumpers) and the front guard rails (Figure 20). These boxes can be deformed by absorbing all the energy in a collision at 15 km/h and they can prevent a more expensive damage that might happen in the car chasis. In Figure 21, the same length of aluminium foamed and non-foamed stainless steel 304 steel is given axial deformation under pressure (Yavuz, 2010; Doğan et al., 2015).

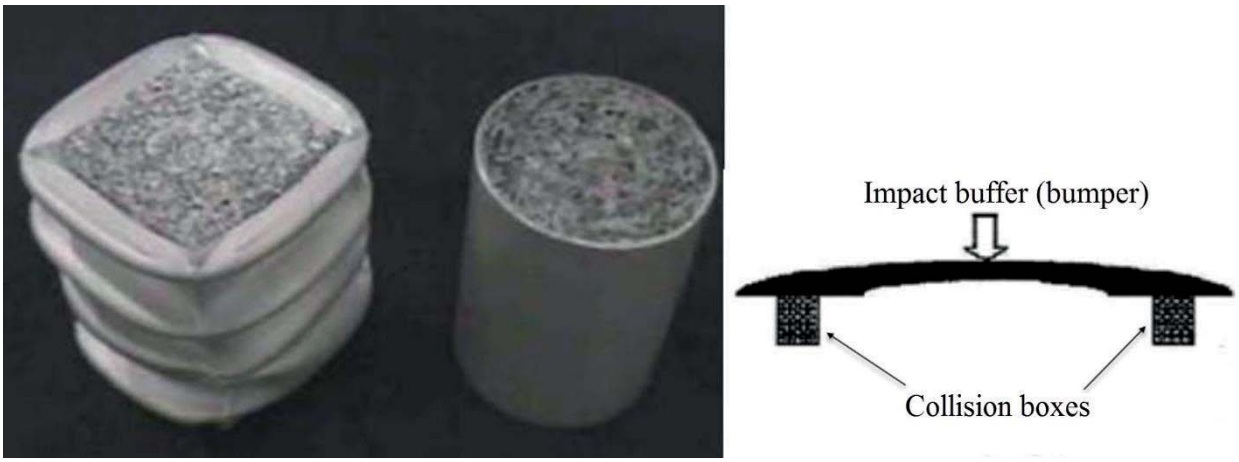

Figure 20. Collision boxes used in automobiles

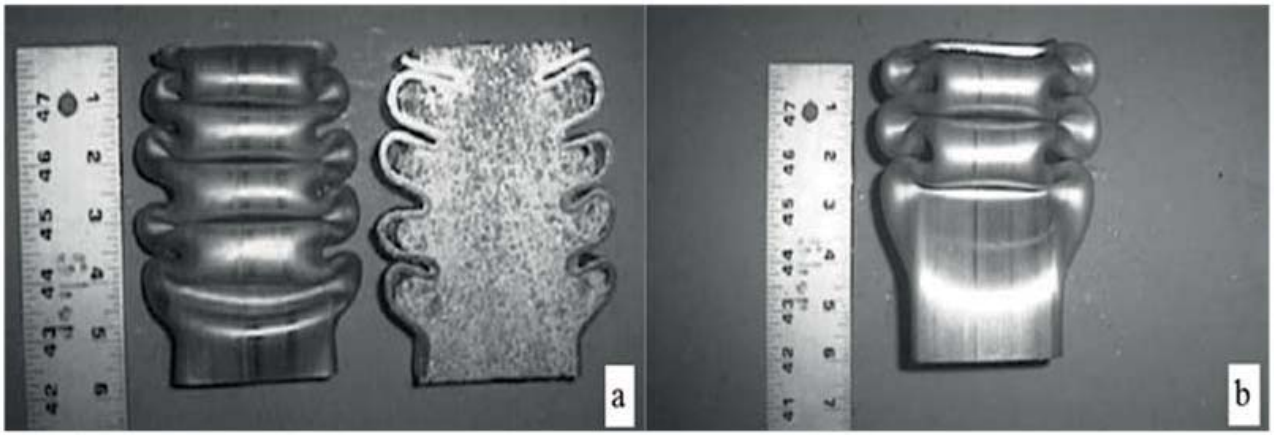

Figure 21. Deformation images of stainless steel 304 under axial pressure: a) in aluminium foam filled state, b) in non-foam state

As can be seen in Figure 21a, the aluminium foam-filled steel has undergone further deformation in the axial direction and it is folded up to 4 stratums. In Figure 21.b, the non-foam steel can only be folded 2 stratums. According to this result, it can be clearly seen that the aluminium foam padded steel can better absorb the impact energy.

In the internal combustion engines, non-stationary parts carrying moving parts such as crankshaft, camshaft, which allow linear motion of the piston to be turned into rotational motion, are given the name "bearings" and their surfaces are called "bearings surface". Sliding bearings used in motors work under difficult conditions such as variable load, temperature and pressure. In order to be able to respond to the specified challenging conditions, bearings metals are made from alloys. The most important of these are; white metals, copper-based metals and bronzes. White metals consist of elements such as lead, tin and aluminium. They are soft compared to copper-based metals and they are preferred in high-speed engines due to their good lubrication properties. Copper and bronze bearings are preferred for high power and low speed engines. Bearings in this type are difficult and costly to manufacture. To increase the resistance of the main bearings and to eliminate other problems during engine running, the researches on this subject are continuing at a rapid pace. Manufacture of bearings to be used in internal combustion engines by conventional methods is expensive and labour-intensive. Many problems are encountered in the manufacture of bearings by traditional methods. In traditional methods; it is unfortunately not possible to produce bearings having a low surface roughness, easy process able and easy to cast. Also, in traditional methods, the bearings metal is spun or normally cast. The connection rod is chemically cleaned and tin plating is done. The bearings prepared in this way are milled and the ring bearings are cut in half right through the middle. The flat one is cut along the bearings and pressed into a half circle. This situation not only reduces the productivity of the production but also increases the cost considerably in terms of time. FSM, one of the surface coating methods developed in recent years, is successfully used in many areas. In FSM, elements with different chemical and physical properties are mixed homogeneously and the surface can be easily coated with a powder spray gun (Figure 22) (Halamoğlu, 2003; Öner & Can, 2007).

Figure 22. Crankshaft master bearings coated by FSM using a new alloy of Pb, Sn, Cu and ZrO_2 powders

4. CONCLUSION

In this study, the theoretical knowledge about the processing principles of PM methods and the developments of these methods in the automotive sector are given. The innovations and advantages that PM methods bring to the automotive sector are explained in detail by examples. It has also been extensively involved in the study why automakers have chosen PM methods in vehicle production. As a general conclusion, automakers focus on; weight reduction efforts in vehicles, the discovery of new materials that will provide fuel efficiency and the reduction of emission values. These requirements have been successfully implemented by PM methods in recent years. In the coming years, it is thought that PM will provide contributions to many areas in automotive sector.

REFERENCES

Akgun, S., & Sahin, S. (2006). Influence of age hardening on mechanical properties at SiC/AA7075 composites produced by P/M. Proceedings of 11th International Materials Symposium, Türkiye, Denizli

Apelian, D., Healy, J. J., Gummeson, U., & Kasouf, C. J. (2015). Powder metallurgy parts, in: D.C. Mowery (Ed.), U.S. Industry in 2000: Studies in Competitive Performance, National Academy Press, Washington D.C.

Arslan, Z., Şimşir, M., Onurlubaşgil, T. Y., Karaca, B., & Akkan, H. (2015). Toz metalurjisi yöntemi ile kompozit kam üretimi ve karakterizasyonu. Uluslararası Katılımlı III. Ege Kompozit Malzemeler Sempozyumu, Türkiye, Aydın/Kuşadası

Banhart, J. (2001). Manufacture, Characterization and application of cellular metals and metallic foams. Progress in Materials Science, 46(6), 559-632. DOI: 10.1016/S0079-6425(00)00002-5

Banhart, J. (2000). Properties and applications for cast aluminum sponges, Adv. Eng. Mat., 2, 168-179. DOI:10.1002/(SICI)1527-2648(200004)2:4<188::AID-ADEM188>3.0.CO;2-G

Baumgartaer, F., Duarte, I., & Banhart, J. (2000). Industrialization of Powder Compact Foaming Process. Advanced Eng. Mat., 2(4), 168-174. DOI: 10.1002/(SICI)1527-2648(200004)2:4<168::AID-ADEM168>3.3.CO;2-F

Chang, I., & Zhao, Y. (2013). Advances in powder metallurgy properties, processing and applications (3rd ed.). USA, Woodhead Publishing Limited.

Çinici, H. (2004). Toz metalürjisi yöntemi ile alüminyum esaslı metalik köpük üretimi", M.S. thesis, Graduate School of Natural And Applied Sciences, Ankara.

Doğan, A., Atmaca, İ., & Özbalcı, O. (2015). Metal köpük malzemeler ve yüzey soğutmada kullanımı. 12. Ulusal Tesisat Mühendisliği Kongresi. Türkiye, İzmir.

Erdem, O. (2010). Toz enjeksiyon yöntemiyle kalıplanmış MgO takviyeli alüminanın mekanik özelliklerinin araştırılması, M.S. thesis, Graduate School of Natural And Applied Sciences, Ankara.

Ergüney, S. M. (2005). Toz enjeksiyon kalıplamada kullanılan besleme stoklarının kalıplanabilirliklerinin incelenmesi, M.S. thesis, Graduate School of Natural And Applied Sciences, Ankara.

Ertan, R., & Yavuz, N. (2010). Balata malzemelerinde kullanılan yapısalların balatanın tribolojik ve fiziksel özelliklerine etkisi. Uludağ Üniversitesi Mühendislik-Mimarlık Fakültesi Dergisi, 15(1), 169-177.

Esmaeelzadeh, E., & Simci, A. (2007). Formability and compressive properties of AlSi7-3 vol.% SiC-0.5 wt.% TiH2 powder compact. Materials Letters, 62(10-11), 201-215. doi.org/10.1016/j.matlet.2007.09.044

Fan, K., Chen, S., Chen, J., & Liao, W. (2010). Development of auto defect classification system on porosity powder metallurgy parts. NDT&E International, 43(6), 451-460. doi.org/10.1016/j.ndteint.2010.04.005

Fujiki, A. (2001). Present state and future prospects of powder metallurgy parts for automotive applications. Materials Chemistry and Physics, 67(1-3), 298-306. doi.org/10.1016/S0254-0584(00)00455-7

Gergely, V., Degischer, H. P., & Clyne, T. W. (2000). Recycling of MMCs and production of metallic foams. Comprehensive Composite Materials, 3, 797- 820.

German, R. M. (2007). Toz Metalurjisi ve Parçacıklı Malzeme İşlemleri. Ankara, Uyum Ajans.
German, M.R. (1990). Powder Injection Molding. USA, Metal Powder Industries Federation.

German, R. M. (1984). Powder Metallurgy Science. New Jersey, MPIF Princeton.

Gökçe, A., Findik, F., & Kurt, A. O. (2011). Microstructural examination and properties of premixed Al–Cu–Mg powder metallurgy alloy. Materials Characterization, 62(7), 730-735. doi.org/10.1016/j.matchar.2011.04.021

Halamoğlu, T. (2003). Metal püskürtme yöntemiyle aşınmaya dayanıklı kaplamalar. Yüzey İşlemler Dergisi, 3(1), 154-159.

Karataş, Ç., & Sarıtaş, S. (1998). Toz Enjeksiyon Kalıplama: Bir Yüksek ve Teknoloji İmalat Metodu. Journal of the Faculty of Engineering and Architecture of Gazi University, 13(2), 193-228.

Karataş, Ç. (1997). Toz Enjeksiyon Kalıplamada Karışımın Reolojisi, Ph.D. thesis, Graduate School of Natural And Applied Sciences, Ankara.

Kevorkijan, V. (2003). Engineering wear-resistant surfaces in automotive aluminum. The Journal of the Minerals, 55(2), 32-34. DOI: 10.1007/s11837-003-0223-7

Matijasevic, B., Banhard, J., Fiechter S., Görke, O., & Wanderka, N. (2006). Modification of TiH_2 for improved Al Foam Manufacture. Acta Meterialla, 54(7), 1887-1900. doi.org/10.1016/j.actamat.2005.12.012

Öner, C., & Can, İ. (2007). Toz püskürtme yöntemiyle krank mili ana yatağının yeni bir alaşım ile kaplanması. Makine Teknolojileri Elektronik Dergisi, 1(2), 77-81.

Simone, A. E., & Gibson, L. J. (1998). The effects of cell face curvature and coruscations on the stuffiness and strength of metallic foam. Acta Materialla, 46, 3926-3935.

Stöbener, K., Baumaster, J., Lehmhus, D., Stanzick, H., & Zöllner, V. (2003). Composite based on metallic foams: phenomenology; production; properties and principles. Int. Conf. On Advanced Metallic Materials, Slovakia, 2003, 157-168.
Sundararajan, G., Joshi, S. V., & Krishna, L. R. (2016). Engineered surfaces for automotive engine and power train components. Current Opinion in Chemical Engineering, 11, 1-6. doi.org/10.1016/j.coche.2015.10.001

Thümmler, F., & Oberacker, R. (1993). An introduction to powder metallurgy (1st ed.). London, The Institute of Materials.

Toptan, F., Kumdalı, F., & Kerti, I. (2016). Al-B4C kompozitlerinin fren diski olarak kullanılabilirliğine genel bir bakış. TMMOB Metalurji ve Malzeme Mühendisleri Odası- Metalurji Dergisi, 145, 37-46.

Turo, A., Chavez, J. A., Hernandez, M. J. G., Bulkai, A., Tomek, P., Toth, G., Girones, A., & Jordi, S. (2013). Ultrasonic inspection system for powder metallurgy parts. Measurement, 46(3), 1101-1108. doi.org/10.1016/j.measurement.2012.10.016

Türker, M. (2009). Proceedings from IATS'09: Toz metalürjisi yöntemi ile alüminyum köpük üretimi. Turkey, Karabük.

Upadhyaya, G. S. (2002). Powder Metallurgy Technology. England, Cambridge International Science Publishing.

Yang, C. C., & Nakae, H. (2000). Foaming characteristics control during production of aluminum alloy foam. Journal of Alloys and Compounds, 313, 188-191. DOI: 10.1016/S0925-8388(00)01136-1

Yavuz, İ. (2010). Metalik köpük malzemeler ve uygulama alanları. Electronic Journal of Vehicle Technologies (EJVT), 2(1), 49-58.

Yavuz, İ., Başpınar, M. S., & Bayrakçeken, H. (2009). Metalik Köpük Malzemelerin Taşıtlarda Kullanımı. Teknolojik Araştırmalar: TATED, 3(1), 43-51.

Yu, P., Mei, Z., & Tjong, S. C. (2005). Structure, thermal and mechanical properties of in situ Al-based metal matrix composite reinforced with Al2O3 and TiC submicron particles. Materials Chemistry and Physics, 93(1), 109–116. doi.org/10.1016/j.matchemphys.2005.02.028

Yu, X. X., & Lee, W. B. (2000). The design and fabrication of an alumina reinforced aluminum composite material. Composites: Part A, 31(3), 245–258. doi.org/10.1016/S1359-835X(99)00068-8

MÜHENDİSLİK FAKÜLTESİ

Uluslararası Mühendislik Araştırma ve Geliştirme Dergisi

International Journal of Engineering Research and Development

Cilt/Volume:9 Sayı/Issue:3 Aralık/December 2017 https://doi.org/10.29137/umagd.349964

Araştırma Makalesi / Research Article

Effect of Composite Patch Geometry in Notched Plates Under Low Velocity Impact

Umut ÇALIŞKAN[*1], Recep EKİCİ[1], Mustafa Kemal APALAK[1]

[1]*Erciyes University, Faculty of Engineering, Kayseri, TURKEY*

Başvuru/Received: 08/10/2017 **Kabul/Accepted**: 01/12/2017 **Son Versiyon/Final Version**: 26/12/2017

Abstract

The repair technique of the composite patch with bonding adhesive are used with the purpose of repairing materials and increasing working life of the materials. In this study, the impact strength of notched metal materials repaired by composite patch investigated by numerically. Fiber reinforced laminated composite patch was modeled by using finite element model. Composite patch was bonded to damaged materials, and this structure was subjected to impact test. The geometrical and material non-linearities were considered in the explicit dynamic analysis. The notched plate was made of aluminum 6061-T6. The effects of design parameters, such as composite patch geometry, on the impact energy absorption of the plates were investigated. The metal notched plates were modeled as a Johnson-Cook material model and the composite patches were modeled orthotropic elastic material model and Hashin damage. In the analysis results, the damage mechanisms of composite patch were exhibited and strength of damaged materials was exhibited in terms of contact force, kinetic energy and stress distributions. The effect of patch geometries was also investigated in terms of absorbing impact energies. As the plates without patch perforated, repaired metal notched plates with composite patch did not perforate.

Key Words

"Composite Patch, Notched Materials, Impact, Non-linear Finite Element Method."

*** ucaliskan@erciyes.edu.tr***

the prediction of the initiation and propagation of the damages in the composite materials needs various damage models to be considered.

The other important subject is that the occuring damages at the composite and metal materials repair. The repair technique of the composite patch with bonding adhesive are used with the purpose of repairing materials and increasing working life of the materials. The damages in different size occur at the nose cone of the air crafts, cockpit glasses, the outside of the aerofoils, horizontal and vertical stabilizator because of extrinsic factors such as birds, hail, lightning, impact vehicles on the ground. The damage in different size occur again at the car bumper and hood cause of the crashing other cars and objects. Different repair technique and patch are used to prevent damage progression, increasing static and fatigue strength again, increasing the working life. The determining other issues are that choosing the suitable patch for the damaged materials, measuring the strength of the damaged materials after applying the patch. Mall and Conley (2009) presented a crack growth behavior of cracked panels repaired with bonded composite patch using a two-dimensional finite element analysis. Their experimental tests about fatigue were carried out precracked aluminum specimens of two thicknesses (1 and 6.35 mm), with and without debond, and repaired asymmetrically. Four and ten times relative to unrepaired cases were extended fatigue lives of thick and thin repaired panels, respectively. Their experimental values at the unpatched face were in good agreement the predicted fatigue crack growth rates but not at the patched face. Thus, the present analysis provided a conservative assessment of durability and damage tolerance of repaired thin and thick panels. Shams and El-Hajjar (2013) studied on the overlay repair of scratch damage in carbon- fiber/epoxy composite laminates numerically and experimentally. The scratch damage severed several load bearing plies and results in a lack of symmetry in an originally symmetric multidirectional laminate. The effects of the repair patch variables on the overall efficiency of the repair procedure and the lamina level stress states were investigated using the ply-by-ply p-version finite element model. Their results showed that interlaminar crack propagation in the direction parallel to the surface kept back with careful selection of repair parameters. Albedah et al. (2016) investigated the fatigue behavior of aluminum alloy 2024 T3 v-notched specimens repaired with composite patch under block loading experimentally. Two different loading blocks were applied as increasing and decreasing at two stress ratio: R = 0 and R = 0.1. Their damaged specimens were observed using scanning electron microscope at different magnifications to analyze their fractured surfaces. The results showed that the crack growth is accelerated for both repaired and unrepaired specimens. Cheng et al. (2014) studied notched composite plates repaired with external circular patches. In the case of a strong adhesive joint, the stiffness of the patches had to be optimized to release high stress concentration and obtained the best repair performance. Their results showed that the damage progression of the repairs depended not only on the patch stiffness but also on the stacking sequence. Constantin et al. (2013) presented a behaviour of repaired Al panels which are bonded composite repair patches under lateral pressure loads for the different geometries and materials. Their finite element models were validated by experiments in a number of cases, and then used to evaluate the whole proposed range of repair patching configurations. Errouane et al. (2014) investigated a composite patch repair aluminum plate consisting a central crack for the optimization. The patch was bonded over a cracked aluminum sheet using a small adhesive layer placed in between. The numerical model allowed to predict the patch effect on the behavior of the cracked plate under tensile loading. Several stacking sequences and material properties were also investigated to reduce the stress concentration in the vicinity of the crack tip, leading to strong volume reduction. Benyahia et al. (2015) studied the behaviour of aged bonded composite repair of aircraft structures experimentally and numerically. The accelerating aging of the patch was realized by immersion in water for 120 days. Their experimental results showed that the fatigue life of the aircraft structures could be significantly improved with the patch repair. The patch aging reduced the repair performances because of the reduction of the composite rigidity by humidity absorption. Sabelkin et al. (2007) studied several parameters/factors for the mechanical and fatigue behaviors of a cracked 7075-T6 aluminum panel repaired with one-sided adhesively bonded composite patch by experimentally and analytically. The effects of cool-down temperature during patch bonding were also investigated. Residual thermal stresses, developed during patch bonding, requires the knowledge of temperature at which adhesive becomes effective in creating a bond between the specimen and patch. The bonded patch repair of a cracked panel provides a considerable increase in the residual strength as well as fatigue life.

This paper aims to investigate the low velocity impact response of repaired notched plates with composite patches and the effects of composite patch geometry for the various impact energies. ABAQUS/Explicit was used to predict the dynamic response of repaired notched plates. A special care was paid for the behavior of impacted regions and composite patches geometry.

2. **Finite element model**

The low velocity impact behavior of notched plates was studied using ABAQUS/Explicit (version 6.14)(ABAQUS/Explicit). The impact behavior was investigated for different composite patch geometry under three impact energy levels of 50, 100 and 150 J. Notched metal plate was in dimension of 100x100 mm and its thickness was taken as 2 mm. Notch geometry was in dimenson of 1x1x30 mm.

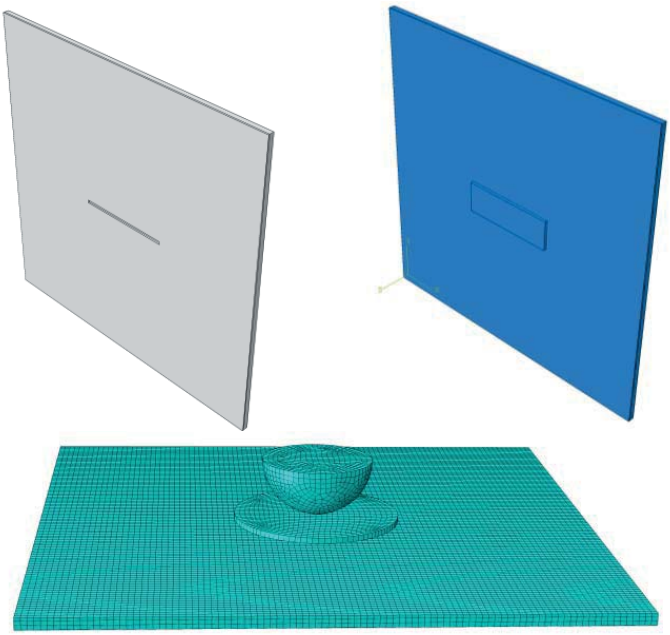

Figure 1. Finite element model

Two different types patch geometries were used as circular and rectangular. Circular composite patch radius was in dimension of 15 mm and thickness of 1 mm. The rectangular composite patch geometry was in dimension 1x10x30 mm. Damaged metal with notched, circuler and rectangular composite patch models were shown in Figure 1. The stress and strain curve of notched metal plate of AA6061-T6 was shown in Figure 2.

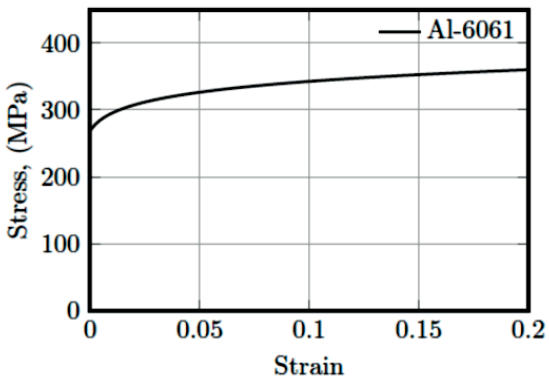

Figure 2. Stress-Strain curve of AA 6061 – T6.

The non-linear behaviour of face-sheets materials was modeled using Johnson-Cook material model. The Johnson-Cook dynamic failure model is used as a specific case of the ductile damage initiation criterion for metals in ABAQUS/Explicit. The important parameneters used in Johnson-Cook dynamic failure model were given in Table 1 for aluminum 6061 T6.

Table 1. Constants for Johnson-Cook dynamic failure model of Aluminum Al6061 T6

Aluminum 6061 T6	Johnson-Cook Model
ρ (kg/m 3)	2700
E (GPa)	70
v	0.33
C_p (J/kgK)	910
α (K^{-1})	$2.30x10^{-5}$
$\dot{\varepsilon}$ (s^{-1})	597.2
A (MPa)	270
B (MPa)	154.3
C	0.1301
n	0.2215
m	1.34
T_f(K)	925
d_1	-0.77
d_2	1.45
d_3	0.47
d_4	0.0
d_5	1.6

The impactor was modeled as a rigid body behavior. The encastered boundary condition was applied to the model. Composite patches were modelled using a continuum shell element with 8-node hexahedron (SC8R). The mechanical contact between the impactor and plate was simulated by the GENERAL CONTACT ALGORITHM in Abaqus/Explicit. Composite patches were modelled as four layer and unidirectional laminate fiber angle of 0◦(Fig. 2). The material damage initiation capability for fiber-reinforced materials requires that the behavior of the undamaged material is linearly elastic, is based on Hashin's theory and can be used in combination with the damage evolution model described in “Damage evolution and element removal for fiber-reinforced composites” in the Abaqus/Explicit code.

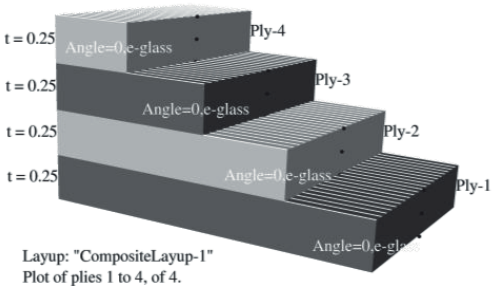

Figure 2. Py orientation of fiber composite patch

Damage initiation refers to the onset of degradation at a material point. In Abaqus the damage initiation criteria for fiber-reinforced composites are based on Hashin's theory. These criteria consider four different damage initiation mechanisms: fiber tension, fiber compression, matrix tension, and matrix compression and mechanical properties for the composite plates E-glass/epoxy are given in Table 2 (Singh et al. (2015)).

Table 2. Elastic and strength properties for composite patch

Longitudinal modulus, E_{11}	40 (GPa)
Transverse modulus, $E_{22} = E_{33}$	10 (GPa)
Shear modulus, $G_{22} = G_{33}$	3.15 (GPa)
Shear modulus, G_{23}	4.32 (GPa)
Volume fraction of fiber, V_f	0.54
Poisson's ratio, $\mu_{12} = \mu_{13}$	0.3
Poisson's ratio, μ_{23}	0.21
Density	1780 (kg/m^3)
Longitudinal tensile strength, X_T	988 (MPa)
Transverse tensile strength, $Y_T = Z_T$	44 (MPa)
Longitudinal compressive strength, X_C	1432 (MPa)
Transverse compressive strength, $Y_C = Z_C$	285 (MPa)
In-plane shear strength $S_{12} = S_{13}$	60.6 (MPa)
Interlaminar shear strength, S_{23}	22 (MPa)

The initiation criteria have the following general forms:

Fiber tension ($\widehat{\sigma_{11}} \geq 0$)

$$F_f^t = \left(\frac{\widehat{\sigma_{11}}}{X^T}\right)^2 + \alpha\left(\frac{\widehat{\tau_{12}}}{S^L}\right)^2 \tag{1}$$

Fiber compression ($\widehat{\sigma_{11}} < 0$)

$$F_f^c = \left(\frac{\widehat{\sigma_{11}}}{X^C}\right)^2 \tag{2}$$

Matrix tension ($\widehat{\sigma_{22}} \geq 0$)

$$F_m^t = \left(\frac{\widehat{\sigma_{22}}}{Y^T}\right)^2 + \alpha\left(\frac{\widehat{\tau_{12}}}{S^L}\right)^2 \tag{3}$$

Matrix compression ($\widehat{\sigma_{22}} < 0$)

$$F_m^c = \left(\frac{\widehat{\sigma_{22}}}{2S^T}\right)^2 + \left[\left(\frac{Y^C}{2S^T}\right)^2 - 1\right]\frac{\widehat{\sigma_{22}}}{Y^C} + \left(\frac{\widehat{\tau_{12}}}{S^L}\right)^2 \tag{4}$$

$\widehat{\sigma_{11}}, \widehat{\sigma_{22}}, \widehat{\tau_{12}}$ are components of the effective stress tensor, $\hat{\sigma}$, that is used to evaluate the initiation criteria and which is computed from:

$$\hat{\sigma} = M\sigma \tag{5}$$

Where σ is the true stress and is the damage operator:

$$M = \begin{bmatrix} \frac{1}{(1-d_f)} & 0 & 0 \\ 0 & \frac{1}{(1-d_m)} & 0 \\ 0 & 0 & \frac{1}{(1-d_s)} \end{bmatrix} \tag{6}$$

d_f, d_m, and d_s are internal (damage) variables that characterize fiber, matrix, and shear damage, which are derived from damage variables , d_f^t , d_f^c, and , d_m^c corresponding to the four modes previously discussed, as follows :

$$d_f = \begin{cases} d_f^t & if\ \widehat{\sigma_{11}} \geq 0 \\ d_f^c & if\ \widehat{\sigma_{11}} < 0 \end{cases} \tag{7}$$

$$d_m = \begin{cases} d_m^t & if\ \widehat{\sigma_{22}} \geq 0 \\ d_m^c & if\ \widehat{\sigma_{22}} < 0 \end{cases} \quad (8)$$

$$d_s = 1 - (1 - d_f^t)(1 - d_f^c)(1 - d_m^t)\,(1 - d_m^c) \quad (9)$$

3. Results

Impact analyses were performed for impact energies of 50, 100 and 150 J, respectively. The impactor was spheral tip geometry of 20 mm in diameter, and 5.045 kg of a mass. The geometrical design parameter of composite patch geometry was investigated to improve the impact energy absorption capability of the structure and avoid damage. The temporal variations of the contact force and kinetic energy were determined for three impact energy levels of 50, 100 and 150 J, respectively. Two different types of composite patch geometry were used for repairing notched metal plate as circular and rectangular. Impact analyses were also performed for without patch for three energy levels. These three situations were compared in terms of contact force histories, kinetic energy levels and stress distributions on the notched metal plate of AA6061 – T6. E-glass/epoxy (UD) was used for composite patch material and thickness of 1 mm (4 layer).

Figure 3 shows the effect of composite patch geometry on the temporal variations of the contact force and kinetic energy histories for three impact energy levels, respectively. The peak contact forces are measured as 11.92, 14.29 and 13.81 kN under the impact energy level of 50 J notched plate without patch, with circular patch and with rectangular patch, respectively, and the corresponding peak contact times are nearly similar for all specimens in about 3 ms. The impact analyses are completed in the total contact times of 4.5, 4.2 and 4.3 ms. The peak contact forces are measured as 13.75, 22.91 and 19.53 kN under the impact energy level of 100 J notched plate wihout patch, with circular patch and with rectangular patch, respectively, and the corresponding peak contact times are nearly similar for all specimens in about 2.5 ms. The impact analyses are completed in the total contact times of 4.62, 3.76 and 3.86 ms. The peak contact forces are measured as 13.75, 31.47 and 21.63 kN under the impact energy level of 150 J notched plate, circular patch and rectangular patch, respectively, and the corresponding peak contact times are nearly similar for all specimens in about 2 ms. The impact analyses are completed in the total contact times of 7.02, 3.58 and 43.78 ms. As the impact energy is increased, the peak contact force levels are increased and the total contact durations are decreased for notched metal with circular and rectangular patch. However, the notched metal plate without patch is perforated in the impact energies of 100 and 150 J. The minimum peak contact force appeared in notched metal plate without patch and the maximum peak contact force was appeared in circular patch geometry model.

The notched metal plate without patch, with circular patch and with rectangular patch reduce impact energy of 50 J to kinetic energy levels of 8.36, 11.20 and 10.54 J, respectively; thus, the impact energies are dissipated by 83.28, 77.6 and 79.2%, respectively. For the impact energy level of 100 J the models reduce to kinetic energy levels of 6.75, 14.65 and 13.23 J, respectively and the impact energies are dissipated by 93.25, 85.35 and 86.77%, respectively. They also reduce impact energy of 150 J to kinetic energy levels of 3.03, 16.9 and 12.97 J, respectively; thus, the impact energies are dissipated by 96.97, 83.1 and 87.03%, respectively. The notched metal without patch could absorb more much impact energy, however these plates were perforated in the impact energy levels of 100 and 150 J.

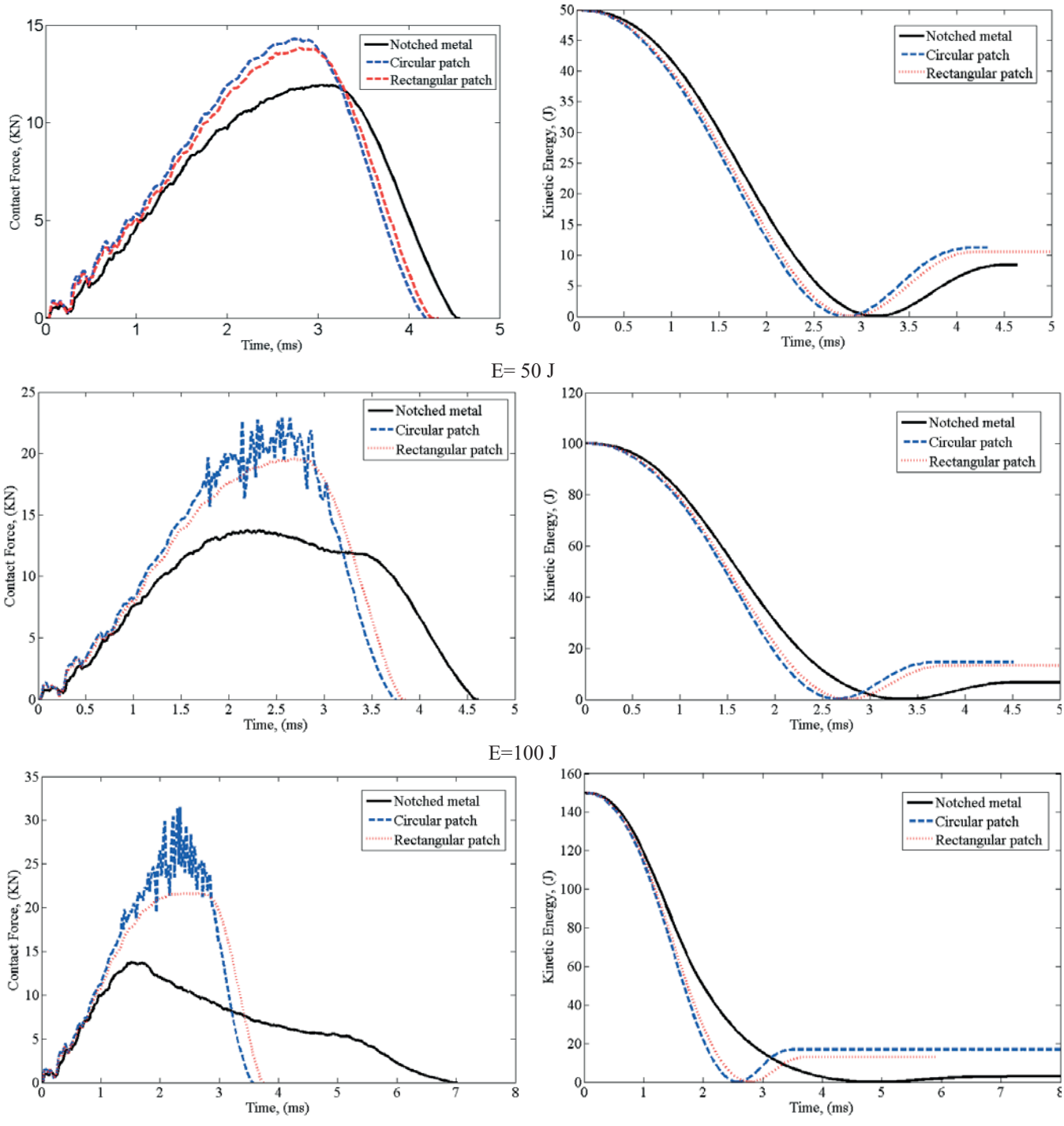

Figure 3. Effect of the composite patch geometry on the variations of contact force and kinetic energy for the impact energies of 50, 100 and 150 J.

Figure 4 shows the stress distributions of the notched plate without patch for the impact energy levels of 50, 100 and 150 J. As the impact energy is increased, the stress levels increase naturally. The maximum von-misses stress levels for the impact energy levels of 50, 100 and 150 J are 344, 358 and 403 MPa, respectively. The results showed that, If the composite patch is not used, plate can be perforated under impact energy levels of 100 and 150 J.

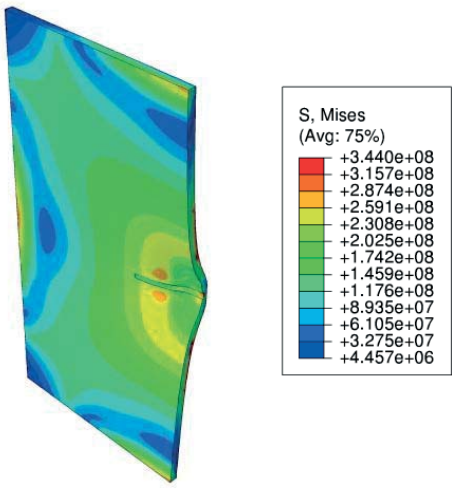

a) E= 50 J

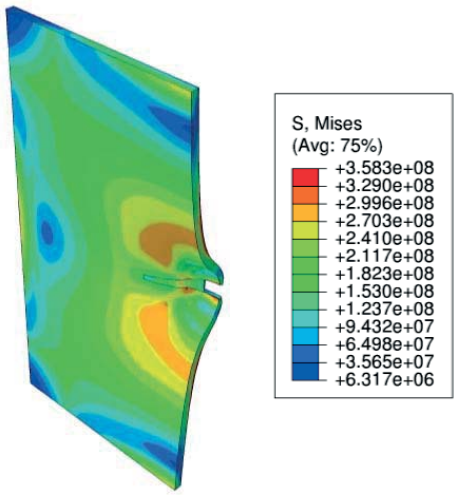

b) E= 100 J

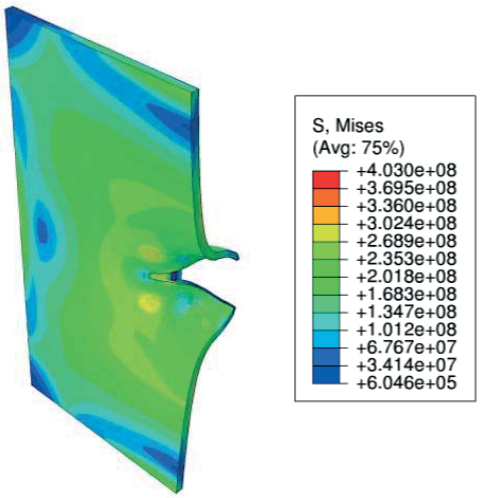

c) E= 150 J

Figure 4. The effect the impact energy level on the stress distribution of the notched metal plate without patch.

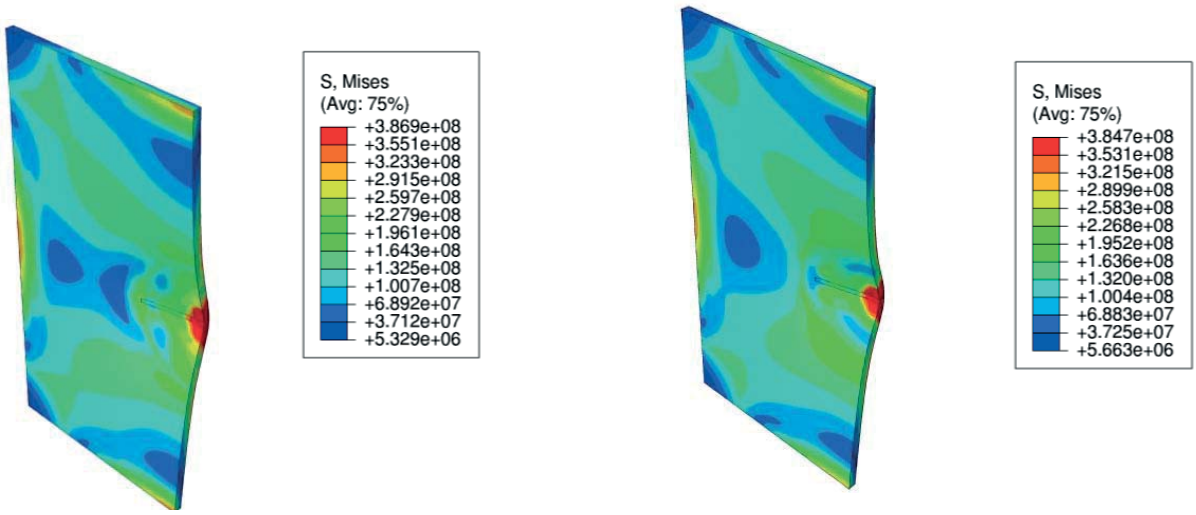

a) E= 50 J

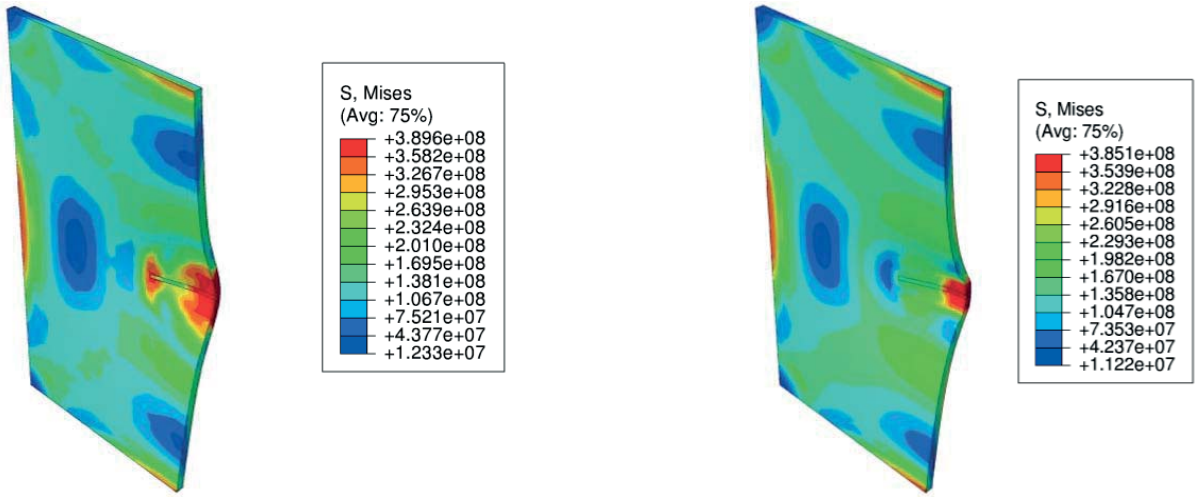

b) E= 100 J

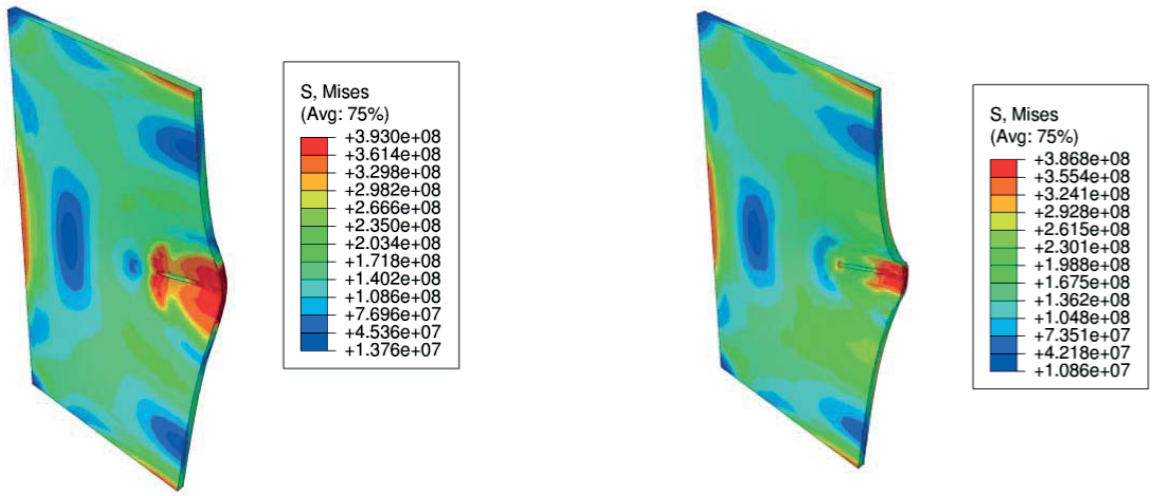

c) E= 150 J

Figure 5. The effect the impact energy level on the stress distribution of the nothced metal plate with composite circular patch .

Figure 5 shows the stress distributions of the notched metal plate with circular and rectangular composite patches for the present impact energies. Composite circular and rectangular patches prevented perforation of the notched plates

with increasing impact energy and also stress levels of composite circular and rectangular patches remain same nearly with increasing impact energy. Deformation types are related with composite patch geometry as shown in Figure 5. The patch geometry as a rectangular geometry is more significant from circular geometry. Because deformation area is smaller than circular geometry and the stress levels is also.

4. Conclusion

This study addresses the low velocity impact response of repaired notched plates with composite patch for different composite patch geometries and impact energies. The temporal variations of contact force, kinetic energies and the stress distributions of notched plates repaired with composite patch were determined numerically. The results of using the composite patch were also significant in terms of impact resistance. The Johnson-Cook material model was implemented for modelling notched plates. Composite patches were modeled using continuum shell element with orthotropic elastic material model and Hashin damage initiation criterion using composite lay-up technique in available Abaqus/Explicit. Increasing impact energy resulted in the contact force levels to increase whereas the total contact durations decrease. The minimum peak contact forces appeared for the model with notched plate without composite patch. But the maximum peak contact forces appeared for the model with repaired notched plate with circular patch. The notched metal without patch could absorb more much impact energy, however these plates were perforated in the impact energy levels of 100 and 150 J. Composite circular and rectangular patches prevented perforation of the notched plates with increasing impact energy and also stress levels of composite circular and rectangular patches remain same nearly with increasing impact energy.

Acknowledgements

Authors would like to thank for the financial support of The Scientific and Technological Research Council of Turkey (TUBİTAK) under the contract: 216M519.

References

Mall, S. and Conley, D.S. (2009). Modeling and validation of composite patch repair to cracked thick and thin metallic panels. Composites: Part A, 40, 1331-1339. https://doi.org/10.1016/j.compositesa.2008.08.007.

Shams, S.S. and El-Hajjar, R.F. (2013). Overlay patch repair of scratch damage in carbon fiber/epoxy laminated composites. Composites: Part A, 49, 148-156, https://doi.org/10.1016/j.compositesa.2013.03.005.

Albedah, A., Khan, S.M.A., Benyahia, F. and Bouiadjra, B.B. (2016). Effect of load amplitude change on the fatigue life of cracked Al plate repaired with composite patch. International Journal of Fatigue, 88, 1-9, https://doi.org/10.1016/j.ijfatigue.2016.03.002.

Cheng, P., Gong, X.J., Aivazzadeh, S. and Xiao, X. (2014). Experimental observation of tensile behavior of patch repaired composites. Polymer Testing, 34, 146-154, https://doi.org/10.1016/j.polymertesting.2014.01.007.

Constantin, N., Sandu, M. and Sorohan, Ş. (2013). Restoration of the mechanical performance of damaged Al panels using bonded composite repair patches. International Journal of Adhesion & Adhesives, 42, 69-76, https://doi.org/10.1016/j.ijadhadh.2013.01.003.

Errouane, H., Sereir, Z. and Chateauneuf, A. (2014). Numerical model for optimal design of composite patch repair of cracked aluminum plates under tension. International Journal of Adhesion & Adhesives, 49, 64-72, https://doi.org/10.1016/j.ijadhadh.2013.12.004 .

Benyahia, F., Aminallah, L., Albedah, A., Bouiadjra, B.B. and Achour, T. (2015). Experimental and numerical analysis of bonded composite patch repair in aluminum alloy 7075 T6. Materials and Design, 73, 67-73, https://doi.org/10.1016/j.matdes.2015.02.009.

Sabelkin, V., Mall, S., Hansen, M.A., Vandawaker, R.M. and Derriso, M. (2007). Investigation into cracked aluminum plate repaired with bonded composite patch. Composite Structures, 79, 55-66, https://doi.org/10.1016/j.compstruct.2005.11.028.

ABAQUS/Explicit (Version 6.14), User's manual, Finite Element Software. Available from: http://www.simulia. com.

Manes, A., Serpellini, F., Pagani, M., Saponara, M. and Giglio, M. (2014). Perforation and penetration of aluminium target plates by armour piercing bullets. International Journal of Impact Engineering, 69, 39-54, https://doi.org/10.1016/j.ijimpeng.2014.02.010.

Singh, H., Namala, K. K. and Mahajan, P. (2015). A damage evolution study of E-glass/epoxy composite under low velocity impact. Composites Part B,76, 235-248, https://doi.org/10.1016/j.compositesb.2015.02.016.

MÜHENDİSLİK FAKÜLTESİ

Uluslararası Mühendislik Araştırma ve Geliştirme Dergisi

International Journal of Engineering Research and Development

Cilt/Volume:9 Sayı/Issue:3 Aralık/December 2017 https://doi.org/ 10.29137/umagd.350725

Araştırma Makalesi / Research Article

PID Controller Design for a Fractional Order System using Bode's Ideal Transfer Function

Tufan DOĞRUER[1*], Ali YÜCE[2], Nusret TAN[2]

[1]Gaziosmanpaşa University, Department of Electronic and Automation, Tokat, TURKEY
[2]İnönü University, Faculty of Engineering, Electrical and Electronics Engineering, Malatya, TURKEY

Başvuru/Received: 08/10/2017 **Kabul/Accepted**: 01/12/2017 **Son Versiyon/Final Version**: 26/12/2017

Abstract

In this paper, an optimization method is proposed to design a fractional order system with PID controller by taking Bode's ideal transfer function as reference model. In the study, PID controllers are preferred because of their simplicity, reliability and robustness. PID controller parameters can be obtained by optimization method. In order to obtain the desired time response, it is sufficient to set two parameters in the Bode's ideal transfer function. The Bode's ideal transfer function was considered as the reference model and compared with the generated model. The error in the output signal is minimized by the integral performance criteria, and the PID controller parameters are optimized. Integral performance criteria are frequently used in evaluating the performance of control systems. In Simulink model, Matsuda's 4th order integer approximation model is used for fractional order control system. Finally, the success of the optimization method is seen in the given numerical example.

Key Words

"Controller design, Optimization, Fractional order control systems, PID Controller"

tufan.dogruer@gop.edu.tr

1. INTRODUCTION

Fractional calculus is a branch of mathematics and it is possible to see many applications in the different areas. Control engineering is one of these application areas. In the control system design, the system to be controlled may be fractional order, or the controller may be fractional order (Monje et al.,2010). In this study, a fractional order system is controlled by an integer order controller. Fractional order systems can better model physical systems than integer order systems. Due to this advantage, interest in fractional order systems is increasing in today's world. There are many approaches model that are used to obtain integer order models of fractional order systems. The most well-known approach models are Matsuda, Oustaloup, Carlson, Krishna, Chareff approaches method [2-6]. In the study, Matsuda's 4th-order integer approximation model was used while modeling a fractional order system.

Controller design is one of the most fundamental issues in control engineering. In this study, an optimization method is presented about design a controller for a fractional order system. An ideal control system is required to meet expectation. In monitoring the performance of the control system, the transient behavior is often used. Percent overshoot value and time parameters of the control system in unit step response are very important for performance appraisal. In the study, Bode's ideal transfer function is accepted as the reference model. It is aimed to obtain the controller parameters by making sure that the system output to be controlled has the same characteristics as the reference model. The controller parameters are obtained by optimization method. The ITSE (integral time squared error) performance criterion is used to minimize the error in the optimization method [7].

In the study, the preferred PID (proportional integral derivative) controller structure was used because of its many advantages. PID controllers are still the most commonly used controller structure [8]. There are many tuning methods used in the literature for calculating PID controller parameters. Ziegler-Nichols, Aström-Hagglund are the most known PID tuning methods [8, 9]. In parallel with improvements in computers, the use of optimization methods is steadily increasing. Some of the optimization methods used in the literature are genetic algorithm, particle swarm optimization, ant colony algorithm. The optimization method used in the study was created in Matlab / Simulink environment.

The remainder of the paper is organized as follows. Section 2 briefly introduces Bode's ideal transfer function. Section 3 contains the PID controller design. In this section, the structure of the PID controller, the optimization approach and the application of the method are given. Finally, conclusions are drawn in Section 4.

2. BODE'S IDEAL TRANSFER FUNCTION

In 1945, H. W. Bode defined the open-loop transfer function of a feedback control system as given in Equation 1 [10]. Where ω_c is the gain crossover frequency and γ is the slope of the amplitude curve that can be expressed in fractional or integers on a logarithmic scale.

$$L(s)=\left(\frac{\omega_c}{s}\right)^{\gamma} \tag{1}$$

The block diagram of the fractional order control system with Bode's ideal transfer function is given in Figure 1. The closed loop transfer function of the block diagram in Figure 1 is given in Equation 2 [11].

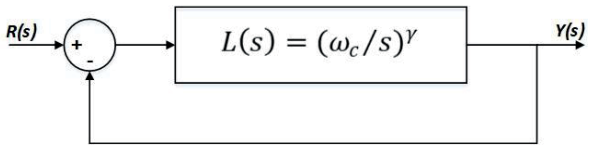

Figure 1: Fractional order transfer function with Bode's ideal transfer function

$$\mathrm{G}(s)=\frac{L(s)}{1+L(s)}=\frac{1}{\left(\frac{s}{\omega_c}\right)^{\gamma}+1},1<\gamma<2 \tag{2}$$

Frequency and time domain characteristics for Bode's ideal transfer function can be obtained. The Maximum overshoot value is expressed as in Equation 3.

$$M_p \cong 0.8(\gamma-1)(\gamma-0.75),\ \ 1<\gamma<2 \tag{3}$$

When the ω_c is taken as 1 rad/s, the maximum overshoot according to the γ parameter change are given in Table 1. When Table 1 is examined, it is seen that as the γ parameter increases, the maximum overshoot increases.

Table 1: Overshoot value for reference model (ω_c=1 rad/s)

γ	Overshoot (%)		γ	Overshoot (%)
1.0	0		1.5	30
1.1	2.8		1.6	40.8
1.2	7.2		1.7	53.2
1.3	13.2		1.8	67.2
1.4	20.8		1.9	82.8

The time parameters such as peak time, rise time and settling time can be calculated by the following equations, depending on the γ and ω_c parameters [12].

$$t_p \cong \frac{1.106(\gamma - 0.255)^2}{(\gamma - 0.921)\omega_c} \tag{4}$$

Table 2 and Table 3 show the change in peak time and rise time, respectively, depending on the γ and ω_c parameters.

Table 2: Peak time for reference model (ω_c=1 rad/s)

γ	Peak time (t_p)		γ	Peak time (t_p)
1.0	7.7704		1.5	2.9608
1.1	4.4118		1.6	2.9467
1.2	3.5401		1.7	2.9645
1.3	3.1868		1.8	3.0035
1.4	3.0271		1.9	3.0571

$$t_r \cong \frac{0.131(\gamma + 1.157)^2}{(\gamma - 0.724)\omega_c} \tag{5}$$

Table 3: Rise time for reference model (ω_c=1 rad/s)

γ	Rise time (t_r)		γ	Rise time (t_r)
1.0	2.2083		1.5	1.1918
1.1	1.7748		1.6	1.1367
1.2	1.5289		1.7	1.0956
1.3	1.3730		1.8	1.0645
1.4	1.2670		1.9	1.0410

When Table 2 is examined, it is noteworthy that the peak time changes slightly with respect to the γ parameter. When Table 3 is examined, it is seen that the rise time is shortened as the γ parameter grows.

Tolerance values allowed for settling time are usually values exceeding 2% and 5%. The equations for these two tolerance values are as follows. Table 4 was prepared for the 5% value of settling time.

$$t_s(\%2) \cong \frac{4}{\cos(\pi - \pi/\gamma)\omega_c} \tag{6}$$

$$t_s(\%5) \cong \frac{3}{\cos(\pi - \pi/\gamma)\omega_c} \tag{7}$$

Table 4: Settling time for reference model (ω_c=1 rad/s)

γ	Settling time (t_s)		γ	Settling time (t_s)
1.0	3		1.5	6.0000
1.1	3.12		1.6	7.8394
1.2	3.4641		1.7	10.9624
1.3	4.0080		1.8	17.2763
1.4	4.8116		1.9	36.3287

Figure 2 shows the unit step response curves of Bode's ideal transfer function according to the change of γ parameter (1<γ<2). While the ω_c parameter remains constant, the maximum overshoot value increases as the γ parameter grows. It is seen that minimum the overshoot value is γ = 1.1, while the maximum overshoot value is at γ = 1.9 [13].

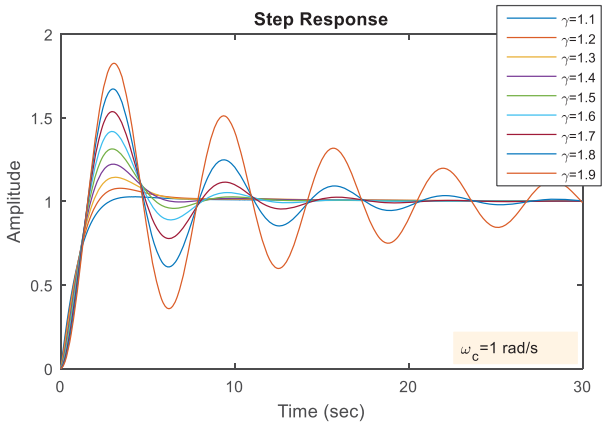

Figure 2: Step responses of reference system for different γ parameters

3. PID CONTROLLER DESIGN

3.1. PID Controller Structure

The purpose of the control system is to ensure that the signal applied to the input is followed in the shortest time and at the least error. At this point, PID controllers offer great ease of use in the best operating conditions of the system. The simplicity and durability of the structure, to be well-known controller, the low number of parameters to be calculated is the reason for the PID controller's preference [8].

The transfer function of a conventional PID controller is given in Equation 8 [14]. Here, the proportional term is Kp, the coefficient of integral term is Ki, and the coefficient of the derivative term is Kd.

$$C(s) = K_p + \frac{K_i}{s} + K_d.s \tag{8}$$

The PID controller compares the feedback signal to the input signal. According to the error between the two signals, the PID controller makes an effect to reduce the error and sends it to the output. In this way, feedback signal is performed until the error is reduced to the minimum. The block diagram of the close-loop control system with PID controller is given in Figure 3.

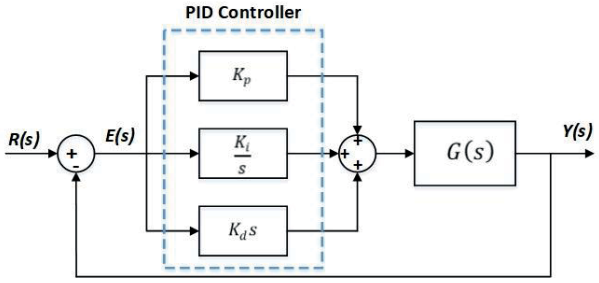

Figure 3: Block diagram of close-loop control system with PID controller

3.2. Optimization Approach

The block diagram of the model used to set the PID controller parameters is given in Figure 4.

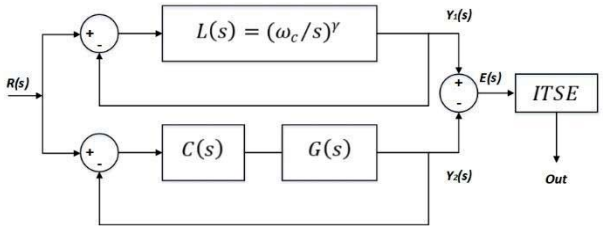

Figure 4: Block diagram of the model created

In the model, it is aimed to calculate the controller parameters by minimizing the error between output of the Bode's ideal transfer function and output of the controlled system. Integral performance criteria are often used to minimize the error. The ITSE performance criterion is chosen for this study. The ITSE criterion is given in Equation 9 [7].

$$J_{ITSE} = \int_0^\infty t.e^2(t)dt \tag{9}$$

Where, t denotes the time and $e(t)$ denotes the error occurring in the control system. The error is defined as the difference between the input signal and the output signal in a system with unit feedback and is expressed by Equation 10 [7].

$$e(t) = r(t) - y(t) \tag{10}$$

Optimization algorithm begins by entering initial values in parameters K_p, K_i and K_d. In the reference model, If appropriate values of γ and ω_c are entered, the most suitable PID controller parameters are obtained by applying Equation 9.

3.3. Implementation of the Method

Consider the control system of Figure 4 with transfer function

$$G(s) = \frac{3}{s^{0.1}(s+0.6)} \tag{11}$$

PID controller parameters are obtained for different γ and ω_c values in Bode's ideal transfer function. When the controller parameters are obtained, the error is minimized according to the ITSE performance criterion, and the system is optimized according to the reference model. The PID controller parameters obtained for different γ and ω_c values are given in Table 5. PID controller parameters applying to the fractional order system, the unit step responses are obtained and presented graphically [13].

Table 5: PID controller parameters for different γ

γ	K_p	K_i	K_d
	ω_c=0,5 rad/s		
1.1	0,159	0,094	0,006
1.3	0,472	0,173	0,741
1.5	0,233	0,215	0,549
1.7	0,073	0,255	0,603
	ω_c=1 rad/s		
1.1	0,334	0,2	0,0001
1.3	0,325	0,313	0,077
1.5	0,27	0,475	0,173
1.7	0,229	0,796	0,456
	ω_c=2 rad/s		
1.1	0,717	0,429	0,001
1.3	2,51	1,664	0,774
1.5	2,759	4,836	1,417
1.7	1,54	5,948	1,332
	ω_c=3 rad/s		
1.1	1,12	0,67	0,001
1.3	3,618	3,499	0,696
1.5	2,959	6,802	0,81
1.7	1,702	8,654	0,735

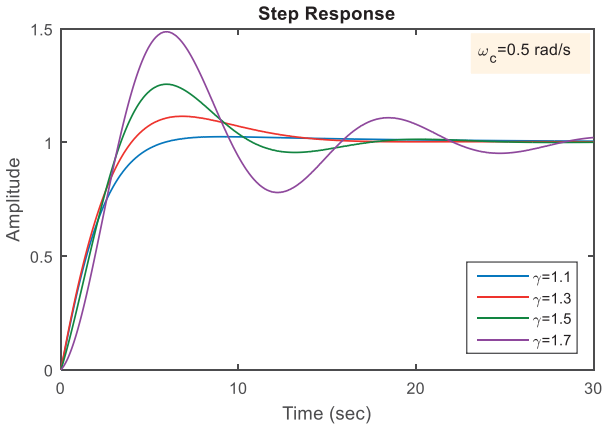

Figure 5: Unit-Step response with controller (ω_c=0.5 rad/s)

Figure 5 shows the unit step response for ω_c= 0.5 rad/s according to various γ parameter. When the figure is examined, it is clear that the maximum overshoot value of the system increases as the γ parameter grows. Moreover, as the γ parameter increases, the rise and peak time become shorter and the settling time becomes longer.

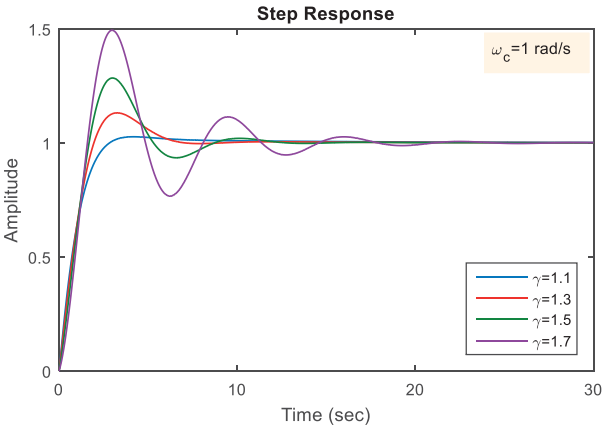

Figure 6: Unit-Step response with controller (ω_c=1 rad/s)

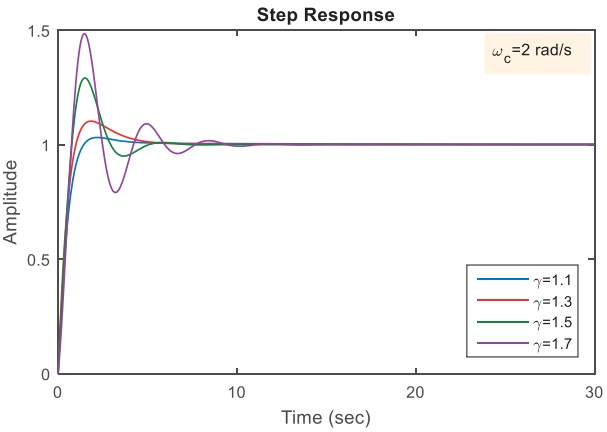

Figure 7: Unit-Step response with controller (ω_c=2 rad/s)

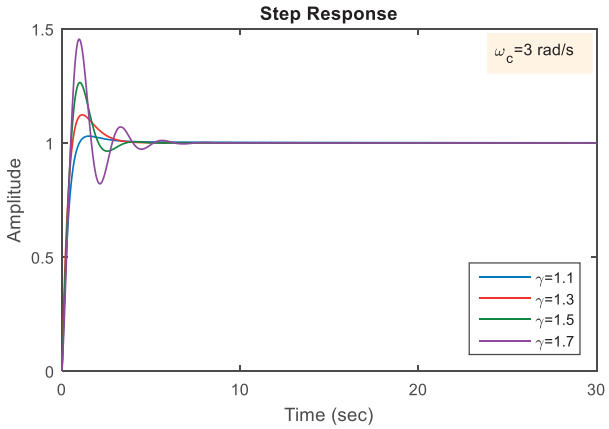

Figure 8: Unit-Step response with controller (ω_c=3 rad/s)

Similarly, Figures 6, 7 and 8 show the unit step response curves of the controlled system for ω_c= 1 rad/s, ω_c= 2 rad/s and ω_c= 3 rad/s, respectively. When the figures are examined, it is noticed that the maximum overshoot values do not change with ω_c parameter but vary with γ parameter. The maximum overshoot values and time parameters for the figures are given in Table 6 in detail.

Table 6: Time response parameters and overshoot value

	γ=1.1	**γ=1.3**	**γ=1.5**	**γ=1.7**
ω_c=0,5 rad/s				
Rise time	3,59	2,93	2,58	2,38
Settling time	5,30	13,39	15,78	28,28
Peak time	9,09	6,83	5,94	5,95
Overshoot (%)	1,95	11,20	25,51	45,51
ω_c=1 rad/s				
Rise time	1,78	1,46	1,29	1,18
Settling time	5,33	5,95	8,15	16,71
Peak time	4,18	3,27	3,00	2,98
Overshoot (%)	2,49	13,06	28,38	49,20
ω_c=2 rad/s				
Rise time	0,90	0,71	0,59	0,57
Settling time	3,11	4,41	4,55	7,28
Peak time	2,19	1,84	1,50	1,47
Overshoot (%)	2,98	10,20	29,09	48,44
ω_c=3 rad/s				
Rise time	0,59	0,43	0,39	0,38
Settling time	2,21	2,82	3,04	4,74
Peak time	1,52	1,14	1,00	0,97
Overshoot (%)	2,92	12,32	26,49	45,49

The PID controller parameters obtained for constant γ and variable ω_c values are given in Table 7. The graphs obtained by applying the PID controller parameters to the fractional order system are given in Figures 9, 10 and 11.

Table 7: PID controller parameters for different ω_c

ω_c	K_p	K_i	K_d
	$\gamma=1.2$		
0.5	0,457	0,133	0,624
1	0,359	0,254	0,062
2	2,273	0,952	0,585
3	2,654	1,323	0,425
	$\gamma=1.5$		
0.5	0,239	0,217	0,561
1	0,27	0,475	0,173
2	0,578	1,286	0,075
3	1,384	3,241	0,199
	$\gamma=1.8$		
0.5	0,136	0,459	1,431
1	0,211	1,172	0,821
2	1,011	6,505	1,361
3	1,189	10,183	0,82

Figure 9 shows the unit step response curves of the system controlled according to variable ω_c values. When the figure is examined, it is seen that the maximum overshoot values do not changed by changing the ω_c parameter. However, the change in time parameters is clearly visible.

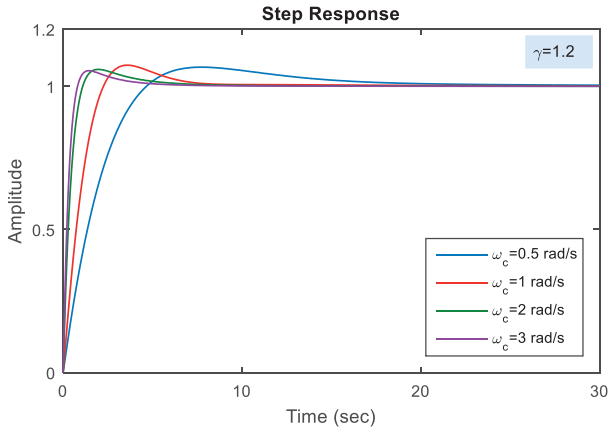

Figure 9: Unit-Step response with controller (γ=1.2)

Similarly, Figure 10 and 11 are obtained according to γ =1.5 and γ =1.8, respectively. It is noticed that the maximum overshoot values do not change while the γ parameter remains constant. Time parameters are seen to be shortened as ω_c values increase.

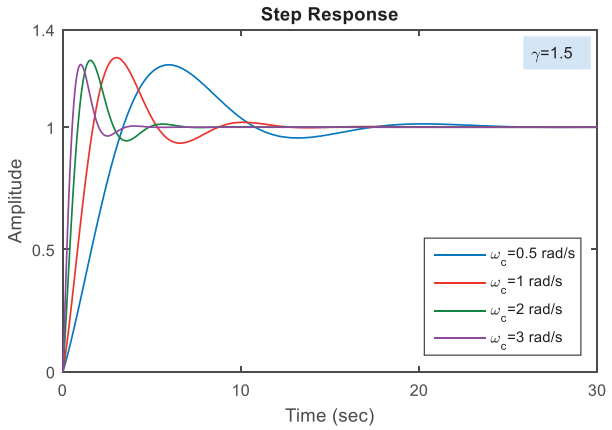

Figure 10: Unit-Step response with controller (γ=1.5**)**

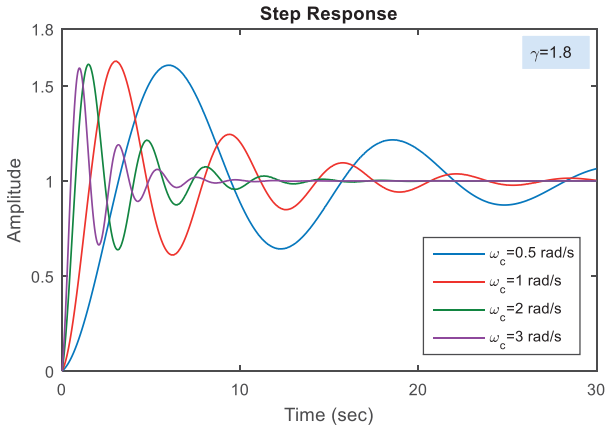

Figure 11: Unit-Step response with controller (γ=1.8)

The maximum overshoot values and time parameters for the figures are detailed in Table 8.

Table 8: Time response parameters and overshoot value

	ωc=0, 5	***ωc=1***	***ωc=2***	***ωc=3***
γ=1.2				
Rise time	3,25	1,60	0,73	0,53
Settling time	14,55	6,44	4,67	3,44
Peak time	7,74	3,59	1,96	1,45
Overshoot (%)	6,29	7,21	5,88	5,44
γ=1.5				
Rise time	2,57	1,29	0,64	0,40
Settling time	15,75	8,15	4,42	2,98
Peak time	5,93	3,00	1,54	1,00
Overshoot (%)	25,44	28,38	27,35	25,67
γ=1.8				
Rise time	2,37	1,14	0,56	0,37
Settling time	29,28	26,04	11,71	6,79
Peak time	5,99	3,02	1,49	0,98
Overshoot (%)	51,13	62,47	61,32	59,37

4. RESULTS

In this paper, an optimization method is presented related to determine PID controller parameters using Bode's ideal transfer function. The Bode's ideal transfer function is considered as the reference model. In the reference model, the desired unit step response can be obtained by setting two parameters (γ ve ω_c). The unit step response of the controlled system was obtained as having the same characteristic as the Bode's ideal transfer function. The controller parameters are obtained by minimizing the difference between the reference model and the system. A number of simulation studies have been carried out in the study and the results are presented in graphical and tabular form.

It has been shown that the PID controller parameters can be obtained according to the desired unit step response output for a fractional order system. The method has been shown to be successful from the results obtained.

ACKNOWLEDGMENT

This work is supported by the Scientific and Research Council of Turkey (TÜBİTAK) under Grant no. EEEAG-115E388.

REFERENCES

(Monje et al.,2010) C. A. Monje, Y. Chen, B. M. Vinagre, D. Xue, and V. Feliu-Batlle, *Fractional-order systems and controls: fundamentals and applications*. Springer Science & Business Media, 2010.

(Carlson et al., 1964) G. Carlson and C. Halijak, "Approximation of fractional capacitors $(1/s)^{(1/n)}$ by a regular Newton process," *IEEE Transactions on Circuit Theory,* vol. 11, no. 2, pp. 210-213, 1964.

(Charef et al.,1992) A. Charef, H. Sun, Y. Tsao, and B. Onaral, "Fractal system as represented by singularity function," *IEEE Transactions on Automatic Control,* vol. 37, no. 9, pp. 1465-1470, 1992.

(Krishna, 2011) B. Krishna, "Studies on fractional order differentiators and integrators: A survey," *Signal Processing,* vol. 91, no. 3, pp. 386-426, 2011.

(Matušů, 2011) R. Matušů, "Application of fractional order calculus to control theory," *International journal of mathematical models and methods in applied sciences,* vol. 5, no. 7, pp. 1162-1169, 2011.

(Oustaloup et al., 2000) A. Oustaloup, F. Levron, B. Mathieu, and F. M. Nanot, "Frequency-band complex noninteger differentiator: characterization and synthesis," *IEEE Transactions on Circuits and Systems I: Fundamental Theory and Applications,* vol. 47, no. 1, pp. 25-39, 2000.

[7] D. Atherton, *Control engineering*. Bookboon, 2009.

[8] K. J. Åström and T. Hägglund, "The future of PID control," *Control engineering practice,* vol. 9, no. 11, pp. 1163-1175, 2001.

[9] J. G. Ziegler and N. B. Nichols, "Optimum settings for automatic controllers," *trans. ASME,* vol. 64, no. 11, 1942.

[10] H. W. Bode, "Network Analysis and Feedback Amplifier Design," 1945.

[11] R. S. Barbosa, J. T. Machado, and I. M. Ferreira, "Tuning of PID controllers based on Bode's ideal transfer function," *Nonlinear dynamics,* vol. 38, no. 1, pp. 305-321, 2004.

[12] O. Katsuhiko, "Modern control engineering," ed, 2010.

[13] T. Doğruer and N. Tan, "Bode'nin İdeal Transfer Fonksiyonunu Kullanarak Lag/Lead Kontrolör Tasarımı," presented at the TOK 2014 Otomatik Kontrol Ulusal Toplantısı, 2014.

[14] N. Tan, "Computation of stabilizing PI and PID controllers for processes with time delay," *ISA transactions,* vol. 44, no. 2, pp. 213-223, 2005.

MÜHENDİSLİK FAKÜLTESİ

Uluslararası Mühendislik Araştırma ve Geliştirme Dergisi

International Journal of Engineering Research and Development

Cilt/Volume:9 Sayı/Issue:3 Aralık/December 2017 https://doi.org/ 10.29137/umagd.350831

Araştırma Makalesi / Research Article

Stratigraphy of The Region Erbaa (Tokat)

Özlem TOPRAK [*1], Mehmet AKYAZI[2]

[1] *Gaziosmanpaşa University, Tokat Vocational High School*
[2] *Cumhuriyet University,Faculty of Engineering,*

Başvuru/Received: 08/10/2017 **Kabul/Accepted**: 01/12/2017 **Son Versiyon/Final Version**: 26/12/2017

Abstract

The Permo-Triassic basement rocks form the basis of the study area, which is located on the North Anatolian Fault and immediate vicinity of the Erbaa District on the north. The primary covering units overlying the basement rocks consist of a thick deposit, deposited in the depression in front of the Eurasian continent during the Liassic-Upper Eocene time interval. The first cover units, unconformably overlying the basic rocks, are overlaid by conglomerate, sandstone, mudstone, marl and oolitic limestones and Lower-Middle Jurassic rocks composed of volcano-clastic rocks, Upper Jurassic-Lower Cretaceous aged neritic and pelagic clayey limestones, the Santonian-Campanian aged sedimentary rocks in the pyroclastic character accompanied by the volcanic-volcanosedimentary rocks formed by the submarine volcanic activity in the Upper Cenomanian, Maestrichtian-Paleocene sandy limestones, Lower-Middle Eocene conglomerate, volcanogenic sandstone, sandy limestone and nummulites limestones and Upper Eocene basalt, pillow lavas, andesite, tuff, tuffite, aglomera, sandstone and siltstone intercalation unconformably. Secondary cover units, composed of loosely adhered conglomerates and sandstones that collapse during terrestrial atmospheric conditions in depressions formed along the North Anatolian Fault zone, are covered by the Quaternary aged alluvium, slope rubble and deposit cones, which constitute the youngest units of the study area.

Key Words

"Erbaa, General Geology, Stratigraphy"

ozlem.toprak@gop.edu.tr

1. INTRODUCTION

The survey area covers d1, d2, d3 of the Tokat G37 Paftas which is located on the North Anatolian Fault and just north of the Erbaa District and its immediate surroundings.

Numerous different geological studies have been carried out in the study area, especially with tectonic contents. Among these studies, (Akyazı & Tunç, 1992), (Aktimur et al., 1992), (Alp, 1972), (Ambraseys , 1970), (Ambraseys , 1971), (Arpat & Saroğlu , 1975), (Barka et al. , 2000), (Blumentha , 1950), (Kavak et al. , 2006), (Özcan et al. , 1980), (Öztürk, 1979), (Toprak, 2014), (Serdar et al., 1975), (Sezen et al., 1975) and (Yoldaş et al., 1985) available.

For the purpose of this study, detailed geological-paleontological-biostratigraphic features of the units in the target area will be revealed and the geological and stratigraphic location of the study area will be tried to be interpreted.

Figure 1. Location map of the study area

2.GENERAL GEOLOGY OF ERBAA (TOKAT) REGION

The Permo-Triassic basement rocks form the base of the study area, which is located on the North Anatolian Fault and just north of the Erbaa District and its immediate surroundings. The first covering units overlying the basement rocks consist of a thick deposit deposited in the depression in front of the Eurasian continent during the Liassic-Upper Eocene time interval. Upper Jura-Lower Cretaceous aged neritic and pelagic clayey limestones, Upper Cenomanian limestones, Upper Cenozoic limestones, Upper Cenozoic limestones, Upper Cenozoic limestones, Maastrichtian-Paleocene sandy limestones, Lower-Middle Eocene aged conglomerate, volcanogenic sandstone, sandy limestone and nummulitesite limestones and basalts of the Upper Eocene age, with the volcanic-volcanosedimentary rocks formed due to submarine volcanic activity, pillow lavas, andesite, tuff, tuffite, agglomerate, sandstone and siltstone alternation. Second cover units composed of loosely adhered conglomerates and sandstones that collapse during the North Anatolian Fault zone and in terrestrial atmospheric conditions are covered by the Quaternary aged alluvium, slope rubble and deposit cones, which constitute the youngest unit of the study (Toprak, 2014).

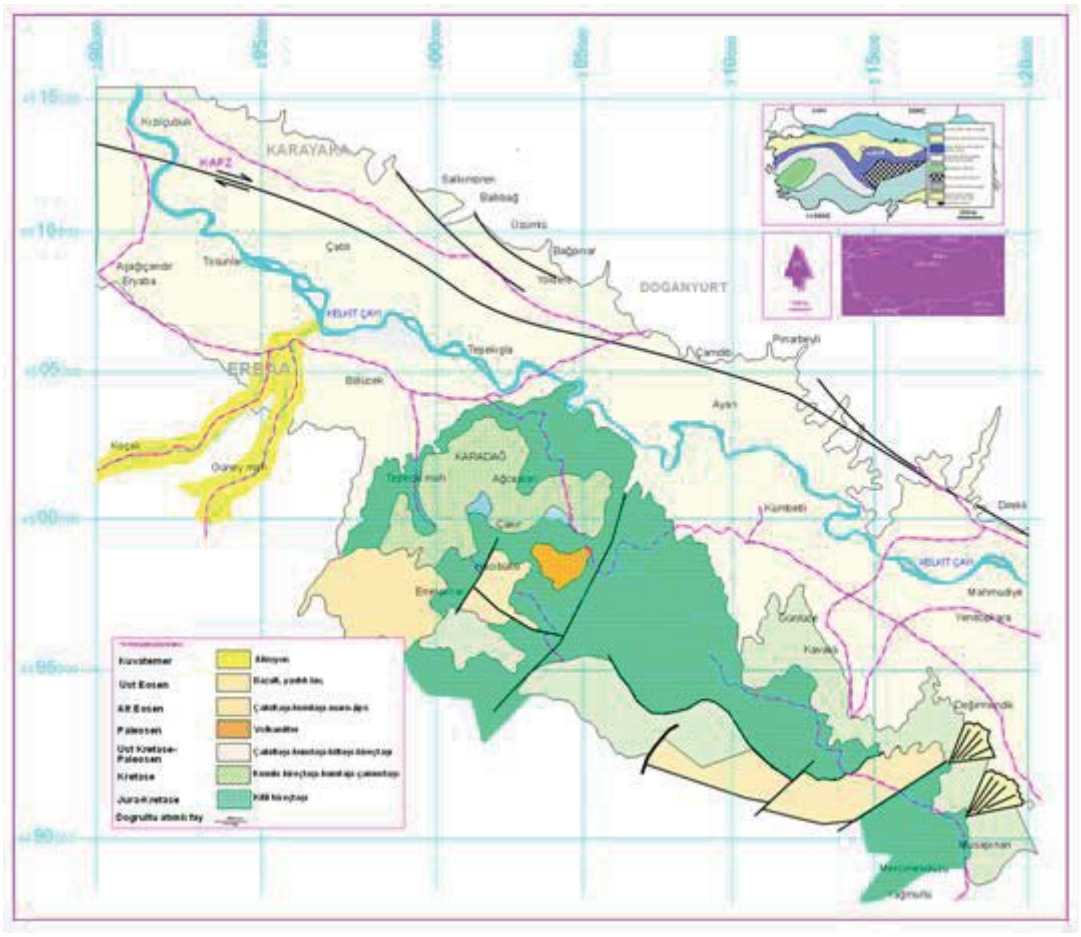

Figure 2. The geological map of Erbaa(Tokat) region

3.STATIGRAPHY OF ERBAA(TOKAT) REGION

Permo-Triassic: The basement rocks bearing low-grade metamorphic rocks are composed of metamorphic matrix composed of quartzite, calcschist, epidote schist, milonitgniss, micaschist, metaclastic and metacvar sandstones and recrystallized limestone / limestone blocks floating in this matrix (Akyazı & Tunç, 1992). Studies on thin sections of the samples taken from crystallized limestones show that the *Schwagerina* sp., *Neoschwagerina* sp. and *Polydiexodina* sp. Fossils were identified. For this reason, the age of crystallized limestones was accepted as Permian in this study. Considering that the Lower-Middle Jurassic and Upper Jura-Lower Cretaceous units, which are located on the metamorphic matrix with Permian aged blocks, do not undergo metamorphism, the metamorphic rocks are Permo-Triassic and have metamorphism before the Upper Jurassic.

Thickness cannot be clearly defined in the survey area but it can be 300-350 m thick. The unit is located in the south of the Niksar district in the south of the study area and the south of the Erbaa district in the west (Figure 3).

Lower-Middle Jura: It begins with polygenic conglomerates containing metasedimanter-metavolcanic pebbles composed of limestone gravels of calcschist, gneiss, muskovitshist, marble and Permian aged with yellowish red colored carbonate cement. It is formed by dark gray-blackish colored, fine to medium, coarsely grained, to medium-bedded sandstone with tightly bonded carbonates. At the top of the unit a thin limestone band containing mudstone plaster was observed. Dark colored, thick bedded aglomera, andesitic lava flows and pillow lavas and light cream colored, thin-medium bedded tuffs were added in the sediments of pebbles, sandstones and thin mudstones above, depending on submarine volcanic activity parallel to sedimentation.

Within the area of the sandstones and limestones of the study area, the thickness of which is determined as 150-200 m; *Andersenolina elongata* (Leupold), *Pseudocyclammina liasica* Hottinger, *İnvolutina* sp., *Triloculina* sp., *Quinqueloculina* sp., *Phylloceras* sp. and *Pentacrinus* sp. Fossils were identified. According to these fossils that have been determined, the Lower-Middle Jurassic age is given (Figure 3).

In the central part of the study area, the unit which confronts between the Direkli and the Kümbetli Villages; agglomeratic levels, andesitic lava flows and pillow lavas, although occasionally, show that the unit under which the submarine volcanism is active has collapsed.

Upper Jura-Lower Cretaceous: The unit begins with medium-thick bedded sandy sparitic sandstones at the lower levels and continues upward with the Titonik facies tempered limestones in the micro-biophysics of calpionellibiomicrite containing claystone and mudstone levels.

Oxfordian-Kimmericy: Lower levels of limestones in fossiliferous oopelsparitmicrofibres, unconformably overlying the Lower-Middle Jurassic units, are composed of pozzolithic and pseudolithic inclusions of chert layers and lenses, grayish, creamy and occasionally pinkish, occasionally dark gray, beige colored, medium-thick layered, with a massive appearance in places and a cracked structure.

Within the unit, Clypeinajura Favre, Oxophene-kimmericyen age, *Clypeina jurassica* Favre, *Protopeneroplis striata* Weynschenk, *Globuligerina* sp., *Apthycus* sp. and *Pseudocyclammina* sp. Fossils were identified. The thickness of the unit is measured as 160 m in the survey area.

Tithonian-Berriyasiyen: *Mesoendothyra* sp., *Pseudotextularia* sp., *Triloculina* sp., *Saccacoma* sp., in the clayey limestones with gray-colored, fossiliferous biosparitemicrobiofacies, which are intercalated on the Oxfordian and *Quinqueloculina* sp. Fossils were identified. Depending on the fossil content and stratigraphic location, it is thought that these levels of the unit may be Lower Titanian.

The unit continues upward with gray-dark gray colored clayey limestones with the Titonik facies in the micro-biophysical calpionibiomicrite, including claystone-mudstone levels. The clayey pelagic limestones at these levels of the unit contain Titonian-Berriyan age; *Calpionellopsis simplex* (Colom), *Calpionellopsis oblonga* (Cadisch), Radiolaria and spongel spicules were detected in *Tintinnopsella carpathica* (Murgeanui ve Filipescu), *Crassicollaria intermedia* (Durand Delga), *Crassicolaria parvula* Remane, *Calpionella alpina* Lorenz, *Calpionella elliptica* Cadisch, *Remaniella cadischiana* (Colom). Studies on Calpionel biostratigraphy have identified and identified Crassicollaria intermedia, Calpionellaalpina, Calpionellaelliptice, Calpionellosis simplex-Calpionellopsis oblanga calpionel biozones in the unit of the Titonic Facies.

The Upper Jurassic-Lower Cretaceous units measuring 455 m in thickness in the study area are exposed in the central Montenegro region of the study area and indicate the conditions of pelagic environment sedimentation at the upper levels while the basal neritic environment features are shown.

It can be said that the lower levels are thick-bedded, and the upper levels are composed of abundant cherts, micritic limestone, clayey and muddy limestone lithologies, and this unit has collapsed in a deepening marine environment.

Upper Cretaceous: Starting with reddish colored, tightly adherent conglomerates and upwardly gray, brown colored, thin-medium bedded, carbonate-cemented sandstones; marble-mudstone with variegated colored carbonate marl-mudstones and their partially metamorphosed derivatives and recrystallized limestones, and the volcanic intercalated sandstone-marl-limestone alternation developed in flysch facies with hard, fragile textured limestones in clay, globotruncanized biomicrite microbiophysi are available. The measurable thickness of the unit is measured as 325 m.

Cenomanian-Coniacian: It is observed that the lower levels of conglomerate, sandstone, marl mudstone and their partially metamorphosed derivatives and sedimentary rocks composed of crystallized pelagic limestones are accompanied by volcanic gneisses consisting of volcanic pebble breccias and andesites and tuffites. The accompanying volcanic and volcanosedimentary rocks of the crushed sedimentary rocks indicate the volcanic activity in the Upper Cretaceous region. Fossils of *Paraeoglobotruncanita gibba* Klaus, *Dicarinella imbricata* (Mornod), *Helvetoglobotruncana helvetica* (Bolli), *Marginotruncanita sigali* (Reichel), *Marginotruncana pseudolinneiana* Pessagno and *Whiteinella* sp. were found in the Cenomanian-Koniasian aged levels of carbonate marls and limestones at lower levels of the unit (Figure 3).

Santonian-Campanian: Globotruncana biolochiibiomicritis consists of hard, fragile textured limestones in the microbiobiophysi, and volcanic intercalated sandstone-limestone-marl intercalations in the upper levels. The unit of Santoian-Campanian age, *Globotruncana bulloides* Vogler, *Globotruncanita elevata* (Brotzen), *Globotruncana lapparenti lapparenti* Brotzen, *Rosita fornicata* (Plummer), *Globotruncana* sp. planktonic foraminifera were detected.

Maastrichtian: The yellowish-colored, thin-medium bedded fossiliferous biosparite consists of sandy limestones with microbiofaciesty developed. Within the unit, the foraminifera of *Sirelina orduensis* İnan, *Orbitoides medius* (D'archiac), *Hellenocyclina beotica* Reichel, *Siderolites calcitrapoides* Lamarck, *Omphalocyclus macroparus* (Lamarck) and *Discocyclina* sp., bentik were determined. According to the determined fossils, this unit, which is determined to have collapsed at the age of Cenomanian-Maastrichtian age, has a fault-controlled area around NW-SE direction to the south of the study area (Figure 3).

Paleocene: The unit, which consists of fossiliferous biosparitemicrobiophase with dark gray colored medium-bedded, hard-textured, bi-directional joints and composed of slightly sandy limestone, has a thickness of approximately 220 m. In the unit, *İdalina sinjarica* Grimsdale, *Missisippina binkhorsti* Reuss and *Rotalia trochidiformis* fossils, which gave Paleocene age, were determined. Unit-owned exposures offer a wide range of fault-controlled landscapes starting from the south-eastern part of the Erbaa county and continuing along the southern coast of the Kelkit River to the southeast.

Lower-Middle Eocene: The units which are very wide spreading in the study area are composed of grayish and somewhat variegated colored medium to thin bedded units in the upper levels with yellowish brown colored conglomerate, pebbly sandstone, sandstone, mudstone, claystone, marl and units in turbiditic flysch facies, consists of shallow marine limestone, which is locally laminated mostly decayed.

Within the unit, *Nurdanella boluensis* Özgen *Alveolina stercusmaris* Mayer-Eymar, *Asterigerina rotula* Kaufmann, *Alveolina* sp., *Assilina* sp., *Nummulites* sp., *Aktinocyclina* sp. and *Valvulina* sp. as well as benthic foraminifera like *Turritella* sp. and *Ostrea* sp. Many macrofossils belonging to Gastropoda, Lamellibranchiata, Brachioopoda branches which were not defined on the basis of breed were observed.

The conglomerates at the base of the unit are variegated colored, poor-medium sized, composed of pebbles, limestone, metamorphic rock fragments and quartzites. The conglomerates have a gray, yellowish-brown colored, bi-directional sandstone with fine-to-medium bedding.

The mudstone levels of the unit are gray, yellowish-reddish colored, soft-textured structure and it is lined with yellow, greenish, fine claystones in places. In the upper levels, the unit is accompanied by mudstone-sandstone alternations, white-cream colored, thin-medium bedded marls.

The highest levels of the unit are shallow marine limestones with grayish, white, abundant Nummulitic, massive textured, thick bedded, some levels brecciated, Nummulitic biosparit microbiophysical features. The presence of agglomerates composed of volcanic gravels and blocks, which are generally found in a matrix of volcanic materials, is an indication of the intensification of volcanism towards the end of the Middle Eocene.

The gravels forming the unit are derived from basalt, andesite and metamorphic rocks. This lithology, which consists of dark colored pebbles in quite different sizes, is rarely accompanied by sandstones, mudstones and clayey veins and coal veins in some regions.

Tuffs, which form a matrix of the agglomeratic unit where massive-looking basalts are also observed, and which are observed as interlayer in places, are observed as grayish white colored, massive, thick layers.

Upper Eocene: It consists of dark agglomerate, volcanogenic sandstone, basalt, andesite, tuff, tuffite and sandstone-siltstone intercalated volcanic rocks and dark gray-black column basalts and hard-textured andesites that cut them in dykes. Considering the stratigraphic location of the unit, it is accepted that it may be Upper Eocene aged (Aktimur et al., 1992).Starting from the eastern Niksarcounty to the north of the study area, the width of the unit which measures a wide area extending to the northwest of Doğanyurt is 180 m.

Miocene-Pliocene: The second cover units that collapsed in the depressions along the North Anatolian Fault zone and in the terrestrial environment consist of loose and / or unconfigured conglomerate-sandstone-claystone alternations and travertines with mudstone, gypsum interbeds in general and unconformably overlapped units of all self-aged units.

The unit, which is in deteriorated construction and presents a low relief morphology, is somewhat thin-walled and often looks like a conglomerate of volcanic material, carbonate-cemented matrix, surrounded by gravels of varying sizes.

Green-brown, cross-bedded, pebbly sandstones and red colored mudstone alternations are observed in the unit, which are products of a stream environment with seasonal regime change. River channel fill and meander river sediments are located on fine-grained flood plain deposits. Consistent with all these lithologies, there are travertines that offer thin-medium strata.

Within the unit which is assumed to be Oligo-Miocene-Piliocene age, giving the fossil content and the stratigraphic position, which is the Erbaa district and south of Gökçeli, *Ostracoda* sp. was detected and the approximate thickness of the unit in the study area is 150 m.

Quaternary: The youngest sediments of the study area are alluviums containing gravel-small pebbles. The alluviums are exposed to an ever-expanding area of Kelkit vineyard, north and south, from the Erbaa and Niksar districts. During the Kelkit valley, especially in the flood areas in the south and north, red limestone, radiolarite and loose textured conglomerates containing pebbles derived from metamorphic rocks and gravelly, sandy and clayey materials. Alluviums come in different grain sizes derived from various units in the world and do not show continuity in the lateral and vertical directions.

In the study area, Quaternary elderly units are composed of detritic and / or poorly fixed detritic units. These units, which characterize various sub-environments of the terrestrial environment, are observed as alluvial and kolivial specks in the central parts of the study area and in the broken parts of the formation in the upper part and in the physical comminution products, The skirt rashes in the region, the accumulation cones, and the streamside utensils are detritics that have been found in the Quaternary. The Kelkit River valley and the current bed contain the current Quaternary sediments which are composed of river equipme

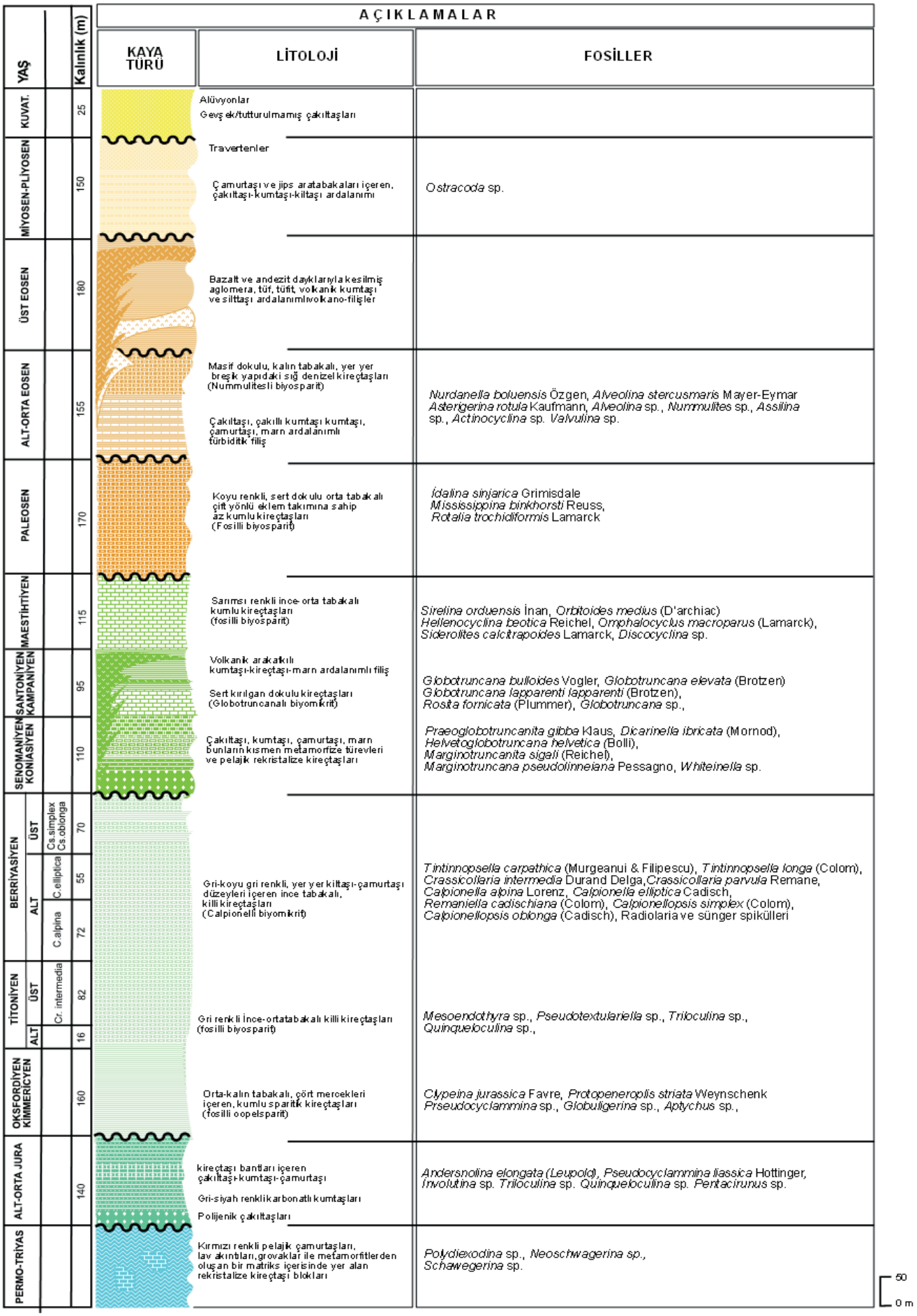

Figure 3. The generalized stratigraphic section of Erbaa(Tokat) region

4. ERBAA TERRITORY MEASURED STRATIGRAPHY SECTIONS

4.1. Çakır Measured Stratigraphic Section: This section taken from the east of the Cakir Village in the southeast of Erbaa District located in the G37 d1 Paftas in the study area covering certain parts of the Tokat G 37 Paftas and taken to the southwest, is taken at 8 02 950 latitude, 45 00 100 longitude start and 8 02 100 latitude 44 96 96 longitude finish The coordinates are approximately 1500 m in the direction of SW. A total of 286 m thickness was measured and 46 specimens were collected (Figure 4).

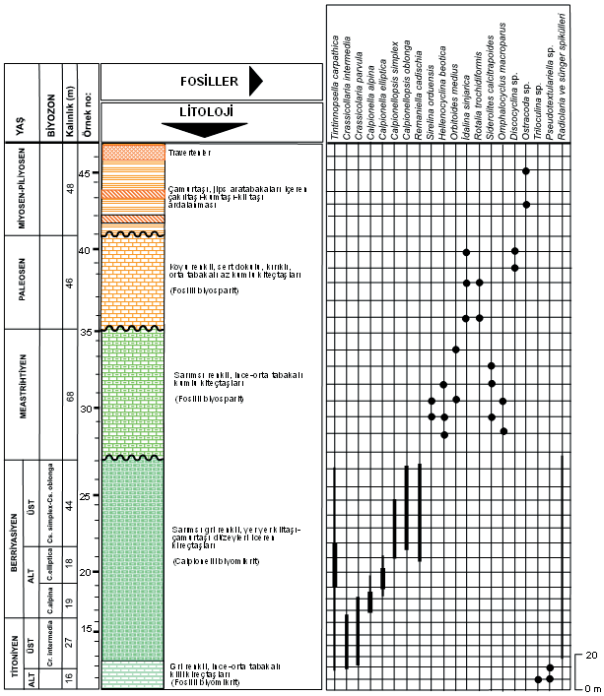

Figure 4. *Çakır measured stratigraphic section.*

4.2. EnekpınarMeasured Stratigraphic Section: This section, taken from the north of Enekpınar to the south-east of Erbaa District in the G37 d1 Paftas in the study area covering certain parts of Tokat G 37 Paftas, is taken from west to southwest, 799 200 latitude, 44 99 150 longitude start and 7 98 500 latitude 44 98 800 between the longitude end coordinates, is about 1000 m in the direction of SW. A total of 667 m thickness was measured and 64 specimens were collected (Figure 5).

4.3. İverönü Measured Stratigraphic Section This section, which is located in the area G37 d1 in the study area covering certain parts of the Tokat G37 Paftas, is taken from west to northwest of the Inverönü northeastern southeast of the Erbaa District, 7,700 latitude, 45 01 400 longitude start and 7 97 300 latitude 45 02 100 longitude end The coordinates are approximately 1840 m in the direction of the NW. A total of 665 m thickness was measured in this section and 84 specimens were collected (Figure 6).

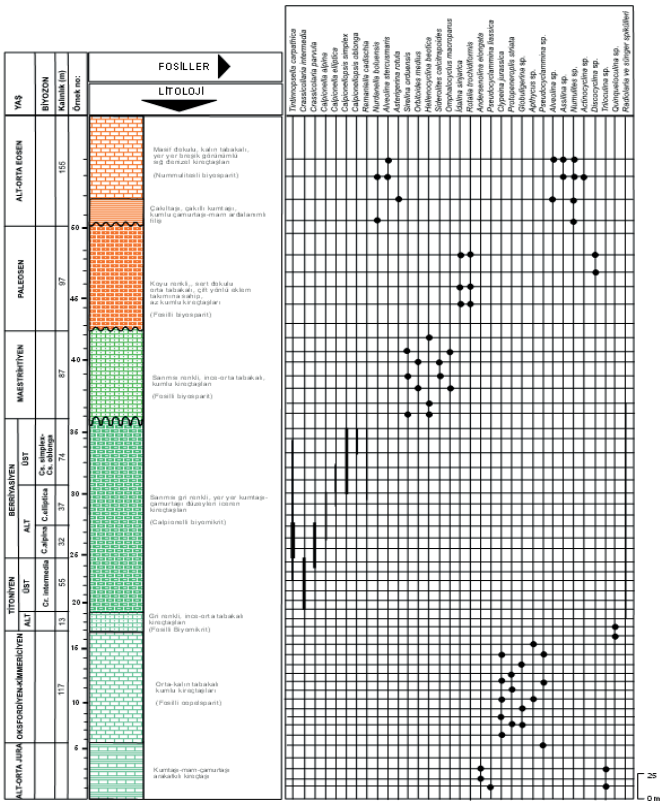

Figure 5. *Enekpınar measured stratigraphic section.*

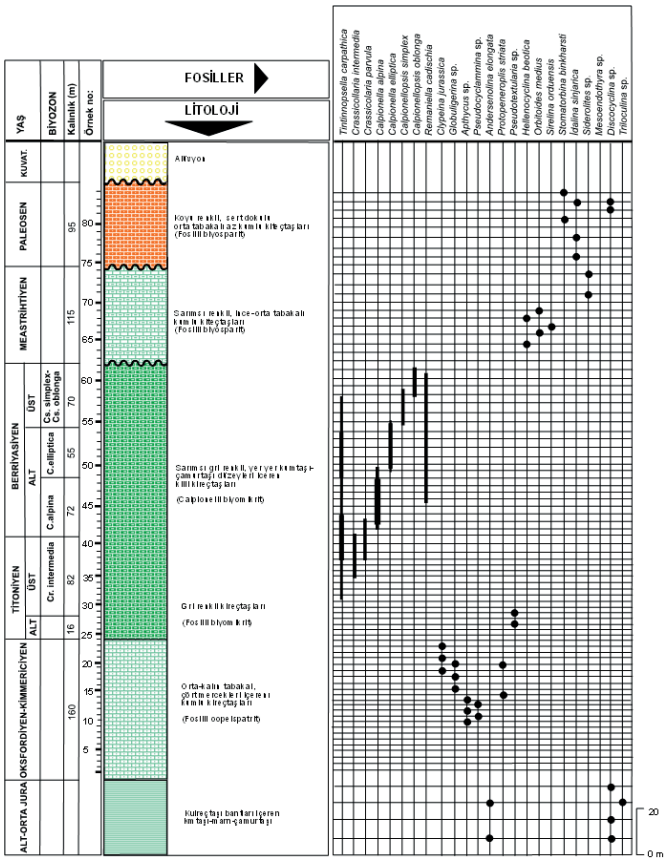

Figure 6. *İverönü measured stratigraphic section.*

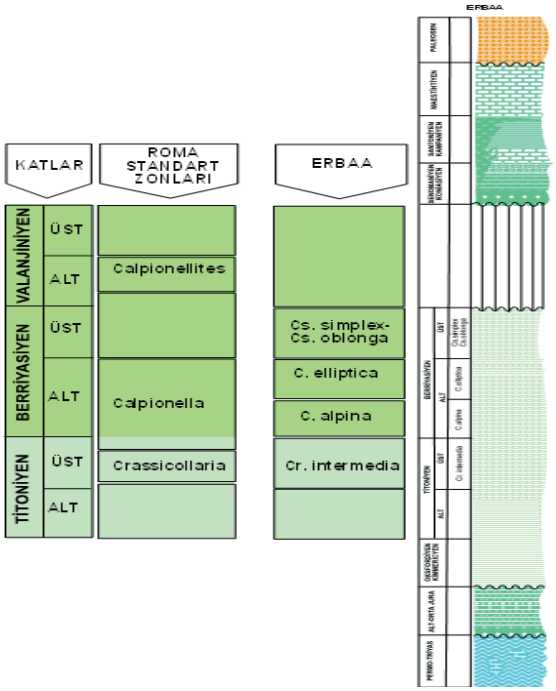

Figure7 . *Detected biozones were compared to the Roman Standard Zone*

5. CONCLUSIONS

- Geological, stratigraphic, paleontologic and biostratigraphic features of the Upper Mesozoic region have been tried to be revealed in this study, which was carried out in certain parts of Tokat H37 d1, d2 and d3 dated to 1 / 25.000 in Erbaa (Tokat) region.
- In the detailed paleontologic and biostratigraphic studies on rock samples taken systematically from sites with abundant titanic facies and Calpionel abundance, resulting in the formation of *Tintinnopsella carpathica* (Murgeanui ve Filipescu), *Crassicollaria intermedia* (Durand Delga), *Crassicolaria parvula* Remane, *Calpionella alpina* Lorenz, *Calpionella elliptica* Cadisch, *Remaniella cadischiana* (Colom), *Calpionellopsis simplex* (Colom), *Calpionellopsis oblonga* (Cadisch), 5 calpionel species and 8 species belonging to these species were identified and systematized.
- In biostratigraphic investigations of the late Titonian-Early Valanjinian aged, titanic facies developed calpionelli and radiolarialbiomicriticmicrobiophysical limestones revealed four calpionelbiozones, Crassicollaria intermedia, Calpionella alpina, Calpionella elliptica, Calpionellopsis simplex-Calpionellopsis oblonga.
- The detected biozones were compared to the Roman Standard Zone and the Crassicollaria intermedia-Calpionella zone boundary was observed to be incompatible with the Roman Standard Zone boundary.
- It is observed that the upper limit of the Calpionellopsis zone in the Erbaa region, which is located in the east of the Central Pontides, does not correspond to the Roman Standard Zone boundary.
- It is determined that the sequence of the Titonic facies in the region is missing from the top.
- Upper Jurassic-Lower Cretaceous aged limestones, which are located in the Pontide basin, are mostly found to be rich in titonic facies and rich in calpionel content.
- Although the Upper Jurassic-Lower Cretaceous aged limestones that appear on the Pontide basin are usually composed of thin-bedded micritic limestones with the formation of titonic facies, it is observed that the entire does not include Calpionel. This is a sign that the calpions are locally provincial, although not real.

REFERENCES

Akyazı, M. ve Tunç, M. (1992). Zile (Tokat) Yöresinin Stratigrafisi. TJK Bülteni, C. 35/2. s.36

Aktimur, H. T., Ateş, Ş., Yurdakul, M.E., Tekirli, M.E., ve Keçer, M., (1992), Niksar-Erbaa ve Destek Dolayının Jeolojisi. MTA Dergisi 114, 25-36,

Alp, D. (1972) Amasya yöresinin jeolojisi. İ.Ü. Fen Fakültesi
Monografileri, Sayı; 22, 10 s.

Ambraseys N.N. (1970): Some characteristics features of the Anatolian fault zone. Tectonophysics 9, 143 –165.

Ambraseys N.N. (1971): On the value of historical records of earthquakes. Nature 232, 375–379.

Arpat, E. Şaroğlu, F. 1975. Türkiye'deki bazı önemli genç tektonik olaylar. Türkiye Jeoloji Kurumu Bülteni, 18/1, 91-101.

Barka, A.A., Cohen, H., Aky.Z, S. & Watchorn, F. (2000). Tectonic evolution of the Niksar and Tasova-Erbaa pull-apart basins, North Anatolian fault zone: their significance for the motion of the Anatolian block. Tectonophysics 322, 243-264.

BlumenthaL, M.M. 1950. Beitr.ge zur Geologie des landschaften am Mittleren und unteren Yeşil Irmak (Tokat, Amasya, Havza, Erbaa,Niksar). Mineral Research and Exploration Institute of Turkey (MTA) Special Publication D 4, 153 p.

Kavak, Sezen, F. Koçbulut, O. Tatar, H. Gürsoy, B.L. Mesci,K.S.Kavak, Z. Akpınar, A. Polat, G. Kanaat veH.T. Demirel, 2006, Esençay Fayı'nın Erbaa güney batısı ve Niksar güneyindeki bölümünün jeomorfolojik özellikleri, 2006, ATAG 10. Toplantısı Bildiri Özleri Kitapçığı , s.74.

Serdar, H.S., Yarman, M. Kazdal, R.A. ve Seymen, İ. (1975) Kelkit vadisi kesiminde Kuzey Anadolu fayzonunun tektonik özelliği, Doktora Tezi, İ.T.Ü. Maden Fakültesi Yayınları 192 s.

Sezen, F. Koçbulut, O. Tatar, H. Gürsoy, B.L. Mesci,K.S.Kavak, Z. Akpınar, A. Polat, G. Kanaat ve H.T. Demirel, 2006, Esençay Fayı'nın Erbaa güneybatısı ve Niksar güneyindeki bölümünün jeomorfolojik özellikleri, 2006, ATAG 10. Toplantısı Bildiri Özleri Kitapçığı , s.74.

Özcan, A., Erkan, A., Keskin, A,, Keskin, E., Oral, A., Özer, S.,Sümengen, M. ve Tekeli, O. (1980) Kuzey Anadolu Fayı ile Kırşehir Masifi arasının temel jeolojisi: MTA Enst. Rapor No: 6722, 139 s. (yayımlanmamış).

Öztürk, A., 1979. Ladik-Destek yöresinin stratigrafisi: TJ.K, Bült., 22, 27,34.

Toprak, Ö., (2014). Batı-Orta Karadenizde yüzeyleyen Jura-Kretase yüzleklerinin stratigrafisi. Doktora Tezi (Yayınlanmamış)

Yoldaş, R., Keskin, B., Korkmaz, S., Didik, S.. Kalkan, l., Ağrıdağ, D.S. ve Besbelli, B. (1985) Samsun ve dolayı (Kızılırmak-Yeşilırmak arasındaki bölgenin) jeolojisi ve petrol olanakları: MTA Rap., 8130 (yayımlanmamış), Ankara.

MÜHENDİSLİK FAKÜLTESİ

Uluslararası Mühendislik Araştırma ve Geliştirme Dergisi

International Journal of Engineering Research and Development

Cilt/Volume:9 Sayı/Issue:3 Aralık/December 2017 https://doi.org/10.29137/umagd.350588

Araştırma Makalesi / Research Article

Weight and Diameter Estimation Using Image Processing and Machine Learning Techniques on Apple Images

Onur CÖMERT[1*], Mahmut HEKIM[2], Kemal ADEM[3]

[1] *Gaziosmanpaşa University, Faculty of Engineering, Mechatronics Engineering*
[2] *Gaziosmanpaşa University, Faculty of Engineering, Electrical and Electronics Engineering*
[3] *Gaziosmanpaşa University, Department of Informatics*

Başvuru/Received: 08/10/2017 **Kabul/Accepted**: 01/12/2017 **Son Versiyon/Final Version**: 26/12/2017

Abstract

Classification of table fruits according to size is traditionally hand made. But human factors are the cause of faulty classifications. Automatically performing this process with the machines is important in terms of speeding up the process, reducing costs, and minimizing errors. In this study, weight and diameter estimations were made on "Starking" type apples using image processing techniques. Firstly 50 photographs were taken with NIR camera and 830nm long pass filter. Afterwards, edge detection algorithms and morphological operations were performed on the images to obtain the boundaries of the images. Diameter and area information obtained from the binary image were used as attributes. These attributes were given as input to Linear Regression method and estimated. As a result, 93% of the diameters of the apples and 96.5% of the weights could be estimated.

Key Words

"Starking Apple, Image Processing, Linear Regression"

onur.comert@gop.edu.tr

1. INTRODUCTION

According to FAO (2010), Turkey, which has come after China and the USA in the production of apples, tends to move this place to the upper level every passing day. Apple is one of the most fruit produced in the world after bananas, grapes and oranges. In Turkey, fruit is the most produced fruit after grape (Anonymous,2016).

Automation systems are increasingly important in the food industry based on agricultural products. In this sector, the classification of vegetables and fruits according to their qualities and specifications is usually done manually by quality control workers. However, this method does not provide a complete standard and sometimes misclassifications can be made. For this reason, the automatic determination of the size of the apples is important in terms of speeding up the classification process and making it cheaper (Kondo, 2010).

In this study, the dimensions and weights of the apples were automatically estimated using image processing and machine learning methods on apple images transmitted digitally through a camera, thus facilitating classification.

2. LITERATURE

Looking at the scientific studies on image processing and machine learning methods used on fruits and vegetables, it was generally seen that industrial type cameras with CCD (Er et al., 2013), (Sofu et al., 2013), (Tonguç & Yakut, 2009), (Xiaobo et al., 2007) or Monochrome (Unay, 2005), (Unay & Gosselin, 2005) technology are used.

In some studies have used usually between 450nm and 1000nm band-pass NIR (Near Infrared) filters. A large number of images were taken with these filters and analyzed on these images. This makes it easier to foreground the desired region in the image (Unay, 2005), (Unay & Gosselin, 2005), (Unay & Gosselin, 2005).

Conventional methods were preferred for image processing and feature extraction stages. Filtering (Er et al., 2013) and color space transformations (Er et al., 2013), (Tonguç & Yakut, 2009), (Xiaobo et al., 2007) in the preprocessing phase, thresholding (Er et al., 2013), (Unay, 2005), (Unay & Gosselin, 2005) in the segmentation phase, and statistical and graphical properties (Unay, 2005), (Unay & Gosselin, 2005) in the feature extraction phase were used.

Support Vector Machine and Artificial Neural Networks (Unay, 2005), (Unay & Gosselin, 2005), (Unay & Gosselin, 2005), (Xiaobo et al., 2007) as classification methods and Linear Regression and Decision Trees (Er et al., 2013) as estimation methods were used.

3. MATERIAL AND METHOD

In this section, firstly, how to get the images used in working is explained. Then, the image processing techniques used on the images are explained according to the order of application. Finally, the results obtained by the estimation process are given.

The process flow diagram showing the sequence of operations performed in Figure 1 is shown.

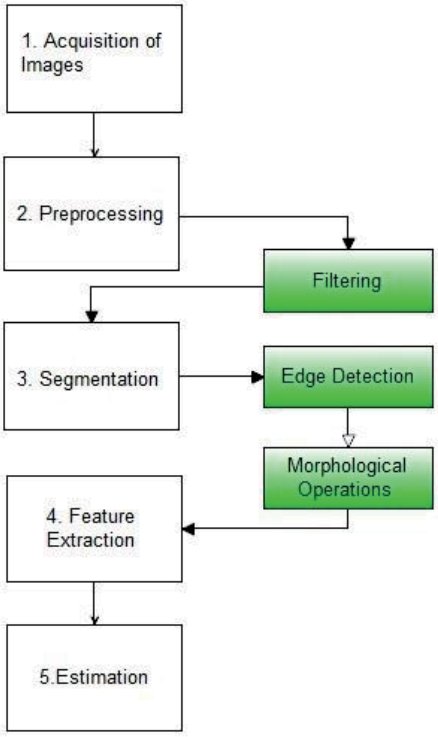

Figure 1: Process flow diagram

As you can see in Figure 1, there are five main groups of operations. These operations are explained in detail in the ongoing sub-headings.

3.1. Obtaining Data

The images used in the study were obtained by means of a pre-established image acquisition platform. The platform was designed to be able to transmit light from outside and contains artificial lighting elements (Tungsten Halogen Lamps). Within the platform, there are NIR camera, lens and longpass filter for image acquisition. Since the camera can transfer data directly to the computer via Ethernet, no other intermediate card is needed. The NIR camera features used are given in Table 1.

Table 1: Teledyne DALSA Genie Nano NIR features

Model Type	Mono/NIR
Shutter	Global
Sensor Type	CMOS
Sensor Model	On-Semi Python2000
Active Resolution	1900x1200dpi
Max frame rate	50
Image Size	2.2 Megapixel
Sensor Format	2/3”
Pixel Size	4.8x4.8µm
Data Format	8 or 10bit Mono
Connection Type	Gigabit Ethernet (1000Mbit/s)
Lens Mount	C-mount
Exposure Control	Programmable

Table 2. Fujinon HF16HA-1B features

Mount Type	C-mount
Focus size	2/3",1/2", 1/3"
Min. Focus distance	16mm
Iris interval	F1.4~F16
Iris	Manually
Focus	Manually
Max angle of view	17°04' horizantal, 12°50' vertical
Min object distance	10cm
Macro	No
Dimensions	29.5 x 29.5 x 29.5mm
Weight	45gr

The lens type determined by considering the scanning area and the object distance is Fujinon brand HF16HA-1B model. The lens properties are given in Table 2.

A computer with a 4-core processor with a clock speed of 2.6 GHz was used to record and process images. The image acquisition system used in Figure 2 is shown.

As shown in Figure 2, a matte black material was preferred for the floor on which the apples are to be placed. This fabric material used on the roof does not reflect the infrared rays, so the background is seen as black. The reason for this is to make it easier to distinguish the hand from the background.

Mirrors were placed on the inner walls of the platform to distribute the light evenly over the entire apple surface and to prevent shading.

A 830 nm Long-pass filter was used in front of the lens. Thanks to this filter, the beams in the visible region can not reach the camera, so a clearer image is obtained.

A 830 nm Long-pass filter was used in front of the lens. Thanks to this filter, the beams in the visible region cannot reach the camera, so a clearer image is obtained. Tungsten Halogen lamps have a very wide wavelength range (Anonymous,2017). Therefore, Tungsten Halogen lamps have been chosen as the lighting element for the wavelength range to be suitable for this filter. There are also white leds on the platform, but these beams did not used with NIR camera because they do not appear in the infrared region. Leds have a narrower wavelength range than Halogen Lambs, but Leds have better image performance for lighting purposes (Anonymous,2012) Therefore, LEDs was used with color camera.

The Matlab program was installed on the computer to receive and process the image data. 50 Starking type apples were used to create image data. The apples were randomly selected from an ordinary grocery store. Images were taken from six different directions of the hand and a total of 300 images were obtained. Then, these apples were weighed with a precision electronic scale and their diameters measured with a caliper. These values were recorded and actual diameter and weight data were created. The following table shows the measured diameter and weight values of the apples.

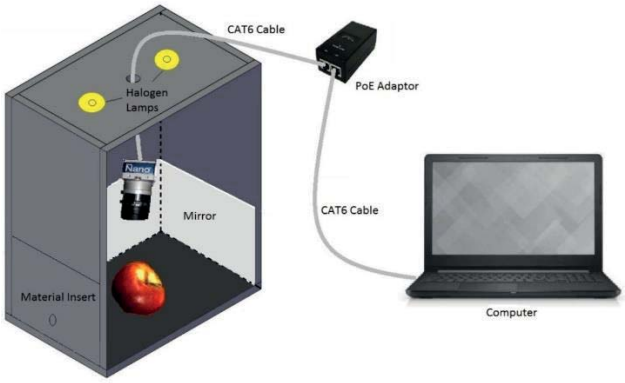

Figure 2: The image processing system

Table 3: Measured diameter and weight values of apples

No	*Weight (gr)*	*Dia(mm)*		*No*	*Weight(gr)*	*Dia(mm)*
1	143	71		*26*	231	85
2	125	69		*27*	166	73
3	124	65		*28*	182	79
4	126	71		*29*	152	73
5	124	65		*30*	202	80
6	151	72		*31*	160	73
7	134	67		*32*	184	75
8	115	64		*33*	167	72
9	156	72		*34*	190	77
10	114	64		*35*	129	68
11	117	65		*36*	196	75
12	136	67		*37*	155	74
13	143	71		*38*	154	72
14	117	67		*39*	181	78
15	141	71		*40*	183	76
16	132	72		*41*	110	68
17	126	67		*42*	130	68
18	119	66		*43*	135	69
19	131	68		*44*	146	70
20	169	73		*45*	137	69
21	218	81		*46*	133	70
22	224	80		*47*	127	66
23	189	77		*48*	170	75
24	184	77		*49*	98	63
25	136	73		*50*	123	67

3.2. Preprocessing

As is known, preprocessing is a process or process group performed to remove unwanted portions of an image. In the preprocessing phase of the paper, a cropping at fixed width was first made in the image. On this count, parts without apples have been removed from the image. The second process is to soften the image to provide a better segmentation. Figure 3 shows how cropping is done.

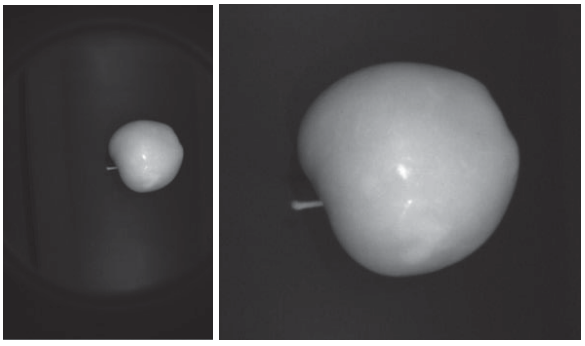

Figure 3: The preprocessing stage

Figure 3 shows two images. The image on the left shows the original image transferred from the image acquisition system to the computer, while the image on the right shows the image clipped on the computer.

3.3. Segmentation

Segmentation is the process of separating the part or parts of interest in the image from the background. In this phase, the image is usually converted to binary by specifying a manual threshold value.

In this work, it was aimed to separate the apple object in the image from the background. For this, a more dynamic method was preferred rather than a fixed threshold value. First, boundaries of apple in the image were determined by applying the Prewitt edge extraction algorithm. On this obtained binary image, closing, filling and opening processes were applied in order to obtain a binary image in which area covered by apple object is white and the other parts are black. It is seen that these operations are applied as below.

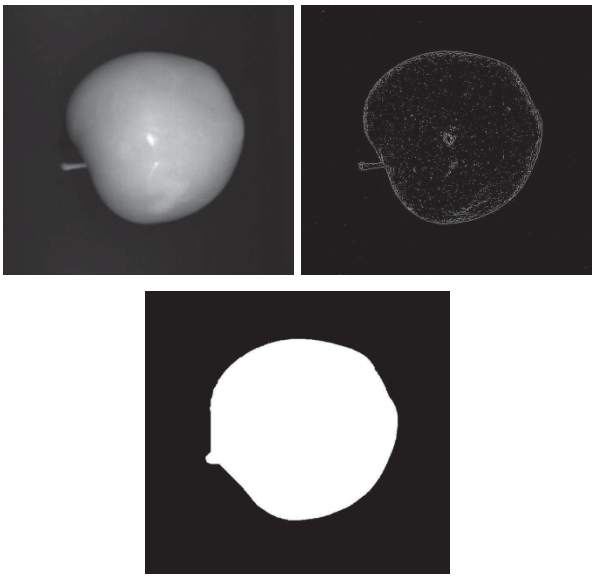

Figure 4: The segmentation stage

In Figure 4, the second image is the binary image formed after the edge detection process. The third image is an image in which the closing, filling and opening process has been applied and the background is completely separated from the apple. This image will be used for feature extraction during forecasting.

3.4. Feature Extraction

In the feature extraction phase, the goal is to obtain the sequence of values that will be input into the machine learning methods. These properties may be statistical properties of the objects in the image, as well as shape features such as the area and size of the objects.

Since our aim in our study is to estimate the weight and the diameter of the apple, the area and the diameter of the object in pixels are determined. In order to obtain the diameter information of the apple, the environment was first determined. Then, its diameter was obtained considering the circular structure of the apple. The figure below shows the diameter and area information of the apple.

Figure 5 shows the green pixel area and diameter information on the apple.

In Table 4, the obtained area and diameter information are presented in pixels.

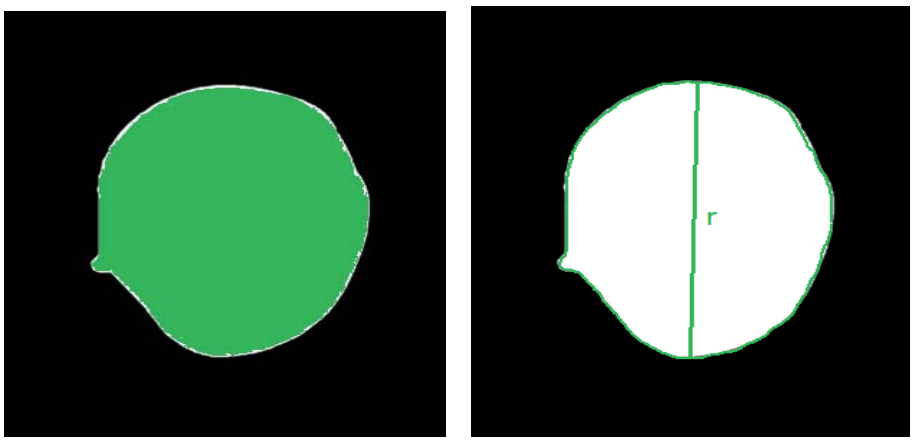

Figure 5: The feature extraction stage

Table 4: Estimated area and diameter values of apples

No	*Area(pixel)*	*Dia(pixel)*		*No*	*Area(pixel)*	*Dia(pixel)*
1	140280	388		*26*	206409	543
2	123991	363		*27*	170761	444
3	126773	363		*28*	173632	452
4	125506	390		*29*	145991	405
5	121553	356		*30*	186005	568
6	138326	405		*31*	158168	443
7	130484	368		*32*	166489	485
8	118524	358		*33*	131539	439
9	138467	408		*34*	160422	505
10	116143	354		*35*	134015	384
11	122808	359		*36*	143398	497
12	133099	372		*37*	142392	435
13	134406	393		*38*	157447	414
14	119072	354		*39*	159849	477
15	136068	377		*40*	159111	484
16	132257	370		*41*	117214	354
17	128564	367		*42*	123008	408
18	118435	350		*43*	130398	382
19	130089	368		*44*	141205	401
20	153238	449		*45*	130797	418
21	211526	533		*46*	136551	376
22	185908	536		*47*	131009	369
23	193931	485		*48*	172087	490
24	172420	527		*49*	106462	333
25	139245	385		*50*	130753	375

As shown in Table 4, area and diameter values are directly proportional to each other. This shows the correctness of the calculated values. These values will be used for estimation at the next stage.

3.5. Estimation

Linear Regression method was used to estimate the diameters and weights of the apples. This method was preferred because data is linear and it is a rapid method.

Linear Regression

Regression is the simplest method for classifying and predicting (making the right adjustments) on a given dataset. There are two approaches for regression: linear and nonlinear. The linear regression approach assumes that there is a specific error between the weighted sum of the input variables and the output variable. In this case there is a linear connection between the input variables and the output. The multiple linear regression equation used for input data with multiple properties is shown in Equation-1.

$$Y = W_0 + \sum_{j=1}^{N} W_j X_j + E \qquad (1)$$

W_j in Equation 1 represents the weight values, X_j is the feature vector of the data, N is the total number of features in the data, E is the error, and Y is the target variable. The important thing here is to find the W_j values. The most common method for this is the least squares method (Chapra & Canale, 2003). The least squares method is based on finding the equation coefficients that minimize the sum of squared errors. The main principle of this method is based on the smallest of the Mean Squared Error (MSE) expressed in Equation 2 below.

$$MSE = \frac{1}{N} \sum_{i=1}^{N} (d_i - \bar{d}_ı)^2 \qquad (2)$$

$$RMSE = \sqrt{MSE} \qquad (3)$$

$d_i - \bar{d}_ı$ in Equation 2 indicates the distance (error) between each target variable and the correct equation to be calculated. Root Mean Square Error (RMSE) in Equation-3 is used to determine the error rate between the measured values and the estimates. The approach of the RMSE value to zero means that the estimation capability of the system is increased (Singh et al., 2009).

A 10-part cross validation has been applied to test the classification success. As a result, the diameters of the apples 93% and the weights 96.5% could be correctly estimated.

4. RESULTS

In this study, it was aimed to estimate the diameter and weight values of the Starking apples which are the most grown apple varieties in Turkey by image processing methods. Through a generated image acquisition system, features were extracted from images taken from 6 different directions of 50 apples. These properties were used as an input to the Linear Regression method for estimating the diameters and weights of the apples and as a result, the diameters of the apples 93% and their weights 96.5% were correctly estimated.

ACKNOWLEDGMENT

This study was supported by Gaziosmanpaşa University Institute of Natural and Applied Sciences as BAP project (2016/28).

REFERENCES

Anonymous, “Light-emitting diode”. Wikipedia, https://en.wikipedia.org/wiki/Light-emitting_diode#cite_note-56 (24.04.2017), 2017a.

Anonymous, “Halogen Lamp”. Wikipedia, https://en.wikipedia.org/wiki/Halogen_lamp (24.04.2017), 2017b.

Anonymous, “Dünya meyve suyu sektörüne bakış”. MEYED/Meyve Suyu Endüstrisi Derneği, http://www.meyed.org.tr/userfiles/file/sektor_istatistikleri/dunya_meyve_suyu_sektorune_bakis_akdag.pdf (08.04.2016), 2016.

Anonymous, “All in 1 LED Lighting Solutions Guide. PhilipsLumileds”, https://web.archive.org/web/20130314111003/http://www.philipslumileds.com/uploads/221/PG01-pdf (24.04.2017). 2012.

Chapra, S. C. and Canale, R. P. “Yazılım Ve Programlama Uygulamalarıyla Mühendisler İçin Sayısal Yöntemler”. Literatür Yayıncılık, ISBN: 975-8431-83-8. 2003.

Er, O., Cetişli, B., Sofu, M. M. and Kayacan, M. C., “Gerçek Zamanlı Otomatik Elma Tasnifleme”. Süleyman Demirel Üniversitesi Fen Bilimleri Enstitüsü Dergisi, 17(2), 31-38. 2013.

Kondo, N., “Automation on fruit and vegetable grading system and food traceability”. Trends in Food Science Technology, 21, (145-152). 2010.

Singh, K.P., Basant, A., Malik, A. and Jain, G. “Artificial neural network modeling of the river water quality-A case study”, Ecological Modelling, 220(6), 888-895. 2009.

Sofu, M. M., Er, O., Kayacan, M. C. and Cetişli, B., “Elmaların Görüntü İşleme Yöntemi ile Sınıflandırılması ve Leke Tespiti”, Gıda Teknolojileri Elektronik Dergisi, 8(1), 12-25. 2013.

Tonguç, G. and Yakut, A. K., “Fruit grading using digital image processing”. Tarım Makinaları Bilimi Dergisi, 5(1), 93–101. 2009.

Unay, D., “A stem-and/calyx recognition system based on pattern recognition for ‘jonagold’ apples”. Tech. Rep., TCTS Labs., Faculte Poly- technique de Mons. 2005.

Unay, D. and Gosselin, B., “Artifical Neural Network-Based Segmentation and Apple Grading”. IEEE International Conference on Image Processing, 2, 630-633. 2005.

Unay, D. and Gosselin, B., “Thresholding-Based Segmentation And Apple Grading By Machine Vision”. Tech. Rep., TCTS Labs., Faculte Poly- technique de Mons. 2005.

Xiaobo, Z., Jiewen, Z. and Yanxiao, L., “Apple color grading based on organization feature parameters”. Pattern Recognition Letters, 28, 2046–2053. 2007.

MÜHENDİSLİK FAKÜLTESİ

Uluslararası Mühendislik Araştırma ve Geliştirme Dergisi

International Journal of Engineering Research and Development

Cilt/Volume:9 Sayı/Issue:3 Aralık/December 2017 https://doi.org/10.29137/umagd.347702

Araştırma Makalesi / Research Article

Organometallic compound derivates as a novel efficient electron injection layer for hybrid light-emitting diodes

Yasemin TORLAK[1*]

[1]*PamukkaleUniversity, Cal Vocational High School*

Başvuru/Received: 08/10/2017 **Kabul/Accepted**: 01/12/2017 **Son Versiyon/Final Version**: 26/12/2017

Abstract

In this study we have presented the use of a organometallic compounds derivates (Keggin type polyoxometalates) for the production of powerful electron injection layer between the emissive polymer layer (PFO) and cathode layer (Al) . Electron transport studies in organometallic compounds layers showed efficient electron transport in very thin structures. High efficiency solution-processed organic light emitting diodes (OLEDs) are achieved by organometallic compounds such as Keggin type polyoxometalates used as electron injection or transport layers with superb electron mobilities and hole blocking capacities. These results indicate the potential for organometallic compounds derivates as a variable, emerging new class of efficient electron injection/transport molecular materials for high performance air-stable HyLEDs. The Keggin type polyoxometalates show unique features such as superior ionization energy and low electron affinity which conversion them as efficient electron injection/hole blocking layers and, immensely high electron mobility.

Key Words

"Polyoxometalate, hybrid light-emitting diode, Keggin."

ytopal@pau.edu.tr

INTRODUCTION

Recently organic light-emitting diodes (OLED) derived from conductive polymers have be a focus of interested as they are marked the most prospect elements for the low cost generation of following lineage flexible screens and solid-state enlightenment references (Komoda et al., 2008).

In turn for organic light-emitting diodes derived from conductive polymers to acquire their complete potential, limit of operating voltage, perfect performance and device stability are called for and important progress to solve these matters has been made in recent years. On the other hand, organic light-emitting diodes arise from conductive polymers efficiency and operating voltage are unfortunately restricted by the fairly large energetic gap among the generally high lying lowest unoccupied molecular orbital level (LUMO) of most conductive polymers and the large work-function of non degradable in air cathode like Al metal electrodes (Brown et al., 2001), alongside some polymers low electron mobility (Laquai et al., 2007). Nowadays, superior electron mobility inorganic metal oxides (Bolink et al., 2007), (Haque et al., 2007) solution-processable conjugated polyelectrolytes (Tokmoldin et al., 2009), (Wang et al., 2006) dielectrics and have been suggested as differents to low work-function metals increase electron injection, lower the operating voltage and device balance.

Organometallic compound derivates especially, transition metal oxides with a energy states close to the ground-state level like ZnO (4.2 eV) and TiO_2 (3.8 eV) (Wang et al., 2006) also dielectric oxides like ZrO_2 (3.0 eV) (Jin et al., 2008) have been utilized as electron injection (EIL)/transport (ETL) layers as they decrease the injection obstacle at the cathode between polymer interface. In a study by Glezos et al. has indicate that a agency of the category of polyoxometalates (POMs) (Pope et al., 1991), a member of water soluble inorganic molecular transition oxides whose various chemistry admits for facile regulation of their structural, optical and electronic properties, shows a excellent electron mobility (Glezos et al., 2003) and has a low lying conduction-band edge deposited at 4.0 eV. Moreover, electron transport works in polyoxometalate layers exhibited excellent electron transport in very thin structures (Douvas et al., 2008). These properties make it a very appealing candidate for use as an elecron injection layer hybrid light-emitting diodes.
In this study we reported for the use of a two different derivates of water-soluble POMs (B1-W and B1-Mo) exhibiting the lacunary Keggin structure polyoxometalates ($PW_{12}O_{40})^{3-}$) (Glezos et al., 2003) as a novel electron injection layer in HyLEDs. In particular, green fluorescent OLEDs using PFO as the emissive layer and B1-Mo as the electron transport material gave 19.5 lm W^{-1} and 40.0 cd A^{-1} capacity and luminous efficiency, respectively. POM derivates as a novel efficient electron injection layer with a LUMO level lying between that of the emissive polymer layer and the Fermi level of Al, ensures an medium step for easing and enhancement electron injection between Al and the polymer LUMO, as incorporated between the light-emitting layer and Al. All this conclusions in a decreased turn-on voltage and a important reduce of the operating voltage also a high increase increase in the high current density, normalized intensity and luminance, enhancing the total efficiency of the hybrid light-emitting diodes.

2. EXPERIMENTAL SECTION

Synthesis of organometallic compounds derivates (POMs). $Na_2WO_4{\cdot}2H_2O$ (181.5 g, 0.550 mol) dissolved in 300 mL water and were incorporated 50 mL of H_3PO_4 1M and 88 mL of glacial CH_3COOH. The solution was stirred throughout one hour. Next, KCl (60 g, 0.805 mol) were added to solution also the white precipitate washed with cooled deionized water and dried in at room temperature to obtain the B-1-W (Contant, 1987).

Devices preparation. The devices are processed according to the sequence of coatings shown so that the measurement is ready. These process are as follows;

a-) Surface abrasion and Uv ozone treatment (The conductive layer of part of our HNO_3-HCl-Si devices is removed to avoid short circuit.) For the anode ITO coated on glass is used. ITO electrodes are cut in 1.5 cm x 1.5 cm in the construction of the OLED device and a 0.3-0.5 cm edge is removed by chemical etching. Prepared bases are cleaned with acetone, isopropyl alcohol and distilled water respectively for 15 minutes in ultrasonic bath and dried with nitrogen gun. Uv ozone treatment (Cleaning effect is generated by scattering these rays on the surface with appropriate bulbs which can generate enough energy in the ultraviolet spectrum.) This reactive ozone is the process of removing organic impurities from the oxygen separated from the atoms. Thus, the volatile hydrocarbons released from the surface are expelled. Oxygen plasma at 60 watt and 5cc is applied for 2 minutes to increase the (oxygen) μ-oxo group, which removes nano-sized dirt on the surface of the cleaned glass and allows the organic molecules to adhere better to the surface. By separating the hydrocarbons from the surface, ultra clean ITO coated surfaces with high wettability are obtained and ready for use.

b-) Coating of thin films. The glass surfaces are cleaned with pressurized nitrogen before the ITO glasses with increased hydrophilic properties by Uv-ozone are introduced into the coating process and immediately placed in the spin coating device. Poly (3,4-ethylenedioxythiophene) poly (styrenesulfonate) (PEDOT: PSS) with high conductivity is used as the void transfer material so that the glass surface is completely covered. After filtering to 0.45 μm, it is coated on ITO by spin coating method at 4000 rpm for 40 seconds. The coated glass is placed on a clean glass surface and cleaned by wiping the PEDOT: PSS layer with water by 3 mm. The reason for cleaning the PEDOT:PSS layer about 3 mm is that the bottom electrode will come to this area and

this area will be covered with Al. After the PEDOT:PSS (40 nm) coating and cleaning process is finished, the glasses are dried under vacuum at 120 ° C.

c-) Coating of light-emitting layer (PFO). 10 mg / ml solutions of organic materials were used. Since the prepared OLED device contains different layers, some layers require spin coating and some require vacuum evaporation. The light is coated at 1000 rpm with cyclic coating (100 nm) as the light-emitting layer (PFO). Organic solvent-soluble materials such as PFO can be coated with a spin coating on the PEDOT: PSS layer, but when the coated layer must not be covered with another material soluble in the same class solvent, the vacuum evaporation system is preferred at this stage.

d) Coating of POM, which is an electron acceptor, that is n type semiconductors. 10 mg / mL solutions of POM material were used. Coated with cyclic coating at 4000 rpm for 40 seconds. In order to make the anode contact, these layers were wiped with a cotton ball with their own solvents (water, methanol, acetonitrile) after each coating. After the cleaning process is finished, the glasses are dried under vacuum at 120 ° C.

e) Finally, the cathode (Al) contacts are covered with a thermal metal evaporation system (PVD) in a nitrogen atmosphere in a thickness of 100 nm.

Characterization methods.

Structural analyzes of the synthesized compounds were investigated by ^{31}P-NMR, ^{1}H-NMR, TGA and FT-IR, optical properties UV, electrochemical properties of alternating voltammetry and surface properties by SEM and AFM techniques. The characterization of the structures of the synthesized polyoxometallates was confirmed by FT-IR (Bruker Vertex 70), UV-vis (Hitachi-U4100), SEM (ZeissEvo LS10), AFM (NT- MDT, Ntegra Solaris), 31P- 400, CH instruments (660B Electrochemical workstation) were used.

The Ocean Optics USB 2000 fiber optic spectrophotometer was used to characterize the luminances and electroluminescence spectra and the Lambertian emission profile was used to evaluate the luminance. The current density-voltage characteristics were gauged with a Keithley 2400 source measurement unit.The Veeco atomic force microscope (AFM) was used to study the surface morphology of POM and PFO layers coated on ITO, and all measurements were performed at room temperature in general.

RESULTS AND DISCUSSION

The vibrational frequencies observed for the $[PW_{11}O_{39}]^{7-}$ anions in tetrabutylammonium $(Bu_4N)^{+}$ salts are very close to those of the anions due to the electronic properties of the anions. Monolacunary α-$K_{7-x}Na_x[PW_{11}O_{39}]\cdot 14H_2O$ (B-1) and trilacunary α-$K_9[PW_9O_{34}]\cdot 16H_2O$ (B-2) Keggin type Polyoxometalates, are prepared according to the method of Contant (Contant, 1987).

Infrared spectroscopy analysis shows some frequencies for the P-O_i stretch observed at the PO_4 tetrahedron center, which is consistent with literature data at 1086 and 1043 cm^{-1} for B-1 and 1054 and 1003 cm^{-1} for B-2 (as seen in Figure 1). The B-2 compound is formed by the alkalisation of the control of the B-1 compound formed by the acidification of the $WO4^{2-}$ oxo anion in the aqueous solution.

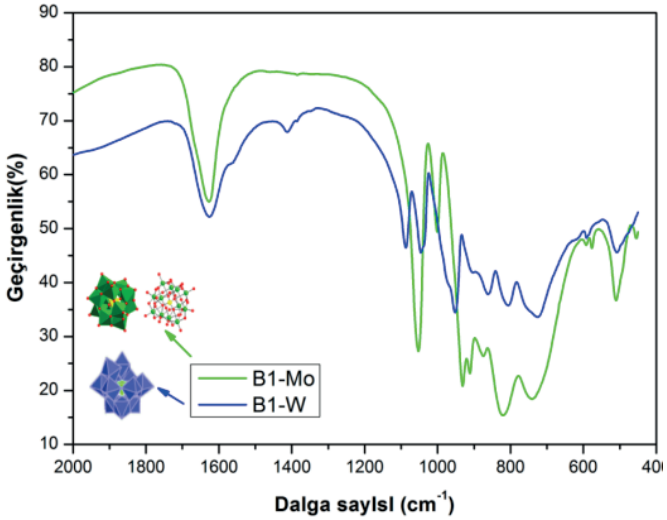

Figure 1. Comparison of FT-IR spectra of α-$K_{7-x}Na_xPW_{11}O_{39}\cdot 14H_2O$ (B-1) and α-$K_{7-x}Na_xPMo_{11}O_{39}\cdot 14H_2O$ (B1-Mo) compounds.

The ^{1}H-NMR and ^{31}P-NMR results of the synthesized Keggin structure of POMs and their W, Mo derivatives are given below. Chemical shift values are given above the spectra.

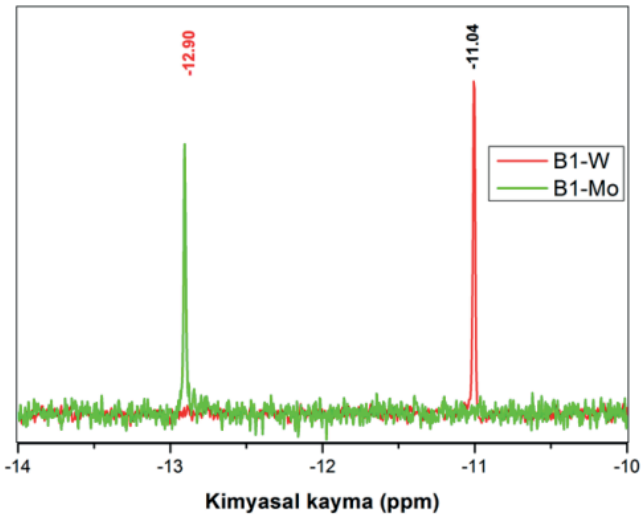

Figure 2. Comparison of ^{31}P NMR (121.49 MHz, D_2O) spectra of B1 and B1-Mo compounds in DH_2O-d6 at room temperature

When an external magnetic field is applied, a magnetic field is formed in the opposite direction of the external magnetic field in the electron cloud surrounding the core. As electrons are affected from this area, the ^{31}P nuclei with different chemical entrances enter the resonance in the negative magnetic field and the spectra of the POM compounds appear in the negative region. OLED devices structure including used to polyfluorene copolymer used in the emissive layer, B1-W and B1-Mo polyoxometalates used in the electron transport layer respectively, in the Figure 1a is shown.

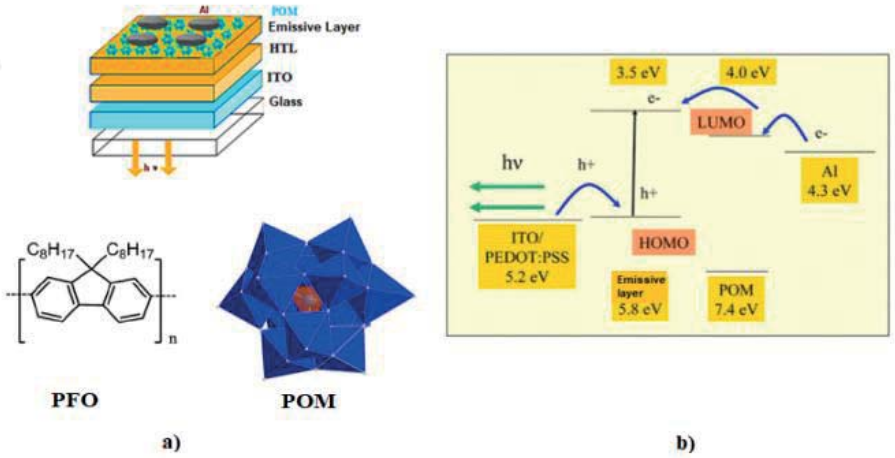

Figure 3. a-b. a) OLED with POM and PFO active layer **b)** Energy diagram

The fluorescent OLEDs were fabricated via spin coating to serve as PFO as the emissive layer, POM to operate as the electron injection/transport layers. Finally, the cathode (Al) contacts are coated in a nitrogen atmosphere with a thermal metal evaporation system (PVD) to be 100 nm thick. The schematic illustration in Figure 4. shows a sample OLED device preparation scheme used in our studies.

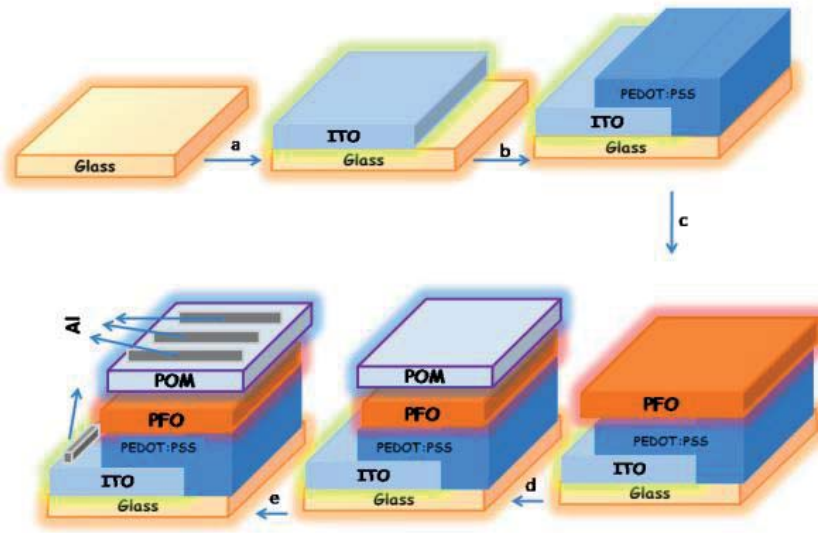

Figure 4. Scheme for the preparation of OLED device.

The results obtained in the studies conducted are examined below Figure 5. also shows the electroluminescence graph against the current values of the OLED.

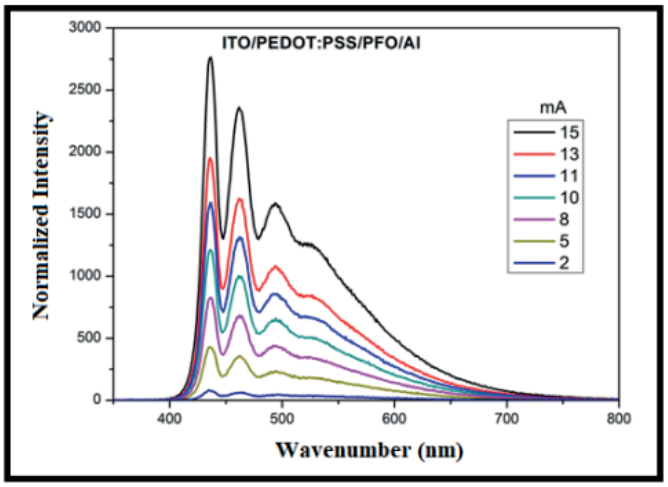

Figure 5. Electroluminescence graph of OLED devices with PFO based not doped with POM at different current intensities

As can be seen in Figure 5, a steady increase in electroluminescence has been observed in measurements made at a current density of 15 mA comparative graph of the reference OLED structure without POM for the same current value.

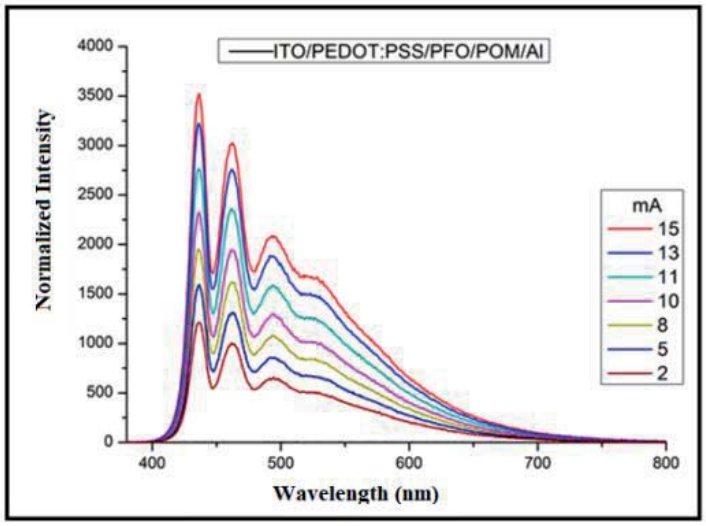

Figure 6. Electroluminescence graph of PFO based OLEDs doped with POM at different current intensities

Figure 5. and Figure 6. shows comparative radiation intensity-current density plots of POM-doped and undoped OLEDs coated with spin at 4000 rpm. When POM-doped OLED and non-doped OLED were compared, the highest light intensity observed at 2,700 cd/ m^2 in the undoped OLED structure reached a value of around 3,500 cd /m^2 by the addition of POM. This corresponds to an increase of nearly 23%.

The variation on the surface topography and include between the POM film on ITO and the POM to the PFO polymer film also the inhomogeneities offer in both cases as can be seen from the comparison of Figure 7. Polar hydrophilic molecules on the surface of this difference can be due to different wetting rates. To evaluate the AFM topographic images, although the POM layer is homogeneously coated on the PFO layer, the increased leakage current flow and the nanostructures between aluminum and POM increase the interface – is anticipated to be advantages for charge injection because of the high local electric field existing in the surroundings of POM fields.

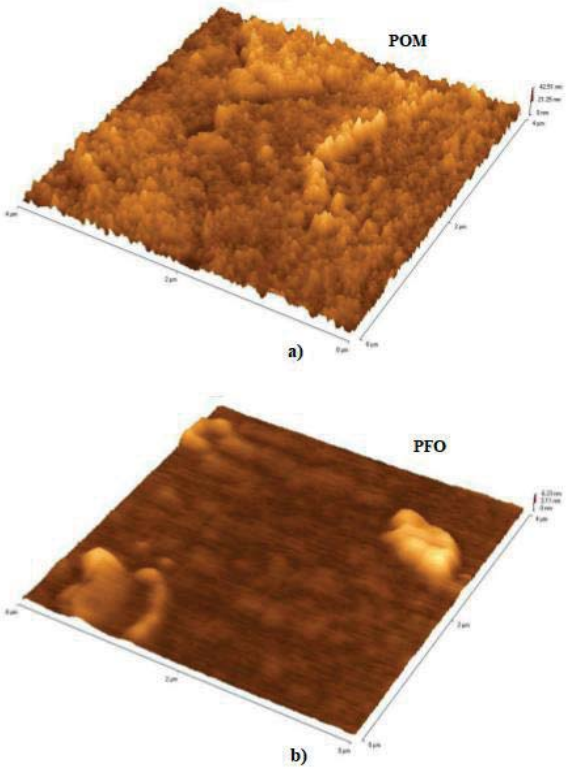

Figure 7. 3D AFM topographic images of (a) POM coated indium tin oxide (b) emissive layer (PFO) film

A wide interfacial contact area with rised surface roughness was sighted as POM was added at the PFO/Al interface. When this result is evaluated that technique was used to interpret electron mobilities of POM including films and the thicknesses of POM films, the resulting values are usually highly equal and very high. These high efficiency values are coherent with efficient device process in both fluorescent and phosphorescent OLEDs as confirmed from our input.

4. CONCLUSIONS

In summary, we have showed the use of a the Keggin structure lacunary polyoxometalates soluble in water, the B1-W and B1-Mo for the formation of a novel thin, exhibit the advantages of the superior electron injection and electron mobility characteristics high ionization energy and low electron affinity for use as electron transport materials in OLED devices. These results show that fine designing of an electron transport materials with a view to join different attractive properties is an powerful aspect to further increase performance of next generation the next generation of display technologies.

ACKNOWLEDGMENT

This study was supported by Pamukkale University Institute of Natural and Applied Sciences as BAP project (2017KKP131).

REFERENCES

A.M. Douvas, E. Makarona, N. Glezos, P. Argitis, J.A. Mielczarski, E. Mielczarski, “Polyoxometalate-based layered structures for charge transport control in molecular devices”, ACS Nano 2, 733, 2008.

T. Komoda, N. Ide, J. Kido, J.,”High Efficient OLEDs and Their Application to Lighting”, Light Vis. Environ. 32, 75., 2008.

T.M. Brown, R.H. Friend, I.S. Millard, D.J. Lacey, J.H. Burroughes, F. Cacialli, “Efficient electron injection in blue-emitting polymer light-emitting diodes with LiF/Ca/Al cathodes”, Appl. Phys. Lett. 79,174, 2001.

F. Laquai, G. Wegner, H. Bässler, Phil., “What determines the mobility of charge carriers in conjugated polymers?”,Trans. R. Soc. A 365,1473, 2007.

H.J. Bolink, E. Coronado, D. Repetto, M. Sessolo, Hybrid organic-inorganic light emitting diodes: effect of the metal oxide, Appl. Phys. Lett. 91,223501, 2007. 223501.

S.A. Haque, S. Koops, N. Tokmoldin, J.R. Durrant, J.S. Huang, D.D.C. Bradley, E. Palomares, “A Multilayered Polymer Light-Emitting Diode Using a Nanocrystalline Metal-Oxide Film as a Charge-Injection Electrode”, Adv. Mater. 19, 683, 2007.

N. Tokmoldin, N. Griffiths, D.D.C. Bradley, S.A. Haque, “A Hybrid Inorganic–Organic Semiconductor Light-Emitting Diode Using ZrO_2 as an Electron-Injection Layer”, Adv. Mater. 21,1, 2009.

L. Wang, B. Liang, F. Huang, J. Peng, Y. Cao, “Utilization of water/alcohol-soluble polyelectrolyte as an electron injection layer for fabrication of high-efficiency multilayer saturated red-phosphorescence polymer light-emitting diodes by solution processing”, Appl. Phys. Lett. 89, 151115, 2006.

Y. Jin, G.C. Bazan, A.J. Heeger, J.Y. Kim, K. Lee, “Improved electron injection in polymer light-emitting diodes using anionic conjugated polyelectrolyte”, Appl. Phys. Lett. 93, 123304, 2008.

N. Glezos, P. Argitis, D. Velessiotis, C.D. Diakoumakos, “Tunneling transport in polyoxometalate based composite Materials”, Appl. Phys. Lett., 83, 488 ,2003.

M.T. Pope, A. Muller, “Polyoxometalates: From Platonic Solids To Anti-Retroviral Activity”, Angew. Chem., Int. Ed. Engl. 30,34, 1991.

R. Contant, “Relation entre les tungstophophates apparentés à l’anion $PW_{12}O_{40}^{3-}$. Synthèse et propriétés d’un nouveau polyoxotungstophosphate lacunaire $K_{10}P_2W_{20}O_{70}\cdot 24H_20$”, Can. J. Chem., 65, 568-573., 1987.

MÜHENDİSLİK FAKÜLTESİ

Uluslararası Mühendislik Araştırma ve Geliştirme Dergisi

International Journal of Engineering Research and Development

Cilt/Volume:9 Sayı/Issue:3 Aralık/December 2017 https://doi.org/10.29137/umagd.348004

Araştırma Makalesi / Research Article

Maximum Power Point Tracking in Solar Power Systems by Using Differential Evolution Methods with Embedded Systems

Volkan YAMAÇLI[1]*, Kadir ABACI[2]

[1,2]Mersin University, Faculty of Engineering, Electrical and Electronics Engineering, Mersin, 33343 Turkey

Başvuru/Received: 08/10/2017 **Kabul/Accepted**: 01/12/2017 **Son Versiyon/Final Version**: 26/12/2017

Abstract

In this paper, one of the most important problems, Maximum Power Point Tracking (MPPT), in renewable solar power is studied and analyzed. In order to obtain the maximum power point in solar cells and panels the voltage and current should be maximized, simultaneously. Thus, the easiest way to achieve the maximum power point is tracking the solar energy, daylight, by measuring the light intensity in a solar cell or panel coaxially. In this work, the MPPT is achieved by optimizing the light intensity vector on a solar panel after measuring the daylight physically with the help of newly designed embedded system, and processing the real world values by using Differential Search Algorithm which is a new and improved method based on differential evolutionary principles.

Key Words

"Solar Power, Maximum Power Point Tracking, Renewable Energy, Differential Search, Optimization."

* *vyamacli@mersin.edu.tr*

1. Introduction

As electricity plays a vital role in the economy and industrial activity of a country, electric power systems have extensively expanded in the past decades. Electricity is generated in stations, transmitted by high voltage transmission networks, and delivered to consumers. With the ever-growing energy demand, power systems become more complex and difficult to control because the systems are being operated under highly stressed conditions such as unscheduled power flows and higher losses (Abaci et al., 2016). In the recent years, despite the technological progress on science; the problem of lack of energy continues by being much more vital. As the quality and accuracy of mathematical and psychical models of electrical systems improve, renewable technologies become the focus of theoretical and practical studies. In particular, solar energy attracts much attention. The utilization of photovoltaic (PV) conversion energy is today an emerging technology, characterized by gradually declining costs and increasing acquaintance with the technology (Belarbi et al., 2016). An accurate equivalent model of PV devices is an important task for determining and designing optimal PV systems. In total, three different models are required to model the electrical power output of a PV system for given irradiance and ambient temperature. These include a thermal model for finding the PV cell temperature, a radiation model for finding the solar energy absorbed in the PV cells and an electrical model for calculating the electrical characteristics of the PV system for the calculated absorbed radiation and cell temperature. Over the years, electrical models for varied complexities and accuracies have been developed for PV system. These include analytical models based on PV cell physics, empirical models and a few models which combine these two approaches (Siddiqui, 2013). But there is also a difficult task having similar importance with PV modeling, the maximum power point tracking problem. Thus, it is necessary to study MPPT method to extract the maximum power from PV panels. Various algorithms of power tracking are being researched or used in PV application (De Vrito, 2013). Those methods include the constant voltage tracking (CVT), the perturbation and observation algorithm (P&O), the incremental conductance algorithms (INC), OVC method, IC and IC Based on PI method, System Oscillation and Ripple Correlation, Beta Method, Temperature Method, Fixed Duty Cycle method and artificial intelligence methods such as fuzzy logic method, neural network method (Zhiqianf et al., 2017).

In order to simulate and realize the MPPT behavior and solve the problem, PV cells should be modeled and classified. In literature, the cells are modeled in two basic types which are one diode equivalent model and two diodes equivalent model. The quality and accuracy of a model increase as the number of parameters of the model increase but concerns of mathematical difficulties and simulation duration cause model parameters to be chosen fixed or neglected. There have been various studies on PV cell modeling and parameter estimation. Marion (Marion et al., 2004) determined the current and voltage curves by using interpolation technique while King (King et al., 2004) develops an experimental model for PV devices. Townsend (Townsend, 1989) developed a PV model equivalent circuit model by using four parameters and which neglects and chooses the shunt resistance infinite. Due to the accuracy issues of four parameter model, Beckman (Duffie, 1991) asserted a new model and mathematical solution which is called five parameter model in which the parameters can be defined as I_L, I_0, a, R_s, R_{sh} where shunt resistance is also processed despite causing nonlinearity. Later, new methods are developed for determining the solution set of parameters by using the I-V curve (Desoto et al., 2006) and the five parameter model is improved (Valerio et al., 2010).

Due to nonlinearity of the model, it is not possible to find a definite solution set for both PV model and MPPT numerically. Thus, estimation and optimization methods are used to determine these parameters with the purpose of converging to measured or simulated parameters as soon as possible. There are different methods have been used to estimate the parameters in literature. In some studies nonlinear solver scripts are used to determine the parameters while solving the equations numerically by defining and fixing a parameter in some others (Boyd et al., 2011), (Villavla et al., 2009) or solving the nonlinear equations iteratively with the minimum convergence error (Carrero et al., 2016). In various numerical and heuristic optimization techniques are used to estimate the model parameters for different characteristics of PV cells. Levenberg-Marquardt optimization technique and simplex search algorithm are used in literature recently (Ikegami et al., 2001), (Siddiqui, 2011).

Fuzzy optimization (Chen, 2001), (Lin, 2010) neural network based methods (Chen, 2010), (Chen, 2011) and heuristic methods (Moldovan et al., 2009) are used to determine the model parameters of a PV cell.

Recently, a population based method, differential search algorithm (DSA), which is a new and effective differential evolutionary method based algorithm for solving real-valued numerical optimization problems is presented by Pinar Civicioglu (Civicioglu, 2012). In this paper, a novel DSA-based approach is proposed for the purpose of solving the OPF problem. The main contribution of this paper is determining the MPPT and position of PV panel by using DS algorithm. The accuracy of the estimated parameters by using DS algorithm are compared to simulated base model and results are presented.

2. PV Cell Modeling

The equivalent circuit shown in Figure 1 consists of a light generated current source, a p-n junction diode and two resistances. I–V relationship in the equivalent circuit of Figure 1 is expressed by Eq. (1). The characteristic of any PV device are included in the model by five model parameters (I_L, I_o, a, R_s, R_{sh}). The model that describes the electrical performance of a PV device represented by Figure 1 using Eq. (1) is called the five parameter model (Siddiqui, 2013).

$$I = I_L - I_0\left(\exp\left(\frac{V+I.R_S}{a.V_T}\right)-1\right) - \frac{V+I.R_S}{R_{sh}} \qquad \left(V_T = \frac{k.T_c}{q}\right) \tag{1}$$

where q, k and Tc are elementary charge, Boltzmann's constant and cell temperature, respectively.

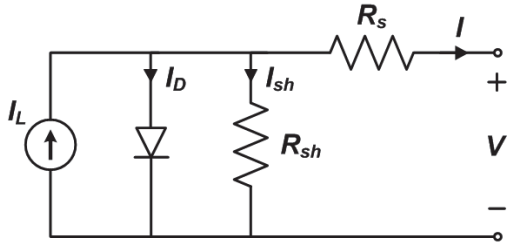

Figure 1: Equivalent circuit of a PV cell (Gray, 2011)

Eqs. (2) - (6) can be used to calculate the parameters in a desired operating condition which is dependent on cell temperature, solar radiation and band-gap energy of the PV material. Thus, the I-V and P-V characteristic of the PV cell can be predicted by using Eq. (1).

$$a = a_{ref}\left(\frac{T_c}{T_{ref}}\right) \tag{2}$$

$$I_L = \frac{S}{S_{ref}}(I_{L,ref} + (T_c - T_{ref}) \tag{3}$$

$$I_0 = I_{0,ref}\left(\frac{T_c}{T_{ref}}\right)^3 \exp\left(\left(NCS.\frac{T_{ref}}{a_{ref}}\right)\left(\left(\frac{E_{g,ref}}{T_{ref}}\right) - \left(\frac{E_g}{T_c}\right)\right)\right) \tag{4}$$

$$R_{sh} = R_{sh,ref}\left(\frac{S_{ref}}{S}\right) \tag{5}$$

$$R_s = R_{s,ref} \tag{6}$$

The notation of ref describes the parameters at standard test conditions (STC) where temperature and solar radiation are 25°C and 1000W/m^2 respectively in general. NCS and E_g represents the number of cells and band-gap energy, respectively. Eq. (7) can be used to calculate the band-gap energy for a current condition for different values of temperature where E_g = 1.43eV for GaAs type of material (Desoto et al., 2006).

$$E_g = E_{g,ref}\left(1 - 0.0003174\left(\frac{T_c}{T_{ref}}\right)\right) \tag{7}$$

2.1. PV Cell Objective Function

In order to achieve a valid solution set for the model parameters by using evolutionary methods, the objective function must be described in desired constraints and rules. The objective function namely fitness function is used to calculate and minimize the global error which leads the algorithm to a better solution set in the current space. The objective function, the normalized error function, is given in Eq. (8) below where m and e subscripts represent modeled and estimated values of variables, respectively.

$$ne = abs\left(\frac{I_{MP,m} - I_{MP,e}}{I_{MP,e}}\right) + abs\left(\frac{V_{MP,m} - V_{MP,e}}{V_{MP,e}}\right) + abs\left(\frac{I_{SC,m} - I_{SC,e}}{I_{SC,e}}\right) + abs\left(\frac{V_{OC,m} - V_{OC,e}}{V_{OC,e}}\right) \tag{8}$$

The electrical characteristic of the model is given by Table 1. I-V and P-V curves for the assumed model parameters are given by Figure 2 and Figure 3, respectively.

Table 1: Electrical characteristics of the PV model

Characteristic	Value
Short circuit current (I_{sc})	3.14 A
Open circuit voltage (V_{oc})	19.29 V
MPP current (I_{MP})	2.83 A
MPP voltage (V_{MP})	12.57 V
Number of cells in series (NCS)	32-cells

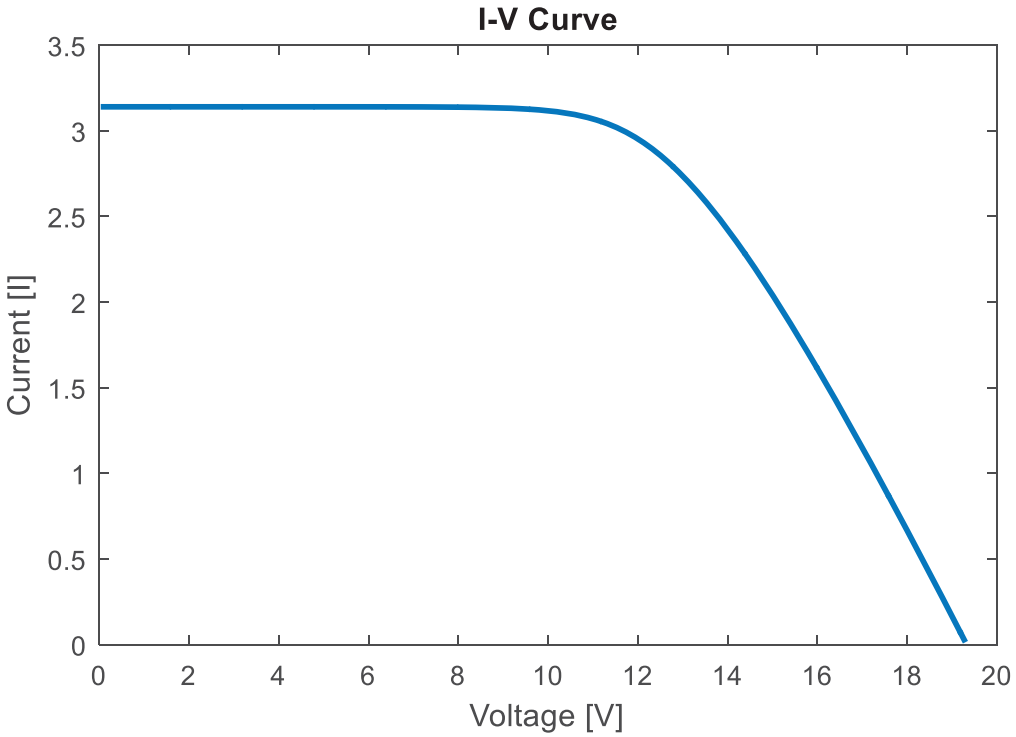

Figure 2: I-V curve for assumed parameters

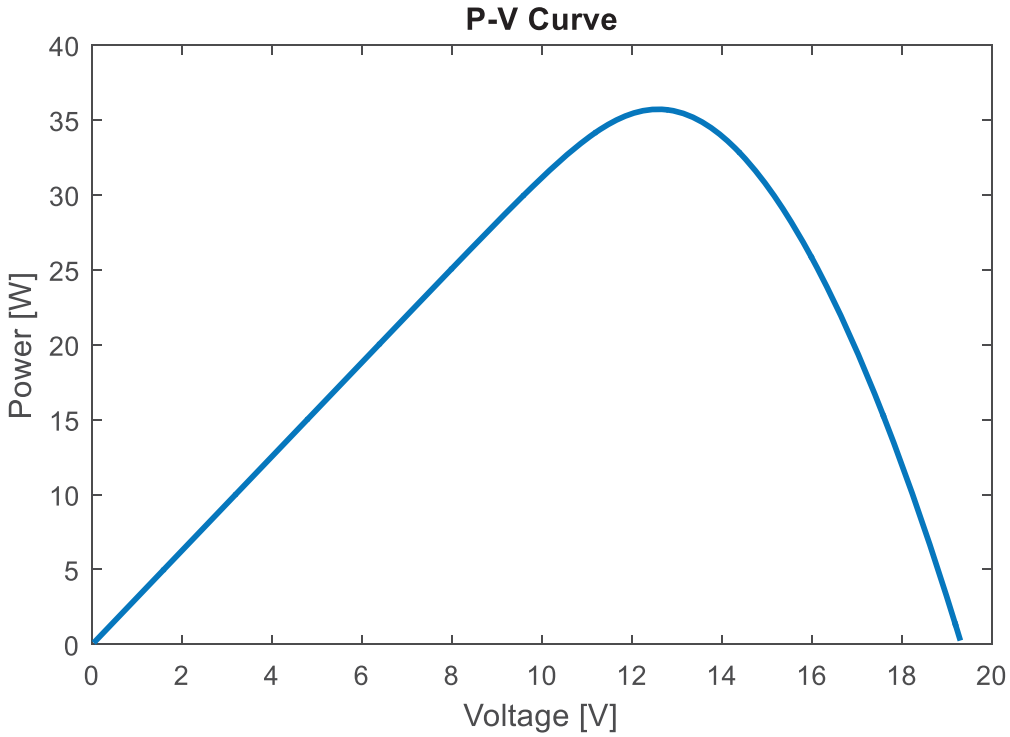

Figure 3: P-V curve for assumed parameters

3. Differential Search Algorithm (DS)

DS is a newly developed optimization algorithm based on differential evolutionary principles which simulates the Brownian-like random-walk movement used by a living organism to migrate.

Quality and efficiency of the food sources in the nature such as meadows and lakes may vary because of the climatic changes during a year, decade or century. In order to find high quality food sources and overcome the famine, living organisms migrates seasonally through intervals. This behavior assures the organism move to a new environment where the food source is of a high quality and variation.

The migrating organisms form a super organism which comprises large number of individuals, and the superorganism starts to change its location by moving to areas containing high quality food sources. Movement of a super organism can be described by a Brownian-like random-walk model. The behavior of superorganisms has been modeled using a number of computational intelligence algorithms, such as PSO, cuckoo search, ant colony, and artificial bee colony. Many species of predatory living beings, before moving or migrating to a site, control the fertility of this one. In other words, if a superorganism desires to move to a new site that can meet its needs, this superorganism settles in this new site at least for a period of time. However, if a more fertile area is found, the superorganism continues its migration (Civicioglu, 2012).

It is assumed, in DS algorithm, that a population made up of random solutions of the respective problem corresponds to an artificial-superorganism migrating. In DS algorithm, artificial-superorganism migrates to global minimum value of the problem. During this migration, the artificial-superorganism tests whether some randomly selected positions are suitable temporarily during the migration. If such a position tested is suitable to stop over for a temporary time during the migration, the members of the artificial-superorganism that made such discovery immediately settle at the discovered position and continue their migration from this position on (Civicioglu, 2012).

The pseudo-code indicating the DS algorithm is given by Figure 4, where N is the population size, D is the dimension of the problem and G is the maximum number of generation.

As shown in the formulation above, the DS algorithm employs multiple random numbers in order to generate new artificial organisms and select artificial organisms randomly for the purpose of converging to global optimum. Primarily, there are 4 numbers; randg, rand1, rand2, rand3 randomly generated in each iteration which are used to generate new artificial organisms. Also, there are 6 randomly generated numbers; rand6, rand7, rand8 rand9, rand10 are used in the process of random selection. Thus, the processes aforementioned lead the algorithm to diverge from local minimum and search for possible global optimum meanwhile keeping the variables in constraints (Abaci & Yamacli, 2016).

N: $Size\ of\ the\ population$
D: $Dimension\ of\ the\ problem$
G: $Number\ of\ the\ maximum\ generation$

1: $Superorganism = initialize(\,), where\ Superorganism = [ArtificialOrganism_i]$
2: $y_i = Evaluate(ArtificialOrganism_i)$
3: $for\ \ cycle = 1{:}G\ do$
4: $\quad donor = SuperOrganism_{Random_{Shuffling(i)}}$
5: $\quad Scale = randg[2{\times}rand_1]{\times}(rand_2 - rand_3)$
6: $\quad StopoverSite = SuperOrganism + Scale{\times}(donor - Superorganism)$
7: $\quad p_1 = 0.3{\times}rand_4\,, p_2 = 0.3{\times}rand_5$
8: $\quad if\ rand_6 < rand_7\ then$
9: $\quad\quad if\ rand_8 < p_1\ then$
10: $\quad\quad\quad r = rand(N, D)$
11: $\quad\quad\quad\quad for\ Counter1 = 1{:}N\ do$
12: $\quad\quad\quad\quad\quad r(Counter1, :) = r(Counter1, :) < rand_9$
13: $\quad\quad\quad\quad endfor$
14: $\quad\quad\quad else$
15: $\quad\quad\quad r = ones(N, D)$
16: $\quad\quad\quad\quad for\ Counter2 = 1{:}N\ do$
17: $\quad\quad\quad\quad\quad r(Counter2, randi(D)) = r\big(Counter2, randi(D)\big) < rand_{10}$
18: $\quad\quad\quad\quad endfor$
19: $\quad\quad\quad endif$
20: $\quad\quad else$
21: $\quad\quad\quad r = ones(N, D)$
22: $\quad\quad\quad for\ Counter3 = 1{:}N\ do$
23: $\quad\quad\quad\quad d = randi(D, 1, [p_2{\times}rand{\times}D])$
24: $\quad\quad\quad\quad for\ Counter4 = 1{:}size(d)$
25: $\quad\quad\quad\quad\quad r\big(Counter3, d(Counter4)\big) = 0$
26: $\quad\quad\quad\quad endfor$
27: $\quad\quad\quad endfor$
28: $\quad\quad endif$
29: $\quad individuals_{I,J} \leftarrow r_{I,J} > 0 \mid I \in i, J \in [1\ D]$
30: $\quad StopoverSite\big(individuals_{I,J}\big) \coloneqq Superorganism\big(individuals_{I,J}\big)$
31: $\quad if\ StopoverSite_{i,j} < low_{i,j}\ or\ StopoverSite_{i,j} > up_{i,j}\ then$
32: $\quad\quad StopoverSite_{i,j} \coloneqq rand{\times}(up_j{-}low_j) + low_j$
33: $\quad endif$
34: $\quad y_{StopoverSite;i} = Evaluate(StopoverSite_i)$
35: $\quad y_{Superorganism;i} \coloneqq \begin{Bmatrix} y_{StopoverSite;i} & if\ y_{StopoverSite;i} < y_{Superorganism;i} \\ y_{Superorganism;i} & else \end{Bmatrix}$
36: $\quad ArtificialOrganism_i \coloneqq \begin{Bmatrix} StopoverSite_i & if\ y_{StopoverSite;i} < y_{Superorganism;i} \\ ArtificialOrganism_i & else \end{Bmatrix}$
37: $endfor$

Figure 4: Pseudo-code of DS algorithm

3.1. DSA Implementation

DSA is similar to those other population based heuristic methods which use randomly generated possible solution sets of pre-determined dimensions (D) in upper and lower constraints. In DSA, N number of artificial organisms composed of D components determined initially forms a super organism. The super organism represents the candidate solution sets consist of PV cell parameters such as I_L, I_0, a, R_s, R_{sh}. The fitness values of each solution set are calculated and determined by applying the objective function given by Eq. (8).

Stopover site, which contributes the migration motion of artificial organisms, is generated among an artificial organism and a randomly selected donor based on Brownian-like random walk model during the DSA process. It is worthwhile to note that stopover site is generated by using a scale factor which can be a pre-determined fixed value as well as a randomly generated number. This scale factor lets the current artificial organism move and change direction in its constrained D dimensional space based on the size and direction of donor. The stopover site is chosen and replaces the direction of current artificial organism with the condition of

having a better fitness and also necessitated being in the upper and lower constraints aforementioned. Thus, a new migration motion in D dimensional space is formed spontaneously in each iteration by determining the best solution set which leads the super organism to the global optimal solution.

For the purpose of using the proposed DSA method for parameter estimation problem can be summarized as;

1. Load the system data and constraints.
2. Specify the DSA parameters such as number of individuals and maximum cycle.
3. Initialize a superorganism consisting a number of solution sets (individuals) for the first iteration.
5. Evaluate the fitness of the results, determine the best individual within the superorganism.
6. Generate new individuals depending on the best individual of the previous iteration
7. Increase cycle number by 1.
8. Evaluate the fitness value of newly produced superorganism.
9. Memorize the best global solution found so far.
10. Check if the maximum cycle met; stop the iteration process or jump to step 5.

4. Solar Power and Embedded Systems

In order to achieve both simulation and realization of MPPT problem, the solar panel and embedded systems are designed by using 2.4 GHz wireless transceiver modules (nRF24L01+) on embedded board which is chosen as Arduino Uno R3. The light dependent resistors (LDR) placed on each corner of solar panel, which has dimensions of 29x19 inches, and the light intensity is measured through analog outputs of LDR modules.

The solar power system can be divided in 2 sub-systems; The field system, which is namely transmitter system, contains solar panel, LDR modules, embedded development board and 2.4 GHz transceiver module. The diagram of first system is shown in Figure 5.

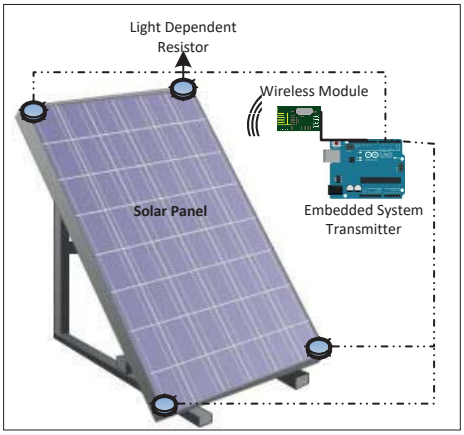

Figure 5: Transmitter field module of the MPPT system

The second system is designed as a receiver computer system, containing a 2.4 GHz transceiver module, embedded development board which is connected to a computer via USB protocol and MATLAB software. Receiver system diagram is shown in Figure 6.

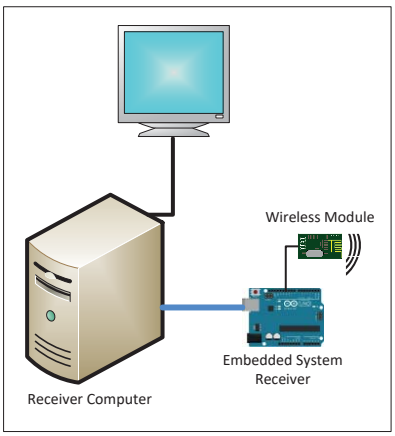

Figure 6: Receiver and computation module of the MPPT system

The embedded transmitter system code is shown if Figure 7. It is seen that the sensor values of LDRs are measured and sent through the 2.4 GHz wireless transmitter module.

```
#include  <SPI.h>
#include "nRF24L01.h"
#include "RF24.h"
sensor_firstPin = A0; // select the input pin for LDR 1
int sensor_secondPin = A1; // select the input pin for LDR 2
int sensor_thirdPin = A2; // select the input pin for LDR 3
int sensor_fourthPin = A3; // select the input pin for LDR 4
int sensorValues(De Vrito, 2013) = {0, 0, 0, 0}; // sensor measurement variable

void setup() {
Serial.begin(9600); //serial port settings for Radio communication
radio.begin(); // Start RF module
radio.openWritingPipe(pipe); //Define the pipe to send data}

void loop() {
sensorValue[0] = analogRead(sensor_firstPin); // read the value from the sensors
sensorValue(Abaci et al., 2016) = analogRead(sensor_secondPin);
sensorValue(Belarbi et al., 2016) = analogRead(sensor_thirdPin);
sensorValue(Siddiqui, 2013) = analogRead(sensor_fourthPin);

radio.write(sensorValue[0]); //send the values coming from the sensors to receiver system
radio.write(sensorValue(Abaci et al., 2016));
radio.write(sensorValue(Belarbi et al., 2016));
radio.write(sensorValue(Siddiqui, 2013));
delay(100);}
```

Figure 7: Embedded transmitter system code

Embedded receiver system code is shown in Figure 8. The receiver system reads the data by using wireless module and sends the same data to computer by serial communication protocol in order to process and optimize the values. So the MPPT optimization can be achieved by using the modeled PV panel and the light intensity vector by which is obtained with 2.4 GHz embedded transceiver modules.

```
#include  <SPI.h>
#include "nRF24L01.h"
#include "RF24.h"
int sensorValues(De Vrito, 2013) = {0, 0, 0, 0}; // sensor measurement variable

void setup() {
Serial.begin(9600); //serial port settings for PC communication
radio.begin(); // Start RF module
radio.openReadingPipe(1,pipe);
radio.startListening();//Define the pipe to read data}

void loop() {
s = 0;
if (radio.available()){
bool done = false;
while (!done){
done = radio.read(message, 1); //read the values coming from the transmitter
sensorValues[s] = message;
Serial.println(sensorValues[s]); //send sensor values to PC
s = s+1;
}}}
```

Figure 8: Embedded receiver system code

Thus, the optimization process continues for defined time ranges while receiver system gets the LDR values to computer continuously. The flowchart of the complete system is given by Figure 9. In the figure below, it can be seen that the receiver component optimizes system parameters by using the light intensity values obtained by transmitter module in order to optimize the solar panel model assumed in Section 2.

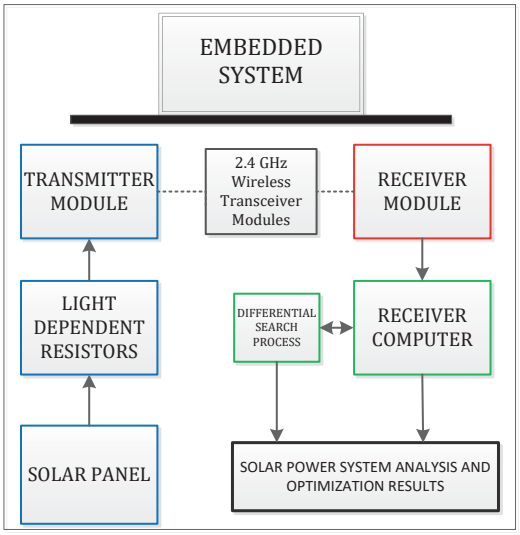

Figure 9: System flowchart

5. Results and Discussion

In order to estimate the parameters and optimize the system, the assumed parameters given by Table 1 are searched in 5-dimensional space consisting of these variables by using DS algorithm. The fitness values for each iteration are calculated and new super organisms are produced with the purpose of converging the global normalized error, given by Eq. (8), to zero. In addition, with measuring and sampling the light intensity vector obtained by embedded systems, the optimal position of the solar panel and the best light intensity vector for designed system is obtained when the maximum power point is achieved.
In parameter estimation process, the upper and lower values of parameters are limited. Constraints and limit values of five parameter model are given by Table 2 below. If the parameter value violates the upper or lower limit, the upper or lower limit value is assigned as the new parameter value respectively.

Table 2: Electrical characteristics of the PV model optimized to obtain maximum power point

Parameter	Value
Short circuit current (I_{sc})	3.18 A
Open circuit voltage (V_{oc})	17.49 V
MPP current (I_{MP})	2.87 A
MPP voltage (V_{MP})	12.53 V
Number of cells in series (NCS)	32-cells

The I-V and P-V curves for assumed and estimated parameter values of series connected PV cells are given by Figure 7 and Figure 8, respectively. It can be stated that the calculated Voc value by using the estimated parameters is 17.49V while it is 19.29V in the assumed model. The power at maximum power point is 35.96W for estimated parameter while same variable is 35.57W in the assumed model. The I-V and P-V curves of the realized PV model are shown in Figures 10 and 11, respectively.

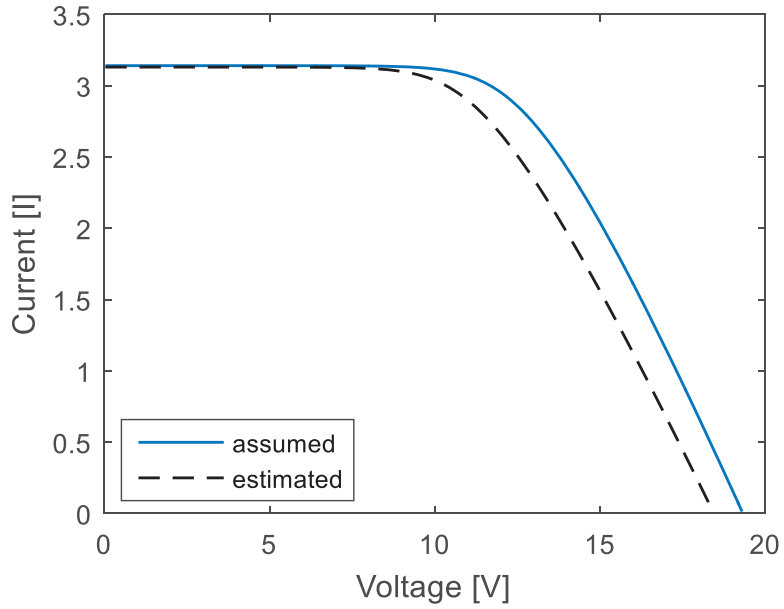

Figure 10: Figure 7: I-V curve of series PV cell for assumed and estimated parameters

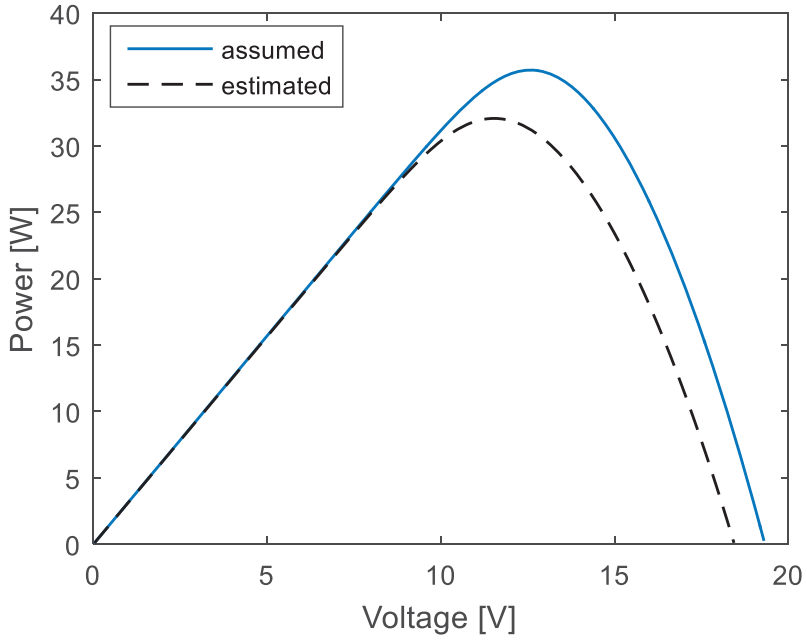

Figure 11: P-V curve of series PV cell for assumed and estimated parameters

6. Conclusions

In this paper a differential evolution based optimization method, DSA, is proposed and successfully applied to solve a multi objective function within the constraints regarding to solar cell modeling and maximum power point tracking problem. The results obtained by using the proposed DSA method, which are presented in detail, are compared with assumed model and maximum power point in paper and the efficiency of the DSA is demonstrated. Thus it is concluded that DSA provides a good solution performance, robustness and superiority and can effectively be used in large scaled, non-linear and non-convex problems in parameter estimation and maximum power point tracking area owing to its high solution quality and rapid convergence speed.

References

Abaci, K., Yamacli, V., Akdagli, A. (2016). Optimal power flow with svc devices by using the artifcial bee colony algorithm. Turkish Journal of Electrical Engineering & Computer Sciences, 24, 341-353.

Abaci, K., Yamacli, V. (2016). Differential search algorithm for solving multi-objective optimal power flow problem. International Journal of Electrical Power & Energy Systems, 79, 1-10.

Belarbi, M., Boudghene, A., Belarbi, E.H., Haddouche, K. (2016). A new algorithm of parameter estimation of a photovoltaic solar panel. Turkish Journal of Electrical Engineering & Computer Sciences, 24, 276-284.

Boyd, M.T., Klein, S.A., Reindl, D.T., Dougherty, B.P. (2011). Evaluation and validation of equivalent circuit photovoltaic solar cell performance models. Journal of Solar Energy Engineering, 133(2), 1-13.

Carrero, C., Ramírez, D., Rodríguez, J. Platero, C.A. (2016). Accurate and fast convergence method for parameter estimation of pv generators based on three main points of the I-V curve. Renewable Energy, 36(11), 2972–2977.

Chen C.W. (2001). A fuzzy ahp-based fault diagnosis for semiconductor lithography process", International Journal of Innovative Computing. Information and Control, 7(2), 805–816.

Chen C.W. (2001). Fuzzy control of interconnected structural systems using the fuzzy Lyapunov method. Journal of Vibration and Control, 17(11), 1693–1702.

Chen C.W. (2010). GA-based adaptive neural network controllers for nonlinear systems. International Journal of Innovative Computing, 6(4), 1793–1803.

Chen C.W. (2011). Stabilization of adaptive neural network controllers for nonlinear structural systems using a singular perturbation approach. Journal of Vibration and Control, 17(8), 1241–1252.

Civicioglu P. (2012). Transforming geocentric cartesian coordinates to geodetic coordinates by using differential search algorithm. Computers & Geosciences, 46, 229-247.

De Brito, M.A.G., Galotto, L., Sampaio, L.P., de Azevedo e Melo, G., Canesin, C.A. (2013). Evaluation of the main MPPT techniques for photovoltaic applications. IEEE Transactions on Industrial Electronics. 60(3), 1156–1167.

Desoto, W., Klein, S.A., Beckman, W.A. (2006). Improvement and validation of a model for photovoltaic array performance. Solar Energy, 80, 78–88.

Duffie, J.A., & Beckman, W.A. (1991). Solar engineering of thermal processes (2nd ed.). New York, John Wiley & Sons.

Gray, J.L. (2011). The physics of the solar cell, in handbook of photovoltaic science and engineering. New York, John Wiley & Sons.

Ikegami, T., Maezono, T., Nakanishi, F., Yamagata, Y., Ebihara K. (2001). Estimation of equivalent circuit parameters of pv module and its application to optimal operation of pv system. Solar Energy Materials and Solar Cells, 67, 389–395.

King, D.L., Boyson W.E., Kratochvil J.A. (2004). Photovoltaic array performance model. Sandia National Laboratories, Albuquerque, NM.

Lin M.L. (2010). Application of fuzzy models for the monitoring of ecologically sensitive ecosystems in a dynamic semi-arid landscape from satellite imagery. Engineering Computations, 27(1), 5–19.

Moldovan, N., Picos, R., Garcia-Moreno, E. (2009). Parameter extraction of a solar cell compact model using genetic algorithms. Spanish Conference on Electron Devices Proceedings, 379–382.

Marion B., Rummel S., Anderberg A. (2004). Current–voltage curve translation by bilinear interpolation. Progress in Photovoltaics, 12, 593–607.

Siddiqui, M.U. (2011). Multiphysics modeling of photovoltaic panels and arrays with auxiliary thermal collectors, MSc Thesis, King Fahd University of Petroleum & Minerals, Saudi Arabia.

Siddiqui, M.U., Abido, M. (2013). Parameter optimization for five- and seven-parameter photovoltaic electrical models using evolutionary algorithms. Applied Soft Computing, 13(12), 4608-4621.

Valerio, L.B., Orioli, A., Ciulla, G., Di Gangi, A. (2010). An improved five-parameter model for photovoltaic modules. Solar Energy Materials and Solar Cells, 94(8), 1358–1370.

Villalva, M.G., Gazoli, J.R., Filho, E.R. (2009). Comprehensive approach to modeling and simulation of photovoltaic arrays. IEEE Transactions On Power Electronics. 24(5), 1198–1208.

Townsend, T.U. (1989). A method for predicting the long-term performance of directly-coupled photovoltaic systems, MSc thesis, University of Wisconsin, Madison

Zhiqiang Gao, Song L., Xuesong Z., Youjie M., Jian Z. (2017). A new maximum power point tracking method for pv system. 29th Chinese Control And Decision Conference Proceedings, 544–548.

MÜHENDİSLİK FAKÜLTESİ

Uluslararası Mühendislik Araştırma ve Geliştirme Dergisi

International Journal of Engineering Research and Development

Cilt/Volume:9 Sayı/Issue:3 Aralık/December 2017 https://doi.org/10.29137/umagd.348072

Araştırma Makalesi / Research Article

Energy Consumption Analysis of Sintering Temperature Optimization of Pure Aluminum Powder Metal Compacts Sintered by Using The UHFIS

Mehmet TAŞTAN[1], Hayrettin GÖKOZAN[2], Pınar SARI ÇAVDAR[3], Gürkan SOY[4], Uğur ÇAVDAR[5]*

[1, 2] Manisa Celal Bayar University, Turgutlu Vocational School, Department of Electric & Energy
[3]Manisa Celal Bayar University, Turgutlu Vocational School, Department of Construction
[4, 5]Manisa Celal Bayar University, Turgutlu Vocational School, Department of Machinery

Başvuru/Received: 08/10/2017 **Kabul/Accepted**: 01/12/2017 **Son Versiyon/Final Version**: 26/12/2017

Abstract

In this study, pure aluminum (Al) powder metal (PM) compacts are sintered conventional or induction systems. PM compacts are sintered by furnace at 600ºC in 60 minutes in the conventional sintering process. In the other process, PM compacts are sintered by induction system at seven different sintering temperatures from 550□C to 610□C in 4 minutes. 2.8 kW, 900 kHz ultra-high frequency induction system (UHFIS) used for heating application of induction sintering process. Densities and hardness values are investigated for both processes. During these sintering processes, all energy consumption results are measured and calculated, then compared with each other. The effects of the sintering time increase in the induction sintering process on energy cost have been analyzed. Optimum sintering temperature of the induction sintering process is determined. It has been seen that the cheaper energy cost is obtained by the induction system for sintering application.

Key Words

"Aluminum, PM, Induction, Energy cost, Energy consumption."

1. Introduction

Powder metallurgy (PM) (Amirjan et al., 2013), (Sedlak et al., 2015) is a form of production, which facilitates the manufacture of particularly complex parts, made by mixing pure or alloyed powders of suitable specifications with a mixer, compressing them in a suitable mold with the desired shape to be mixed, and heating them to a temperature below the melting temperature (Angelo,2008).

Sintering (Pozzoli et al., 2015), (Caliman et al.,2015) is the most important production process of powder metallurgy. It is the process of increasing the grain size of the powder particles by increasing the strength of the particles and the strength of the powder components by heating them at a temperature below the melting temperature (Kang,2004).

PM based compacts are sintered by atmosphere controlled furnace, ultra-high frequency induction system (UHFIS) (Çavdar,2014), (Xun et al., 2014), (Gökozan et al.,2016), (Çavdar & Çavdar, 2015).

Induction system could be using different processes like; forging (Çavdar, 2015), heat treatment (Taştan et al.,2015), welding (Çavdar & Kusoglu, 2014), (Çavdar & Gulsahin, 2014) or casting. Also PM based compacts are sintered by microwave sintering (Baghani et al., 2015), (Reddy et al., 2016) spark plasma sintering (Mackie et al., 2016), (Dutel et al., 2017), laser sintering (Wudy et al., 2016), (Yasa et al., 2016) and conventional Sintering (Sharma & Majumdar, 2016), (Lemke et al., 2017)

In the study of Bisht et al (Bist et al., 2017) Al-GNP alloy (Graphene nanoplatelets) was sintered at 550 ° C for 40 min. In the study of Guo et al (Guo et al., 2017) Al-CNTs alloy (carbon nanotubes (CNTs) were sintered at 590-630 ° C for 30 min under argon. In the study of Ghasali et al (Ghasali et al., 2016) Al-VC (vanadium carbide) alloy was sintered by conventional sputter plasma sintering at 600 ° C for 60 minutes at 600 ° C and at 450 ° C for 60 minutes. In the study of Cooke et al (Cooke et al., 2016) Al-Sc alloy was sintered at 400, 450, 500 or 550 ° C for 2 min. In the study of Durowoju et al (Durowoju et al., 2015) Gr-Al (graphite aluminum) alloy was sintered at 500, 550 and 580 ° C for 10 min. In the study of Firestein et al (Firestein et al., 2017) aluminum-based BN, AlB2 and AlN doped alloys were sintered at 600 ° C for 60 min. In the study of Sweet et al (Sweet et al., 2014) in commercial purity and 0.4 wt% magnesium-doped aluminum powders were sintered at 400-600 ° C for 30s, 120s, and 300s.

Taskin and Gokozan (Taskin&Gokozan, 2011) used current and voltage data from a three-phase induction motor.In their work, Ozdemir and Tastan (Özdemir&Taştan, 2014) used the power furnace of the arc furnace used in metal melting processes in the industry using the LabVIEW based measurement system used in this study.

In this study, pure Al PM samples were sintered using conventional method or induction. The results obtained are compared among themselves and the optimum sintering temperature is found by induction. In addition, energy consumption and energy cost analysis were performed as a result of induction and conventional sintering of Al PM samples.

2. Materials and Methods

In the study, pure Al PM samples were separated into 2 different groups, some sintered in batch type furnace and the other part in induction system. The image of the induction system used in the sintering process is given in Figure 1.

In order to obtain a homogeneous mixture, Al powders were mixed with a V-type mixer at 20 rpm for 30 minutes and then produced by single-axis single-acting hydropar press with 300 MPa cold pressing method. The resulting PM compacts have a diameter of 18 mm and a height of 2 mm. The sizes of the aluminum powders are 45-106 μm.

Figure 1: Image of induction system

The first group of samples was sintered using an induction system with a 900 kHz ultra-high frequency and a power of 2.8 kW. The induction temperature is measured and controlled without contact with the infrared thermometer in the system. Al PM compacts were sintered with UHFIS aid at 7 different temperatures between 550-610°C for 4 minutes dwell time in 10^{-1} thoor vacuum environment. PM compacts are cooled naturally.

The image of the sample for the induction sintering is given in Figure 2. Sintered images of the sample at three different sintering temperatures with induction are given in Figure 3.

Figure 2 (a)

(b)

Figure 2(Cont) a) Induction sintering process b) Sintering in a vacuum environment

Figure 3: a) 550°C b) 600°C c) 610°C specimens sintered by induction.

The second group of samples was sintered in an open atmosphere at 600°C for 60 minutes using Proterm brand Chember Furnace at 2 kW power. PM compacts are cooled naturally. Figure 4-a shows the sintered Al PM sample in the furnace. All the operations of the presented work are given in Figure 5.

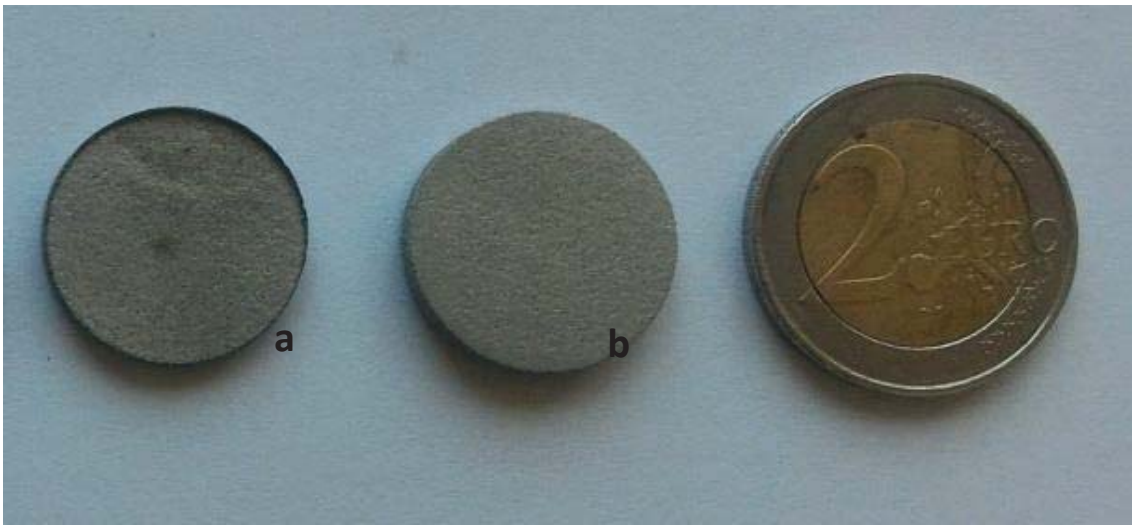

Figure 4: a) Sintered Al PM sample in furnace b) Non-sintered Al PM sample

The hardness measurements of the samples were made with the TIME TH-140 Digital Hardness tester. The hardness values were taken from 5 different points of each sample and the results were found by calculating the average hardness values.

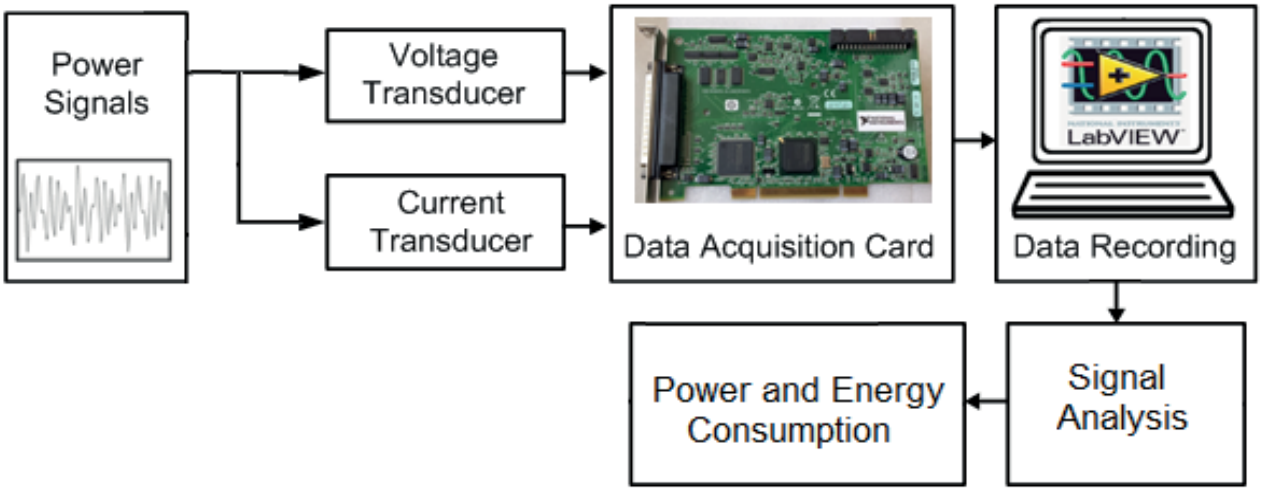

Figure 6: The block structure of the LabVIEW-based data acquisition and recording system.

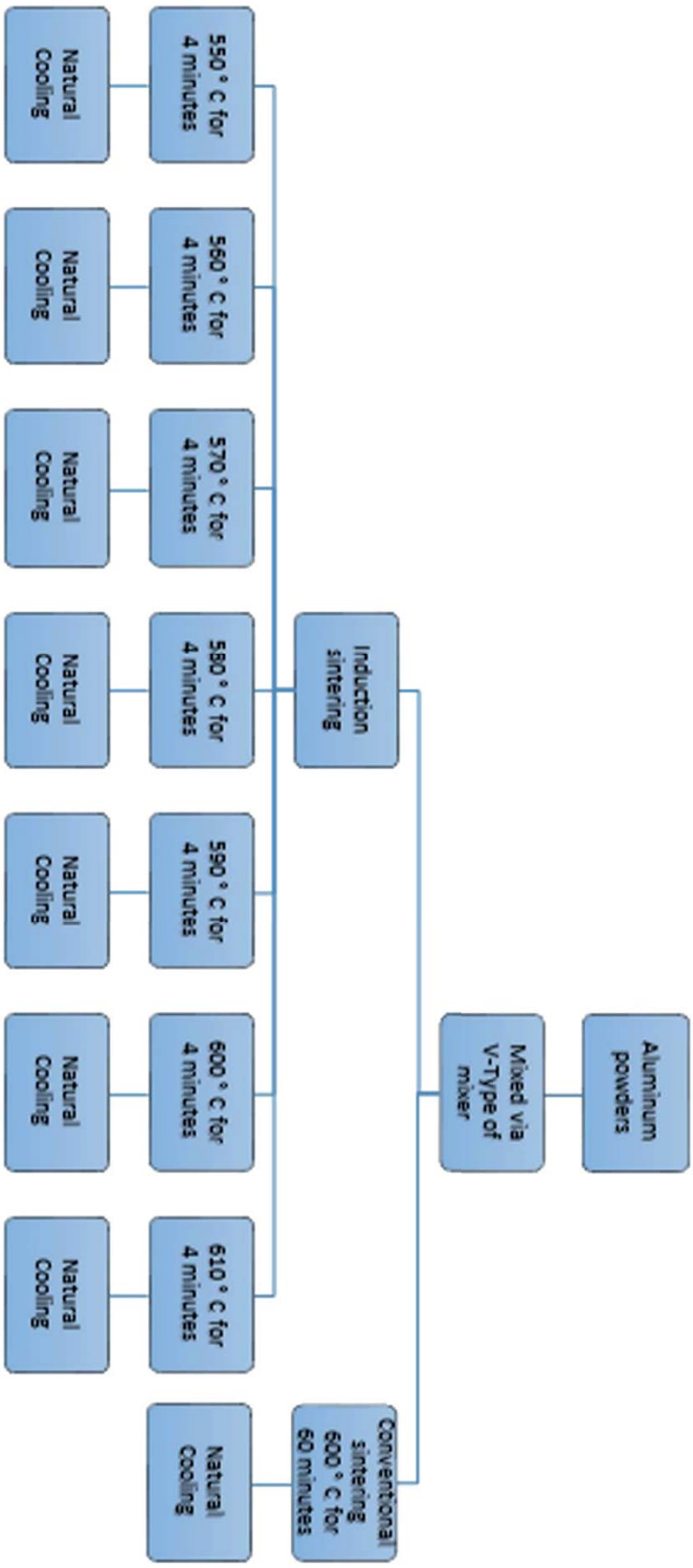

Figure 5: Flow chart of all processes.

Figure 6 shows the structure of the data acquisition and recording system based on LabVIEW. Electrical data such as current, voltage, and power factor for the experimental runs were recorded with the LabVIEW 8.5 graphical interface program on a National Instruments data acquisition card in accordance with the relevant IEC standards via current and voltage sensors. By using these power parameters obtained with this data collection system, necessary power calculations (Taskin&Gokozan,2011), (Özdemir&Taştan, 2014) have been made.

3. Results and Discussion

Figure 7 shows the change of the current graph of induction sintering of Al PM at 600°C for the first 20 seconds. It is seen that the current value decreases as the sample set temperature reaches about 4 seconds after sintering starts. An average current of approximately 16 A was drawn from the system until the sample set reached temperature. The system has continued to operate with a current of around 5 A after the set temperature has been reached.

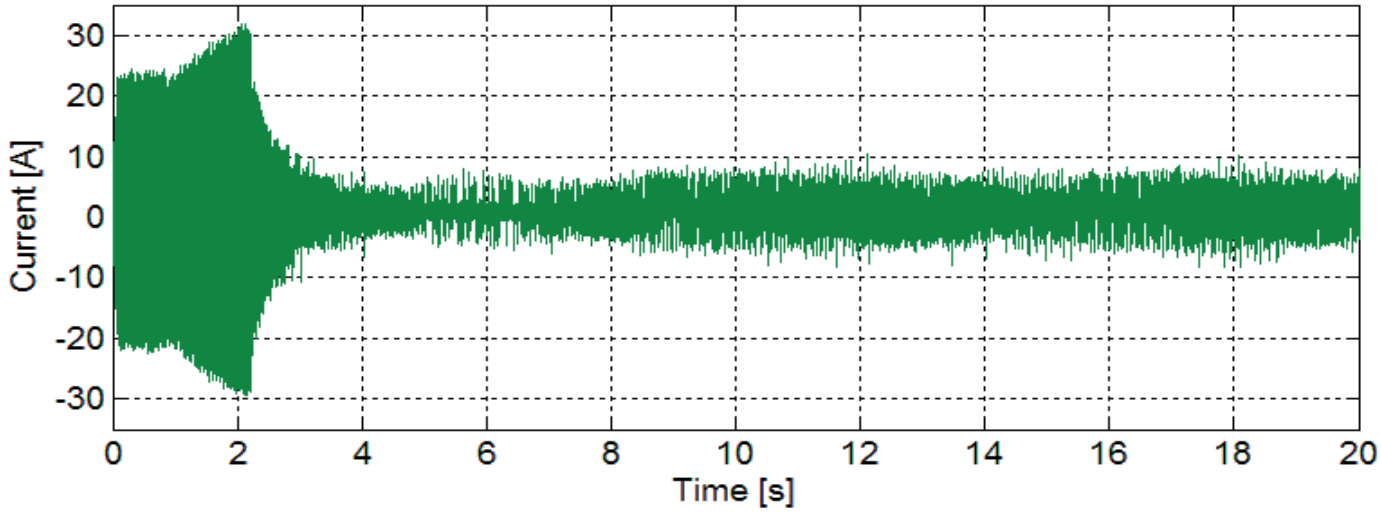

Figure 7: Current graph of the sintering process at 600°C temperature.

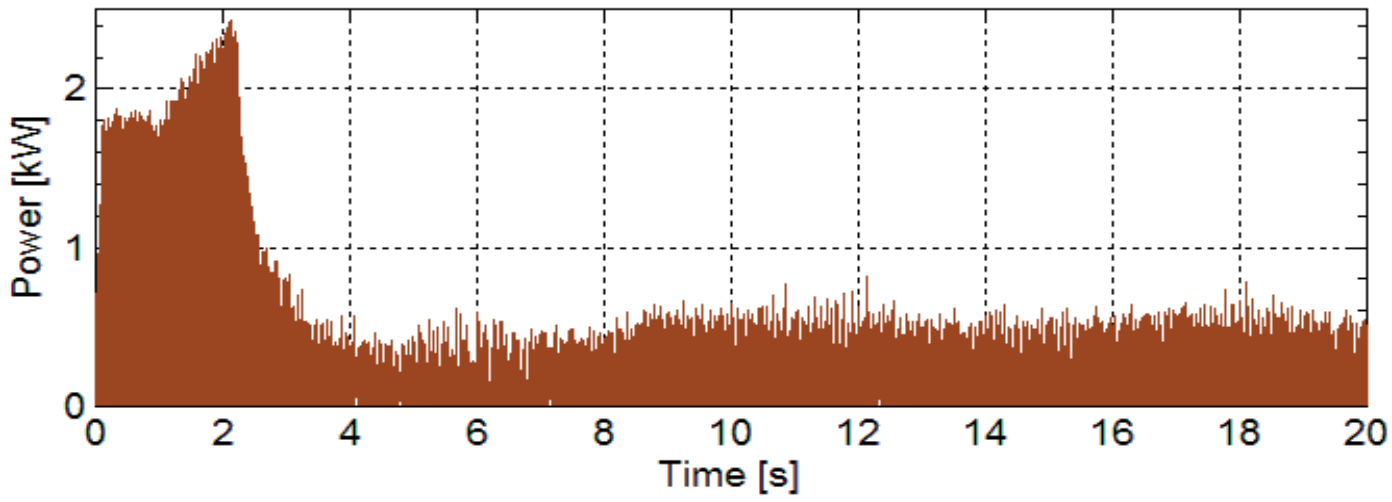

Figure 8: Power change graph of the sintering process at 600°C temperature.

Figure 8 shows the time-dependent power change graph of the induction sintering process of the Al PM specimen at a temperature of 600°C. The graph shows the change of the first 20 s. The sample reaches the set temperature within approximately 4 s and the

average instantaneous power consumption during this time ranges from 1 to 1.5 kW. After the sample reaches the set temperature, the system continues to operate with an average of 0.3-0.4 kW instantaneous power consumption.

Table 1: HB hardness and density values of aluminum samples

Al PM Compacts	Induction Sintering (4 minutes)							Conventional Sintering
	550 °C	560 °C	570 °C	580 °C	590 °C	600 °C	610 °C	600°C (60 min.)
Hardness (HB)	24	25	27	30	32	34	42	35
Density(g/cm^3)	2,239	2,271	2,309	2,388	2,426	2,450	2,610	2,475
% Density	82,6	83,8	85,2	88,1	89,5	90,4	96,3	91,3

PM The hardness and density values of aluminum materials after both sintering methods are given in Table 1. The PM compacts were found to have a hardness of 35 HB hardness and a density of 2,475 g / cm3 in a furnace at 600°C for 600 minutes in an argon atmosphere using a conventional method. The same hardness and density values were achieved in 4 minutes sintering time under vacuum using UHFIS. It is seen that the hardness and density values increase with the increase of the induction sintering temperature.

When the values are examined, it can be seen that at the temperature of 550-580°C during induction sintering, the samples are not sinterable enough and cannot form bonds. Although hardness and dense values at 610°C are the best results, it is seen that the eruptions occur in the sample as shown in Figure 3-c. It has therefore been determined that temperatures above 600°C are too high for sintering for Al PM samples. Compared with conventional sintering and induction sintering methods, the optimum sintering temperature was determined to be 600°C. When induction and conventional sintering times are compared, it is seen that the conventional sintering time is 15 times higher.

Table 2: Energy consumption and energy cost values of aluminum samples as a result of induction and conventional sintering.

Al PM compacts	Induction Sintering (4 minutes)							Conventional Sintering (60 minutes)
	550°C	560°C	570°C	580°C	590°C	600°C	610°C	600°C
Energy Consumption (kWh.kg^{-1})	4.987	5.030	5.087	5.134	5.227	5.254	5.324	2.053
Cost ($.kg^{-1})	0.4883	0.4925	0.4981	0.5029	0.5118	0.5144	0.5212	0.2011

Table 2 shows the energy consumption and energy cost values of Al PM samples for induction and conventional sintering processes. Sintering with induction at 600°C for 4 minutes resulted in a cost of 0.5144 $.kg^{-1} for energy consumption of 5.254 Wh.kg^{-1}. Conventional sintering at 600°C for 1 hour resulted in a cost of 0.2011 $. Kg^{-1} for energy consumption of 2.053 kWh.kg^{-1}.

4. Conclusions

In the work done, pure Al PM wastes were sintered UFIHS or conventionally. The results obtained are given below.

- It has been determined that the increase of the induction-induced sintering temperature increases the production cost and power.
- It has been determined that the optimum sintering temperature of Al PM compacts by induction is 600°C.
- Compared with the conventional sintering and induction sintering processes, Al-based PM samples were found to be sintered in 15 times shorter time using induction. When the hardness and density values are compared, the values are almost the same.
- Compared with induction and conventional sintering, it was found that the induction process cost is about 2.5 times higher than the process cost.

Acknowledgment

In this study, UHFIS was using for this resarch was ensured by Manisa Celal Bayar University BAP project and TUBİTAK project (FBE 2012-022 and 214M414)

References

Amirjan, M., Khorsand, H., Siadati, M. H., and Farsani, R. E., "Artificial Neural Network prediction of Cu–Al_2O_3 composite properties prepared by powder metallurgy method", *Journal of Materials Research and Technology*, *2*(4), 351-355, 2013.

Angelo, P. C., and Subramanian, R., *Powder metallurgy: science, technology and applications*. PHI Learning Pvt. Ltd., 2008.

Baghani, M., Aliofkhazraei, M., and Poursalehi, R., "Microwave-assisted Sintering of Fe-Al2O3 Nanocomposites: Study of Corrosion and Wear Properties", *Procedia Materials Science*, *11*, 689-694, 2015.

Bisht, A., Srivastava, M., Kumar, R. M., Lahiri, I., and Lahiri, D., "Strengthening mechanism in graphene nanoplatelets reinforced aluminum composite fabricated through spark plasma sintering", *Materials Science and Engineering: A*, *695*, 20-28, 2017.

Caliman, L. B., Bichaud, E., Soudant, P., Gouvea, D., and Steil, M. C., "A simple flash sintering setup under applied mechanical stress and controlled atmosphere", *MethodsX*, *2*, 392-398, 2015.Cooke, R. W., Kraus, N. P., and Bishop, D. P., "Spark plasma sintering of aluminum powders prealloyed with scandium additions", *Materials Science and Engineering: A*, *657*, 71-81, 2016.

Cavdar, P. S., and Cavdar, U., "The evaluation of different environments in ultra-high frequency induction sintered powder metal compacts", *Revista de Metalurgia*, *51*(1), e036, 2015.

Çavdar, U., and Atik, E., "Investigation of conventional-and induction-sintered iron and iron-based powder metal compacts", *JOM*, *66*(6), 1027-1034, 2014.

Çavdar, U., and Gulsahin, I., "Ultra high frequency induction welding of powder metal compacts", *Revista de Metalurgia*, *50*(2), 2014.

Çavdar, U., and Kusoglu, İ. M., "Effects of coil design on induction welding of sintered iron based compacts", *Materials Testing*, *56*(11-12), 973-979, 2014.

Çavdar, U., "Mechanical properties of hot forged ANSI 1050 steel", *Materials Testing*, *56*(3), 208-212, 2014.

Durowoju, M. O., Sadiku, E. R., Diouf, S., Shongwe, M. B., and Olubambi, P. A., "Spark plasma sintering of graphite–aluminum powder reinforced with SiC/Si particles", *Powder Technology*, *284*, 504-513, 2015.

Dutel, G. D., Langlois, P., Tingaud, D., Vrel, D., and Dirras, G., "Data on the influence of cold isostatic pre-compaction on mechanical properties of polycrystalline nickel sintered using Spark Plasma Sintering", *Data in Brief*, *11*, 61-67, 2017.

Firestein, K. L., Corthay, S., Steinman, A. E., Matveev, A. T., Kovalskii, A. M., Sukhorukova, I. V., ... and Shtansky, D. V., "High-strength aluminum-based composites reinforced with BN, AlB 2 and AlN particles fabricated via reactive spark plasma sintering of Al-BN powder mixtures", *Materials Science and Engineering: A*, *681*, 1-9, 2017.

Ghasali, E., Pakseresht, A. H., Alizadeh, M., Shirvanimoghaddam, K., and Ebadzadeh, T., "Vanadium carbide reinforced aluminum matrix composite prepared by conventional, microwave and spark plasma sintering", *Journal of Alloys and Compounds*, *688*, 527-533, 2016.

Gökozan, H., Taştan, M., Taşkin, S., Çavdar, P., and Çavdar, U., "Comparative Energy Consumption Analyses Of an Ultra High Frequency Induction Heating System For Induction Heating, Welding and Sintering Applications" *Materials testing*, 58, 1009-1013, 2016.

Guo, B., Ni, S., Yi, J., Shen, R., Tang, Z., Du, Y., and Song, M., "Microstructures and mechanical properties of carbon nanotubes reinforced pure aluminum composites synthesized by spark plasma sintering and hot Rolling", *Materials Science and Engineering: A*, *698*, 282-288, 2017

Kang, S. J. L. *Sintering: densification, grain growth and microstructure*. Butterworth-Heinemann, 2004.

Lemke, F., Rheinheimer, W., and Hoffmann, M. J., "A comparison of power controlled flash sintering and conventional sintering of strontium titanate", *Scripta Materialia*, *130*, 187-190, 2017.

Mackie, A. J., Hatton, G. D., Hamilton, H. G., Dean, J. S., and Goodall, R., "Carbon uptake and distribution in spark plasma sintering (SPS) processed Sm (Co, Fe, Cu, Zr)", *Materials Letters*, *171*, 14-17, 2016.

Özdemir, A., and Taştan, M., "PLL based digital adaptive filter for detecting interharmonics", *Mathematical Problems in Engineering*, 1-10, 2014.

Pozzoli, V. A., Ruiz, M. S., Kingston, D., and Razzitte, A. C., "Entropy Production during the Process of Sintering", *Procedia Materials Science*, *8*, 1073-1078, 2015.

Reddy, M. P., Ubaid, F., Shakoor, R. A., Mohamed, A. M. A., and Madhuri, W., "Structural and mechanical properties of microwave sintered Al Ni 50 Ti 50 composites", *Journal of Science: Advanced Materials and Devices*, *1*(3), 362-366, 2016.

Sedlak, J., Rican, D., Piska, M., and Rozkosny, L., "Study of Materials Produced by Powder Metallurgy Using Classical and Modern Additive Laser Technology", *Procedia Engineering*, *100*, 1232-1241, 2015.

Sharma, P., and Majumdar, J. D., "Studies on nano-crystalline CoNiCrAlY consolidated by conventional and microwave sintering", *Advanced Powder Technology*, *27*(1), 72-84, 2016.

Sweet, G. A., Brochu, M., Hexemer, R. L., Donaldson, I. W., and Bishop, D. P., "Microstructure and mechanical properties of air atomized aluminum powder consolidated via spark plasma sintering", *Materials Science and Engineering: A*, *608*, 273-282, 2014.

Taskin, S., and Gokozan, H., "Determination of the spectral properties and harmonic levels for driving an induction motor by an inverter driver under the different load conditions", *Elektronika ir Elektrotechnika*, *108*(2), 75-80, 2011.

Tastan, M., Gokozan, H., Taskin, S., and Çavdar, U., "Comparative energy consumption analyses of an ultra high frequency induction heating system for material processing applications", *Revista de Metalurgia*, *51*(3), 2015.

Wudy, K., Lanzl, L., and Drummer, D., "Selective Laser Sintering of Filled Polymer Systems: Bulk Properties and Laser Beam Material Interaction", *Physics Procedia*, *83*, 991-1002, 2016.

Xun, W., Jie, Z., and Qiang, L., "Multi-objective optimization of medium frequency induction heating process for large diameter pipe bending", *Procedia Engineering*, *81*, 2255-2260, 2014.

Yasa, E., Poyraz, O., Solakoglu, E. U., Akbulut, G., and Oren, S., "A Study on the Stair Stepping Effect in Direct Metal Laser Sintering of a Nickel-based Superalloy", *Procedia CIRP*, *45*, 175-178, 2016.

.

MÜHENDİSLİK FAKÜLTESİ

Uluslararası Mühendislik Araştırma ve Geliştirme Dergisi

International Journal of Engineering Research and Development

Cilt/Volume:9 Sayı/Issue:3 Aralık/December 2017 https://doi.org/10.29137/umagd.348871

Araştırma Makalesi / Research Article

Subject-Dependent and Subject-Independent Classification of Mental Arithmetic and Silent Reading Tasks

Mustafa Turan Arslan[1] , Server Goksel Eraldemir[2], Esen Yildirim[3]

[1]Mustafa Kemal University, Hatay,31000,Turkey
[2]Iskenderun Technical University, Hatay, 31200, Turkey
[3]Adana Science and Technology University, Adana,1410,Turkey

Başvuru/Received: 08/10/2017 **Kabul/Accepted**: 01/12/2017 **Son Versiyon/Final Version**: 26/12/2017

Abstract

In this study, the electrical activities in the brain were classified during mental mathematical tasks and silent text reading. EEG recordings are collected from 18 healthy male university/college students, ages ranging from 18 to 25. During the study, a total of 60 slides including verbal text reading and arithmetical operations were presented to the subjects. EEG signals were collected from 26 channels in the course of slide show. Features were extracted by employing Hilbert Huang Transform (HHT). Then, subject-dependent and subject-independent classifications were performed using k-Nearest Neighbor (k-NN) algorithm with parameters k=1, 3, 5 and 10. Subject-dependent classifications resulted in accuracy rates between 95.8% and 99%, whereas the accuracy rates were between 92.2% and 97% for subject independent classification. The results show that EEG data recorded during mathematical and silent reading tasks can be classified with high accuracy results for both subject-dependent and subject-independent analysis.

Key Words

"EEG classification, Hilbert Huang Transform, k-Nearest Neighbors"

** mtarslan@mku.edu.tr*

1. INTRODUCTION

Studies on Human-Computer Interaction (HCI) systems increased rapidly in the last decade (Lughofer et al., 2009; Lughofer et al., 2011; Vézard et al., 2015). The goal of these systems is to provide interactive communication between humans and computers. Automatic voice response systems and search engines are some examples of above-mentioned systems. A specialized version of these systems is Brain-Computer Interface (BCI) in which the systems are driven by brain signals. These interfaces are extremely useful for specifically disabled individuals with difficulty of using their muscles or skeletal systems (Kottaimalai et al., 2013; Liao et al., 2014; Liao et al., 2012). In these systems, the analysis of the signals produced in the brain is performed, mostly, in real time. Electrical signals, magnetic field and hemodynamic changes that occur during the processes in brain can be measured by Electroencephalography (EEG), Magnetoencephalography (MEG) and Functional Magnetic Resonance Imaging (fMRI), modalities respectively. The most commonly used method in BCI systems is EEG due to its ease of use, mobility and low cost (Ruan et al., 2014; Schalk, 2008; Wolpaw et al., 2006).

EEG signals are non-stationary and non-linear signals like many other physiological signals (Kaplan et al., 2005; Lo et al., 2009). Wavelet Transform, which is known to be more effective in analyzing nonlinear signals, is widely used (Eraldemir & Yildirim, 2015; Handojoseno et al., 2013), although Fourier Transform (FT) is used in some studies (Dkhil et al., 2015; Samiee et al., 2015; Wang et al., 2016) in EEG signal analysis. A relatively new method, Hilbert Huang Transform (HHT), was proposed by Norden E. Huang in 1996. HHT is an adaptive and efficient signal processing method and it is convenient for processing non-linear and non-stationary signals (Huang et al., 1996). The method has been used for EEG feature extraction in many studies (Guang et al., 2005; Rahul Kumar Chaurasiya et al., 2015; Wang et al., 2015; Yang et al., 2006). HHT is used in areas such as detection of alcohol dependence (Lin et al., 2015), detection of automatic sleep level (Fraiwan et al., 2011; Liu et al., 2010), diagnosis (Bajaj & Pachori, 2013) and prediction (Ozdemir & Yildirim, 2014) of epileptic seizure, measurement of anesthesia depth (Shih et al., 2015) and BCI applications (Jerbic et al., 2015). k-Nearest Neighbor (k-NN) is one of the popular classification methods that have been used in many EEG signal classification studies. (Eraldemir et al., 2014) have classified mathematical tasks using wavelet-based features from EEG signals with k-NN classifier and have reported 79.3%, 74.9%, 72.4% and 68.6% accuracy for k=1, 3, 5, and 10 respectively. (Noshadi et al., 2014) used empirical mode decomposition and k-NN for cognitive tasks classification with 97.78 % accuracy. (Yazdani et al., 2009) used autoregressive (AR) models and wavelet decomposition transform for feature Extraction and k-NN for classification of EEG signals of five different mental tasks.

In this study, EEG signals collected during a slide show consisting of mental arithmetic operation and silent reading slides are classified by means of k-NN. Features used for classification are extracted using HHT methodology. Subject dependent and independent classification performances are presented. The rest of the paper is organized as follows. Section 2 briefly describes the collection of EEG data, extraction of features and classification algorithm. The classification results obtained by k-NN are given in Section 3 and the conclusion is given in Section 4.

2. MATERIALS AND METHOD

This section describes the details of the materials and methods used during experimental study, which include the experimental tasks, dataset description, Hilbert Huang Transform and description of classifier and the discussion of their performance parameters. The main steps used in the study is summarized in Fig. 1.

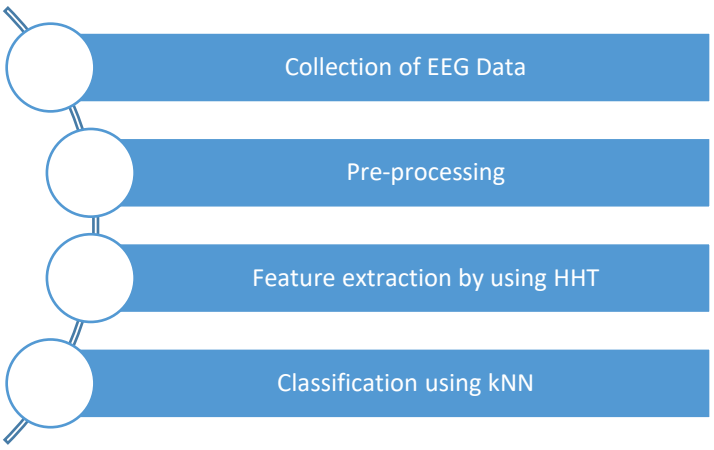

Fig. 1. The basic steps of the experimental study

2.1. Collection of EEG Data

In this study, EEG signals are collected from 18 voluntary healthy males who are university/college students. EEG electrodes were positioned according to the 10-20 international system and signals were collected from 22 electrodes forming 26 channels with a sampling frequency of 1 kHz.

26 channels which was used on EEG device are attained by using reference points. The names of those are Fp1-A1, Fp2-A2, F3-A1, F4-A2, C3-A1, C4-A2, P3-A1, P4-A2, O1-A1, O2-A2, F7-A1, F8-A2, T3-A1, T4-A2, T5-A1, T6-A2, Fp2-O2, Fp1-O1, Fp1-Fp2, F7-F8, F3-F4, T3-T4, C3-C4, T5-T6 P3-P4 and O1-O2, respectively.

Subjects were warned prior to the recording sessions about not to move their muscles, blink or swallow to minimize possible artefacts in EEG signals. EEG recordings were collected in a quiet and comfortable environment. In addition, subjects were asked to have short and clean hair and they were warned not to use any medical drug.

30 arithmetic and 30 verbal slides, each 13.25 seconds long, 5 were shown the subjects. Sample arithmetic and verbal slides are shown in Fig. 2. and Fig. 3., respectively.

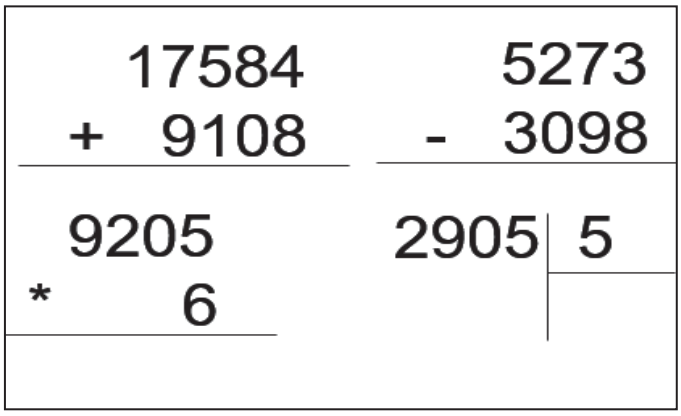

Fig. 2. The examples of numeric slide

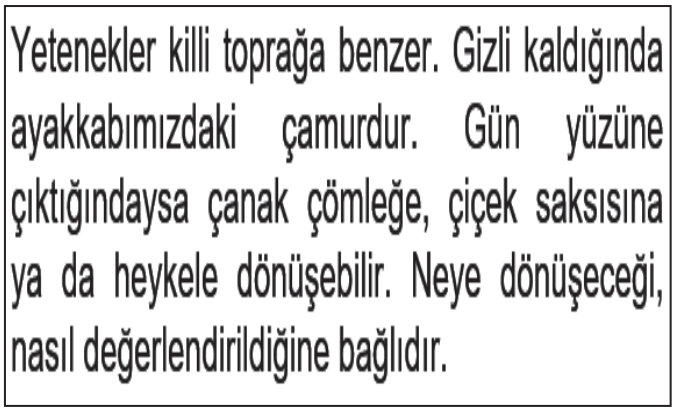

Fig. 3. The examples of verbal slide

The subjects were asked to focus on the arithmetic operation or reading the text instead of being in a rush to complete the process.

2.2. Feature Extraction

50 Hz line noise was directly cleaned by the EEG device and a band-pass filter between 0.5 and 120 Hz was applied to the EEG recordings. The first and the last slides were not used because of the synchronization problem in segmenting the raw EEG data. After this pre-processing step features are extracted using HHT.

HHT is presented by Huang et al. in 1996 (Huang et al., 1996). HHT associates Empirical Mode Decomposition (EMD) with well-known Hilbert transform to form the Hilbert spectrum. HHT is a more developed technique than other techniques such as Fourier Transform and Wavelet Transform, which expand the signal by predetermined basis functions. This technique is an adaptive data

analysis method, which extracts the basis function from the data itself, designed privately for analyzing data from nonlinear and nonstationary signals.

The main step of the HHT is the EMD method with which a complicated data set can be decomposed into components named intrinsic mode functions (IMF). Hilbert transform is applied to the IMFs to obtain the energy-frequency-time distribution, designated as Hilbert spectrum.

The instantaneous frequencies can be calculated by means of the Hilbert Transform, with which any real valued function x(t) can be presented as an analytic function, z(t), with the complex part, y(t) computed as:

$$y(t) = \frac{1}{\pi} P \int_{-\infty}^{\infty} \frac{x(\tau)}{t-\tau} \tag{1}$$

where the P represents the Cauchy principle value of the singular integral. Finally the analytic function is:

$$z(t) = x(t) + jy(t) = a(t)e^{j\theta(t)} \tag{2}$$

where

$$a(t) = (x^2 + y^2)^{1/2} \; ; \; \theta(t) = \tan^{-1}\frac{y}{x} \tag{3}$$

Here a is the instantaneous amplitude, and θ is the phase function; and the instantaneous frequency is indicated as follows.

$$\omega = -\frac{d\theta}{dt} \tag{4}$$

2.3. Classification

EEG signals collected during mental mathematical operations and silent readings are classified using a k Nearest Neighbor (k-NN). The k-NN algorithm is one of the machine learning algorithms used in many fields (Cover & Hart, 1967). The algorithm is also a simple and intuitive method of classifier used by many researchers typically for classifying EEG signals. The k-NN classification is based on finding closest training samples to a test sample and assigning it to the most dominant class.

We need to specify the value of "k" closest neighbor for binary classification. In this experiment, we try different "k" values ranging from 1 to 10, namely 1, 3, 5 and 10. "Euclidean" distance measure is used in order to calculate distance between test sample and training samples in the feature space.

$$d(p,q) = \sqrt{\sum_{i=1}^{n} (p_i - q_i)^2} \tag{5}$$

where $d(p,q)$ is the distance between the samples p and q, n represents the number of features and the ith feature of the sample are described as p_i and q_i, respectively (Ahangi et al., 2013).

3. RESULTS AND DISCUSSION

In this study, we considered the effect of HHT and k-NN method on classification result, considering that HHT based features show better classification performance. The features were obtained by using HHT from EEG signals and these features were binary classified as mathematical operation / verbal reading using k-NN algorithm.

The performance of k-NN was computed using the most commonly used parameters such as accuracy, precision and f-measure (Subasi & Gursoy, 2010).

The values of k in the k-NN algorithm used in the study were selected as 1, 3, 5, and 10. The 10 fold cross-validation approach was used in an attempt to test to performance of k-NN algorithm. The results were compared as both subject-dependent and subject-independent. The results of subject-dependent studies are shown in Table 1-4.

The classification results of 26-channel EEG data are given in Table 1 for k = 1. Examining Table 1, it is seen that the number of subjects with accuracy of 99% and above is 11. The lowest accuracy rate is 94.80% for the subject 3 while the highest accuracy rate was 99.9% for the subject 14 and subject 15. The average accuracy rate of 18 subjects was 99.01%. In addition, there are two subjects with 99.9% accuracy in this table. In analysis of 26-channel EEG data, precision and f-measure were 99.01% and 99.01%, respectively on the average.

Table 1: The results of subject-dependent with k=1

1-NN			
No of Subject	**Accuracy**	**Precision**	**F-Measure**
Subject1	0.984	0.984	0.984
Subject2	0.987	0.987	0.987
Subject3	0.948	0.949	0.948
Subject4	0.987	0.987	0.987
Subject5	0.996	0.996	0.996
Subject6	0.988	0.988	0.988
Subject7	0.996	0.996	0.996
Subject8	0.998	0.998	0.998
Subject9	0.990	0.990	0.990
Subject10	0.993	0.993	0.993
Subject11	0.987	0.987	0.987
Subject12	0.997	0.997	0.997
Subject13	0.996	0.996	0.996
Subject14	0.999	0.999	0.999
Subject15	0.999	0.999	0.999
Subject16	0.988	0.988	0.988
Subject17	0.992	0.992	0.992
Subject18	0.996	0.996	0.996

Table 2 shows the results when the k parameter is selected as 3. The k-NN algorithm yielded the highest performance for the subject 7 with the accuracy of 99.7%. The average classification performances of EEG data with 18 subjects was found as 97.72%, 97.75% and 97.72% with accuracy, precision and f-measure, respectively. Table 2 demonstrated that there are only 6 subjects whose performance are 99% or above for accuracy.

Table 2: The results of subject-dependent with k=3

3-NN			
No of Subject	**Accuracy**	**Precision**	**F-Measure**
Subject1	0.966	0.966	0.966
Subject2	0.964	0.965	0.964
Subject3	0.901	0.905	0.901
Subject4	0.973	0.973	0.973
Subject5	0.993	0.993	0.993
Subject6	0.968	0.968	0.968
Subject7	0.997	0.997	0.997
Subject8	0.990	0.990	0.990
Subject9	0.971	0.971	0.971
Subject10	0.982	0.982	0.982
Subject11	0.973	0.973	0.973

Table 2 (Cont): The results of subject-dependent with k=3

3-NN			
No of Subject	**Accuracy**	**Precision**	**F-Measure**
Subject12	0.988	0.988	0.988
Subject13	0.991	0.991	0.991
Subject14	0.994	0.994	0.994
Subject15	0.996	0.996	0.996
Subject16	0.972	0.972	0.972
Subject17	0.984	0.984	0.984
Subject18	0.987	0.987	0.987

As can be seen from Table 3, the subject 7 has the best performance metrics with %99.4 while the subject 3 has the worst achievement on accuracy, precision and f-measure with 87.9%, 88.6% and 87.8%, respectively. In addition, the average accuracy, precision and f-measure were 96.75%, 96.79% and 96.74%, respectively. It is also worth to note that, k=5 resulted in 99% or above accuracy for only 3 subjects.

Table 3: The results of subject-dependent with k=5

5-NN			
No of Subject	**Accuracy**	**Precision**	**F-Measure**
Subject1	0.950	0.950	0.950
Subject2	0.938	0.939	0.938
Subject3	0.879	0.886	0.878
Subject4	0.969	0.969	0.969
Subject5	0.985	0.985	0.985
Subject6	0.943	0.943	0.943
Subject7	0.994	0.994	0.994
Subject8	0.983	0.983	0.983
Subject9	0.963	0.963	0.963
Subject10	0.972	0.972	0.972
Subject11	0.967	0.967	0.967
Subject12	0.973	0.973	0.973
Subject13	0.987	0.987	0.987
Subject14	0.992	0.992	0.992
Subject15	0.990	0.990	0.990
Subject16	0.966	0.966	0.966
Subject17	0.978	0.978	0.978
Subject18	0.986	0.986	0.986

Table 4 shows that k-NN algorithm achieved the best results on subject7 when the value of k was selected as 10. Subject3 has the poorest performance values with 85.9%, 86.7% and 85.8% for accuracy, precision and f-measure respectively. In addition, the average accuracy of 95.81% was obtained. The results show that there is no subject with an accuracy of 99% or above for k=10.

Table 4: The results of subject-dependent with k=10

10-NN			
No of Subject	**Accuracy**	**Precision**	**F-Measure**
Subject1	0.941	0.941	0.941
Subject2	0.921	0.923	0.921
Subject3	0.859	0.867	0.858
Subject4	0.967	0.967	0.967
Subject5	0.979	0.979	0.979
Subject6	0.932	0.932	0.932
Subject7	0.988	0.988	0.988
Subject8	0.970	0.970	0.970
Subject9	0.956	0.957	0.956
Subject10	0.964	0.964	0.964
Subject11	0.950	0.951	0.950
Subject12	0.965	0.965	0.965
Subject13	0.981	0.982	0.981
Subject14	0.984	0.984	0.984
Subject15	0.982	0.982	0.982
Subject16	0.957	0.957	0.957
Subject17	0.970	0.970	0.970
Subject18	0.980	0.980	0.980

It is demonstrated that the best classification results are obtained for k = 1 in subject-dependent study, and EEG signals recorded during mathematical and silent reading tasks are classified with an accuracy of %99.01 on average.

In this study, EEG signals were also classified as subject-independent using k-NN algorithm. In a subject independent study, training and testing are performed on EEG data that are collected from a group of subjects, whereas for subject dependent study these procedures are performed on only one subject's recordings. The values of 'k' is considered as 1, 3, 5 and 10 for subject independent study as in subject dependent studies for comparison purposes.

As it is shown in Table 5, k-NN algorithm performs very well on this dataset, with 99.01% for accuracy, precision and f-measure for k=1 in subject-dependent study on average.

Table 5: The average results of subject-dependent analysis

k	Accuracy	Precision	F-Measure
1	0.9901	0.9901	0.9901
3	0.9772	0.9775	0.9772
5	0.9675	0.9679	0.9674
10	0.9581	0.9588	0.9581

Table 6 shows that the best accuracy is achieved as 97.02% for k=1, as for the subject dependent case. As expected, subject dependent studies resulted in better accuracy values since each subject is trained with and tested on their own recordings. Nevertheless, the results achieved for subject–independent study are substantial.

Table 6: The results of subject-independent analysis

k	Accuracy	Precision	F-Measure
1	0.9702	0.9702	0.9702
3	0.9492	0.9494	0.9493
5	0.9389	0.9390	0.9390
10	0.9225	0.9225	0.9225

It is clearly seen that the HHT-based features extracting during mental arithmetic and silent reading tasks are classified with high accuracy for both subject-dependent and subject-independent analysis.

4. CONCLUSION

In this paper we have presented an approach to cognitive tasks based on the processing of EEG. The study presented the use of Hilbert Huang transform along with machine learning algorithms for the classification of spontaneous EEG signals recorded during a cognitive tasks.

For classification, k-NN was employed and its performance was evaluated for cognitive task discrimination. The classification results of k-NN demonstrated above 97% accuracy with features extracted using HHT method. The Hilbert transform is a powerful and useful tool to classify the EEG signals corresponding to complex cognitive tasks, and it will be helpful for EEG classification in clinical applications, such as epilepsy, depression, and stress diagnosis.

REFERENCES

Ahangi, A., Karamnejad, M., Mohammadi, N., Ebrahimpour, R., & Bagheri, N. (2013). Multiple classifier system for EEG signal classification with application to brain–computer interfaces. *Neural Computing and Applications*, *23*(5), 1319–1327. https://doi.org/10.1007/s00521-012-1074-3

Bajaj, V., & Pachori, R. B. (2013). Epileptic seizure detection based on the instantaneous area of analytic intrinsic mode functions of EEG signals. *Biomedical Engineering Letters*, *3*(1), 17–21. https://doi.org/10.1007/s13534-013-0084-0

Ben Dkhil, M., Wali, A., & Alimi, A. M. (2015). Drowsy driver detection by EEG analysis using Fast Fourier Transform. In *2015 15th International Conference on Intelligent Systems Design and Applications (ISDA)* (pp. 313–318). IEEE. https://doi.org/10.1109/ISDA.2015.7489245

Cover, T., & Hart, P. (1967). Nearest neighbor pattern classification. *IEEE Transactions on Information Theory*, *13*(1), 21–27. https://doi.org/10.1109/TIT.1967.1053964

Eraldemir, S. G., & Yildirim, E. (2015). Comparison of wavelets for classification of cognitive EEG signals. In *2015 23nd Signal Processing and Communications Applications Conference (SIU)* (pp. 1381–1384). IEEE. https://doi.org/10.1109/SIU.2015.7130099

Fraiwan, L., Lweesy, K., Khasawneh, N., Fraiwan, M., Wenz, H., & Dickhaus, H. (2011). Time Frequency Analysis for Automated Sleep Stage Identification in Fullterm and Preterm Neonates. *Journal of Medical Systems*, *35*(4), 693–702. https://doi.org/10.1007/s10916-009-9406-2

Handojoseno, A. M. A., Shine, J. M., Nguyen, T. N., Tran, Y., Lewis, S. J. G., & Nguyen, H. T. (2013). Using EEG spatial correlation, cross frequency energy, and wavelet coefficients for the prediction of Freezing of Gait in Parkinson's Disease patients. In *2013 35th Annual International Conference of the IEEE Engineering in Medicine and Biology Society (EMBC)* (pp. 4263–4266). IEEE. https://doi.org/10.1109/EMBC.2013.6610487

Huang, N. E., Long, S. R., & Shen, Z. (1996). The Mechanism for Frequency Downshift in Nonlinear Wave Evolution. *Advances in Applied Mechanics*, *32*, 59–117C. https://doi.org/10.1016/S0065-2156(08)70076-0

Jerbic, A. B., Horki, P., Sovilj, S., Isgum, V., & Cifrek, M. (2015). Hilbert-Huang Time-Frequency Analysis of Motor Imagery EEG Data for Brain-Computer Interfaces (pp. 62–65). Springer, Cham. https://doi.org/10.1007/978-3-319-11128-5_16

Kaplan, A., Fingelkurts, A., Fingelkurts, A., & Borisov, S. (2005). Nonstationary nature of the brain activity as revealed by EEG/MEG: methodological, practical and conceptual challenges. *Signal Processing*, *85*(11), 2190–2212. Retrieved from http://www.sciencedirect.com/science/article/pii/S0165168405002094

Kottaimalai, R., Rajasekaran, M. P., Selvam, V., & Kannapiran, B. (2013). EEG signal classification using Principal Component Analysis with Neural Network in Brain Computer Interface applications. In *2013 IEEE International Conference ON Emerging Trends in Computing, Communication and Nanotechnology (ICECCN)* (pp. 227–231). IEEE. https://doi.org/10.1109/ICE-CCN.2013.6528498

Liao, F., Zhang, C., Bian, Z., Xie, D., Kang, M., Li, X., … Yi, M. (2014). Characterizing Heat-Sensitization Responses in Suspended Moxibustion with High-Density EEG. *Pain Medicine*, *15*(8), 1272–1281. https://doi.org/10.1111/pme.12512

Liao, L.-D., Chen, C.-Y., Wang, I.-J., Chen, S.-F., Li, S.-Y., Chen, B.-W., … Lin, C.-T. (2012). Gaming control using a wearable and wireless EEG-based brain-computer interface device with novel dry foam-based sensors. *Journal of NeuroEngineering and Rehabilitation*, *9*(1), 5. https://doi.org/10.1186/1743-0003-9-5

Lin, C.-F., Su, J.-Y., & Wang, H.-M. (2015). Hilbert-Huang Transformation Based Analyses of FP1, FP2, and Fz Electroencephalogram Signals in Alcoholism. *Journal of Medical Systems*, *39*(9), 83. https://doi.org/10.1007/s10916-015-0275-6

Liu, Z.-W., Faraguna, U., Cirelli, C., Tononi, G., & Gao, X.-B. (2010). Direct Evidence for Wake-Related Increases and Sleep-Related Decreases in Synaptic Strength in Rodent Cortex. *Journal of Neuroscience*, *30*(25), 8671–8675. https://doi.org/10.1523/JNEUROSCI.1409-10.2010

Lo, M.-T., Tsai, P.-H., Lin, P.-F., Lin, C., & Hsin, Y. L. (2009). The Nonlinear and Nonstationary Properties in EEG Signals: Probing The Complex Fluctuations by Hilbert–Huang Transform. *Advances in Adaptive Data Analysis*, *1*(3), 461–482. https://doi.org/10.1142/S1793536909000199

Lughofer, E., Bouchot, J.-L., & Shaker, A. (2011). On-line elimination of local redundancies in evolving fuzzy systems. *Evolving Systems*, *2*(3), 165–187. https://doi.org/10.1007/s12530-011-9032-3

Lughofer, E., Smith, J. E., Tahir, M. A., Caleb-Solly, P., Eitzinger, C., Sannen, D., & Nuttin, M. (2009). Human–Machine Interaction Issues in Quality Control Based on Online Image Classification. *IEEE Transactions on Systems, Man, and Cybernetics - Part A: Systems and Humans*, *39*(5), 960–971. https://doi.org/10.1109/TSMCA.2009.2025025

Meng Hu, Guang Li, Qiuping Ding, & Jiaojie Li. (2005). Classification of Normal and Hypoxia EEG Based on Hilbert Huang Transform. In *2005 International Conference on Neural Networks and Brain* (Vol. 2, pp. 851–854). IEEE. https://doi.org/10.1109/ICNNB.2005.1614755

Ozdemir, N., & Yildirim, E. (2014). Patient specific seizure prediction system using Hilbert spectrum and Bayesian networks classifiers. *Computational and Mathematical Methods in Medicine*, *2014*, 572082. https://doi.org/10.1155/2014/572082

Rahul Kumar Chaurasiya, R. K., Jain, K., Goutam, S., & Manisha. (2015). Epileptic seizure detection using HHT and SVM. In *2015 International Conference on Electrical, Electronics, Signals, Communication and Optimization (EESCO)* (pp. 1–6). IEEE. https://doi.org/10.1109/EESCO.2015.7253660

Ruan, X., Kun Xue, & Mingai Li. (2014). Feature extraction of SSVEP-based brain-computer interface with ICA and HHT method. In *Proceeding of the 11th World Congress on Intelligent Control and Automation* (pp. 2418–2423). IEEE. https://doi.org/10.1109/WCICA.2014.7053100

Samiee, K., Kovacs, P., & Gabbouj, M. (2015). Epileptic Seizure Classification of EEG Time-Series Using Rational Discrete Short-Time Fourier Transform. *IEEE Transactions on Biomedical Engineering*, *62*(2), 541–552. https://doi.org/10.1109/TBME.2014.2360101

Schalk, G. (2008). Brain–computer symbiosis. *Journal of Neural Engineering*, *5*(1), P1–P15. https://doi.org/10.1088/1741-2560/5/1/P01

Shih, M.-T., Doctor, F., Fan, S.-Z., Jen, K.-K., & Shieh, J.-S. (2015). Instantaneous 3D EEG Signal Analysis Based on Empirical Mode Decomposition and the Hilbert–Huang Transform Applied to Depth of Anaesthesia. *Entropy*, *17*(3), 928–949. https://doi.org/10.3390/e17030928

Subasi, A., & Ismail Gursoy, M. (2010). EEG signal classification using PCA, ICA, LDA and support vector machines. *Expert Systems with Applications*, *37*(12), 8659–8666. https://doi.org/10.1016/j.eswa.2010.06.065

Vézard, L., Legrand, P., Chavent, M., Faïta-Aïnseba, F., & Trujillo, L. (2015). EEG classification for the detection of mental states. *Applied Soft Computing*, *32*, 113–131. https://doi.org/10.1016/j.asoc.2015.03.028

Wang, M., Lv, Y., Wen, M., He, S., & Wang, G. (2016). A Fan Control System Base on Steady-State Visual Evoked Potential. In *2016 International Symposium on Computer, Consumer and Control (IS3C)* (pp. 81–84). IEEE. https://doi.org/10.1109/IS3C.2016.31

Wang, R., Wang, Y., & Luo, C. (2015). EEG-Based Real-Time Drowsiness Detection Using Hilbert-Huang Transform. In *2015 7th International Conference on Intelligent Human-Machine Systems and Cybernetics* (pp. 195–198). IEEE. https://doi.org/10.1109/IHMSC.2015.56

Wolpaw, J. R., Loeb, G. E., Allison, B. Z., Donchin, E., Do Nascimento, O. F., Heetderks, W. J., … Turner, J. N. (2006). BCI Meeting 2005—Workshop on Signals and Recording Methods. *IEEE Transactions on Neural Systems and Rehabilitation Engineering*, *14*(2), 138–141. https://doi.org/10.1109/TNSRE.2006.875583

Yang, Z., Yang, L., & Qi, D. (2006). Detection of Spindles in Sleep EEGs Using a Novel Algorithm Based on the Hilbert-Huang Transform. In *Wavelet Analysis and Applications* (pp. 543–559). Basel: Birkhäuser Basel. https://doi.org/10.1007/978-3-7643-7778-6_40

MÜHENDİSLİK FAKÜLTESİ

Uluslararası Mühendislik Araştırma ve Geliştirme Dergisi

International Journal of Engineering Research and Development

Cilt/Volume:9 Sayı/Issue:3 Aralık/December 2017 https://doi.org/10.29137/umagd.349107

Araştırma Makalesi / Research Article

An Investigation on Internet of Things Technology (IoT) In Smart Houses

Tolga KILIÇ[1] , Esra BAYIR[1]

[1]MSGSU, Faculty of Architecture, Interior Design Department,

Başvuru/Received: 08/10/2017 **Kabul/Accepted**: 01/12/2017 **Son Versiyon/Final Version**: 26/12/2017

Abstract

Existing scientific developments have enabled new technological approaches to emerge. 'Internet of Objects' (IoT) technology is one of these approaches. Using the standard internet protocol, this technology can transfer wirelessly the data obtained by digitizing the data of the object or the domain of the adapter that it is adapting to the server. Digitized data; can be humidity, noise, temperature, pressure, of an environment etc., as well as the number of uses of any device, energy consumption, damage analysis, physical condition or security management. A server or interconnected objects can be controlled remotely by the user via the Internet. In this regard, IoT technology offers significant opportunities for use in living spaces. The emergence of applications such as 'Smart Connected Homes' can be expressed in this context. In the literature review, it is seen that there are many academic studies about the use of IoT technology in smart houses. In the literature review, it is seen that there are many academic studies about the use of IoT technology in smart houses. In these researches, IoT technology is used in smart houses; Security, privacy, personalization and physical environment control.

This study aims to examine the academic studies on the use of IoT in smart homes through a systematic literature review from the beginning of the 2000s. Scanned work is classified according to their content and keywords and analyzed in detail within the scope of examining IoT technology. With this study, it is also aimed to draw attention to the untouched points by foreseeing future use of IoT in intelligent houses.

Key Words

"Internet of Things, Technology, Smart House, Interior Design."

** tolga.kilic@msgsu.edu.tr*

1. GENERAL DESCRIPTION AND THEORETICAL BASIS

In this part of the study, IoT and smart home technologies, which are the subjects of the research, are given.

1.1. Internet of Things (IoT)

In the literature, the term 'Internet of Objects' (IoT) is found in the article by David Brock, who is a researcher in the Auto-ID group, about the 'Electronic Product Code' (Uckelmann vd., 2011). While there is no universal and definite definition for IoT in the literature, the core concept includes that daily objects can be equipped with identification, perception, networking and processing capabilities. Through these capabilities, objects can communicate with each other, with other devices and services over the internet (Whitmore vd., 2014). On the other hand, IoT is a concept that seamlessly integrates the virtual world's information technology with real objects. With this technology, the real world becomes more accessible to both business and everyday scenarios through computers and devices connected to the network. More sophisticated information access has allowed management to move from micro level to macro level, measurable, planned and feasible. However, IoT, which has a much more potential than managing business processes more effectively and efficiently, also reveals a more comfortable life style (Uckelmann vd., 2011).

Gartner, a technology consulting company that makes predictions about the future of emerging technological trends, announces the expectations of these trends every year through a graphic named 'Hype Cycle'. In the hype cycle chart published in 2016, the expectations regarding IoT are shown in Figure 1 (URL-1, 2017).

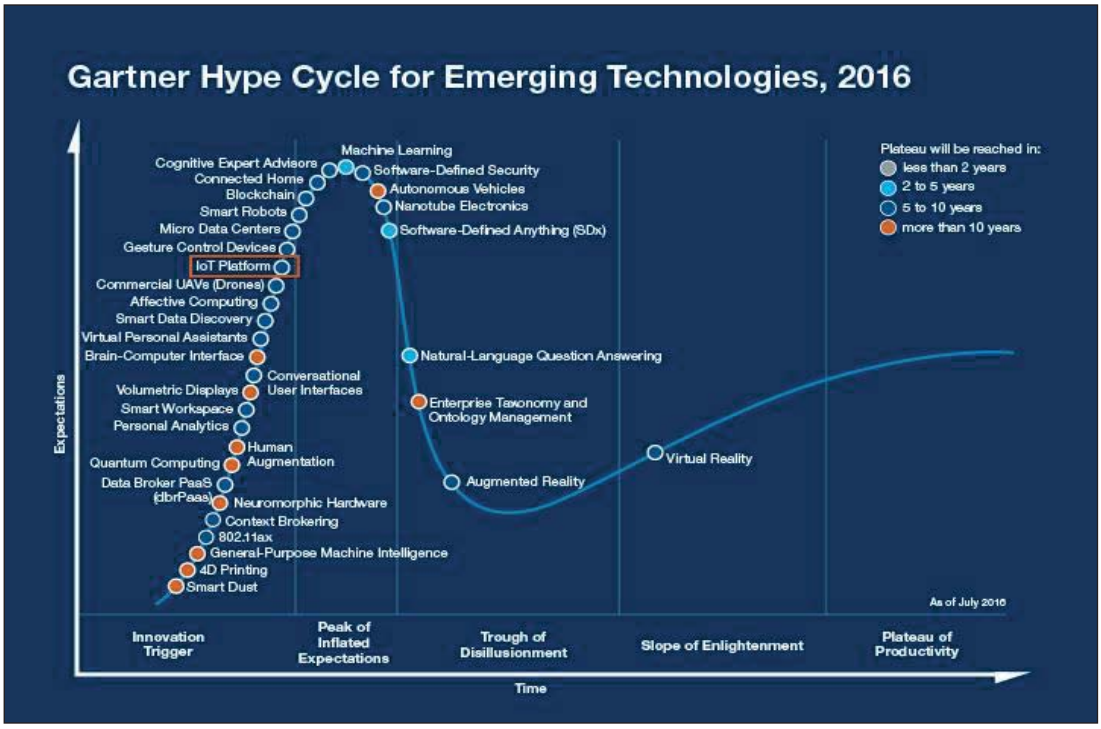

Figure 1. The position of IoT technology in the cycle of Hype Cycle (URL-1, 2017).

In order to identify objects in the environment as IoT objects', these objects must have some electronic devices. These devices are sensors, actuators and devices that perform tasks such as 'Radio Frequency Identification' (RFID). These sensors can analyze the various parameters such as heat, humidity, motion, sound, position according to the need, and transmit it to another connected object or center through the network to which it is connected. These sensors, which are embedded in the objects in a whole, are placed on the chips which are expressed as 'Programmable Card' (PIC). Some of these cards are seen in Figure 2 (URL-2, 2017). 'Raspberry Pi', 'Arduino', and 'BeagleBone' cards are included in these chips. The communication chips that are added to the IoT chip are called 'Wide Area Network' (WAN), 'Personal Area Network' (PAN), 'Local Area Network' (LAN), ' (Bluetooth) and 'Near Field Communication (NFC). During communication, it personalizes communication using a unique network identity such as 'Internet Protocol' (TCP / IP) and 'Media Access Control' (MAC) (Holler vd., 2014).

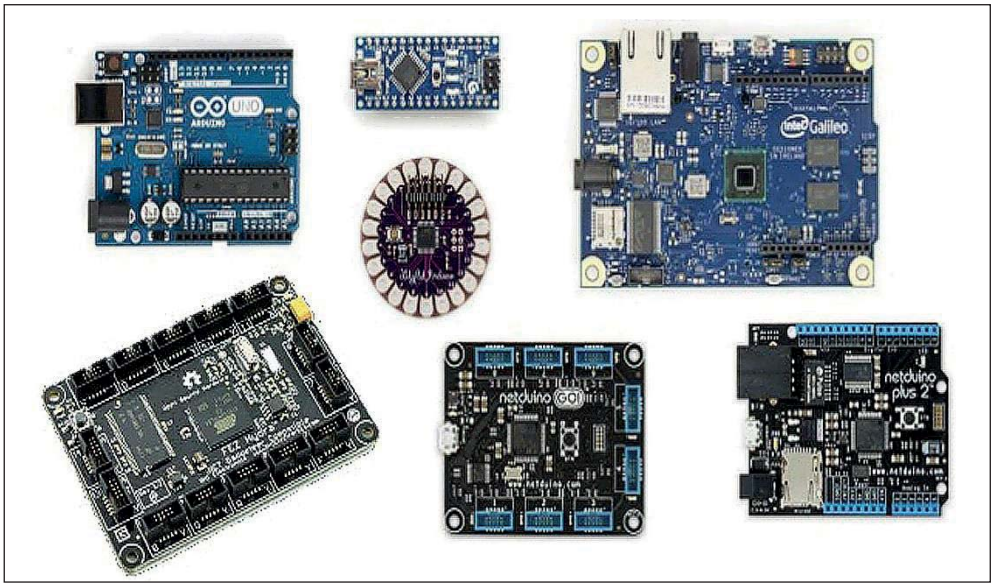

Figure 2. Some programming cards used in IoT project development.

In addition, Pêrez and Barbolla have stated that an IoT system consists of three main layers:

- Hardware Ecosystem (Physical Devices)
- Software Layer
- User Layer (Pêrez&Barbolla, 2014).

On the other hand, three main use cases are defined within the IoT industry. These; sensors, actuators and labels. These uses determine the software and hardware configuration of the IoT device (Mirocha, 2015). With reference to this point, it is possible to formulate IoT technology as follows; Physical Object + Control Devices / Sensors / Actuators + Internet = IoT (McEwen& Cassimally, 2014).

In addition, it is possible to mention that many objects, such as smart TVs, refrigerators, lighting elements, plugs, which are current technology, have IoT technology ready in its place. These objects are characterized as 'intelligent' objects by virtue of their possessions.

Existing scientific developments have played an important role in the spreading of IoT, both in terms of size reduction of communication technologies such as RFID, NFC, Wi-Fi and sophisticated sensors used in IoT technology, and of increasing prices to more reasonable levels. Detecting physical conditions through sensors, collecting and processing detailed data, real-world changes can be answered instantly. Totally interactive and responsive, communications network offers significant potential for businesses and end users (Uckelmann vd., 2011).

1.2. Iot Based Smart Home System

Today, many companies are trying to equip modern houses with the technology used by a single device to control all systems and devices in the house. The targeted solutions seem to focus primarily on environmental monitoring, energy management, life support assistant, comfort and convenience. The IoT -based smart home system relies on open platforms that use an intelligent sensor network to provide information about the state of the house. These sensors perform tasks such as power generation and measurement, heating / ventilation / air conditioning (HVAC), lighting, security system control (Vermesan&Friess, 2014). The user can access the collected information by touching devices such as touch screens, personal computers and mobile phones. Figure 3 depicts an smart home system based on IoT.

IoT-based smart home (IoT SH) refers to a system where all the devices in the house are connected and synchronized. The system that collects information about the user provides an estimate of its behavior and habits. For this reason, the IoT SH system can be characterized as a measurable analytical ecosystem of sensors and actuators designed to automate and control living areas (Mirocha, 2015). In the coming period, IoT SH applications are likely to become a 'social laboratory' where the behavior and preference patterns of users are transformed into data and examined by various social engineering techniques in order to increase sustainability and economic efficiency.

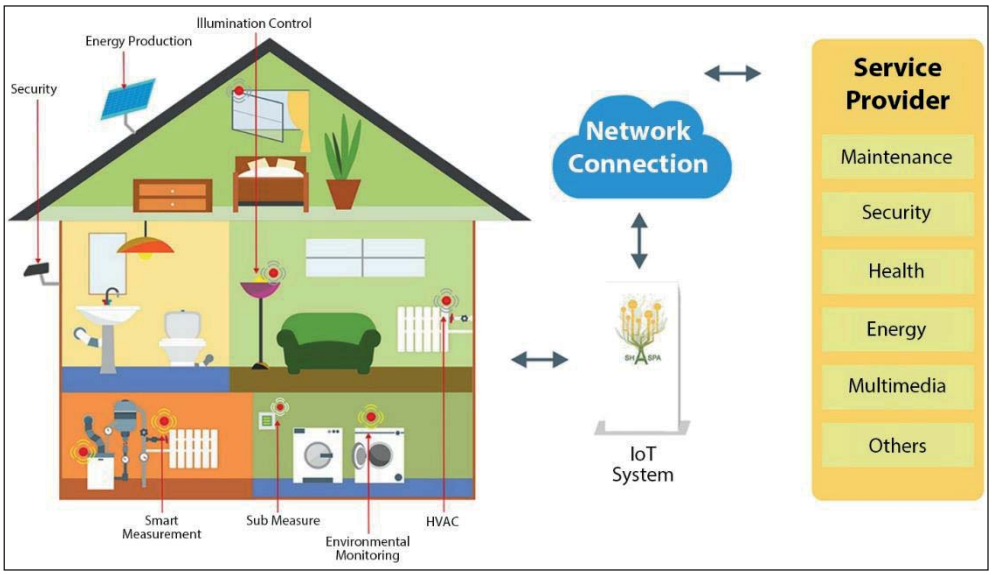

Figure 3. Schematic of the operation of an smart home system based on IoT (Vermesan&Friess, 2014).

When viewed from a different angle, interacting with smart houses and IoT devices is far from being a seamless and hassle-free experience because IoT technology has many different interfaces. While smart home research addresses the growing number and heterogeneity of devices, services and technologies, it emphasizes the growing difficulty of being able to grasp easily and interact smoothly for users (Brush vd., 2011). Technical difficulties in bringing such systems together in smart homes have been recognized by long-standing research communities (Edwards&Grinter, 2001). It is intended to create an integrated interface that combines this kind of technology to prevent the complexity of multiple devices, to provide partial control of interconnected devices and to create a common approach. When this is done, users will feel that they are interacting with the house as a single entity rather than having to feel that they are interacting with more than one system and interface. Tool interfaces such as Apple's "Siri", Amazon's "Alexa", or Microsoft's "Cortana" are another approach to the abstracting of such complexity and provide functionality through speech. These technologies provide a unified interface that allows users to access the natural language spoken, rather than navigate through complex and deep menu structures (Mennicken vd., 2016).

IoT system solutions are divided into 5 different categories in the market: smart wearable, smart business, smart environment, smart city, smart home (Perrera vd., 2015). The focus of this work is on smart home applications and topics that use IoT technology.

2. RESEARCH STRUCTURE

The study focuses on determining which areas of the housing context are weighted by scanning articles on IoT and smart homes. It is another purpose of the study to address future practical problems in this sense and future prospects about possible IoT applications not specifically addressed in the residence. It is also aimed to contribute to the IoT and researchers who work in smart house subjects.

2.1. Research Method

The method of study is systematic literature review. For this purpose, the key words were searched in six separate academic databases. IoT and Residential ',' IoT and Home 'and' IoT and Smart Infrastructure ', considering the scope of the subject. These key words were scanned in the databases 'Scopus', 'Google Scholar', 'ScienceDirect', 'IEEE Xplore', 'ACM Digital Library' and 'Academic Search Premier'. As a result of scanning, 26 articles were accessed. These articles have been carefully analyzed and classified by focusing on what subjects they focus on.

2.2. Classification Method

There are four main categorizations according to the content of the studies obtained in the literature search: smart home system (SH), smart home human-machine interaction (SH -HCI), smart home environment supported life (SH - AAL), smart home privacy and security (SH - The S & P). Some of these categories are later divided into subcategories. The classification made is seen in Table 1.

Table 1. Table prepared according to literature review (Tolga Kılıç).

Main Category	Sub Category	Sub Sub Category
SH System	System Model Suggesiton	Various System Approaches
	Device Management	General Studies
SH HCI	HCI	Device/Smart Plug Control
SH AAL	Person Monitoring	
	System Monitoring	
SH S&P	General Residence Security	
	Bathroom Security	
	Awareness	

Within the scope of the study, 15 of the 26 articles surveyed daily from the beginning of the year 2010 include the works suggested by the model, which are directly related to the smart home system. Twelve of these studies present different model proposals for an IoT based smart home system. Two other studies present model proposals for the control of devices in the smart home system. In one study, it was observed that general approaches to IoT based smart home systems have been examined.

As already mentioned, there is no universally definite rule-based IoT system definition. Since the IoT is a technology that is currently evolving and its content is constantly updated, its components are also diversified. Different hardware is assembled with different software and designed according to different needs and integrated into a system. For example; a system developed to provide control of the sockets in a house and a single device that controls the system in the whole house need different hardware and software types. For this reason, it has been evaluated that a search has been made in order to create a healthy and efficient system with different equipment. On the other hand, when we examine the studies that have been compiled, it is seen that there are some chronic problems faced by the IoT systems. These problems are high cost, coverage areas of objects are not wide enough, and the energy consumption of objects is relatively large. Therefore, in the literature, it has been found that model proposals are offered for an integrated IoT system that will address both these problems and meet different needs. Table 2 shows the key words of the IoT-based smart home system. When these key words are examined, it can be seen that different technological approaches in terms of both software and hardware are put forward.

Table 2. Table showing the key words of the studies on smart home system based on IoT based on literature review (Tolga Kılıç).

Main Category	Sub Category	Sub Sub Category	
IoT SH System	System Model Suggestion	Ambient intelligence Android Smartphone Ardunio Arduino microcontroller board Artificial Intelligence AT mega controller Cloud computing technology Component DIY Field programmable gate array Holistic framework Home automation Internet of Things Interworking IoT ISO/IEC/IEEE 21451 KNX Light Emitting Diode Lightweight MAC Low-cost Plug-and-play Relay circuits. Sea Computing Self-configuration Smart grid SmartCities	Smart Home Smart Home requirements Transducer Twisted Pair Visible Light Communication Web Service WiFi Wi-Fi shield Wireless sensor network WSN ZigBee ZigBee wireless sensor technology
	Device Management	Smart Home Android Smartphone Gateway Optical fiber REST Smart Plug	UC/OS II WiFi Zigbee
	General Study	Ambient intelligence Home Automation Internet of Things SmartCities SmartHome requirements	

2.3. Analysis of Obtained Works

The result of the literature review is the IoT based smart home system model proposal. The contents of the studies and their suggestions are briefly mentioned below:

2.3.1. IoT SH Systems

IoT Smart Home Model Proposals

- In the work named '*A review of Internet of Things for smart home: Challenges and solutions*' a cloud-connected smart home system management model proposal that generates its own energy has been put forward. Study; it is seen that the difficulties and problems encountered in this subject are searched by the literature survey (Biljana vd., 2016).

- In this study which has the name '*Designing and Implementing a Lightweight WSN MAC Protocol for Smart Home Networking Applications*', system architecture and GRAFCET (chip programming language / method) design of a network device is presented for IoT based smart home applications. WSN / MAC connection protocol is recommended in the model (Chen vd., 2017).
- In the work titled *'Home Automation and Internet of Things*' presented by Sing et al., An Ardunio based home automation system proposal, which controls all the sensors in the house, is presented. It is emphasized that the model requires low maintenance cost after installation and can be easily modified (Singh vd., 2016).

- A home automation system based on intelligent transducer interactions with energy / cost efficiency has been introduced in the work named *'Home Automation System Based on Intelligent Transducer Enablers*'. The system includes intelligent converter points, home automation gateway and wireless access points. All of these systems; control and management subsystem, communication subsystem and energy converter sub-system (Albela vd., 2016).

- A low cost flexible home monitoring and monitoring system model based on the Android operating system is proposed in the study entitled *'Internet of Things: Ubiquitous Home Control and Monitoring System using Android based Smart Phone*' by Piyare. The system can be managed by intelligent mobile devices. In the model, even if the WI-FI nodule is closed, the system can be accessed with 3G / 4G communication technology (Piyare, 2016).

- A study named *'Research and application on the smart home based on component technologies and Internet of Things*' presents an IoT smart home system based on SOA (service based architecture). In the study, SOA software support has been shown to offer a software proposal that can be controlled over the web to respond to instant needs and requests quickly (Li&Yu, 2011).

- In the work of *'Smart Home Mobile RFID based Internet Systems*', RFID reader architecture was proposed for smart home applications and services. The system has been developed as an alternative to high energy consuming RFID reading models. In this context, it is understood that a high energy efficiency model is targeted. Examples of use of various smart home services such as work washing programs, cooking, shopping and elderly health care are given as examples of systems using the RFID system (Darianian&Michael, 2008).

- The 'Smart Grid' application, named *'System Design of Internet-of-Things for Residential Smart Grid*', provides a large-scale IoT system design that requires fast response time for many home users Viswanath vd., 2016).

- As an alternative to high-cost traditional smart home technology, ZigBee wireless sensor technology with high cost efficiency and IoT smart home model proposal using cloud technology have been proposed as *'The Design and Application of Low-Cost Smart Home Under the Internet of Things and Cloud Computing Platform*' Provided (Wei&Qin, 2013).

- The work *'WiFi Multi Access Point Smart Home IoT Architecture*' offers a wireless sensor network concept specifically designed for smart home applications. The innovative nature of this network is concerned with the simultaneous use of selected sensors serving as access points and network clients for information transfer and routing. In other words, it is thought that sensors serve for multiple purposes in the model proposal (Lech, 2016).

- In this work called *'The Possibility of Using VLC Data Transfer in the Smart Home'*, we propose an IoT model that provides communication through VLC (Visible Light Communication) method based on KNX (Smart Home-Building Automation System) management system (Vanus vd., 2016).

- In the work called *'Smart Home System Based on Internet of Things*', an Ardunio based IoT model proposal was presented, which was developed to control different types of intelligent devices and IoT objects in a house from a single central system. The system is compatible with Android devices and personal computers with HTML access Verma vd., 2016).

IoT Smart Home Device Control

Two academic studies related to smart home systems based on IoT have shown that the proposed model is related to the control of the devices in the smart home system.

- In the work named *'Design for a Residential Gateway Based on IoT Technology'*, a proposal of an IoT model that fulfills the mission of reading wireless meters to measure electricity, water and gas consumption from a remote place (Guan&Wang, 2013).

- In the second study named *'Design of Smart Home System Based on WiFi Smart Plug*', it is seen that a model proposal that provides smart control of smart sockets in smart house is presented. It has also been understood in this study that it is aimed to control electric devices via smart sockets via an energy / cost effective model (Wang vd., 2015).

IoT Smart Home General Review

In the literature survey, one study has been reached which generally examines IoT based smart home systems. This work is briefly mentioned below:

- Based on 'Smart Cities', it has been determined that a roadmap has been developed in order to meet the basic needs of a smart home system in the work called *'Smart Requirements of Smart Homes in Smart Cities Based on Internet of Things Technologies*' (Terence vd., 2016.)

Table 3. Table showing that the key words of IoT SH System and HCI Interaction, IoT SH System and AAL, IoT SH System and Security and Privacy system according to literature survey (Tolga Kılıç).

Main Category	Sub Category	Sub Sub Category
IoT SH System and HCI	HCI	Agent-based interface Artificial psychology Building information modeling Context Awareness Emotional model Home automation Internet of things Interaction technology IoT Location based service Ontologies Personality Pervasive Computing Sensors Smart home Spatial information SWRLs Virtual human-computer
IoT SH System and AAL	Person Monitoring	Activities of Daily Life Ambient Assisted Living Lab Artificial Intelligence Business ecosystem Business-technology Co-design Device and service integration Enterprise information system ExpertSystem Health Monitoring Home Automation systems Industrial information integration engineering In-home health care station Intelligent medicine box Internet of Things KNX Neurological Disorders Robotic Technologies Sensors Turtlebot Vision Processing Algorithms
	Sytem Monitoring	
IoT SH System and Security&Privacy	General Residence Security	Bathroom Safety Big Data Fire protection Fuzzy logic Internet of Things (IoT) Microcontroller Privacy Representational state transfer Security Sensor web Smart home Temperature sensor Wireless Sensor Network
	Bathroom Security	
	Awareness	

In the literature review; '*IoT* SH *System and HCI*' (Human Computer Interaction), '*IoT* SH *System and AAL*' (Ambient Assistant Living), and '*IoT* SH *System Security and Privacy*'. A total of 11 works focused on these issues.

2.3.2. IoT SH and HCI

The contents of the IoT SH System and HCI related studies are briefly summarized below:

- This study aims to develop a location-based technology that can provide improved information services to users depending on their location in the work named *'Developing a the Advanced IoT (Technology of Information) Technology Based on Spatial Information*'. The ultimate goal is to develop an advanced platform for 'Location Based Service' (LBS) using spatial information. It has been seen that the work will ultimately contribute to 'Human Space Interaction' (HSI) (Jang vd., 2016).

- In the study named *'Human machine interactive system on smart home of IoT*', the emotional interaction system in the smart home system based on IoT was examined. For this, the user's emotional reactions, which are spilled out of the way, are given in the form of writing to the user and the user-machine interaction is aimed to be raised to the upper level. Thus, in the future it seems to be aimed at increasing spatial awareness by working with people and machines more harmoniously (Kun-kun, 2013).

- "*Perceptions of Personality Traits in a Smart Home", "Does a smart home need to be a proactive or passive character?" Should we try to socialize with the residents?*" seems to have been tried to be answered by taking center of human-machine interaction. In the study of 41 participants experiencing the generated scenario and giving feedback on the designs, the design of the agent-based IoT interfaces was analyzed in the direction of the participants' preferences and various improvements were proposed (Mennicken vd., 2016).

- It has been seen that users of the work named *'Pervasive semantic representation and integration of context-aware homes in context sensitive cities*' are aiming to present a viewpoint on the interaction of users and IoT ecosystem that collects data from devices and transitions. The ecosystem has been modeled using 'Semantic Web' technologies in the perspective of IoT. Semantic network technology improves by learning and analyzing the environment of the system to which it is connected. In this context, it is aimed to include both home and city measurements of a learned IoT ecosystem (Vlachostergiou, 2015).

2.3.3. IoT SH and AAL

The contents of the IoT SH System and the studies related to the AAL are briefly mentioned below:

- An IoT system model proposal that can be used to collect, analyze and process the necessary information from the patient's home to assist medical specialists in the diagnosis of Parkinson's disease is given in the article titled *'An Approach of a Decision Support and Home Monitoring System for Patients with Neurological Disorders*' It offers. In addition, 'Web Based Home Health Monitoring Portal' model is recommended for patients with Parkinson's disease or other neurological disorders (Chiuchisan&Geman, 2014).
-

- A method for remote control and integration of home health care devices and services has been proposed in the work entitled *'The Internet-Of-Things' of' Design of A Terminal Solution for In-Home Health Care Devices and Services Towards'*. In this framework, it is planned that the model (business model, device / service integration architecture and information system integration architecture) will be realized by organically combining three basic elements with IoT technology (Pang vd., 2013).

- '*Designing the Next Generation of Home Automation Combination IoT and Robotic Technologies*' presents a new home automation system design that combines IoT and robot technologies. In the study, he proposed a model that could help people living alone at home (Christopoulos vd., 2016).

2.3.4. IoT SH and Security & Privacy

The contents of the IOT SH System and the studies related to security and privacy are briefly summarized below:

- The project entitled *'An Internet-of-Things (IoT) System Development and Implementation for Bathroom Safety Enhancement*' presents a holistic conceptual approach to the development and implementation of the IoT system to enhance residential bathroom security. The concept is focused on implementing a large nursing facility as pilot testing environment (Koo vd., 2016).

- '*Developing A Fuzzy Logic Based System For Monitoring And Early Detection of Residential Fire Based on Thermistor Sensors*' named work focuses on the development of a fuzzy logic based IoT system for monitoring and early detection of residential fire based on thermistor sensors (Maksimovic vd., 2014).

- '*Home Automation Using Internet of Things*' seems to develop a system to remotely control home appliances and provide maximum security against problems that would arise when not in the home (Patel vd., 2016).
- The *'On Privacy and Security Challenges in Smart Connected Homes*' software provides a 'new' IoT security approach to prevent smart home users from accessing their private information without permission (Bugeja vd., 2016).

3. CLASSIFICATION RESULTS

When the results obtained by literature review are examined; It seems that IoT technology has not yet become stable and stable in terms of both software and hardware in the smart home system. It is possible to show that one of the most important reasons for this is that the IoT technology is still in its developmental stage. Today, on the market, a wide variety of development cards, sensors and other external equipment used in IoT systems are found. These hardware components are assembled and programmed to meet different needs. But it seems to be difficult to produce a healthy working system and to suggest it as a model with high energy / cost efficiency. It seems that scientists are working with different hardware and software to overcome this problem and to create a stable IoT model for smart houses. In this respect, it has been evaluated that a house concentrates on an IoT SH model proposal, which controls all electrical or electronic devices via a single central device, which can be instantly accessed by users' smart devices or personal computers and has an easy interface. The 12 studies obtained in the literature search are the studies that have been put forward to produce a model proposal in this respect. In other works on smart home management, it is understood that studies have been made specifically about the control / access of certain devices or systems.
In the four studies conducted for the use of IoT in SH, it is seen that the relation of IoT with the user in the place is discussed. In the studies, the emotional interaction of the machine with the users was investigated and the models in which this approach was supported with the learned technology were suggested. It has been understood that the IoT SH systems have been integrated with technologies such as the semantic network to create a concrete infrastructure for this thinking. Therefore, it seems that in these studies, the search for a user-friendly IoT model, in which man-machine interaction becomes more flexible and easier, is aimed at. IoT is a technology where the level of environmental feedback is at a high level. Therefore, it has a promising potential for 'Ambient Assisted Living'. The academic research that has been done has also come up with studies on this subject. In these studies, it has been pointed out that automatic transmission of data about the health status of sick or elderly people living alone to a specific center or taking precautions against the problems that these people will live in their homes. In this context, it is seen that different IoT model proposals for needy users are presented.

Security and privacy issues have high protection in IoT SH systems. In the literature review, four studies were carried out for this subject. All of the works are in contact with different points in terms of security and privacy issues. It has been seen that models have been developed in order to take measures against fire, to provide bathroom security and general home security. It has also been assessed that a model recommendation is provided to ensure the safety of the user's personal data.

4. CONCLUSIONS AND RECOMMENDATIONS

This study aims to examine the academic work on the use of IoT in smart homes through a systematic literature review from the beginning of the 2000's. Key words related to the subject were scanned in six separate academic databases and 26 studies were reached. These studies have been classified in terms of intelligent households, focusing on the points and key words they focus on. Thus, it was aimed to determine the points contacted by academic studies on the use of IoT technology in smart home context. On the other hand, it has been thought that working will also be useful in the discovery of IoT's potential use points in smart home technology, but not addressed.
According to the data obtained through literature review; No work has been done specifically on the interface design for the IoT SH system. It is thought that the interface design, which has a vital prescription to interact with the user, has an impressive role in the performance of the system in interacting with the user. On the other hand, it should be emphasized that the interface design,

which will also affect the outer appearance of the IoT object aesthetically, will reflect directly on the interior space and affect the integrity of the design.

In addition, I need to emphasize that the use of a technology such as 'Face Recognition' in the IoT SH system will be important for the personalization of design patterns. It is possible to produce custom behavior patterns by defining the faces of the users in separate systems. In addition, the integration of Augmented Reality technology with IoT, which combines virtuality and reality, is seen as a potential user environmental awareness.

IoT technology has the ability to integrate furniture in the house. Furniture equipped with actuators, such as various sensors and servo motors, are likely to gain the ability to vibrate or act according to the user's commands. Although not very likely in the near future, an IoT SH system designed in this way stands as an approach that will influence the mobility of the space.

REFERENCES

Albela, M.S., Lamas, P.F., Caramés, T.M.F., Dapena, A., López, M.G., 2016. Home Automation System Based on Intelligent Transducer Enablers, Sensors Journal, 2016, 16, 1595.

Biljana L. Risteska Stojkoska, Kire V. Trivodaliev 2016, A review of Internet of Things for smart home: Challenges and solutions, Journal of Cleaner Production 140 (2017) pp.1454-1464.

Brush, A.B., Lee, B., Mahajan, R., Agarwal, S., Saroiu, S., Dixon, C.,. 2011. Home Automation in the Wild: Challenges and Opportunities. ACM Press, 2115–2124.

Bugeja, J., Jacobsson, A., Davidsson, P., 2016, On Privacy and Security Challenges in Smart Connected Homes, 2016 European Intelligence and Security Informatics Conference, pp.172-175.

Ching-Han Chen, Ming-Yi Lin, Wen-Hung Lin, 2016. Designing and Implementing a Lightweight WSN MAC Protocol for Smart Home Networking Applications, Journal of Circuits, Systems, and Computers,Vol. 26, No. 3, World Scienti c Publishing Company (2017)

Chiuchisan, I., ve Geman, O., 2014. An Approach of a Decision Support and Home Monitoring System for Patients with Neurological Disorders using Internet of Things Concepts, WSEAS TRANSACTIONS on SYSTEMS, Volume 13,2014, pp. 460-469.

Christopoulos, K., Spournias, A., Orfanoudakis, T., Antonopoulos, C., Voros, N., 2016. signing the Next Generation of Home Automation Combining IoT and Robotic Technologies, PCI 2016 Conferences, November 2016.

Darianian, M., Michael, M.P., 2008. Smart Home Mobile RFID-based Internet-Of-Things Systems and Services, 2008 International Conference on Advanced Computer Theory and Engineering, IEEE Computer Society. Pp. 116-120.

Edwards, W.K., Grinter, R.E., 2001. At Home with Ubiquitous Computing: Seven Challenges. Springer-Verlag, 256–272.

Guan, S., Wang, R., 2013. Design for a Residental Gateway Based on IoT Technology, 3rd International Conference on Multimedia Technology (ICMT 2013), Published by Atlantis Press, pp. 105-116.

Holler, Jan., Tsiatsis, Vlasios., Mulligan, Catherine., Karnouskos, Stamatis., Avesand, Stefan., Boyle, David. From Machine-to-Machine to the Internet of Things: Introduction to a New Age of Intelligence, Academic Press, Oxford 2014.

Jang, M.N.R., Suhr, C.H., Lee, Y.G., 2016. Developing a the Advanced IoT (Internet of Things) Technology Based on Spatial Information, HCII 2016 Posters, Part II, CCIS 618, pp. 416–419, Springer International Publishing Switzerland 2016.

Kun-kun, D.K., Zhi-liang, W., Mi, H., 2013. Human machine interactive system on smart home of IoT, The Journal of China Universities of Posts and Telecommunications, ScienceDirect Ağustos 2013, 20 pp. 96-99.

Koo, D.D., Lee, J.J., Sebastiania, A., Kim, J., 2016. An Internet-of-Things (Iot) System Development and Implementation For Bathroom Safety Enhancement, International Conference on Sustainable Design, Engineering and Construction, Procedia Engineering 145 (2016) pp. 396 – 403.

Lech, P., 2016, WiFi Multi Access Point Smart Home IoT Architecture, Automation Control Theory Perspectives in Intelligent Systems, Advances in Intelligent Systems and Computing 466, pp. 247-254, Springer International Publishing Switzerland 2016.

Li, B., Yu, J., 2011. Research and application on the smart home based on component technologies and Internet of Things, / Procedia Engineering 15 (2011) 2087 – 2092.

Maksimović, M., Vujović, V., Perišić, B., Milošević, V., 2014. Developing A Fuzzy Logic Based System For Monitoring And Early Detection of Residential Fire Based on Thermistor Sensors, Computer Science and Information Systems 12(1): pp 63–89.

McEwen, A., Cassimally, H., 2014. Designing the Internet of Things, Wiley, Chichester 2014.

Mennicken, S., Zihler, O., Juldaschewa, F., Molnar, V., Aggeler, D., Huang., E.M., 2016. "It's like living with a friendly stranger": Perceptions of Personality Traits in a Smart Home. UbiComp '16, September 12 - 16, 2016, pp. 120-131. Heidelberg, Germany.

Mirocha, U., 2015. The Internet of Things At The Crossroads: Smart Home And Smart City Implementation Models, Working Paper Delab Uw, No. XX (2/2015 Smart Economy & Innovation, Warshaw.

Pang, Z., Zheng, L., Tian, J., Walter, S.K., Dubrova, E., Chen, Q., 2103. Design of A Terminal Solution For Integration of In-Home Health Care Devices and Services Towards The Internet-Of-Things, Enterprise Information Systems, 9:1, pp. 86-116.

Patel, P., Patel, M., Panchal, V., & Nirmal., V., 2016. Home Automation Using Internet of Things, Imperial Journal of Interdisciplinary Research (IJIR) Vol-2, Issue-5, pp. 648-651.

Perera, C., Liu, C.H., Jayawardena, S., Chen, M., 2014. A Survey on Internet of Things From Industrial Market Perspective, IEEE Access 2015, Volume2 pp. 1660-1669.

Pérez, C.I.,. Barbolla, B., 2014. Exploring Major Architectural Aspects of the Web of Things. in: Internet of Things: Challenges and Opportunities (Smart Sensors, Measurement and Instrumentation), Subras Chandra Mukhopadhyay, ed., Springer, Cham Heidelberg New York Dordrecht London 2014.

Piyare, R., 2016. Internet of Things: Ubiquitous Home Control and Monitoring System using Android based Smart Phone, International Journal of Internet of Things 2013, 2(1): 5-11.

Singh, S., Saha, D., Khaware, P., Das, S., Raj, D., Das, S., Nandi, C.S., 2016. Home Automation and Internet of Things, International Advanced Research Journal in Science, Engineering and Technology Vol. 3, Issue 6, June 2016.

Terence, K.L. Hui, A., Sherratt, R.S., Sánchez D.D., 2016. Major requirements for building Smart Homes in Smart Cities based on Internet of Things Technologies, Future Generation Computer Systems (2016), pp. 1-11.

Uckelmann , D., Harrison, M., Michahelles., F., 2011. Architecting the Internet of Things, , Springer-Verlag Berlin Heidelberg 2011.

Wang, L., Peng, D., Zhang, T., 2015. Design of Smart Home System Based on WiFi Smart Plug, International Journal of Smart Home Vol. 9, No. 6 (2015), pp. 173-182.

Vanus, J., T. Stratil, R. Martinek, P. Bilik, J. Zidek, 2016. The Possibility of Using VLC Data Transfer in the Smart Home ,14th IFAC Conference on Programmable Devices and Embedded Systems PDES 2016, pp. 40-45.

Verma, H., Vikram, A., Jain, M., Verma, G., Goel, K., 2016. Smart Home System Based on Internet of Things, 2016 International Conference on Computing for Sustainable Global Development, pp. 2073-2075.

Vermesan, O., Friess, P., 2014. Internet of Things – From Researvh and Innovation to Market Deployment, River Publishers, Aalborg.

Wei, X., Qin, Q., 2013. The Design and Application of Low-Cost Smart Home Under the Internet of Things and Cloud Computing Platform, LISS 2012: Proceedings of 2nd International Conference on Logistics, Informatics and Service Science, Springer-Verlag Berlin Heidelberg 2013. Pp. 959-965.

Whitmore, A., Agarwal A., Da Xu, L., 2014. The Internet of Things-A survey of topics and trends. Information System Frontiers A Journal of Research and Innovation, pp.267-274. Newyork, Springer.

Viswanath, S.K., Yuen, C., Tushar, W., Li, W.T., Wen, C.K., Hu, K., Chen, C., Liu, X., 2016. System Design of Internet-of-Things for Residential Smart Grid, eprint arXiv:1604.04009.

Vlachostergiou, A., Stratogiannis, G., Siolas, G., Caridakis, G., Mylonas P., 2015. Pervasive Semantic Representation and Integration of Context-Aware Homes in Context Sensitive Cities, 1st Workshop on Artificial Intelligence and Internet of Things.

Internet References

URL-1: http://www.gartner.com/smarterwithgartner/3-trends-appear-in-the-gartner-hype-cycle-for-emerging-technologies-2016/ (Access Time: 5.1.2017)

URL-2: http://www.slideshare.net/ActiveNick/buildingfor-iot-nlandry (Access Time: 6.7.2017)

MÜHENDİSLİK FAKÜLTESİ

Uluslararası Mühendislik Araştırma ve Geliştirme Dergisi

International Journal of Engineering Research and Development

Cilt/Volume:9 Sayı/Issue:3 Aralık/December 2017 https://doi.org/10.29137/umagd.372979

Araştırma Makalesi / Research Article

A New Program Design Developed for AC Load Flow Analysis Problems

Celal YAŞAR[1], Serdar ÖZYÖN[2*], Hasan TEMURTAŞ[3]

[1,2]Dumlupınar University, Faculty of Engineering, Electrical and Electronics Engineering

[3]Dumlupınar University, Faculty of Engineering, Computer Engineering

Başvuru/Received: 08/10/2017 **Kabul/Accepted**: 01/12/2017 **Son Versiyon/Final Version**: 26/12/2017

Abstract

The Newton-Raphson method is generally used for iterative solutions of power systems in load flow analysis. This study focuses on a new program structure designed to solve large size power systems accurately and quickly using AC load flow analysis technique. This program structure will provide both easy and accurate data input in solutions of high-capacity data input problems. The data required for solving the problem at hand was obtained from an Excel, and coded in Matlab R2015b and solutions were printed onto a solution file.

Key Words

"Electrical power generation, AC load flow, Newton-Raphson Method."

serdar.ozyon@dpu.edu.tr

1. INTRODUCTION

With the increasing demand for electricity, the planning and optimal operation of power generation systems have recently become a very important issue. In order to carry out these operations, it is necessary to analyze AC load flow in power systems. In order to perform AC load flow analysis of a power system, net active and reactive powers of all buses and voltage magnitude and angle of the slack bus should be input into the system. If there are voltage-controlled buses in the system, they should be introduced to the system as buses, the voltage amplitudes of which will be kept constant. The power flow solution provides the voltages, amplitudes and phase angles of all buses. Afterwards, active and reactive powers of the slack, power flows and line losses are calculated.

There are many studies on AC load flow analysis in the literature. While some of these studies deal with newly developed methods, some others focus on interface designs to make a given program easier to use. The latter address load flow analysis using a modified Newton-Raphson method (Panosyan et al., 2004), use of probability techniques for AC load flow analysis (Allan et al., 1977), (Dagur et al., 2014), linearized AC load flow applications (Rosoni et al, 2016) and use of evolutionary computation methods in load flow solutions (Revanthi, 2008).

This study used the Newton-Raphson method for load flow analysis. When using this method, it is very important that problem data are input correctly into load flow programs. If data are input incorrectly, it is unlikely that solutions will be correct. Therefore, data input becomes very important, especially in high-dimensional systems. For this reason, this study focused on a new data input design. Data was extracted from an Excel file and coded, and the program software was run using Matlab R2015b. The system used as a sample application consists of 118 buses and 54 generators.

This paper summarizes the load flow method, provides information on the software developed to provide ease of use, and presents the solution to a multi-dimensional sample system to demonstrate the advantage of the software.

2. LOAD FLOW ANALYSIS

Load flow refers to determination of the best mode of operation of existing power systems and calculation of voltage magnitude and phase angle of each bus in a power system. Once the information on buses has been obtained, active and reactive power flows and transmission line losses that occur in transmission lines in the system are calculated (Wood et al., 2013), (Kothari & Dhillon, 2007), (Özyön,2009).

In power flow in a power system, net active and reactive powers for all buses except one bus are determined. Net power (active Pk and reactive Qk) is equal to the difference between the power supplied to the system and the power drawn from the system, which means that it is the difference between the power supplied by the generator and the power the load consumes depending on the bus. If there is a voltage-controlled bus in the system, the bus voltage magnitude that will be kept constant at this bus should be determined. The generation of the bus-dependent reactive power generator and the bus voltage angle are calculated at the end of power flow solution (Wood et al., 2013), (Kothari & Dhillon, 2007), (Özyön,2009).

Buses in a power system are divided into various types as load bus, voltage-controlled bus and slack bus. A system has only one slack bus.

Each bus k in a system is defined by active power P_k, reactive power Q_k, voltage magnitude $|V_k|$ and voltage angle δ_k. Depending on each bus k, two of P_k, Q_k, δ_k and $|V_k|$ values are known and the other two are calculated. The purpose of power flow solutions is to find the two unknown values when the difference between the values of P_k and Q_k and the calculated values are approximated to zero (Wood et al., 2013).

In power flow studies, bus voltage magnitudes |Vk| and angles δk are unknown parameters expect for slack buses. They are, mathematically, independent variables, as their values determine the state of a system. Therefore, a power flow problem can be defined as the determination of values of all state variables using equal number of power flow equations based on input data. Once the values of state variables have been calculated, the entire state of the system is known and all values depending on the state variables can be calculated.

3. DESIGNED PROGRAM AND DATA INPUT

This study focused on designing a new program that facilitates data input in the load flow program. Data input was performed using Excel, and transferred to Matlab R2015b. The load flow solution was obtained by forming the coding of the program as distinct subprograms and results were printed to a file. The data input sheets in Excel are given in Figures 1, 2 and 3. Power base (S_{base}), voltage base (V_{base}) and impedance base (Z_{base}) values used in the system solution are entered in the *Baz_Deg* sheet in Figure 1.

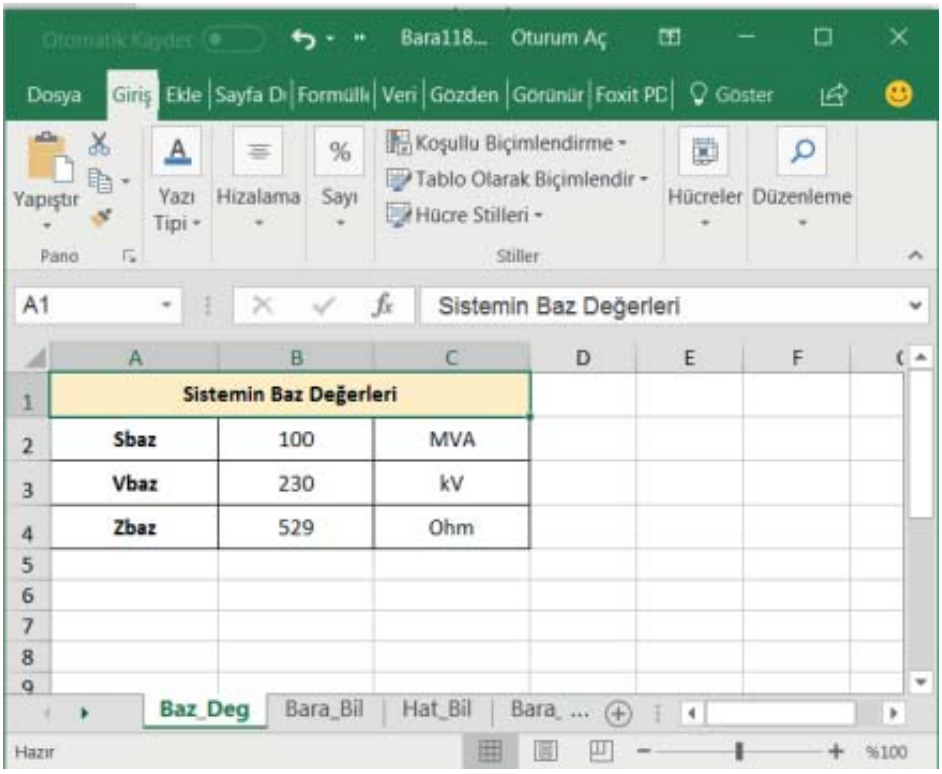

Figure 1. System base values input sheet

The bus numbers, generator bus types (*UreTip*), bus types (*BusTip*), active power generation limits of generators (P_{min}, P_{max}), initial value of active power generation (P_{Gen}), reactive power generation limits of generators (Q_{min}, Q_{max}), initial value of reactive power generation (Q_{Gen}), active and reactive load values at buses (P_{load}, Q_{load}), voltage limits of buses (V_{min}, V_{max}), voltage values of voltage-controlled buses (V_{bus}) and bus angles (*Açı*) used in the solution of the problem are entered in the *Bus_Bil* sheet given in Figure 2.

The line numbers, serial impedance between lines (*R*), parallel admittance (*X*), capacitance values (*B*), transformer transfer ratio (*Tap*), transmission line carrying capacities (S_{limit}) and maximum angle difference between buses (*MaxAf*), which are the transmission line information of the system, are entered in the *Hat_Bil* sheet given in Figure 3.

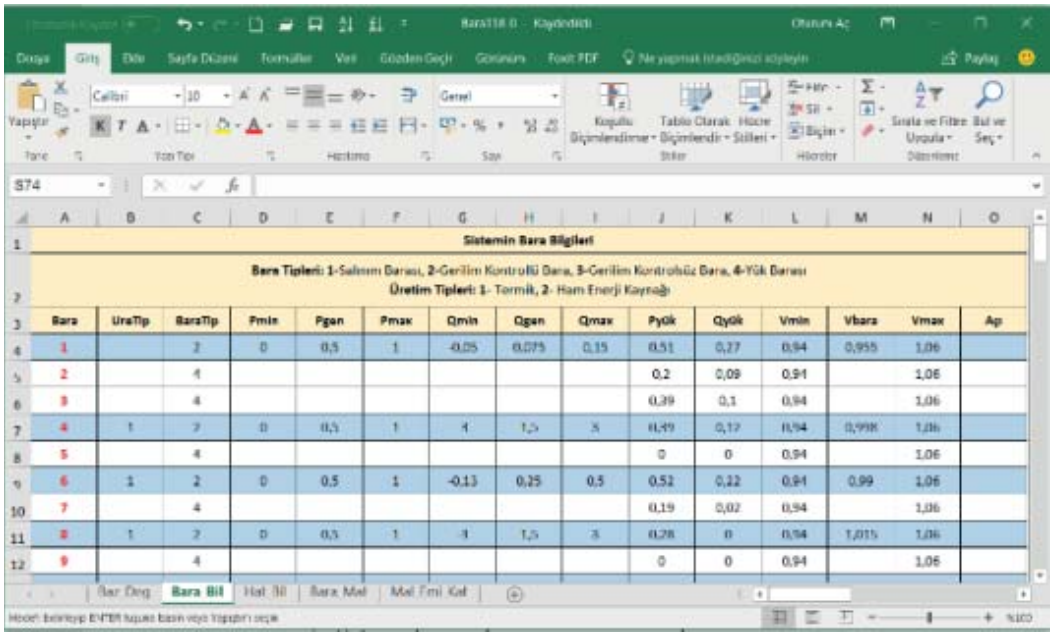

Figure 2. System bus information input sheet

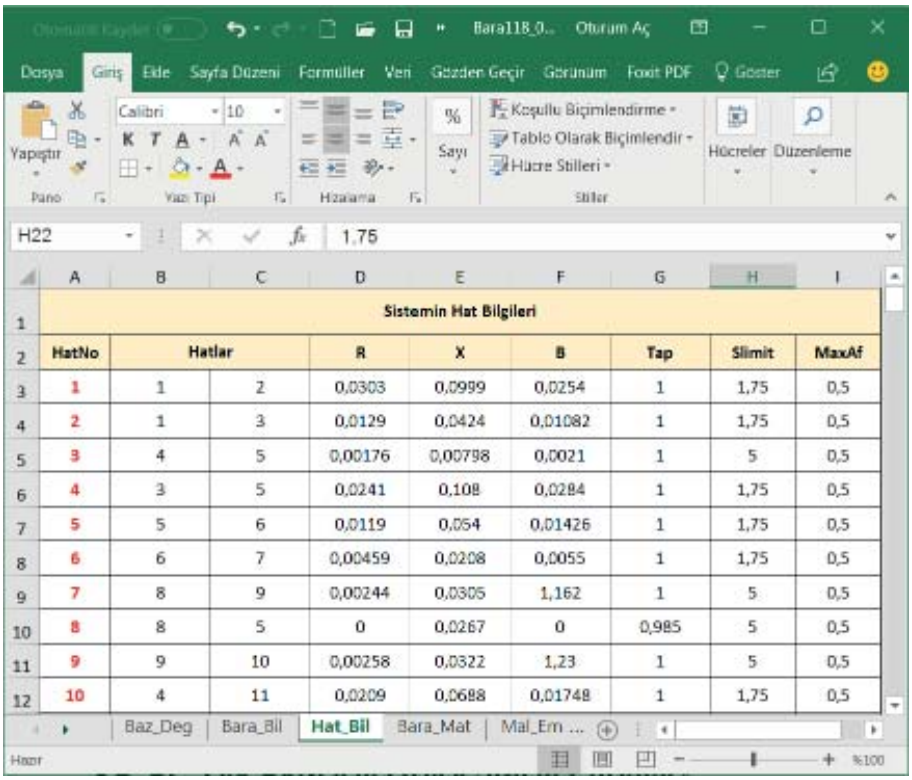

	A	B	C	D	E	F	G	H	I
1	Sistemin Hat Bilgileri								
2	HatNo	Hatlar		R	X	B	Tap	Slimit	MaxAf
3	1	1	2	0,0303	0,0999	0,0254	1	1,75	0,5
4	2	1	3	0,0129	0,0424	0,01082	1	1,75	0,5
5	3	4	5	0,00176	0,00798	0,0021	1	5	0,5
6	4	3	5	0,0241	0,108	0,0284	1	1,75	0,5
7	5	5	6	0,0119	0,054	0,01426	1	1,75	0,5
8	6	6	7	0,00459	0,0208	0,0055	1	1,75	0,5
9	7	8	9	0,00244	0,0305	1,162	1	5	0,5
10	8	8	5	0	0,0267	0	0,985	5	0,5
11	9	9	10	0,00258	0,0322	1,23	1	5	0,5
12	10	4	11	0,0209	0,0688	0,01748	1	1,75	0,5

Figure 3. System line information input sheet

In this design used to input system data, the program can easily be integrated into the new state by adding a sheet or column to the data file for additional information required for a new problem or a new system.

After the system data is uploaded to an Excel file, the following code block generated in Matlab is used to convert the data into a matrix form with a .mat extension. The data converted into a matrix form is uploaded to the Matlab application and their load flow is performed and results are printed.

4. SAMPLE SYSTEM SOLUTION

```
format compact
clear, clc
s = 'Bara118_0';
file = [s,'.mat'];
if exist(file,'file') ~= 2
tic
f = [s,'.xlsx'];
Baz = xlsread(f,1);
Bara = xlsread(f,2);
Hat = xlsread(f,3);
BMat = xlsread(f,4);
MalEmKat = xlsread(f,5);
clear s f
save(file)
toc
end
Data = load(file)
```

A sample power system consisting of IEEE 118 buses, 54 thermal power generation units and 179 transmission lines referred to as single-line diagram in Appendix Figure 1 was selected in order to test the load flow analysis in this section (Power Systems Test Case Archieve, 2017), (MatPower, 2017), (Zahlay, 2016).

This system is one of the high dimensional systems in the literature. Bus no 69 in the system is a slack bus and its voltage is $1.035\angle 0^0$ *pu*. All 54 generators in the system consist of voltage-controlled buses. 9 transmission lines in the system have transformers. The base values of the system were designated as S_{base}=100 *MVA*, U_{base}=230 *kVA* and Z_{base}=529 *Ohm*.

Appendix Table 1 shows the serial impedance, parallel admittance, capacitance values, transformer transfer ratios and line carrying capacities of the nominal π equivalent circuits of the transmission lines in the sample system. 91 buses and their active and reactive load values that remain unchanged at a period of time in the system are given as *pu* in Appendix Table 2. Appendix Table 3 presents the initial values of the load flow of the generation units. The 54 generators in the system are voltage-controlled buses and the bus voltages of these buses are kept constant at the values given in Appendix Table 3. The working limit values of the generation units in the system are given in Appendix Table 4 (Power Systems Test Case Archieve, 2017), (MatPower,2017), (Zahlay, 2016)

The bus voltage magnitude and angle values (V_k, δ_k), active and reactive power generation values (P_k, Q_k) as *pu* in the generation units and transmission line losses obtained from AC load flow in the sample system are given in Annex Table 5. The transmission line losses that occured as a result of AC load flow in the sample system were P_{loss}=0,614601 *pu*. The voltage magnitudes of the buses in the system ranged from 0.94 to 1.06 *pu*. The voltage profile of all the buses showing this state is given in Figure 4. The load flow solution time of the large size sample system at the work statiton with Intel Xeon E5-2637 v4 3.50 GHz processor and 128 GB RAM memory was 0.0719492 sec.

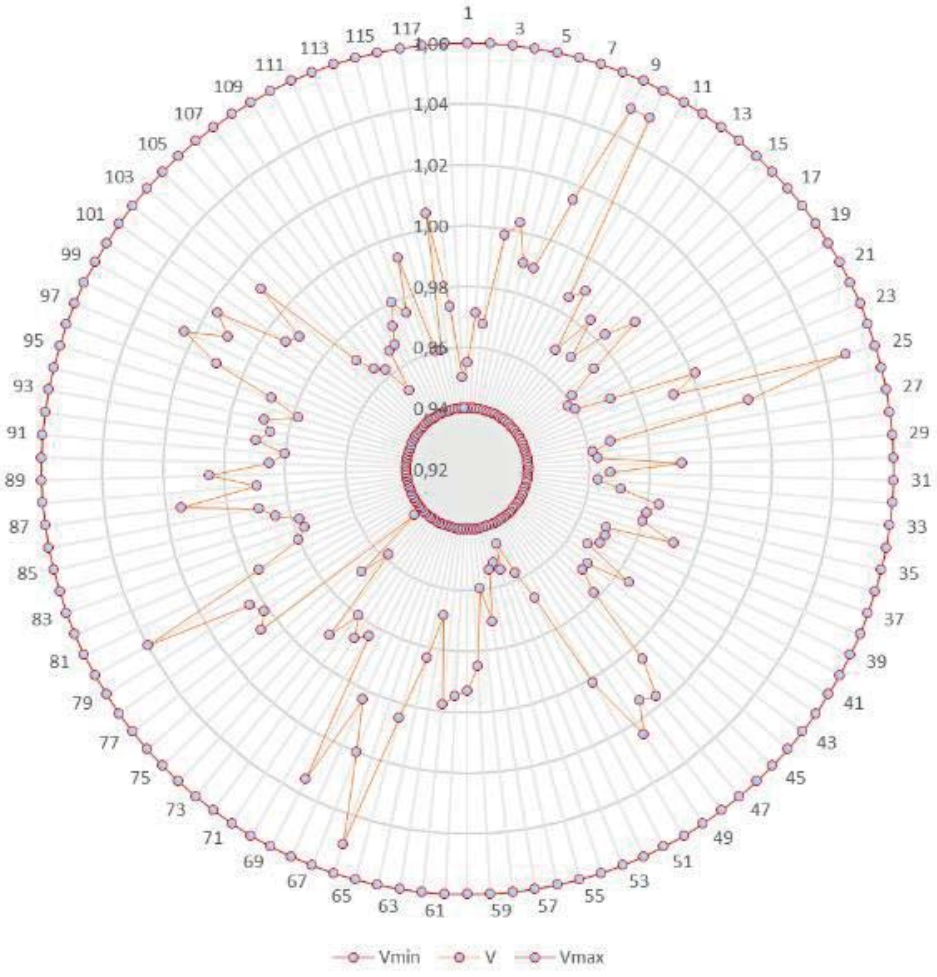

Figure 4. Voltage profile of IEEE 118 bus system at solution point

5. CONCLUSION

In this study, the Newton-Raphson method was used to perform load flow analysis and the new program facilitates the data input for the process. On a different sample system, this new data input method can be used to provide data input without running the

load flow program. This new method makes it easier to correctly input data for the solutions to high-dimensional systems. It also prevents erroneous data input. The data input innovation developed in this study can also be improved for future studies and used for economic power distribution and short term hydrothermal coordination problems.

ACKNOWLEDGMENT

This work was supported by the Dumlupınar University Scientific Research Projects Commission under the 2016-65 project.

REFERENCES

Allan, R.N. and Al-Shakarchi, M.R.G. “Probabilistic techniques in a.c. load-flow analysis”, *Proceedings of the Institution of Electrical Engineers*, vol. 124, no. 2, pp. 154-160, February 1977.

Dagur, D., Parimi, M. and Wagh, S.R., “Prediction of cascade failure using probabilistic approach with AC load flow” IEEE Innovative Smart Grid Technologies-Asia, 2014, pp. 542-547.

Kothari, D.P. and Dhillon, J.S., *Power System Optimization*, PHI, New Delhi, 2007.

Özyön S., The application of genetic algorithm to some environmental economic power dispatch problems, Msc. Thesis, Dumlupınar University, Kütahya, 2009.

Panosyan, A. and Oswald, B.R., “Modified Newton-Raphson load flow analysis for integrated AC/DC power systems” 39th International Universities Power Engineering Conference, 2004, pp. 1223-1227.

Power Systems Test Case Archive. (n.d.). Retrieved September 12, 2017, from https://www2.ee.washington.edu/research/pstca/
MatPower, Retrieved September 12, 2017, from http://www.pserc.cornell.edu/matpower/

Revanthi, A.A., Load flow and optimal power flow analysis using evolutionary computational techniques, Phd Thesis, Anna University, Faculty of Electrical and Electronics Engineering, 2008.

Rossoni, P., Rosa, W.M. and Belati, E.A. “Linearized AC load flow applied to analysis in electric power systems”, *IEEE Latin America Transactions*, vol. 14, no. 9, pp. 4048-4053, September 2016.

Wood, A.J., Wollenberg, B.F. and Sheble, G.B., *Power Generation Operation and Control*, IEEE & Wiley, Third Edition, USA, 2013.

Zahlay, F.D., Strategies, Methods and Tools for Solving Long-term Transmission Expansion Planning in Large-scale Power Systems, Ph.D. Thesis, Spain, 2016.

Appendix

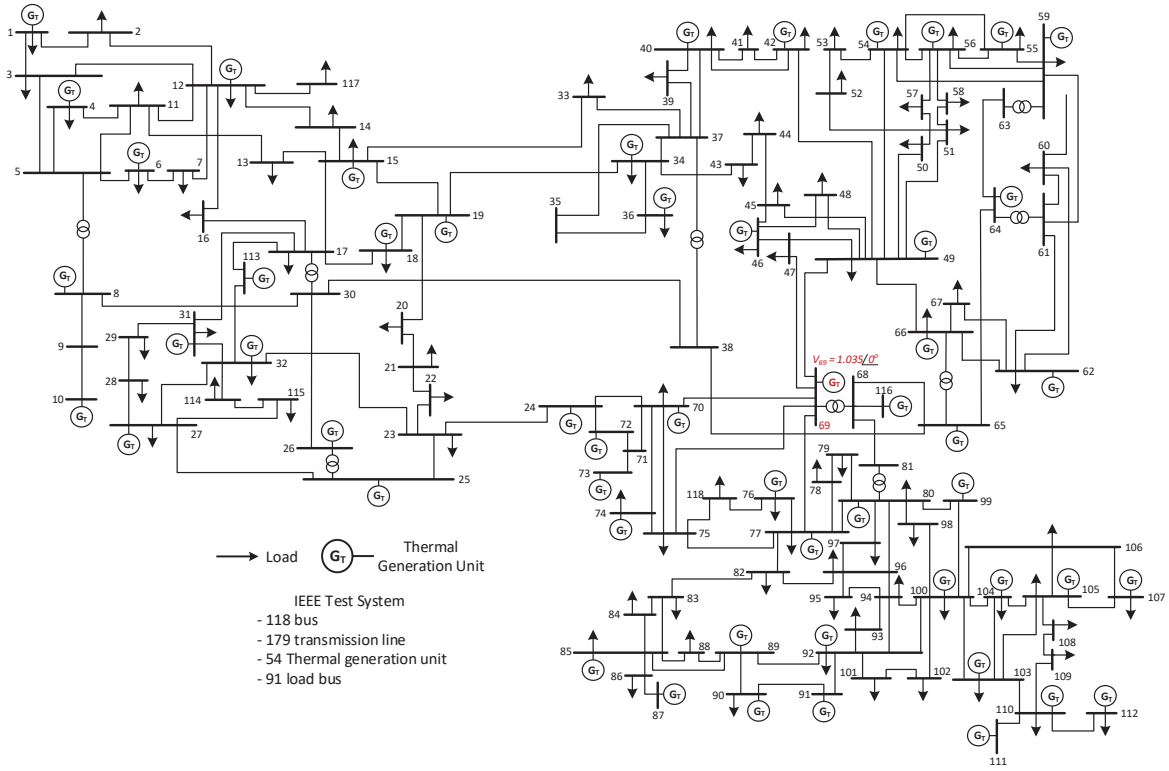

Appendix Figure 1. Single line diagram of the test system.

Appendix Table 1. Values of nominal π equivalent circuits of transmission lines in the sample system

Line no	*From bus*	*To bus*	*R (pu)*	*X (pu)*	*B (pu)*	*Tap*	S_L^{max}
1	1	2	0,03030	0,09990	0,02540	-	1,750
2	1	3	0,01290	0,04240	0,01082	-	1,750
3	4	5	0,00176	0,00798	0,00210	-	5,000
4	3	5	0,02410	0,10800	0,02840	-	1,750
5	5	6	0,01190	0,05400	0,01426	-	1,750
6	6	7	0,00459	0,02080	0,00550	-	1,750
7	8	9	0,00244	0,03050	1,16200	-	5,000
8	8	5	-	0,02670	-	0,985	5,000
9	9	10	0,00258	0,03220	1,23000	-	5,000
10	4	11	0,02090	0,06880	0,01748	-	1,750
11	5	11	0,02030	0,06820	0,01738	-	1,750
12	11	12	0,00595	0,01960	0,00502	-	1,750
13	2	12	0,01870	0,06160	0,01572	-	1,750
14	3	12	0,04840	0,16000	0,04060	-	1,750
15	7	12	0,00862	0,03400	0,00874	-	1,750
16	11	13	0,02225	0,07310	0,01876	-	1,750
17	12	14	0,02150	0,07070	0,01816	-	1,750
18	13	15	0,07440	0,24440	0,06268	-	1,750
19	14	15	0,05950	0,19500	0,05020	-	1,750
20	12	16	0,02120	0,08340	0,02140	-	1,750
21	15	17	0,01320	0,04370	0,04440	-	5,000
22	16	17	0,04540	0,18010	0,04660	-	1,750
23	17	18	0,01230	0,05050	0,01298	-	1,750
24	18	19	0,01119	0,04930	0,01142	-	1,750
25	19	20	0,02520	0,11700	0,02980	-	1,750
26	15	19	0,01200	0,03940	0,01010	-	1,750
27	20	21	0,01830	0,08490	0,02160	-	1,750
28	21	22	0,02090	0,09700	0,02460	-	1,750
29	22	23	0,03420	0,15900	0,04040	-	1,750
30	23	24	0,01350	0,04920	0,04980	-	1,750
31	23	25	0,01560	0,08000	0,08640	-	5,000
32	26	25	-	0,03820	-	0,960	5,000
33	25	27	0,03180	0,16300	0,17640	-	5,000
34	27	28	0,01913	0,08550	0,02160	-	1,750
35	28	29	0,02370	0,09430	0,02380	-	1,750
36	30	17	-	0,03880	-	0,960	5,000
37	8	30	0,00431	0,05040	0,51400	-	1,750
38	26	30	0,00799	0,08600	0,90800	-	5,000
39	17	31	0,04740	0,15630	0,03990	-	1,750
40	29	31	0,01080	0,03310	0,00830	-	1,750
41	23	32	0,03170	0,11530	0,11730	-	1,40
42	31	32	0,02980	0,09850	0,02510	-	1,750
43	27	32	0,02290	0,07550	0,01926	-	1,750
44	15	33	0,03800	0,12440	0,03194	-	1,750
45	19	34	0,07520	0,24700	0,06320	-	1,750
46	35	36	0,00224	0,01020	0,00268	-	1,750
47	35	37	0,01100	0,04970	0,01318	-	1,750
48	33	37	0,04150	0,14200	0,03660	-	1,750
49	34	36	0,00871	0,02680	0,00568	-	1,750
50	34	37	0,00256	0,00940	0,00984	-	5,000
51	38	37	-	0,03750	-	0,935	5,000
52	37	39	0,03210	0,10600	0,02700	-	1,750

53	37	40	0,05930	0,16800	0,04200	-	1,750
54	30	38	0,00464	0,05400	0,42200	-	1,750
55	39	40	0,01840	0,06050	0,01552	-	1,750
56	40	41	0,01450	0,04870	0,01222	-	1,750
57	40	42	0,05550	0,18300	0,04660	-	1,750
58	41	42	0,04100	0,13500	0,03440	-	1,750
59	43	44	0,06080	0,24540	0,06068	-	1,750
60	34	43	0,04130	0,16810	0,04226	-	1,750
61	44	45	0,02240	0,09010	0,02240	-	1,750
62	45	46	0,04000	0,13560	0,03320	-	1,750
63	46	47	0,03800	0,12700	0,03160	-	1,750
64	46	48	0,06010	0,18900	0,04720	-	1,750
65	47	49	0,01910	0,06250	0,01604	-	1,750
66	42	49	0,03575	0,16150	0,17200	-	2,300
67	45	49	0,06840	0,18600	0,04440	-	1,750
68	48	49	0,01790	0,05050	0,01258	-	1,750
69	49	50	0,02670	0,07520	0,01874	-	1,750
70	49	51	0,04860	0,13700	0,03420	-	1,750
71	51	52	0,02030	0,05880	0,01396	-	1,750
72	52	53	0,04050	0,16350	0,04058	-	1,750
73	53	54	0,02630	0,12200	0,03100	-	1,750
74	49	54	0,03993	0,14507	0,14680	-	2,300
75	54	55	0,01690	0,07070	0,02020	-	1,750
76	54	56	0,00275	0,00955	0,00732	-	1,750
77	55	56	0,00488	0,01510	0,00374	-	1,750
78	56	57	0,03430	0,09660	0,02420	-	1,750
79	50	57	0,04740	0,13400	0,03320	-	1,750
80	56	58	0,03430	0,09660	0,02420	-	1,750
81	51	58	0,02550	0,07190	0,01788	-	1,750
82	54	59	0,05030	0,22930	0,05980	-	1,750
83	56	59	0,04070	0,12243	0,11050	-	2,300
84	55	59	0,04739	0,21580	0,05646	-	1,750
85	59	60	0,03170	0,14500	0,03760	-	1,750
86	59	61	0,03280	0,15000	0,03880	-	1,750
87	60	61	0,00264	0,01350	0,01456	-	5,000
88	60	62	0,01230	0,05610	0,01468	-	1,750
89	61	62	0,00824	0,03760	0,00980	-	1,750
90	63	59	-	0,03860	-	0,960	5,000
91	63	64	0,00172	0,02000	0,21600	-	5,000
92	64	61	-	0,02680	-	0,985	5,000
93	38	65	0,00901	0,09860	1,04600	-	5,000
94	64	65	0,00269	0,03020	0,38000	-	5,000
95	49	66	0,00900	0,04595	0,04960	-	8,000
96	62	66	0,04820	0,21800	0,05780	-	1,750
97	62	67	0,02580	0,11700	0,03100	-	1,750
98	65	66	-	0,03700	-	0,935	5,000
99	66	67	0,02240	0,10150	0,02682	-	1,750
100	65	68	0,00138	0,01600	0,63800	-	5,000
101	47	69	0,08440	0,27780	0,07092	-	1,750
102	49	69	0,09850	0,32400	0,08280	-	1,750
103	68	69	-	0,03700	-	0,935	5,000
104	69	70	0,03000	0,12700	0,12200	-	5,000
105	24	70	0,00221	0,41150	0,10198	-	1,750
106	70	71	0,00882	0,03550	0,00878	-	1,750
107	24	72	0,04880	0,19600	0,04880	-	1,750

108	71	72	0,04460	0,18000	0,04444	-	1,750
109	71	73	0,00866	0,04540	0,01178	-	1,750
110	70	74	0,04010	0,13230	0,03368	-	1,750
111	70	75	0,04280	0,14100	0,03600	-	1,750
112	69	75	0,04050	0,12200	0,12400	-	5,000
113	74	75	0,01230	0,04060	0,01034	-	1,750
114	76	77	0,04440	0,14800	0,03680	-	1,750
115	69	77	0,03090	0,10100	0,10380	-	1,750
116	75	77	0,06010	0,19990	0,04978	-	1,750
117	77	78	0,00376	0,01240	0,01264	-	1,750
118	78	79	0,00546	0,02440	0,00648	-	1,750
119	77	80	0,01088	0,03321	0,07000	-	8,000
120	79	80	0,01560	0,07040	0,01870	-	1,750
121	68	81	0,00175	0,02020	0,80800	-	5,000
122	81	80	-	0,03700	-	0,935	5,000
123	77	82	0,02980	0,08530	0,08174	-	2,000
124	82	83	0,01120	0,03665	0,03796	-	2,000
125	83	84	0,06250	0,13200	0,02580	-	1,750
126	83	85	0,04300	0,14800	0,03480	-	1,750
127	84	85	0,03020	0,06410	0,01234	-	1,750
128	85	86	0,03500	0,12300	0,02760	-	5,000
129	86	87	0,02828	0,20740	0,04450	-	5,000
130	85	88	0,02000	0,10200	0,02760	-	1,750
131	85	89	0,02390	0,17300	0,04700	-	1,750
132	88	89	0,01390	0,07120	0,01934	-	5,000
133	89	90	0,01638	0,06517	0,15880	-	8,000
134	90	91	0,02540	0,08360	0,02140	-	1,750
135	89	92	0,00799	0,03829	0,09620	-	8,000
136	91	92	0,03870	0,12720	0,03268	-	1,750
137	92	93	0,02580	0,08480	0,02180	-	1,750
138	92	94	0,04810	0,15800	0,04060	-	1,750
139	93	94	0,02230	0,07320	0,01876	-	1,750
140	94	95	0,01320	0,04340	0,01110	-	1,750
141	80	96	0,03560	0,18200	0,04940	-	1,750
142	82	96	0,01620	0,05300	0,05440	-	1,750
143	94	96	0,02690	0,08690	0,02300	-	1,750
144	80	97	0,01830	0,09340	0,02540	-	1,750
145	80	98	0,02380	0,10800	0,02860	-	1,750
146	80	99	0,04540	0,20600	0,05460	-	2,000
147	92	100	0,06480	0,29500	0,04720	-	1,750
148	94	100	0,01780	0,05800	0,06040	-	1,750
149	95	96	0,01710	0,05470	0,01474	-	1,750
150	96	97	0,01730	0,08850	0,02400	-	1,750
151	98	100	0,03970	0,17900	0,04760	-	1,750
152	99	100	0,01800	0,08130	0,02160	-	1,750
153	100	101	0,02770	0,12620	0,03280	-	1,750
154	92	102	0,01230	0,05590	0,01464	-	1,750
155	101	102	0,02460	0,11200	0,02940	-	1,750
156	100	103	0,01600	0,05250	0,05360	-	5,000
157	100	104	0,04510	0,20400	0,05410	-	1,750
158	103	104	0,04660	0,15840	0,04070	-	1,750
159	103	105	0,05350	0,16250	0,04080	-	1,750
160	100	106	0,06050	0,22900	0,06200	-	1,750
161	104	105	0,00994	0,03780	0,00986	-	1,750
162	105	106	0,01400	0,05470	0,01434	-	1,750

163	105	107	0,05300	0,18300	0,04720	-	1,750
164	105	108	0,02610	0,07030	0,01844	-	1,750
165	106	107	0,05300	0,18300	0,04720	-	1,750
166	108	109	0,01050	0,02880	0,00760	-	1,750
167	103	110	0,03906	0,18130	0,04610	-	1,750
168	109	110	0,02780	0,07620	0,02020	-	1,750
169	110	111	0,02200	0,07550	0,02000	-	1,750
170	110	112	0,02470	0,06400	0,06200	-	1,750
171	17	113	0,00913	0,03010	0,00768	-	1,750
172	32	113	0,06150	0,20300	0,05180	-	5,000
173	32	114	0,01350	0,06120	0,01628	-	1,750
174	27	115	0,01640	0,07410	0,01972	-	1,750
175	114	115	0,00230	0,01040	0,00276	-	1,750
176	68	116	0,00034	0,00405	0,16400	-	5,000
177	12	117	0,03290	0,14000	0,03580	-	1,750
178	75	118	0,01450	0,04810	0,01198	-	1,750
179	76	118	0,01640	0,05440	0,01356	-	1,750

Appendix Table 2. Active and reactive load values in the sample system.

Bus No	P_{load} ***(pu)***	Q_{load} ***(pu)***	***Bus No***	P_{load} ***(pu)***	Q_{load} ***(pu)***
1	0,5100	0,2700	**60**	0,7800	0,0300
2	0,2000	0,0900	**61**	-	-
3	0,3900	0,1000	**62**	0,7700	0,1400
4	0,3900	0,1200	**63**	-	-
5	-	-	**64**	-	-
6	0,5200	0,2200	**65**	-	-
7	0,1900	0,0200	**66**	0,3900	0,1800
8	0,2800	0,0000	**67**	0,2800	0,0700
9	-	-	**68**	-	-
10	-	-	**69**	-	-
11	0,7000	0,2300	**70**	0,6600	0,2000
12	0,4700	0,1000	**71**	-	-
13	0,3400	0,1600	**72**	0,1200	-
14	0,1400	0,0100	**73**	0,0600	-
15	0,9000	0,3000	**74**	0,6800	0,2700
16	0,2500	0,1000	**75**	0,4700	0,1100
17	0,1100	0,0300	**76**	0,6800	0,3600
18	0,6000	0,3400	**77**	0,6100	0,2800
19	0,4500	0,2500	**78**	0,7100	0,2600
20	0,1800	0,0300	**79**	0,3900	0,3200
21	0,1400	0,0800	**80**	1,3000	0,2600
22	0,1000	0,0500	**81**	-	-
23	0,0700	0,0300	**82**	0,5400	0,2700
24	0,1300	-	**83**	0,2000	0,1000
25	-	-	**84**	0,1100	0,0700
26	-	-	**85**	0,2400	0,1500
27	0,7100	0,1300	**86**	0,2100	0,1000
28	0,1700	0,0700	**87**	-	-
29	0,2400	0,0400	**88**	0,4800	0,1000
30	-	-	**89**	-	-
31	0,4300	0,2700	**90**	1,6300	0,4200
32	0,5900	0,2300	**91**	0,1000	-
33	0,2300	0,0900	**92**	0,6500	0,1000
34	0,5900	0,2600	**93**	0,1200	0,0700

35	0,3300	0,0900	**94**	0,3000	0,1600
36	0,3100	0,1700	**95**	0,4200	0,3100
37	-	-	**96**	0,3800	0,1500
38	-	-	**97**	0,1500	0,0900
39	0,2700	0,1100	**98**	0,3400	0,0800
40	0,6600	0,2300	**99**	0,4200	-
41	0,3700	0,1000	**100**	0,3700	0,1800
42	0,9600	0,2300	**101**	0,2200	0,1500
43	0,1800	0,0700	**102**	0,0500	0,0300
44	0,1600	0,0800	**103**	0,2300	0,1600
45	0,5300	0,2200	**104**	0,3800	0,2500
46	0,2800	0,1000	**105**	0,3100	0,2600
47	0,3400	-	**106**	0,4300	0,1600
48	0,2000	0,1100	**107**	0,5000	0,1200
49	0,8700	0,3000	**108**	0,0200	0,0100
50	0,1700	0,0400	**109**	0,0800	0,0300
51	0,1700	0,0800	**110**	0,3900	0,3000
52	0,1800	0,0500	**111**	-	-
53	0,2300	0,1100	**112**	0,6800	0,1300
54	1,1300	0,3200	**113**	0,0600	-
55	0,6300	0,2200	**114**	0,0800	0,0300
56	0,8400	0,1800	**115**	0,2200	0,0700
57	0,1200	0,0300	**116**	1,8400	-
58	0,1200	0,0300	**117**	0,2000	0,0800
59	2,7700	1,1300	**118**	0,3300	0,1500
Total Load		***P_{load}:*** 42,4200		***Q_{load}:*** 14,3800	

Appendix Table 3. AC load flow initial values of the generation units in the sample system

Gen. Unit	*Bus*	*P_i (pu)*	*Q_i (pu)*	*V (pu)*	*Gen. Unit*	*Bus*	*P_i (pu)*	*Q_i (pu)*	*V (pu)*
1	1	0,500	0,075	0,995	**28**	65	2,000	1,000	1,005
2	4	0,500	1,500	0,998	**29**	66	2,000	1,000	1,050
3	6	0,500	0,250	0,990	**30**	69	-	-	1,035
4	8	0,500	1,500	1,015	**31**	70	0,500	0,150	0,984
5	10	2,000	1,000	1,050	**32**	72	0,500	0,500	0,980
6	12	1,000	0,600	0,990	**33**	73	0,500	0,500	0,991
7	15	0,500	0,150	0,970	**34**	74	0,500	0,045	0,958
8	18	0,500	0,250	0,973	**35**	76	0,500	0,120	0,943
9	19	0,500	0,120	0,962	**36**	77	0,500	0,350	1,006
10	24	0,500	1,500	0,992	**37**	80	2,000	1,400	1,040
11	25	1,000	0,700	1,050	**38**	85	0,500	0,120	0,985
12	26	2,000	5,000	1,015	**39**	87	0,500	5,000	1,015
13	27	0,500	1,500	0,968	**40**	89	2,000	1,500	1,005
14	31	0,500	1,500	0,967	**41**	90	0,500	1500	0,985
15	32	0,500	0,210	0,963	**42**	91	0,500	0,500	0,980
16	34	0,500	0,120	0,984	**43**	92	0,500	0,045	0,990
17	36	0,500	0,120	0,980	**44**	99	0,500	0,500	1,010
18	40	0,500	1,500	0,970	**45**	100	1,000	0,750	1,017
19	42	0,500	1,500	0,985	**46**	103	0,500	0,200	1,010
20	46	0,500	0,500	1,005	**47**	104	0,500	0,120	0,971
21	49	1,000	1,000	1,025	**48**	105	0,500	0,120	0,965
22	54	0,500	1,500	0,955	**49**	107	0,500	1,000	0,952
23	55	0,500	0,120	0,952	**50**	110	0,500	0,120	0,973
24	56	0,500	0,075	0,954	**51**	111	0,500	5,000	0,980
25	59	1,000	0,900	0,985	**52**	112	0,500	5,000	0,975

26	61	1,000	1,500	0,995	**53**	113	0,500	1,000	0,993
27	62	0,500	0,100	0,998	**54**	116	0,500	5,000	1,005

Appendix Table 4. Operating limit values of generation units in the sample system.

Gen. Unit	*Bus*	P_{min} *(pu)*	P_{max} *(pu)*	Q_{min} *(pu)*	Q_{max} *(pu)*	V_{min} *(pu)*	V_{max} *(pu)*
1	1	0,0000	1,0000	-0,0500	0,1500	0,9400	1,0600
2	4	0,0000	1,0000	-3,0000	3,0000	0,9400	1,0600
3	6	0,0000	1,0000	-0,1300	0,5000	0,9400	1,0600
4	8	0,0000	1,0000	-3,0000	3,0000	0,9400	1,0600
5	10	0,0000	5,5000	-1,4700	2,0000	0,9400	1,0600
6	12	0,0000	1,8500	-0,3500	1,2000	0,9400	1,0600
7	15	0,0000	1,0000	-0,1000	0,3000	0,9400	1,0600
8	18	0,0000	1,0000	-0,1600	0,5000	0,9400	1,0600
9	19	0,0000	1,0000	-0,0800	0,2400	0,9400	1,0600
10	24	0,0000	1,0000	-3,0000	3,0000	0,9400	1,0600
11	25	0,0000	3,2000	-0,4700	1,4000	0,9400	1,0600
12	26	0,0000	4,1400	-10,0000	10,0000	0,9400	1,0600
13	27	0,0000	1,0000	-3,0000	3,0000	0,9400	1,0600
14	31	0,0000	1,0700	-3,0000	3,0000	0,9400	1,0600
15	32	0,0000	1,0000	-0,1400	0,4200	0,9400	1,0600
16	34	0,0000	1,0000	-0,0800	0,2400	0,9400	1,0600
17	36	0,0000	1,0000	-0,0800	0,2400	0,9400	1,0600
18	40	0,0000	1,0000	-3,0000	3,0000	0,9400	1,0600
19	42	0,0000	1,0000	-3,0000	3,0000	0,9400	1,0600
20	46	0,0000	1,1900	-1,0000	1,0000	0,9400	1,0600
21	49	0,0000	3,0400	-0,8500	2,1000	0,9400	1,0600
22	54	0,0000	1,4800	-3,0000	3,0000	0,9400	1,0600
23	55	0,0000	1,0000	-0,0800	0,2300	0,9400	1,0600
24	56	0,0000	1,0000	-0,0800	0,1500	0,9400	1,0600
25	59	0,0000	2,5500	-0,6000	1,8000	0,9400	1,0600
26	61	0,0000	2,6000	-1,0000	3,0000	0,9400	1,0600
27	62	0,0000	1,0000	-0,2000	0,2000	0,9400	1,0600
28	65	0,0000	4,9100	-0,6700	2,0000	0,9400	1,0600
29	66	0,0000	4,9200	-0,6700	2,0000	0,9400	1,0600
30	69	0,0000	8,0520	-3,0000	3,0000	0,9400	1,0600
31	70	0,0000	1,0000	-0,1000	0,3200	0,9400	1,0600
32	72	0,0000	1,0000	-1,0000	1,0000	0,9400	1,0600
33	73	0,0000	1,0000	-1,0000	1,0000	0,9400	1,0600
34	74	0,0000	1,0000	-0,0600	0,0900	0,9400	1,0600
35	76	0,0000	1,0000	-0,0800	0,2300	0,9400	1,0600
36	77	0,0000	1,0000	-0,2000	0,7000	0,9400	1,0600
37	80	0,0000	5,7700	-1,6500	2,8000	0,9400	1,0600
38	85	0,0000	1,0000	-0,0800	0,2300	0,9400	1,0600
39	87	0,0000	1,0400	-1,0000	10,0000	0,9400	1,0600
40	89	0,0000	7,0700	-2,1000	3,0000	0,9400	1,0600
41	90	0,0000	1,0000	-3,0000	3,0000	0,9400	1,0600
42	91	0,0000	1,0000	-1,0000	1,0000	0,9400	1,0600
43	92	0,0000	1,0000	-0,0300	0,0900	0,9400	1,0600
44	99	0,0000	1,0000	-1,0000	1,0000	0,9400	1,0600
45	100	0,0000	3,5200	-0,5000	1,5500	0,9400	1,0600
46	103	0,0000	1,4000	-0,1500	0,4000	0,9400	1,0600

47	104	0,0000	1,0000	-0,0800	0,2300	0,9400	1,0600
48	105	0,0000	1,0000	-0,0800	0,2300	0,9400	1,0600
49	107	0,0000	1,0000	-2,0000	2,0000	0,9400	1,0600
50	110	0,0000	1,0000	-0,0800	0,2300	0,9400	1,0600
51	111	0,0000	1,3600	-1,0000	10,0000	0,9400	1,0600
52	112	0,0000	1,0000	-1,0000	10,0000	0,9400	1,0600
53	113	0,0000	1,0000	-1,0000	2,0000	0,9400	1,0600
54	116	0,0000	1,0000	-10,0000	10,0000	0,9400	1,0600

Appendix Table 5. The values obtained as a result of AC load flow of all the buses in the sample system.

Bus No	***V (pu)***	***δ (R)***	***P_{gen} (pu)***	***Q_{gen} (pu)***	***Bus No***	***V (pu)***	***δ (R)***	***P_{gen} (pu)***	***Q_{gen} (pu)***
1	0,9550	-0,0326	0,5000	-0,1882	**60**	0,9932	-0,1631	-	-
2	0,9715	-0,0401	-	-	**61**	0,9950	-0,1496	1,0000	-0,3185
3	0,9678	-0,0351	-	-	**62**	0,9980	-0,1523	0,5000	-0,1092
4	0,9980	-0,0012	0,5000	-0,3627	**63**	0,9688	-0,1656	-	-
5	1,0028	0,0007	-	-	**64**	0,9836	-0,1365	-	-
6	0,9900	-0,0185	0,5000	0,0169	**65**	1,0050	-0,0788	2,0000	0,8208
7	0,9893	-0,0265	-	-	**66**	1,0500	-0,1034	2,0000	0,1283
8	1,0150	0,0428	0,5000	-0,2691	**67**	1,0200	-0,1396	-	-
9	1,0500	0,0973	-	-	**68**	1,0032	-0,0699	-	-
10	1,0500	0,1560	2,0000	-0,7807	**69**	1,0350	0,0000	4,5346	-0,5042
11	0,9855	-0,0324	-	-	**70**	0,9840	0,0156	0,5000	-0,1494
12	0,9900	-0,0331	1,0000	0,8467	**71**	0,9869	0,0444	-	-
13	0,9687	-0,0519	-	-	**72**	0,9800	0,1112	0,5000	-0,2242
14	0,9836	-0,0426	-	-	**73**	0,9910	0,0647	0,5000	0,0042
15	0,9700	-0,0394	0,5000	-0,0458	**74**	0,9580	-0,0318	0,5000	-0,1250
16	0,9833	-0,0397	-	-	**75**	0,9686	-0,0436	-	-
17	0,9933	-0,0111	-	-	**76**	0,9430	-0,0703	0,5000	-0,1319
18	0,9730	-0,0244	0,5000	0,1853	**77**	1,0060	-0,0802	0,5000	0,1428
19	0,9620	-0,0345	0,5000	-0,2941	**78**	1,0015	-0,0898	-	-
20	0,9588	-0,0335	-	-	**79**	1,0043	-0,0931	-	-
21	0,9606	-0,0162	-	-	**80**	1,0400	-0,0805	2,0000	1,7349

22	0,9723	0,0164	-	-	**81**	0,9962	-0,0736	-	-
23	1,0012	0,0834	-	-	**82**	0,9801	-0,0946	-	-
24	0,9920	0,0978	0,5000	-0,2436	**83**	0,9767	-0,0823	-	-
25	1,0500	0,1334	1,0000	0,5919	**84**	0,9775	-0,0538	-	-
26	1,0150	0,1484	2,0000	-0,0189	**85**	0,9850	-0,0344	0,5000	-0,0683
27	0,9680	0,0374	0,5000	-0,1697	**86**	0,9898	0,0027	-	-
28	0,9616	0,0154	-	-	**87**	1,0150	0,1038	0,5000	0,0570
29	0,9631	0,0072	-	-	**88**	0,9893	-0,0430	-	-
30	0,9907	0,0161	-	-	**89**	1,0050	-0,0157	2,0000	0,4733
31	0,9670	0,0124	0,5000	0,2063	**90**	0,9850	-0,0655	0,5000	0,4176
32	0,9630	0,0351	0,5000	-0,3544	**91**	0,9800	-0,0304	0,5000	-0,2758
33	0,9709	-0,0858	-	-	**92**	0,9900	-0,0398	0,5000	-0,3647
34	0,9840	-0,1063	0,5000	-0,2759	**93**	0,9858	-0,0624	-	-
35	0,9807	-0,1089	-	-	**94**	0,9889	-0,0741	-	-
36	0,9800	-0,1062	0,5000	-0,0869	**95**	0,9781	-0,0917	-	-
37	0,9921	-0,1060	-	-	**96**	0,9885	-0,0953	-	-
38	0,9694	-0,0608	-	-	**97**	1,0093	-0,0940	-	-
39	0,9705	-0,1643	-	-	**98**	1,0234	-0,0879	-	-
40	0,9700	-0,1828	0,5000	0,1216	**99**	1,0100	-0,0464	0,5000	-0,2875
41	0,9668	-0,2044	0,0000	0,0000	**100**	1,0170	-0,0433	1,0000	1,2848
42	0,9850	-0,2143	0,5000	0,1998	**101**	0,9927	-0,0570	-	-
43	0,9704	-0,1649	-	-	**102**	0,9901	-0,0474	-	-
44	0,9704	-0,2063	-	-	**103**	1,0100	-0,0200	0,5000	0,5789
45	0,9782	-0,2071	-	-	**104**	0,9710	-0,0125	0,5000	-0,1276
46	1,0050	-0,1707	0,5000	0,0329	**105**	0,9650	-0,0128	0,5000	-0,1532
47	1,0173	-0,1611	-	-	**106**	0,9624	-0,0345	-	-
48	1,0149	-0,1778	-	-	**107**	0,9520	-0,0201	0,5000	-0,0441
49	1,0250	-0,1714	1,0000	1,3987	**108**	0,9664	-0,0016	-	-
50	1,0015	-0,2010	-	-	**109**	0,9672	0,0036	-	-

51	0,9677	-0,2393	-	-	**110**	0,9730	0,0233	0,5000	-0,0481
52	0,9577	-0,2542	-	-	**111**	0,9800	0,0639	0,5000	-0,0540
53	0,9464	-0,2665	-	-	**112**	0,9750	0,0085	0,5000	0,2021
54	0,9550	-0,2471	0,5000	0,0191	**113**	0,9930	0,0064	0,5000	-0,0190
55	0,9520	-0,2456	0,5000	-0,0980	**114**	0,9601	0,0263	-	-
56	0,9540	-0,2461	0,5000	-0,2127	**115**	0,9600	0,0256	-	-
57	0,9710	-0,2337	-	-	**116**	1,0050	-0,0755	0,5000	0,4698
58	0,9595	-0,2474	-	-	**117**	0,9738	-0,0600	-	-
59	0,9850	-0,2213	1,0000	0,8911	**118**	0,9501	-0,0640	-	-

Total Active Power	43,034601	***Total P Load***	42,420000	P_{loss}	0,614601
Total Reactive Power	4,419482	***Total Q Load***	14,380000	Q_{loss}	-9,961833
***Time (sec)*:** 0,034583					

e-issn: 1308-5514